



Article

# Mn-Doped Carbon Dots as Contrast Agents for Magnetic Resonance and Fluorescence Imaging

Corneliu S. Stan <sup>1,2,\*</sup>, Adina Coroaba <sup>1</sup>, Natalia Simionescu <sup>1</sup>, Cristina M. Uritu <sup>1,3</sup>, Dana Bejan <sup>1</sup>, Laura E. Ursu <sup>1</sup>, Andrei-Ioan Dascalu <sup>1</sup>, Florica Doroftei <sup>1</sup>, Marius Dobromir <sup>4</sup>, Cristina Albu <sup>1,2</sup> and Conchi O. Ania <sup>1,5,\*</sup>

- Centre of Advanced Research in Bionanoconjugates and Biopolymers, "Petru Poni" Institute of Macromolecular Chemistry, 41A Grigore Ghica Voda Alley, 700487 Iasi, Romania; adina.coroaba@icmpp.ro (A.C.); natalia.simionescu@icmpp.ro (N.S.); cristina-mariana.uritu@umfiasi.ro (C.M.U.); bejan.dana@icmpp.ro (D.B.); ursu.laura@icmpp.ro (L.E.U.); andrei.dascalu@icmpp.ro (A.-I.D.); florica.doroftei@icmpp.ro (F.D.); albuc@ymail.com (C.A.)
- <sup>2</sup> Faculty of Chemical Engineering and Environmental Protection, "Gheorghe Asachi" Technical University of Iasi, 73 D. Mangeron Ave., 700050 Iasi, Romania
- <sup>3</sup> Advanced Center for Research and Development in Experimental Medicine "Prof. Ostin C. Mungiu" (CEMEX), "Grigore T. Popa" University of Medicine and Pharmacy, 16 Universitatii Street, 700115 Iasi, Romania
- <sup>4</sup> Science Research Department, Institute of Interdisciplinary Research, Research Center on Advanced Materials and Technologies (RAMTECH), "Alexandru I. Cuza" University of Iasi, 11 Carol I Boulevard, 700506 Iasi, Romania; marius.dobromir@uaic.ro
- <sup>5</sup> CEMHTI (CNRS, UPR 3079), Université d'Orléans, 45100 Orleans, France
- \* Correspondence: stancs@tuiasi.ro (C.S.S.); conchi.ania@cnrs-orleans.fr (C.O.A.)

### **Abstract**

Carbon nanodots have recently attracted attention as fluorescence imaging probes and magnetic resonance imaging (MRI) contrast agents in diagnostic and therapeutic applications due to their unique optical properties. In this work we report the synthesis of biocompatible Mn (II)-doped carbon nanodots and their performance as fluorescence and MRI contrast agents in in vitro assays. The thermal decomposition of a Diphenylhydantoin-Mn(II) complex assured the incorporation of manganese (II) ions in the carbon dots. The obtained materials display a favorable spin density for MRI applications. The synthesized Mn(II)-CNDs also displayed remarkable photoluminescence, with a bright blue emission and good response in in vitro fluorescence imaging. Cytotoxicity investigations revealed good cell viability on malignant melanoma cell lines in a large concentration range. A cytotoxic effect was observed for MG-63 osteosarcoma and breast adenocarcinoma cell lines. The in vitro MRI assays demonstrated the potentialities of the Mn(II)-CNDs as T2 contrast agents at low dosages, with relaxivity values higher than those of commercial ones. Due to the simplicity of their synthetic pathway and their low cytotoxicity, the prepared Mn(II)-CNDs are potential alternatives to currently used contrast agents based on gadolinium complexes.

**Keywords:** carbon nanodots; manganese complexes; diphenylhydantoin; magnetic resonance imaging; contrast agents; fluorescence imaging

Academic Editor: Paolo Prosposito

Received: 17 May 2025 Revised: 25 June 2025 Accepted: 26 June 2025 Published: 29 June 2025

Citation: Stan, C.S.; Coroaba, A.; Simionescu, N.; Uritu, C.M.; Bejan, D.; Ursu, L.E.; Dascalu, A.-I.; Doroftei, F.; Dobromir, M.; Albu, C.; et al. Mn-Doped Carbon Dots as Contrast Agents for Magnetic Resonance and Fluorescence Imaging. *Int. J. Mol. Sci.* 2025, 26, 6293. https://doi.org/10.3390/ ijms26136293

Copyright: © 2025 by the author. Licensee MDPI, Basel, Switzerland. This article is an open access article distributed under the terms and conditions of the Creative Commons Attribution (CC BY) license (https://creativecommons.org/license s/by/4.0/).

## 1. Introduction

Low-dimensional carbon nanodots (CNDs) are a newer class of carbon materials that consists of a carbon core (amorphous and/or graphitic-like) decorated with avariety of

functional groups on the surface [1,2]. They have garnered significant interest in nanomedicine as efficient platforms for both therapeutic and diagnostic applications [3–7]. The most important properties of CNDs in biomedical applications are their tunable photoluminescence upon their composition [8,9], their dual capacity to act as antioxidants and radical scavengers [10,11] and their biocompatibility [6]. In this regard, while most CNDs are generally considered as biocompatible and low/non-toxic, these features strongly depend on the nature of the precursor and the synthetic route [6,12]. The challenge is to control the optical and structural properties of the prepared CNDs. The incorporation of metallic heteroatoms in carbon dots seems a useful strategy to obtain CNDs with modulated optical and structural properties and expand their use in bio-applications [13-15]. As a few examples, several studies have reported the synthesis of carbon dots doped with transition metal ions (e.g., Ru-, Fe-, Co-, Ni-) and their application in bimodal medical imaging, biosensors, gene detection, and drug delivery [13-17]. Those studies have pointed out metal-doped carbon dots as competitive materials compared to benchmarks in those fields. The difficulty is to avoid the aggregation of the metallic species in their synthesis, as this is responsible for a heterogeneous surface distribution of metal ions.

Numerous studies also report the anti-tumoral effect of carbon dots and their potential application as fluorescent probes and magnetic resonance imaging (MRI) contrast agents [18–24]. For instance, magneto-fluorescent Gd-doped CNDs prepared from starch have shown dual modal fluorescence and worked as MRI contrast agents in diagnosis and brain mapping applications [19]. Another recent study shows the potential use of CND micelles prepared from leek seeds in sensor applications and cancer therapy [20]. In a similar approach, CNDs prepared from red beans were studied as anti-tumoral agents on 16 cell lines such as liver/pancreatic cancer cells, intrahepatic cholangiocarcinoma cells, and colorectal adenocarcinoma cells [21]. CNDs prepared through hydrothermal approaches of microcrystalline cellulose were found to have a dual anti-tumoral and microbicide action through the inhibition of the proliferation of hepatocellular carcinoma and several pathogens (e.g., bacteria and fungi) [22]. Cu-doped CNDs have been investigated as inhibitors of breast cancer's progression [23].

In this context, our recent studies have demonstrated the application of Mn-doped carbon dots obtained from a commercial commodity with a high surface functionalization as theranostic platforms for breast cancer treatment in in vitro/in vivo assays [24]. Based on those previous studies, in this work we explore the synthesis of Mn-doped CNDs from the thermal degradation of a Mn(II) complex and their application as fluorescent probes for fluorescence imaging and as MRI contrast agents. To achieve a homogeneous distribution of the manganese ion, our novel approach is based on the thermal decomposition of the complex Diphenylhydantoin-Mn(II). Diphenylhydantoin (also known as Phenytoin) has a favorable structural configuration able to yield stable transition metal complexes [25,26]. Besides its complexation potential, DPH is biocompatible, since it is used as an anti-seizure and anti-arrhythmias medication. These are important criteria to obtain compatible metal-doped carbon dots for biomedical applications. In this study, the morpho-structural characteristics of the Mn(II)-DPH complex and the Mn-doped CNDs have been investigated in detail, such as their photoluminescence properties, biocompatibility, and cytotoxicity on various cancer cell lines and their efficiency as fluorescent probes and MRI contrast agents from in vitro assays[27–29]. Their performance has been compared to that of commercial contrast agents based on gadolinium complexes.

## 2. Results and Discussion

## 2.1. Characterization of the Mn-Doped Carbon Dots

The thermogravimetric profiles of the Mn-doped CNDs compared to those of the raw ligand (DPH) and the Mn(II)-DPH complex are shown in Figure 1(left). The degradation profile of DPH shows a sharp decomposition between 300 and 400 °C (maximum at around 375 °C) attributed to its complete degradation (the final mass loss is ca. 97.4 wt.%). When the complex is formed, the profile shows several mass losses and a final mass loss of 82 wt.%; this indicates an increased thermal stability compared to pristine DPH. The first weight loss for the complex Mn(II)-DPH occurs in the 80–240 °C range and accounts for ca. 13.8 wt.%. This is attributed to the loss of water molecules within the outer coordination sphere of the Mn(II) cations and the beginning of the structural decomposition of the material (the expected general formula is Mn(C15H10N2O2)2(H2O)x). The second weight loss for the Mn(II)-DPH complex (ca. 14.38 wt.%) is attributed to the continuous intermolecular breaking and incipient decomposition of the molecular structure. The sharp mass loss (50.54 wt.%) at 330 °C accounts for the complete degradation of the complex. It occurs at a lower temperature than DPH, which confirms the binding of the ligand to the manganese ions in the complex. The tail at 375 °C would suggest a minor contribution of free DPH (ca. 5 wt.%).

The thermogravimetric profiles of the Mn(II)-CNDs show several peaks at 150 and 225 °C attributed to the decomposition of labile O- and N- surface moieties. These remnant functional groups are particularly important to achieve photoluminescence properties. The Mn(II)-CNDs showed a final mass loss of ca. 28 wt.%, ca. four times higher than that of the Mn(II)-DPH complex. This indicates a rearrangement of the volatile matter of the complex during the thermal treatment at 490 °C for 10 min. The continuous mass loss above 400 °C indicates the presence of some functional groups and/or volatile matter that would still be decomposed upon further heating over 700 °C.

Figure 1(right) shows the IR spectra of the prepared samples, and Table 1 compiles the main vibration peaks and their attributions to various groups. The spectra of the Mn(II)-DPH complex shows several differences with that of free DPH. For instance, the band located at 3600–3200 cm<sup>-1</sup> characteristic of OH stretching frequencies indicates the presence of water molecules within the outer coordination sphere of the Mn(II) cations (also observed in the thermogravimetric profiles). The small intensity of the N-H stretch signal (3479 cm<sup>-1</sup>) in DPH ligand was no longer visible in the Mn(II)-DPH complex. Small displacements in the vibration signals of C=N and C=O (e.g., 1770–1600 cm<sup>-1</sup>) observed in the complex are attributed to the presence of the coordinative bonding of nitrogen and oxygen atoms with a central Mn(II) cation. The peak at 1010 cm<sup>-1</sup> in free DPH decreased significantly for the complex Mn(II)-DPH, while a new band appeared at 950 cm<sup>-1</sup> in the complex. This can be assigned to (Mn–N) stretching vibrations [30]. Small differences in the fingerprint region 800–400 cm<sup>-1</sup> are attributed to Mn-N metal–ligand bonds in the complex.

*Int. J. Mol. Sci.* **2025**, *26*, 6293 4 of 22

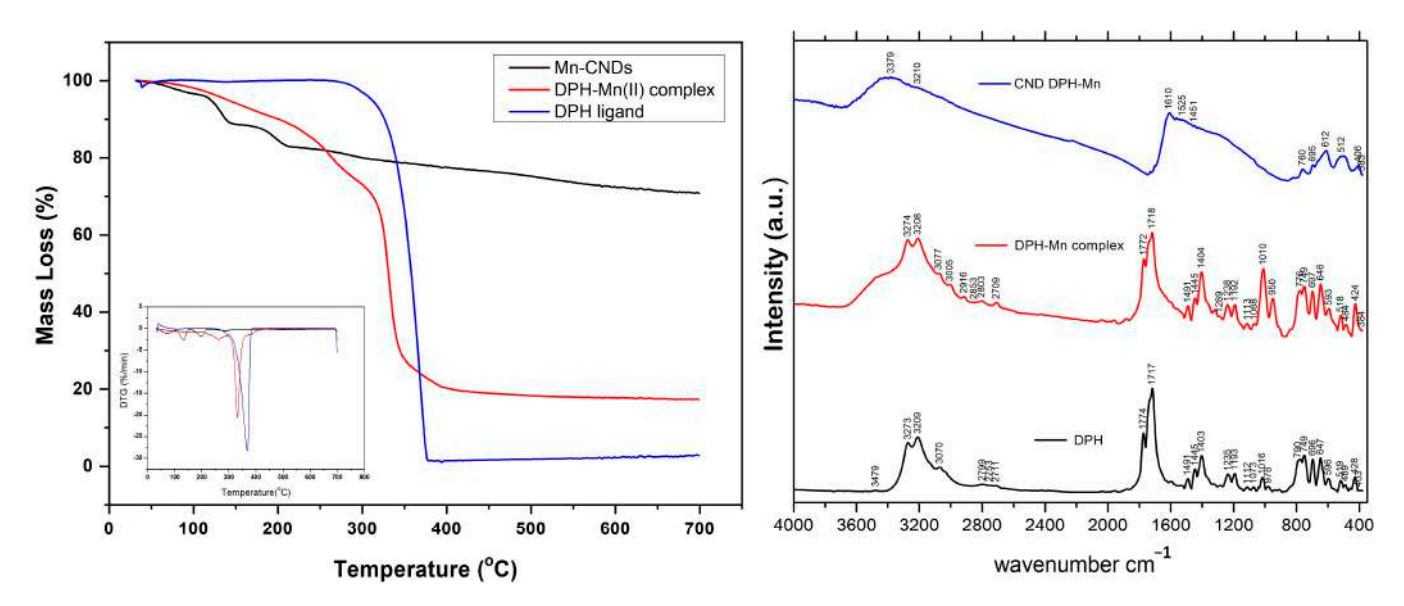


**Figure 1.** (**left**) Thermogravimetric profiles and DTG plots (inset); (**right**) IR spectra recorded for DPH ligand, Mn(II)-DPH complex, and Mn(II)-CNDs.

In the Mn(II)- CNDs, a wide hump at  $3600-3000~\rm cm^{-1}$ , characteristic of OH stretching in different configurations (OH surface groups) in carbon materials, is observed. The bands at  $17,750-1700~\rm cm^{-1}$  of the C=N and C=O vibrations of the DPH and the complex are no longer observed in the Mn-CDs, but the band at  $1610~\rm cm^{-1}$  characteristic of fused aromatic carbon atoms is pronounced. The bands between  $1010~\rm and~900~cm^{-1}$  assigned to M-N vibrations are also not visible after the thermal treatment of the complex.

**Table 1.** Summary of main IR bands and assignment to specific vibration groups recorded for DPH ligand, Mn(II)-DPH complex, and Mn-CNDs.

Description	Recorded Peaks (cm <sup>-1</sup> )							
Description	DPH	Mn(II)-DPH	Mn(II)-CNDs					
N-H stretch	3479	-	-					
OH stretch	3273	3274	included in 3279/3210 broad peak					
C-H stretch	3070	-	included in 3279/3210 broad peak					
C=C/C-C stretch	2799/2711/1235	2709/2703	included in 3279/3210 broad peak					
C=O asym. stretch	1774	1772	included in 1610 broad peak					
C=O sym. stretch	1717	1718	included in 1610 broad peak					
Amide band	-	-	included in 1610, 1529 broad peaks					
C-N-H deformation	1491	1491	1451					
Aromatic ring stretch	1445	1445	included in broad peak of 1610					
N-H def.	1403	1404	-					
N-C=O def.	749/696	749/697	760/695					
C-N-C def.	647	646	612					
C-C=O def.	519	518	512					

The composition of the carbon dots was further evaluated by XPS and EDX. Table 2 presents the elemental composition as determined by EDX (raw data is shown in Figure S4, Supplementary Information), compared to data obtained from XPS (Figure 2 shows the high-resolution core-level spectra of all the detected atoms; wide scan spectra are also shown in Figure S5) and flame atomic absorption spectroscopy (FAAS) for manganese. For comparison purposes, Table 2 also shows the composition of the Mn-doped carbon dots recalculated without chlorine (from the MnCl<sub>2</sub> salt used to form the complex). The amount of bulk manganese detected by EDX and FAAS ranged between 4.8 and 5.8 at.%;

Int. J. Mol. Sci. 2025, 26, 6293 5 of 22

the values are in line with the surface concentration of manganese of ca. 4.3 at.% detected by XPS. This confirms that a substantial amount of manganese has been effectively incorporated into the carbon dot structure.

Table 2. Elemental composition	(at.%) of samples DPH-CNDs (undoped) and Mn(II)-CNDs rec-
orded by EDX, XPS, and FAAS.	

	EDX					XPS				
Element	DPH-	Mn(II)-	Mn(II)-CNDs Normal-	DPH-	Mn(II)-	Mn(II)-CNDs Normal-	Mn(II)-			
	CNDs	CNDs	ized Without Cl	CNDs	CNDs	ized Without Cl	CNDs			
С	90.81	70.32	76.14	86.84	53.06	75.41	-			
N	7.71	5.63	6.10	7.07	4.91	6.95	-			
О	1.48	10.60	11.48	6.09	8.34	11.81	-			
Mn	-	5.81	6.29	-	4.30	6.09	4.83			
Cl	-	7.64	-	-	29.40	-				

The amounts of nitrogen (ca. 6–7 at.%) and oxygen (ca. 11.5–11.8 at.%) in the samples were rather high, which was expected based on the composition of the DPH ligand and the fact that the synthesis was carried out in an ambient (air) atmosphere. The amount of oxygen in the Mn-doped CD and the control without manganese was similar, which suggests a low contribution of oxidized manganese species (also confirmed by XRD and XPS; see discussions below). Other authors have reported similar observations for the preparation of manganese-doped CNDs through hydrothermal approaches with other precursors (citric acid, formamide, o-phenylenediamine) [30,31]. The good agreement between the values of elemental composition determined by bulk and surface techniques indicates the homogenous composition and distribution of the functionalization in the prepared materials (since XPS probes at a ca. 1–10 nm depth, and EDX analyzes depths from 1 to 3  $\mu$ m) [32,33].

The analysis of the high-resolution XPS spectra showed differences among the samples upon the incorporation of manganese (Figure 2, Table 3). The Mn 2p spectrum of the Mn(II)-CNDs exhibits the two main peaks at 642.8 (Mn 2p<sub>3</sub>/<sub>2</sub>) and 654.5 (Mn 2p<sub>1</sub>/<sub>2</sub>) eV (2p<sup>3</sup>/<sub>2</sub>–2p<sup>1</sup>/<sub>2</sub> splitting of 11.7 eV) and a satellite signal at 647.7 eV (≈29%) that confirm the presence of Mn (II) species. The deconvolution of the peaks shows two predominant contributions assigned to Mn-O (642.0 eV, ≈29%) and N-Mn-Cl moieties (643.8 eV, ≈32%), along with a small contribution of Mn-Cl coordination (642.5 eV, ≈10%), as also detected by EDX (Table 2). The position of these peaks is in line with the assignment reported in the literature [34,35]. The deconvolution of the C1s, O1s, and N1s core signals of the Mn(II)-CNDs and their control showed differences for the samples. The signal of N1s was deconvoluted in four main peaks at 398.5 eV attributed to nitride/secondary amines, 399.3 eV attributed to Mn-Nx, 400.2 eV assigned to primary amines/pyridines, and 402.3 eV associated with quaternary amine groups [34,36]. The main differences in the N1s profiles are the appearance of the Mn-Nx peak in the Mn-doped material assigned to the interactions between the nitrogen atoms and Mn ions and the increase in the relative contribution of the peak assigned to nitrogen in quaternary environments. Contributions of peaks at high binding energies related to oxidized nitrogen were not observed, despite the synthesis of the materials being carried out at moderate temperature under air atmosphere.

**Table 3.** Relative abundance distribution (%) and position (eV) of the surface groups detected in sample Mn-CNDs and DPH-CNDs upon deconvolution of the high-resolution core-level XPS spectra.

C1s	Csp <sub>2</sub> (284.6 eV)	C=N (285.6 eV)	C-N/ C-OH/ C-O-C (286.7 eV)	O-C-O/N- C=O/CO-N- CO (288.6 eV)	N-CO-O (289.9 eV)	π-π* (291.7 eV)
Mn-CNDs	53.25	24.75	11.28	4.58	3.35	2.79
DPH-CNDs	74.95	12.74	6.93	1.24	-	4.14
O 1s	Mn-O (530.2 eV)		N-C=O (532.1 eV)	C-O-C/	C-OH/O-C-O	(533.8 eV)
Mn-CNDs	6.72		68.69		24.59	
DPH-CNDs	-		67.11		32.89	
N 1s		litride/ nmines (398.5 eV)	Mn-Nx (399.3 eV)	•	y amines/ s (400.2 eV)	Quaternary amines (402.3 eV)
Mn-CNDs		22.36	8.28	32	7.52	31.84
DPH-CNDs	,	57.87	-	38	3.62	3.51
M - 2 -	M. O	((42 0 - J7)	Mn-Cl	Mı	n-Nx	Satellite (647.7
Mn 2p	Mn-O (642.0 eV)		(642.5 eV)	(643.8	eV, eV)	eV)
Mn-CNDs	29.33		9.78	31.98		28.91
DPH-CNDs	-		-		-	-

The high-resolution XPS spectrum of the C1s of the Mn-CNDs showed five main peaks at 284.6 eV ( $\approx$ 53%, attributed to aromatic sp² carbon atoms), 285.6 eV ( $\approx$ 25%, assigned to C=N), 286.7 eV ( $\approx$ 11%, assigned to C-N/C-OH/C-O-C), 288.6 eV ( $\approx$ 5%, assigned to O-C-O/N-C=O/CO-N-CO), and 289.9 eV ( $\approx$ 3%, assigned to N-CO) [37–40]. A small broad band at 291.7 eV ( $\approx$ 3%) due to the  $\pi$ - $\pi$ \* satellite was also observed. The undoped sample displayed similar peaks, with a higher relative contribution of the peak at 284.6 eV ( $\approx$ 75%) and a lower relative contribution of the peak at 286.7 eV (C-N/C-OH/C-O-C,  $\approx$ 7%). This indicates that the chemical environment of the bonds C-N, C-OH, C-O-C is influenced by the Mn atoms, in line with the Mn-Nx signal observed in the spectra of the N1s core level. A closer analysis of these results suggests that Mn-Nx moieties are most likely in a C-N-C configuration [37–39].

For the O1s, a peak assigned to Mn-O is observed in the Mn(II)-doped sample, with a decrease in the relative contribution of the peaks assigned to oxygen in single-bond moieties after the incorporation of manganese. The XPS high-resolution spectrum of chlorine revealed two main peaks associated with Mn-Cl (199.0–200.6 eV,  $\approx$ 67%) from the MnCl2 precursor and N-Mn-Cl (199.9–201.5 eV,  $\approx$ 33%) coordination [36]. All these confirm differences in the local chemical environment of oxygen and nitrogen atoms upon the incorporation of manganese in the material.

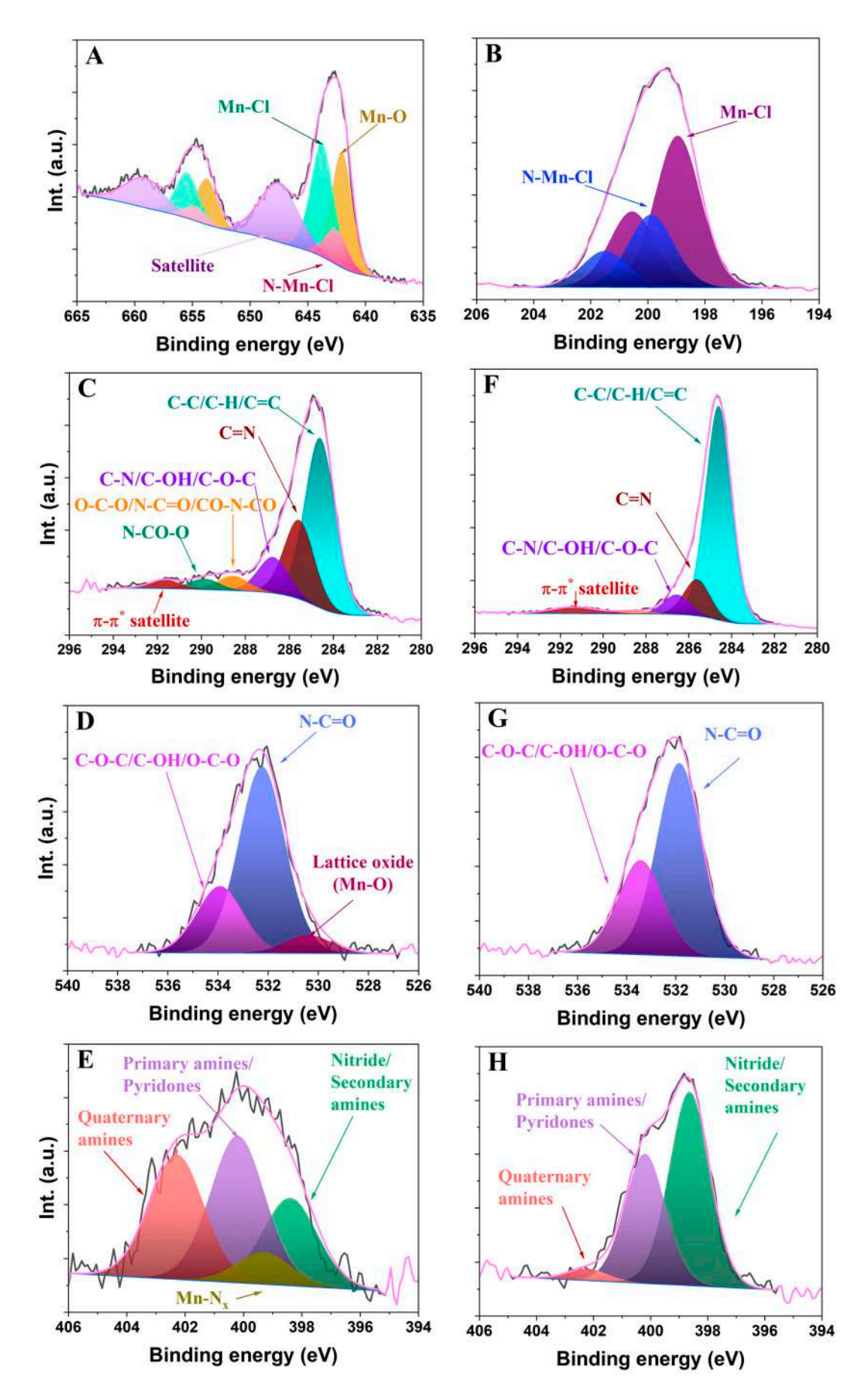
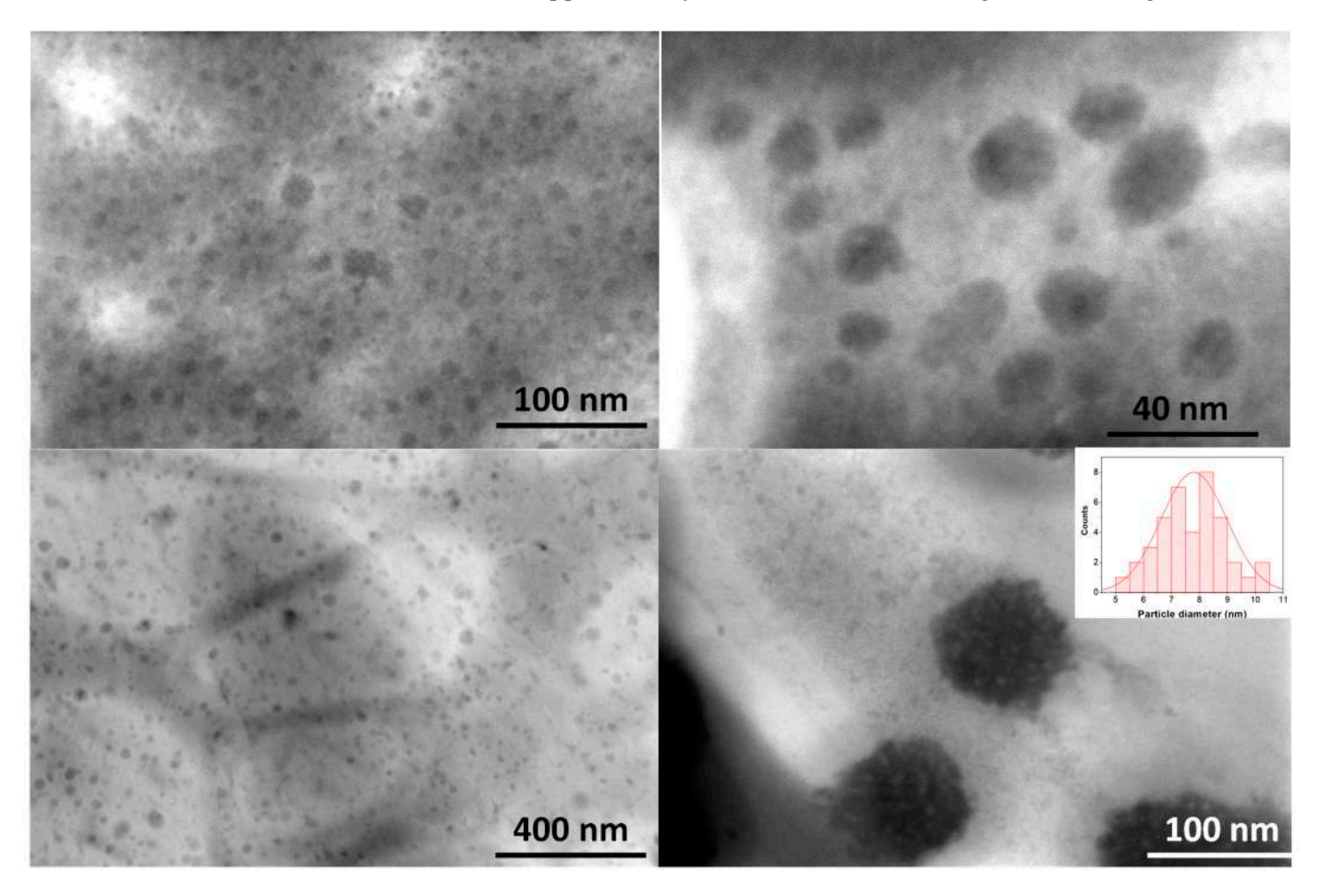


Figure 2. High-resolution XPS spectra of the Mn-CNDs (A) Mn 2p, (B) Cl 2p, (C) C1s,(D) O1s, (E) N1s and of the DPH-CNDs (F) C1s, (G) O1s, (H) N1s.

Differences were also observed in the surface charge distribution of the samples, as evidences by the zeta potential measurements (ca. -16.92 mV and -21.93 mV for DPH-CNDs and Mn-CNDs, respectively). The more negative zeta potential values observed for the Mn-doped sample suggest that amino groups present in the undoped material were either partially removed during synthesis or became coordinated to Mn<sup>+2</sup> ions, as also proposed in the literature [34]. Other authors have reported a more positive zeta potential for Mn-doped CDs ( $-2.50 \pm 0.98$  mV) compared to Mn-free CDs ( $-12.04 \pm 0.25$  mV), which was attributed to the presence of positively charged Mn<sup>2+</sup> ions on the surface [40]. The more negative values in our case imply that Mn<sup>+2</sup> are distributed inside the carbon dot matrix rather than mainly localized on the surface.

The XRD patterns of the prepared samples (both DPH-CNDs and Mn(II)-CNDs) are shown in Figure S6. They show the typical broad peaks at 19.4° and 43.4° assigned to amorphous carbon materials with a turbostratic structure (see Tables S2 and S2) [41]. The narrow peaks between 16 and 22° in the diffractogram of the Mn-doped CNDs are attributed to the presence of crystalline structures (Table S1) assigned to Mn complexes through imidazole–nitrogen as bridging ligand in various configurations (PDF\_02-088-0512, PDF\_02-103-9616, PDF\_05-008-2802).

Figure 3 shows STEM micrographs of Mn-CDs dispersed in ethanol and water. The average particle size of the carbon dots depended on the dispersion solvent. The tendency of carbon dots (CDs) to form clusters upon interaction with different solvents has been widely reported in the literature [14,24,42]. The size of the aggregates was further confirmed by Dynamic Light Scattering (Figure S7), with two distinct particle size populations in water (42 and 197 nm) and water—ethanol mixtures (59 and 361 nm) and polydispersity indexes of 0.58 and 0.29, respectively. Figure 3 (down-right) also revealed that the particles exhibit a granular texture, which suggests a clustered organization of smaller nanostructures of approximately 7–8 nm in size (inset in Figure 3(down-right).



Int. J. Mol. Sci. 2025, 26, 6293 9 of 22

**Figure 3.** STEM micrographs of the Mn-CMDs suspended in ethanol (**top**) and water (**down**) at various magnifications. The inset represents the average size distribution of 40 Mn nanoparticles.

The ethanolic suspensions of the CNDs displayed better stability over time than in water, with a monodispersed population of a 169 nm diameter consistently maintained throughout 2 h. Hence, to prevent any decrease in the photoluminescence of the materials due to particles clustering [14,24,42], the dispersions of Mn(II)-CNDs in ethanol were further used for the bioimaging applications.

## 2.2. Photoluminescence Properties of the Prepared CDs

Figure 4B shows the steady-state photoluminescence emission spectra of the Mn(II)-CND dispersions in water upon excitation within 310–400 nm (10 nm step). The Mn(II)-CNDs displayed a particularly bright emission with broad asymmetric bands (ca. 70–80 nm FWHM) with multiple emission peaks. This behavior is characteristic of samples with various fluorophores contributing to the emission profiles [43]. A markedly higher emission intensity was recorded for the Mn(II)-doped carbon dots compared to the undoped DPH-CND sample (Figure 4A). For the former, the most intense emission was achieved upon excitation at 370 nm (maximum emission at 438 nm), although differences were small among the four excitation wavelengths. In contrast, for Mn(II)-CNDs the highest emission intensity was obtained upon a 330 nm excitation (maximum at 419 nm), with two distinctive emission peaks (417-437 and 413-438 nm) upon excitation at 370 and 390 nm. For the undoped sample, a redshift in the position of the emission peak was observed for excitation above 330 nm. Such excitation-dependent emission behavior is commonly described for carbon dots. According to the literature, excitation above 320 nm involves transitions in surface fluorophores on the carbon dots (as opposed to those in the condensed aromatic carbon core) [14,43,44].

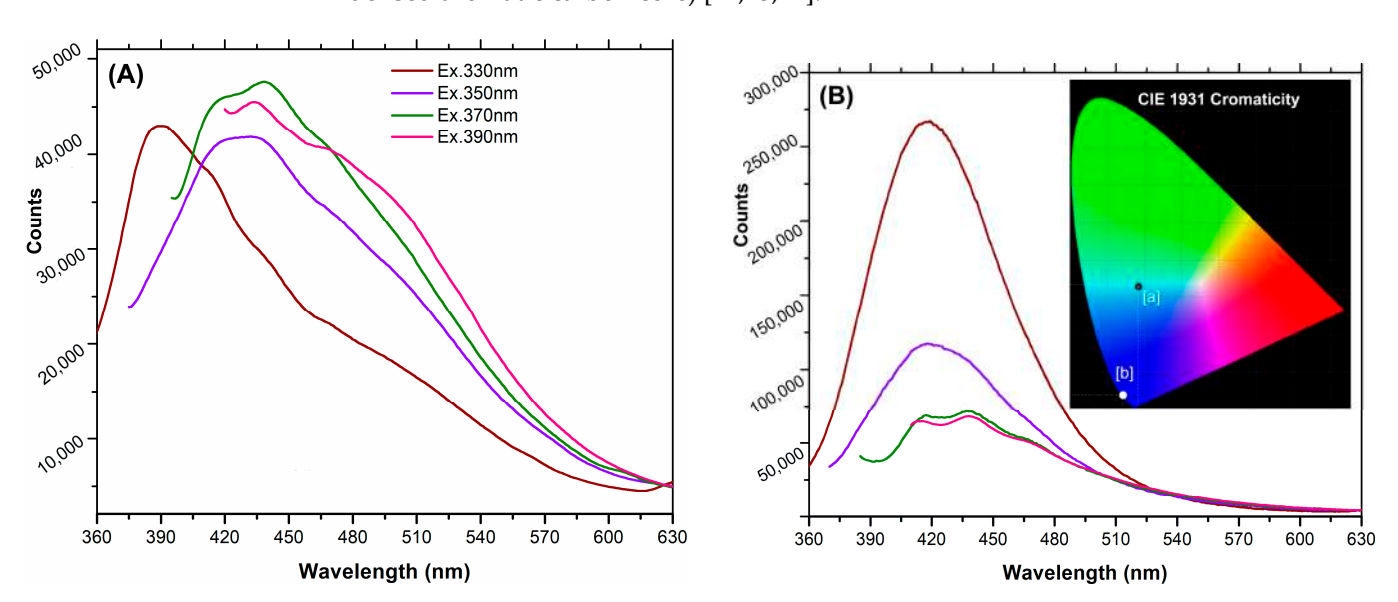


**Figure 4.** Emission spectra of **(A)** DPH-CNDs and **(B)** Mn(II)-CNDs recorded at various excitation wavelengths of 330, 350, 370, and 390 nm. Inset in plot **(b)** shows the chromaticity CIE 1931 chart of both samples.

Table 4 compiles the absolute photoluminescence quantum yield (PLQY) of the Mn(II)-CNDs at four excitation wavelengths. The data showed different trends with the excitation wavelengths. The highest PLQY of 28.30% was obtained for the Mn(II)-CNDs upon excitation at 330 nm, being a value ca. four times higher than that of the undoped DPH-CNDs at the same excitation. While the PLQY of the Mn(II)-CNDs decreased as the

excitation wavelength increased, the opposed trend was observed for the undoped DPH-CNDs. For the latter, the highest PLQY of 10.28% was recorded at a 390 nm excitation. These values of PLQY are similar to (and higher than) those reported in the literature for other N-doped carbon dots [45–48]. The chromaticity characteristics of both samples are also different (Figure 4b inset), with a perceived emission in deep blue for Mn(II)-CNDs (marked as [a] in the CIE 1931 chromaticity chart; x,y coordinates of 0.1872, 0.3456), compared to the blue-green region for the undoped sample (marked as [b] in the chromaticity CIE 1931 chart, x,y coordinates of 0.1545, 0.047). This is attributed to the presence of metallic ions in various structural configurations.

**Table 4.** Absolute PLQY values for sample Mn(II)-CNDs and DPH-CNDs at various excitation wavelengths.

Excitation (nm)	330	350	370	390
DPH-CNDs	6.89	9.17	9.30	10.28
Mn(II)-CNDs	28.30	9.60	4.05	3.51

The lifetimes of the excited states of the Mn(II)-CNDs were measured both in water and EtOH dispersions (Table 5). The decay curves recorded at the 413 and 438 nm emission peaks are shown in Figure S8. Overall, the lifetimes were within the nanosecond range, which is typical for carbon dots [14,24,49]. In each measured condition, three different lifetimes were recorded due to the various emission species within the CNDs' structure. In case of the Mn(II)-CNDs dispersed in water, the main contribution (~75%) is due to the species responsible for longer-lifetime (~12 ns) radiative processes, while in the case of the ethanol-dispersed Mn-CNDs the main contribution (32%) is achieved at 6 ns lifetimes. However, due to the specific conditions of each dispersion medium the contribution of various emissive species is different. The typical lifetimes reported for undoped carbon dots lie within the 4–6 ns range [14,24,49,50].

**Table 5.** Photoluminescence lifetime of the excited states recorded at various emission wavelengths for Mn-CNDs dispersed in H<sub>2</sub>O and EtOH.

Sample Code	τ <sub>1</sub> (ns)	a <sub>1</sub> (%)	τ <sub>2</sub> (ns)	a <sub>2</sub> (%)	τ <sub>3</sub> (ns)	a <sub>3</sub> (%)	<τ> (ns)	χ²
Mn-CNDs-water $\lambda_{em} = 413 \text{ nm}$	12.2	78.5	4.3	17.4	0.82	4.1	11.6	1.05
Mn-CNDs-water $\lambda_{em} = 438 \text{ nm}$	11.6	76.6	3.8	18.9	0.49	4.5	11.0	1.17
Mn-CNDs-ethanol $\lambda_{em} = 413 \text{ nm}$	6.4	58.5	2.2	32.2	0.56	9.3	5.6	1.12
Mn-CNDs-ethanol $\lambda_{em} = 438 \text{ nm}$	6.6	55.0	2.6	32.3	0.61	12.8	5.8	0.98

## 2.3. Biocompatibility and Cytotoxicity

The biocompatibility and cytotoxicity of the synthesized carbon dots was evaluated by in vitro assays on both healthy and cancer cell lines. Gingival fibroblast (HGF) cells were chosen as the healthy cell control for assessing the biocompatibility, while various cancer cell lines were chosen for assessing the cytotoxicity, namely osteosarcoma (HOS, MG-63), breast adenocarcinoma (MCF-7), and malignant melanoma (MeWo) cell lines. The obtained data (Figure 5) evidences the overall good biocompatibility of the Mn(II)-CNDs to HGF cells, with only a slightly decrease in the cell viability (>84%) at all the tested concentrations. Similar studies on the cytotoxicity of carbon dots on HGF cell lines

typically report viabilities above 90% for concentrations of carbon dots lower than those herein reported [51-53], indicating the large range of biocompatibility of our materials (even at high concentrations). On the other hand, large differences in cytotoxicity were observed for the studied cancer cell lines. No significant cytotoxic effects of the Mn(II)-CNDs were observed for HOS (viability >85%) and MeWo (viability >76%) cancer cell lines. In contrast, the Mn(II)-CNDs showed a somewhat cytotoxic effect for breast adenocarcinoma MCF-7 cells at 100 µg/mL (67% cell viability). The effect was more pronounced for MG-63 osteosarcoma cells, where a sharp decrease in the cell viability was observed at concentrations higher than 25 µg/mL. According to the literature, the cytotoxic effects of manganese-derived complexes in breast (MCF7) and bone (MG-63) cancer lines have been associated with the generation of radical oxygen species (ROS) that interfere with several cell functions (e.g., mitochondrial function, certain antioxidant enzyme activities) and induce the apoptosis of tumor cells [54–59]. Hence the strong cytotoxic effect observed for both cell lines would suggest the ability of the prepared Mn-CDs to produce ROS. The lower cytotoxicity of HOS and MeWo may be related to the higher resistance of these cell lines to ROS-induced effects. The different cytotoxic trend for HOS and MG63 (both bone cancer lines) may be explained by the lower stability of MG63 to ROS compared to HOS and further differences in morphology and functional properties that could alter the adhesion (thus interaction with the contrast agent) [60].

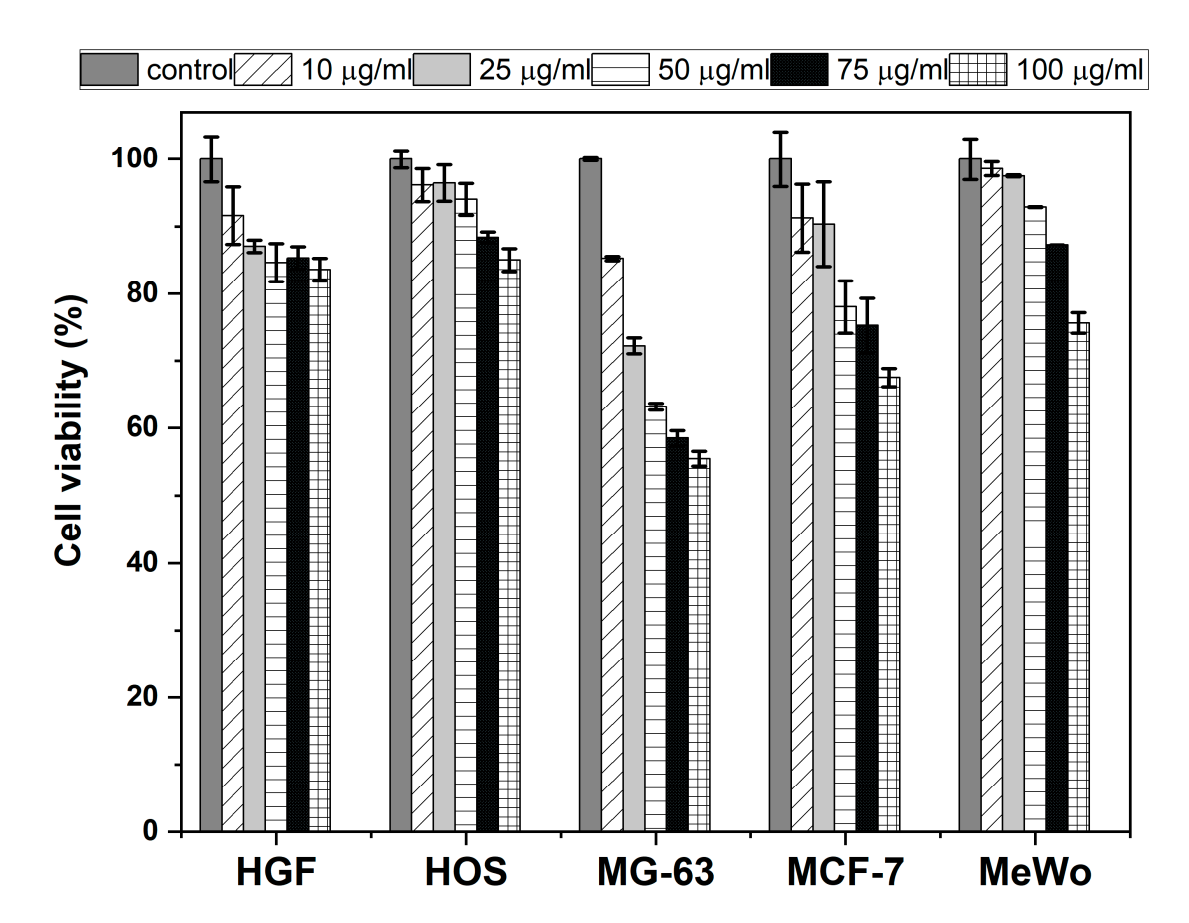


**Figure 5.** Cell viability of HGF, HOS, MG-63, MCF-7 and MeWo cells after 24 h incubation with different concentrations of the Mn-CNDs ranging between 10 and 100  $\mu$ g/mL. The control of the untreated cells is also included for clarity. Data represent average values of three measurements and their respective standard deviation as error bars.

### 2.4. Fluorescence and Magnetic Resonance Imaging Applications of the Mn(II)-CNDs

Based on the bright luminescence of the carbon dot suspensions and their biocompatibility, we have explored their potential application as fluorescence and MRI probes. As discussed above, ethanolic suspensions of the Mn(II)-CNDs were used for bioimaging applications due to their stability over time and a stable average particle size in the colloidal suspensions. While this is not expected to have a large impact on the magnetic resonance response [61,62], it is well known that the clustering of nanoparticles can decrease the photoluminescence of the carbon dots due to internal reabsorption of the emitted light-shielding effects [14,24,42].

Figure 6A shows the in vitro fluorescence optical imaging of phantoms with increasing concentrations of the carbon dots. As seen, the phantoms with the carbon dot suspensions presented a bright fluorescence emission (recorded at 530 nm; seen as green and red colors in the images) under excitation at 465 nm. The control in the absence of carbon dots (phantom C0) showed a poor fluorescence. The intensity of the fluorescence emission signal gradually increased with the amount of carbon dots in the dispersions, and the intensity of the signal was the same as that reported for other fluorescence probes [63,64]. These results demonstrate the great potential of the prepared carbon dots as contrast agents in imaging applications.

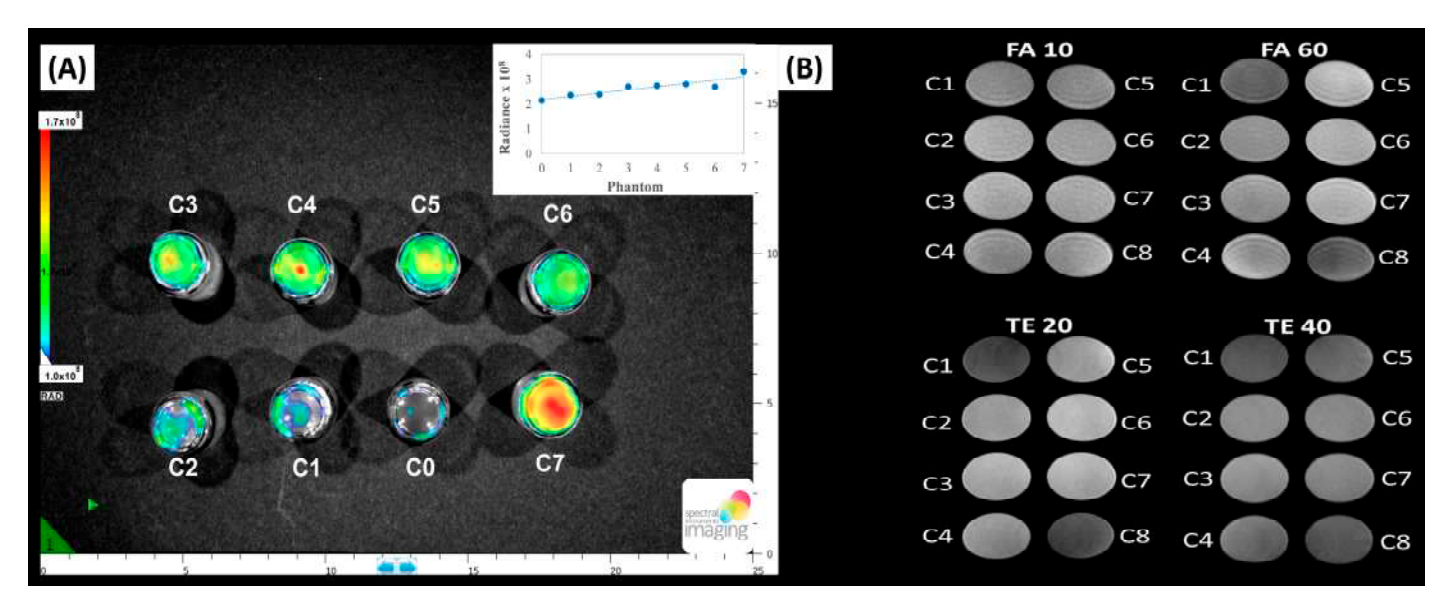


**Figure 6.** (**A**) In vitro fluorescence image of phantoms with increasing concentrations of the carbon dot suspensions. Excitation at 465 nm; emission at 530 nm; inset represents the evolution of the fluorescence intensity for the phantoms with increasing concentrations (from control C0 to C7); (**B**) T1 GRE (upper row) and T2 FSE (bottom row) magnetic resonance images of Mn(II)-CNDs at increasing concentrations from 0.005 to 0.2 mg/mL (C1-C7); C8 corresponds to the control of agarose gel.

To assess the potential of DPH-Mn as a T1 and/or T2 contrast agent, the longitudinal  $(r_1)$  and transverse  $(r_2)$  relaxivity values were determined by applying specific equations to the average signal extracted from images acquired at different concentrations of the compound dispersed in 1% agarose gel [65–67]. Relaxation times were recorded at 20 °C and a physiological pH of 7.4 to simulate normal tissue conditions. Figure 6B presents the magnetic resonance phantom images of the plates. Relaxivity (R) is defined as the reciprocal of the relaxation time (1/T) per unit ion concentration, and it is determined as the slope of the curve as a function of Mn concentration. The data in Figure 6B is expressed as mM of Mn(II), recalculated from the content of manganese in the sample as determined by EDX (Table 2). This ensures consistency with published research on MRI contrast

agents' efficiency—although it should be noted that comparison should be made at similar magnetic fields, since the intensity of the MIR signal depends on this parameter, with higher values for smaller magnetic fields. As observed in the T1 GRE sequence (upper row), at small flip angles (e.g., FA 10°) no significant contrast differences were visible among the wells with different Mn(II)-CNDs concentrations. At a larger flip angle of 60°, the brightness increased with the concentration of manganese in the dispersion (a brighter response in the C7 well), while the control well of agarose gel (C8) and the wells with small amounts of Mn(II)-CNDs (e.g., C1) appeared darker. For the T2 FSE sequences (a constant flip angle of 90°) the opposed trend was observed; the best contrast response was obtained for an echo time of 20 ms, with an increased dark contrast with the concentration of manganese. The  $r_1$  and  $r_2$  relaxivity values represent the efficiency of the contrast agent in T1w and T2w sequences, respectively (specifically T1 GRE and T2 FSE in this study). The representation of R1 (1/T1) and R2 (1/T2) as a function of Mn(II) concentration showed that the relaxation times (T1 and T2) progressively decreased up to a concentration of 0.364 mM Mn(II) (0.08 mg/mL), while R1 and R2 increased (Figure S9). At concentrations of 0.45 and 0.9 mM Mn(II) (0.1 and 0.2 mg/mL), both R1 and R2 decreased, with a more pronounced effect in the T1 GRE mode. This indicates that the last two concentrations fall outside the linear range of relaxation time dependence on concentration and were therefore excluded from further analysis. Consequently, the dependence of R1 and R2 on the concentration of manganese was further analyzed in the range 0.023–0.364 mM Mn(II) (0.005-0.08 mg/mL).

The linear fitting of the data yielded relaxivity values of  $0.932 \text{ s}^{-1} \cdot \text{mM}^{-1}$  for  $r_1$  and  $20.511 \text{ s}^{-1} \cdot \text{mM}^{-1}$  for  $r_2$ . Table 6 shows a comparison of these relaxivity values with those of contrast agents currently used in clinical practice, including gadolinium-based benchmarks. It is evident that while Mn(II)-CNDs exhibits a modest  $r_1$  value, its  $r_2$  value is significantly higher than that of commercial contrast agents based on gadolinium and manganese, which have a maximum reported  $r_2$  of 7.6 mM<sup>-1</sup>·s<sup>-1</sup>. However, it should be mentioned that such a comparison is not straightforward due to the differences in the applied magnetic field strengths (Table 6), as relaxivity values significantly depend on several acquisition parameters. Relaxivity values also depend strongly on the amount of metal ions of the samples [47]. A more adequate comparison with other metal-doped carbon dots reported in our previous studies under similar experimental conditions is also included in Table 6 [24].

**Table 6.** Relaxivity values of the prepared Mn-CDs compared to commercial gadolinium-based contrast agents currently used in clinical practice and other Mn-doped and metal-doped CDs reported in the literature.

Material	<i>r</i> ₁ [mM <sup>-1</sup> ·s <sup>-1</sup> ]	<i>r</i> ₂ [mM <sup>-1</sup> ·s <sup>-1</sup> ]	Magnetic Field (T)	Reference
Gadovist (Gadobutrol) (in plasma, 37 °C)	5.2	6.1	1.5	
Dotarem (Gadoterate Meglumine)	3.6	4.3	1.5	
ProHance (Gadoteridol)	4.1	5.0	1.5	[60]
Magnevist (Gadopentetate Dimeglumine)	4.1	4.6	1.5	[68]
MultiHance (Gadobenate Dimeglumine)	6.3	8.7	1.5	
Omniscan (Gadodiamide)	4.3	5.2	1.5	
Mn carbon dots (up to 1 at. Mn)	9.7 / 4.8/ 6.7	89 / 42/ 67	1.5	[31]
Mn carbon dots (0.1 mM Mn)	2.3		1.5	[47]
Mn <sub>2</sub> A <sub>11</sub> -LDH	0.6	17.9	16.4	[69]
Mno.5Mg2.6A11-LDH	1.2		16.4	[28]
MnFe <sub>2</sub> O <sub>4</sub> @PEGa	0.7	118	9.4	[70]
MnO	0. 5-0.1	1.7-0.4	3	[71]

MnOx-SiO2 hollow@PEG	0.8	27.7	3	[72]
MnO2@PEG	0.007	-	3	[73]
Mn <sub>3</sub> Fe <sub>1</sub> -LDH	0.08		0.5	[74]
MnSO <sub>4</sub>	3.8	19	1	[75]
Mn_CP	2.5	13	1	
CU_CP	5.5	5.5 24		[28]
FU_CP_IE	4	22	1	
Mn(II)-CNDs	1.0	21	1	this work
Material	$r_1$	<i>1</i> ′2	magnetic field	reference
	$[mL mg^{-1} \cdot s^{-1}]$	$[mL mg^{-1} \cdot s^{-}]$	(T)	reference
Mn-CNDs-NHF	17.8	88.6	1	
Fe-CNDs-NHF	0.2	48.7	1	[24]
Gd-CNDs-NHF	10.0	22.1	1	
Mn(II)-CNDs	87.2	1541	1	this work
· · · · · · · · · · · · · · · · · · ·		•	•	

The high  $r_2$  value indicates that spin–spin relaxation effects are predominant in the prepared Mn(II)-CNDs. This points out that the sample is a good T2-weighted (negative) contrast agent, as further confirmed by the relaxivity ratio  $r_2/r_1$  of ca. 22—according to the literature, the  $r_2/r_1$  ratio defines the type of contrast agent, with values up to 5 for positive or T1-weighted and ratios above 10 for negative or T2-weighted contrast agents [67]. We attribute this behavior to the nature of the manganese species in the prepared carbon dots. Indeed, data from XPS and EDX confirmed that manganese is incorporated as Mn(II) ions—either in a Mn-O or Mn-Nx configuration—as higher oxidation states of manganese were not detected. This assures a favorable density of spins (d5 configuration) for MRI applications. Also, the bulk and surface elements composition (Table 2) confirmed that Mn(II) is predominantly located in the external surface of the carbon dots. This environment provides suitable conditions for a fast proton/water exchange, responsible for a strong MRI contrast signal mainly by shortening the transverse relaxation time (T2) to produce dark images (Figure 7). A similar phenomenon has been observed for other superparamagnetic iron oxides acting as negative contrast agents [62].

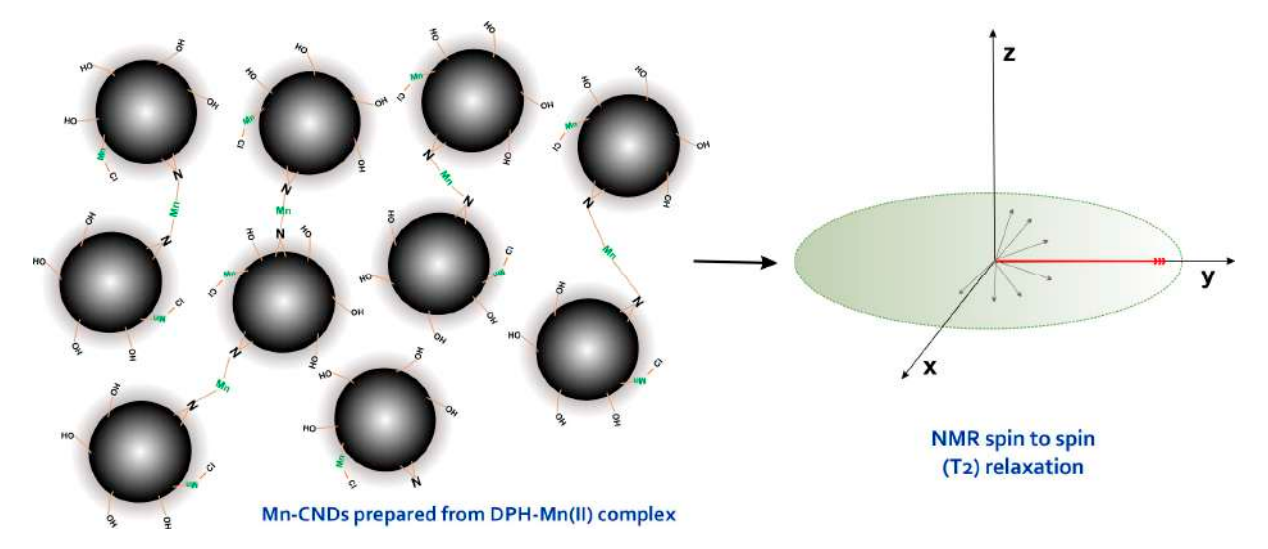


Figure 7. Schematized influence of the prepared Mn(II)-CNDs over the spin to spin (T2) relaxation.

### 3. Materials and Methods

### 3.1. Materials

5,5'-Diphenylhydantoin (DPH, 99%) and MnCl2 (99%) were supplied by Merck Chemicals. Ultra-pure distilled water (Millipore-Direct Q) and ethanol (EtOH, 97%) were used in the synthesis.

### 3.2. Synthesis of the Mn-Doped Carbon Dots

In the first stage, the Mn(II)-DPH complex with a 1:2 metal to ligand ratio was synthesized. In a typical procedure, the adequate amount of DPH is dissolved under stirring in a 1:1 v/v H<sub>2</sub>O/EtOH mixture and then mixed with the appropriate amount of MnCl<sub>2</sub> to reach 1:2 metal–ligand ratio and stirred until the complete dissolution of the manganese salt occurs. Afterwards, the solution containing DPH and MnCl<sub>2</sub> is transferred to a flask with a reflux condenser and heated at 85 °C for 24 h to allow complexation as indicated in the following reaction:

$$2C_{15}H_{12}N_2O_2 + MnCl_2 \rightarrow [Mn(C_{15}H_{11}N_2O_2)_2] + 2HCl\uparrow$$

A pale brown precipitate was recovered by centrifugation at 5000 rpm for 5 min and washed at least three times in distilled water. The purified precipitate of the DPH-Mn(II) complex was dried in vacuum for about 24 h at 80 °C. In the second stage, the DPH-Mn(II) complex powders were thermally processed in a quartz-made reactor equipped with a temperature/flow regulated hot air gun, as described elsewhere [15,25]. In a typical synthesis, about 0.25 g of DPH-Mn(II) complex is heated under atmospheric conditions at 470–490 °C for 10–11 min. Afterwards, the solid remaining in the quartz tube is flooded in 10 mL of cold water (ca. 5 °C). The dispersion was centrifuged at 10,000 rpm for 10 min to remove the large particles, followed by a final filtration stage with a 0.22  $\mu$ m membrane. The clear transparent aqueous suspension with the Mn(II)-CNDs was collected and freeze-dried until further use. For STEM analysis, cold ethanol was used as solvent in the flooding step (instead of water).

### 3.3. Characterization Techniques

Infrared spectra of the samples were recorded in a Shimadzu IRAffinity 1S spectrometer. The dried samples were pressed into KBr pellets (dilution 1:1000). Each spectrum resulted from the accumulation of 256 scans, recorded with a spectral resolution of 1 cm-1 in the 4000–400 cm<sup>-1</sup> spectral domain. Thermogravimetric analyses of the samples were recorded in a thermobalance (Netzsch-STA 449 F1 Jupiter) under an inert atmosphere, with a heating rate of 10 °C/min within 30-700 °C. X-ray photoelectronic spectroscopy (XPS) spectra of the dried samples were collected in a ULVAC-PHI, 5000 VersaProbe spectrometer (physical Electronics) using AlK $\alpha$  radiation (1486.7 eV) operating at 20 mA and 15 kV and with a pass energy of 20 eV and a step size of 0.1 eV. Processing of the highresolution XPS spectra was carried out in CasaXPS (version 2.3.23PR1.0) with the C1s peak of adventitious carbon at 284.6 eV as a reference signal. The binding energy values were accurate within ±0.2 eV. The dimensional analysis, zeta potential (3), and particle size distribution of aqueous dispersions of the samples were recorded on a Zetasizer Advance Pro Red instrument. Prior to the measurements, the solutions were centrifuged twice at 15,000 RPM for 10 min. The concentration of manganese in the carbon dots was determined by flame atomic absorption spectroscopy (FAAS). The detailed methodology is provided in the Supplemental Information. The X-ray diffraction (XRD) patterns of the samples were measured with a Rigaku SmartLab X-ray diffractometer in Bragg-Bretano geometry using a Cu anode (X-ray wavelength of 1.5406 Å). The morphology of the samples was analyzed in a Verios G4 UC scanning electron microscope (Thermo Scientific)

equipped with an energy-dispersive X-ray spectroscopy (EDX) analyzer (Octane Elect Super SDD detector, USA). Scanning transmission electron microscopy (STEM) studies were conducted with the STEM 3+ detector in Bright-Field mode, operating at an accelerating voltage of 25 kV and a spot size of 0.1 nA. The suspensions of the samples were ultrasonicated and deposited on carbon-coated copper grids with a 300-mesh size and air-dried for 24 h in dust-free conditions at ambient temperature. EDX spectra were recorded at an accelerating voltage of 25 kV and a spot size of 6.4 nA. The steady-state fluorescence of freshly prepared dispersions of the samples was measured in a FluoroMax 4P spectrophotometer (Horiba, Japan) at excitation wavelengths between 300 and 400 nm, in quartz cuvettes with a path length of 10 mm (excitation and emission slits of 5 nm). The excitation and emission slits were set at 2 nm. The absolute photoluminescence quantum yield (PLQY) was recorded with a Quanta  $\Phi$  integration sphere module, using FluorEssence software (ver. 3.5.1.20) for the spectral acquisition and the calculation of the PLQY and CIE1931 chromaticity parameters. Excited states lifetimes (LTs) were recorded in a FluoroHub Time-Correlated Single-Photon Counting lifetime module with a 370 nm LED excitation source. Experimental data was fitted to a single or multi-exponential decay model, based on each sample's behavior.

### 3.4. Cell Viability Assay

The biocompatibility and cytotoxicity of the Mn-CNDs were assessed with the CellTiter-Glo® 2.0 Assay (Promega, Madison, WI, USA), according to the manufacturer's instructions. Cells were cultured in complete cell culture medium:  $\alpha$ MEM medium with 10% fetal bovine serum and 1% antibiotic-antimycotic (Penicillin-Streptomycin-Amphotericin B mixture, all from Gibco, Thermo Fisher Scientific, Waltham, MA, USA). A human gingival fibroblast (HGF) cell line was selected to assess the biocompatibility of the prepared materials. Several cancer cell lines have been used to evaluate their cytotoxicity, namely osteosarcoma (HOS, MG-63), breast adenocarcinoma (MCF-7), and malignant melanoma (MeWo) cell lines (all from CLS Cell Lines Service GmbH, Eppelheim, Germany), covering most common types of cancer (breast, skin, bones). The cells were seeded separately into 96-well white opaque tissue culture-treated plates (50,000 cells/mL-HGF and 100 000 cells/mL-cancer cell lines) in complete cell culture medium and allowed to adhere overnight. The next day, the cells were incubated in triplicate experiments with different concentrations of Mn(II)-CNDs (10, 25, 50, 75, 100 µg/mL) for 24 h, following the recommendation outlined in ISO 10993-5:2009 (E) [27]. For the determination of cell viability, CellTiter-Glo® reagent was ad nd luminescence was recorded in a ded, a FLUOstar® Omega V6.20 microplate reader (BMG LABTECH, Ortenberg, Germany). Treated cells' viability was calculated as percentage of untreated cells' viability, and data were represented graphically as means ± standard error of the mean.

## 3.5. In Vitro Fluorescence Imaging

In vitro fluorescence imaging was recorded in a SPECTRAL Ami HT instrument piloted by Aura imaging V.4.0 software. About 1 mL of carbon dot suspensions of varied concentrations was deposited in 5 mL glass phantoms. The imaging procedure included excitation at 430 nm (LED power 60%), emission at 530 nm, an exposure time of 1 s, FOV  $25 \times 17.5$  cm, F-stop 2, and binning 2. The quantification of the fluorescence was conducted over circular regions of interest, covering the whole image of each sample.

### 3.6. In Vitro Magnetic Resonance Imaging (MRI) Assays

The potential application of the prepared materials as MRI contrast agents was evaluated in in vitro cell/tissue cultures of 1% agarose gel prepared in 0.01 M PBS (pH 7.4) to determine values of longitudinal (r1) and transversal (r2) relaxivities, calculated from the

respective T1 and T2 relaxation times. Agarose not only mimics a cellular culture environment but also prevents compound sedimentation upon scanning, which could otherwise significantly impact the results. The prepared carbon dot suspensions were dispersed in this medium as indicated elsewhere [24,28]. Briefly, a stock solution of 2 mg/mL of the CNDs in ultrapure water was prepared by ultrasonication for 30 min. Defined volumes of this solution were subsequently added to the hot 1% agarose solution to achieve concentrations in the range of 0.01-0.4 mg/mL. The solutions were homogenized in their preparation vials and then transferred in 3 mL aliquots into a well plate (wells C1-C7) until complete solidification. A control sample (well C8) was filled with 3 mL of agarose gel without the CNDs. MRI scanning of the well plates was performed in nanoScan PET-MRI equipment provided with a magnetic field strength of 1 Tesla, employing standard T1weighted (T1w) and T2-weighted (T2w) sequences, specifically T1 gradient echo (GRE) and T2 fast spin echo (FSE), with B0 magnetic field shimming and coil calibration at water proton frequency. The plate of the samples was positioned horizontally at the center of the coil's field of view. The main parameters for the T1 GRE imaging acquisition were as follows: the repetition time TR 360 ms, the echo time TE 3.8 ms, the number of excitations NSA 2, slice thickness 3 mm, slice gap 1 mm, and the flip angle (FA) variable (ca. 10, 20, 60, 70°). The T2 FSE acquisition parameters were TR 1895 ms, NSA 2, slice thickness 3 mm, FA 90° with a variable TE (ca. 20, 40, 80, and 120 ms). On the reconstructed MR images, circular regions of interest (ROIs) of 10 mm diameter were drawn inside each sample; a representative slice placed ca. in the middle of the agarose gel volume was selected to assure a uniform MRI signal. T1 relaxation times were determined by a two-point estimation method for the flip angles of 10 and 60° [29], using the formula

$$\ln\left[\frac{(I_1sin\theta_2-I_2sin\theta_1)}{(I_1sin\theta_2cos\theta_1-I_1sin\theta_2cos\theta_1)}\right] = \frac{-TR}{T_1}$$

where I<sub>1</sub>, I<sub>2</sub> are the mean signal intensities measured inside the regions of interest of the samples at 10 and 60 ° flip angles; TR is the repetition time;  $\theta_1$  and  $\theta_2$  are the flip angles.

 $T_2$  relaxation times were obtained from the 1H relaxometry tool of Nucline softwareV1.02, using the equation

$$I = A \cdot e^{\frac{TE}{T2}}$$

where *I* is the mean signal intensity in the ROI, *A* is the initial intensity of the signal, and TE is the echo time.

Examples of the graphical calculations of  $T_1$  and  $T_2$  are shown in the Supplementary Information File (Figures S1–S3).

## 4. Conclusions

In this study we report the preparation of Mn-doped carbon dots prepared by the thermal decomposition at a mild temperature of a Diphenylhydantoin–Mn(II) complex, and their use as a magnetic resonance imaging contrast agent. The choice of the Diphenylhydantoin–Mn(II) complex as a precursor for the preparation of Mn(II)-doped carbon dots has proven to be a good approach to obtain a good dispersion of the metallic cations in the matrix of the carbon nanodots. The Mn(II)-CNDs displayed photoluminescence features with an intense emission in the blue region, which suggests their potential application as a fluorescence marker in biology-related investigations. The cytotoxicity assays revealed the good biocompatibility of the Mn(II)-CNDs on normal gingival fibroblast and malignant melanoma cell lines, with cell viabilities above 80–90% for concentrations of carbon dots higher than those reported in the literature for other nanostructures. In contrast, the Mn(II)-CNDs showed a cytotoxic effect on osteosarcoma (MG-63) and breast adenocarcinoma (MCF-7) cells lines at concentrations above 25 µg/mL. The in vitro magnetic

resonance imaging assays rendered higher r2 relaxivity values for the Mn(II)-CNDs than those reported for commercial gadolinium-based contrast agents. In sum, the simplicity of the synthetic pathway allows a good dispersion of the metallic ions in the carbon dots matrix, along with a low cytotoxicity. As a result, the Mn(II)-CNDs prepared from a complex precursor have the potential to become a viable alternative as T2-weighted contrast agents, offering more accurate MRI signals in combination with T1-weighted contrast agents (e.g., based on gadolinium complexes) in biomedical applications. The next steps should focus on the optimization of their performance under different magnetic field conditions and the assessment of their biocompatibility for clinical applications in in vivo assays.

**Supplementary Materials:** The following supporting information can be downloaded at: https://www.mdpi.com/article/10.3390/ijms26136293/s1.

**Author Contributions:** Conceptualization, C.S.S., C.O.A. and A.C.; methodology, C.S.S., C.M.U., A.C. and C.O.A.; investigation, A.C., C.S.S., N.S., C.M.U., D.B., L.E.U., A.-I.D., F.D., M.D., C.A. and C.O.A.; writing—original draft preparation, C.S.S. and C.O.A.; writing—review and editing, C.S.S., A.C., C.M.U. and C.O.A.; project administration, A.C. and C.O.A.; funding acquisition, A.C. and C.S.S. All authors have read and agreed to the published version of the manuscript.

**Funding:** This research was funded by the Ministry of Research, Innovation, and Digitization, project no. PNRR-III-C9-2022-I8-291, contract no. 760081/23.05.2023, within the National Recovery and Resilience Plan.

**Institutional Review Board Statement:** Not applicable.

**Informed Consent Statement:** Not applicable.

**Data Availability Statement:** The raw data supporting the conclusions of this article will be made available by the authors upon request.

**Acknowledgments:** The authors are thankful for the financial support from the grant of the Ministry of Research, Innovation, and Digitization, project no. PNRR-III-C9-2022-I8-291, contract no. 760081/23.05.2023, within the National Recovery and Resilience Plan.

Conflicts of Interest: The authors declare no conflicts of interest.

### References

- 1. Ozyurt, D.; Al Kobaisi, M.; Hocking, R.K.; Fox, B. Properties, synthesis, and applications of carbon dots: A review. *Carbon. Trends* **2023**, *12*, 100276.
- 2. Etefa, H.F.; Dejene, F.B. Applications of Green Carbon Dots in Personalized Diagnostics for Precision Medicine. *Int. J. Mol. Sci.* **2025**, *26*, 2846.
- 3. Bhattacharya, T.; Shin, G.H.; Kim, J.T. Carbon Dots: Opportunities and Challenges in Cancer Therapy. *Pharmaceutics* **2023**, *15*, 1019.
- 4. Pandey, V.K.; Tripathi, A.; Taufeeq, A.; Hussain Dar, A.; Samrot, A.V.; Rustagi, S.; Malik, S.; Bhattacharya, T.; Kovacs, B.; Shaikh, A.M. Significance and applications of carbon dots in anti cancerous nanodrug conjugate development: A review. *Appl. Surf. Sci. Adv.* **2024**, *19*, 100550.
- 5. Liu, J.; Li, R.; Yang, B. Carbon Dots: A New Type of Carbon-Based Nanomaterial with Wide Applications. *ACS Cent. Sci.* **2020**, *6*, 2179–2195.
- 6. Tian, X.; Zeng, A.; Liu, Z.; Zheng, C.; Wei, Y.; Yang, P.; Zhang, M.; Yang, F.; Xie, F. Carbon Quantum Dots: In vitro and in ivo Studies on Biocompatibility and Biointeractions for Optical Imaging. *Int. J. Nanomed.* **2020**, *15*, 6519–6529.
- 7. Ansari, L.; Hallaj, S.; Hallaj, T.; Amjadi, M. Doped-carbon dots: Recent advances in their biosensing, bioimaging and therapy applications. *Colloids Surf. B Biointerfaces* **2021**, 203, 111743.
- 8. Li, Q.X.; Shen, D.; Xing, D. Carbon quantum dots as ROS-generator and -scavenger: A comprehensive review. *Dyes Pigm.* **2023**, 208, 110784.

9. Osorio, H.M.; Castillo-Solís, F.; Barragán, S.Y.; Rodríguez-Pólit, C.; Gonzalez-Pastor, R. Graphene Quantum Dots from Natural Carbon Sources for Drug and Gene Delivery in Cancer Treatment. *Int. J. Mol. Sci.* **2024**, *25*, 10539.

- Zhang, Q.; Wang, R.; Feng, B.; Zhong, X.; Ostrikov, K. Photoluminescence mechanism of carbon dots: Triggering high-colorpurity red fluorescence emission through edge amino protonation. *Nat. Commun.* 2021, 12, 6856.
- 11. Wang, B.; Lu, S. The light of carbon dots: From mechanism to applications. Matter 2022, 5, 110-149.
- 12. Jiang, Y.; Zhao, T.; Xu, W.; Peng, Z. Red/NIR C-dots: A perspective from carbon precursors, photoluminescence tuning and bioapplications. *Carbon* **2024**, *219*, 118838.
- Gallareta-Olivares, G.; Rivas-Sanchez, A.; Cruz-Cruz, A.; Hussain, S.M.; González-González, R.B.; Cárdenas-Alcaide, M.F.; Iq-bal, H.M.N.; Parra-Saldívar, R. Metal-doped carbon dots as robust nanomaterials for the monitoring and degradation of water pollutants. Chemosphere 2023, 312, 137190.
- 14. Stan, C.S.; Coroabă, A.; Ursu, E.L.; Secula, M.S.; Simionescu, B.C. Fe(III) doped carbon nanodots with intense green photoluminescence and dispersion medium dependent emission. *Sci. Rep.* **2019**, *9*, 18893.
- 15. Shi, Y.; Xia, Y.; Zhou, M.; Wang, Y.; Bao, J.; Zhang, Y.; Cheng, J. Facile synthesis of Gd/Ru-doped fluorescent carbon dots for fluorescent/MR bimodal imaging and tumor therapy. *J. Nanobiotechnol* **2024**, 22, 88.
- 16. Lakshmi Devi, A.; Sreelakshmi, M.; Suneesh, P.V.; Satheesh Babu, T.G. Copper and nickel doped carbon dots for rapid and sensitive fluorescent turn-off detection of bilirubin. *Sci. Rep.* **2025**, *15*, 1262.
- 17. Rub Pakkath, S.A.; Shashank Shankar, C.; Praneetha, S.; Arumugam, V.M.; Yogesh, K.; Periyasamy, L.; Muthukamalam, S.; Sudha, R.S.; Kirankumar, S. Transition Metal Ion (Mn2+, Fe2+, Co2+, and Ni2+)-Doped Carbon Dots Synthesized via Microwave-Assisted Pyrolysis: A Potential Nanoprobe for Magneto-fluorescent Dual-Modality Bioimaging. *ACS Biomater. Sci. Eng.* 2018, 4, 2582–2596.
- 18. Molaei, M.J. Gadolinium-doped fluorescent carbon quantum dots as MRI contrast agents and fluorescent probes. *Sci. Rep.* **2022**, 12, 17681.
- 19. Ali, V.; Kefayati, H.; Shafiee Ardestani, M.; Pourahmad, A. Synthesis and evaluation of new magneto-fluorescent carbon dot based on manganese citrate for MRI imaging. *Magn. Reson. Mater. Phy* **2024**, *37*, 139–148.
- Tsai, T.-H.; Lo, W.; Wang, H.-Y.; Tsai, T.-L. Carbon Dot Micelles Synthesized from Leek Seeds in Applications for Cobalt (II) Sensing, Metal Ion Removal, and Cancer Therapy. J. Funct. Biomater. 2024, 15, 347.
- 21. Xia, J.; Kawamura, Y.; Suehiro, T.; Chen, Y.; Sato, K. Carbon dots have antitumor action as monotherapy or combination therapy. *Drug Discov. Ther.* **2019**, *13*, 114–117.
- 22. Mogharbel, A.T.; Abu-Melha, S.; Hameed, A.; Attar, R.M.S.; Alrefaei, A.F.; Almahri, A.; El-Metwaly, N. Anticancer and microbicide action of carbon quantum dots derived from microcrystalline cellulose: Hydrothermal versus infrared assisted techniques. *Arab. J. Chem.* **2023**, *16*, 104419.
- 23. Wang, M.; Lan, S.; Zhang, W.; Jin, Q.; Du, H.; Sun, X.; He, L.; Meng, X.; Su, L.; Liu, G. Anti-Cancer Potency of Copper-Doped Carbon Quantum Dots Against Breast Cancer Progression. *Int. J. Nanomed.* **2024**, *19*, 1985–2004.
- 24. Tiron, A.; Stan, C.S.; Luta, G.; Uritu, C.M.; Vacarean-Trandafir, I.-C.; Stanciu, G.D.; Coroaba, A.; Tiron, C.E. Manganese-Doped N-Hydroxyphthalimide-Derived Carbon Dots—Theranostics Applications in Experimental Breast Cancer Models. *Pharmaceutics* **2021**, *13*, 1982.
- 25. Damato, A.N. Diphenylhydantoin: Pharmacological and clinical use, Progress. Prog. CardiovasC Dis. 1969, 12, 1–15.
- 26. Puszyńska-Tuszkanow, M.; Daszkiewicz, M.; Maciejewska, G.; Adach, A.; Cieslak-Golonka, M. Interaction of hydantoins with transition metal ions: Synthesis, structural, spectroscopic, thermal and magnetic properties of [M(H<sub>2</sub>O)4(phenytoinate)2] M = Ni(II), Co(II). *Struct. Chem.* **2010**, *21*, 315–321.
- 27. ISO 10993–5:2009; Biological Evaluation of Medical Devices—Part 5: Tests for in Vitro Cytotoxicity. International Organization for Standardization: Geneva, Switzerland, 2009; English version. Available online: https://www.iso.org/standard/36406.html (accessed on 1 July 2024).
- 28. Dragoi, B.; Uritu, C.M.; Agrigoroaie, L.; Lutic, D.; Hulea, V.; Postole, G.; Coroaba, A.; Carasevici, E. MnAl-Layered Double Hydroxide Nanosheets Infused with Fluorouracil for Cancer Diagnosis and Therapy. *ACS Appl. Nano Mater.* **2021**, *4*, 2061–2075.
- 29. Homer, J.; Beevers, M.S. Driven-equilibrium single-pulse observation of T1 relaxation. A reevaluation of a rapid "new" method for determining NMR spin-lattice relaxation times. *J. Magn. Reason.* **1985**, *63*, 287–297.
- 30. Deawati, Y.; Onggo, D.; Mulyani, I.; Iwan Hastiawan, I.; Utami, R.A.; Kurnia, D. Synthesis of [Mn(Salen)Cl] Complex Compound and Superoxide Dismutase Activity Determination through Non-Enzymatic Method. *KEM* **2018**, *811*, 22–27.

31. Stepanidenko, E.A.; Vedernikova, A.A.; Badrieva, Z.F.; Brui, E.A.; Ondar, S.O.; Miruschenko, M.D.; Volina, O.V.; Koroleva, A.V.; Zhizhin, E.V.; Ushakova, E.V. Manganese-Doped Carbon Dots as a Promising Nanoprobe for Luminescent and Magnetic Resonance Imaging. *Photonics* **2023**, *10*, 757.

- 32. Korin, E.; Froumin, N.; Cohen, S. Surface Analysis of Nanocomplexes by X-ray Photoelectron Spectroscopy (XPS). *ACS Biomater*. *Sci. Eng.* **2017**, *3*, 882–889.
- Mourdikoudis, S.; Pallares, R.M.; Thanh, N.T.K. Characterization techniques for nanoparticles: Comparison and complementarity upon studying nanoparticle properties. Nanoscale 2018, 10, 12871–12934.
- 34. Feng, J.; Gao, H.; Zheng, L.; Chen, Z.; Zeng, S.; Jiang, C.; Dong, H.; Liu, L.; Zhang, S.; Zhang, X. A Mn-N3 single-atom catalyst embedded in graphitic carbon nitride for efficient CO<sub>2</sub> electroreduction. *Nat. Commun.* **2020**, *11*, 4341.
- 35. Tariq, M.; Shivalkar, S.; Hasan, H.; Sahoo, A.K.; Sk, M.P. Manganese Doping in Biomass Derived Carbon Dots Amplifies White Light-Induced Antibacterial Activity. *ACS Omega* **2023**, *8*, 49460–49466.
- 36. Li, J.; Chen, M.; Cullen, D.A.; Hwang, S.; Wang, M.; Li, B.; Liu, K.; Karakalos, S.; Lucero, M.; Zhang, H.; et al. Atomically dispersed manganese catalysts for oxygen reduction in proton-exchange membrane fuel cells. *Nat. Catal.* **2018**, *1*, 935–945.
- 37. Ferreyra, D.D.; Sartori, D.R.; Ezquerra Riega, S.D.; Rodríguez, H.B.; Gonzalez, M.C. Tuning the nitrogen content of carbon dots in carbon nitride nanoflakes. *Carbon* **2020**, *167*, 230–243.
- 38. Eroglu, Z.; Ozer, M.S.; Metin, Ö. Nitrogen-Based Imperfections in Graphitic Carbon Nitride New Trend for Enhancing Photocatalytic Activity? *ChemCatChem* **2024**, *16*, e202301560.
- 39. Li, H.; Xia, Y.; Hu, T.; Deng, Q.; Du, N.; Hou, W. Enhanced charge carrier separation of manganese(ii)-doped graphitic carbon nitride: Formation of N–Mn bonds through redox reactions. *J. Mater. Chem. A.* **2018**, *6*, 6238–6243.
- 40. Tian, B.; Liu, S.; Feng, L.; Liu, S.; Gai, S.; Dai, Y.; Xie, L.; Liu, B.; Yang, P.; Zhao, Y. Renal-clearable nickel doped carbon dots with boosted photothermal conversion efficiency for multimodal imaging-guided cancer therapy in the second near-infrared biowindow. *Adv. Funct. Mat.* **2021**, *31*, 2100549.
- 41. Wang, S.; Morelos-Gómez, A.; Lei, Z.; Terrones, M.; Takeuchi, K.; Sugimoto, W.; Endo, M.; Kaneko, K. Correlation in structure and properties of highly-porous graphene monoliths studied with a thermal treatment method. *Carbon* **2016**, *96*, 174–183.
- 42. González-González, R.B.; González, L.T.; Madou, M.; Leyva-Porras, C.; Martinez-Chapa, S.O.; Mendoza, A. Synthesis, Purification, and Characterization of Carbon Dots from Non-Activated and Activated Pyrolytic Carbon Black. *Nanomater* **2022**, *12*, 298.
- 43. Ding, H.; Li, X.-H.; Xiao-Bo Chen, X.-B.; Wei, J.-S.; Li, X.-B.; Xiong, H.-M. Surface states of carbon dots and their influences on luminescence. *J. Appl. Phys.* **2020**, *127*, 231101.
- 44. Ehrat, F.; Bhattacharyya, S.; Schneider, J.; Löf, A.; Wyrwich, R.; Rogach, A.L.; Stolarczyk, J.K.; Urban, A.S.; Feldmann, J. Tracking the Source of Carbon Dot Photoluminescence: Aromatic Domains versus Molecular Fluorophores. *Nano Lett.* **2017**, *17*, 7710.
- 45. Mohandoss, S.; Palanisamy, S.; Priya, V.V.; Mohan, S.K.; Shim, J.-J.; Yelithao, K.; You, S.G.; Lee, Y.R. Excitation-dependent multiple luminescence emission of nitrogen and sulfur co-doped carbon dots for cysteine sensing, bioimaging, and photoluminescent ink applications. *Microchem. J.* 2021, 167, 106280.
- 46. Jiang Y, Han Q, Peng J, Lv Y, Ruan Y, Weng X, Milcovich G, Tailored hydrothermal platforms for fluorescent Q-dots with theranostic application. *Spectrochim. Acta Part A Mol. Biomol. Spectrosc.* **2025**, 331, 125773.
- 47. Gomez-Blanco, N.; Prato, M. Microwave-assisted one-step synthesis of water-soluble manganese-carbon nanodot clusters. *Commun. Chem.* **2023**, *6*, 174–181.
- 48. Sun, S.; Guan, Q.; Liu, Y.; Wei, B.; Yang, Y.; Yu, Z. Highly luminescence manganese doped carbon dots. *Chin. Chem. Lett.* **2019**, 30, 1051–1054.
- 49. Zhang, T.; Zhu, J.; Zhai, Y.; Wang, H.; Bai, H.; Dong, B.; Wang, H.; Song, H. A novel mechanism for red emission carbon dots: Hydrogen bond dominated molecular states emission. *Nanoscale* **2017**, *9*, 13042.
- Bhavikatti, S.K.; Zainuddin, S.L.A.; Ramli, R.B.; Nadaf, S.J.; Dandge, P.B.; Khalate, M.; Karobari, M.I. Green-synthesized carbon dots from ginger: Multifunctional agents against oral pathogens with biocompatibility in human gingival fibroblast cells. Curr. Plant Biol. 2024, 40, 100392.
- 51. Nugroho D, Thinthasit A, Khoris I M, Siriputthaiwan P, Benchawattananon R, Chanthai S, L-histidine doped CDs from Zingiber Montanum using hydrothermal method to enhance its antimicrobial activity and imply for latent fingerprint detection. *Arabian J. Chem.* **2024**, *17*, 105602.
- 52. Marković, Z.M.; Budimir, M.D.; Danko, M.; Milivojević, D.D.; Kubat, P.; Zmejkoski, D.Z.; Pavlović, V.B.; Mojsin, M.M.; Stevanović, M.J.; Todorović Marković, B.M. Structural, optical, and bioimaging characterization of carbon quantum dots solvothermally synthesized from o-phenylenediamine. *Beilstein J. Nanotechnol.* 2023, 14, 165–174.

53. Zmejkoski, D.Z.; Zdravković, N.M.; Mitić, D.D.; Marković, Z.M.; Budimir Filimonović, M.D.; Milivojević, D.D.; Todorović Marković, B.M. Graphene Quantum Dots in Bacterial Cellulose Hydrogels for Visible Light-Activated Antibiofilm and Angiogenesis in Infection Management. *Int. J. Mol. Sci.* 2025, 26, 1053.

- 54. Al-anbaky, Q.; Al-karakooly, Z.; Kilaparty, S.P.; Agrawal, M.; Albkuri, Y.M.; RanguMagar, A.B.; Ghosh, A.; Ali, N. Cytotoxicity of Manganese (III) Complex in Human Breast Adenocarcinoma Cell Line Is Mediated by the Generation of Reactive Oxygen Species Followed by Mitochondrial Damage. *Int. J. Toxicol.* **2016**, *35*, 672–682.
- 55. Isnaini, I.; Permatasari, N.; Mintaroem, K.; Prihardina, B.; Widodo, M.A. Oxidants-Antioxidants Profile in the Breast Cancer Cell Line MCF-7. *Asian Pac. J. Cancer Prev.* **2018**, 29, 3175–3178.
- 56. Choromańska, A.; Saczko, J.; Kulbacka, J.; Kamińska, I.; Skołucka, N.; Majkowski, M. Comparison of the influence of photodynamic reaction on the Me45 and MEWO cell lines in vitro. *Contemp. Oncol.* **2012**, *16*, 240–243.
- 57. Becuwe, P.; Ennen, M.; Klotz, R.; Barbieux, C.; Grandemange, S. Manganese superoxide dismutase in breast cancer: From molecular mechanisms of gene regulation to biological and clinical significance. *Free. Radic. Biol. Med.* **2014**, 77, 139–151.
- 58. Martin, R.C.; Ahn, J.; Nowell, S.A.; Hein, D.W.; Doll, M.A.; Martini, B.D.; Ambrosone, C.B. Association between manganese superoxide dismutase promoter gene polymorphism and breast cancer survival. *Breast Cancer Res.* **2006**, *8*, R45.
- 59. Ali, S.F.; Duhart, H.M.; Newport, G.D.; Lipe, W.; Slikker, W. Manganese-induced reactive oxygen species: Comparison between Mn<sup>+2</sup> and Mn<sup>+3</sup>. *Neurodegeneration* **1995**, *4*, 329–334.
- 60. Tao Y, Ou Y, Yin H, Chen Y, Zhong S, Gao Y, Zhao Z, He B, Huang Q, Deng Q, Deng Q, et al: Establishment and characterization of human osteosarcoma cells resistant to pyropheophorbide-α methyl ester-mediated photodynamic therapy. *Int. J. Oncol.* 2017, 51, 1427–1438.
- Geraldes, C.F.G.C. Manganese Oxide Nanoparticles for MRI-Based Multimodal Imaging and Theranostics. *Molecules* 2024, 29, 5591.
- 62. Van Roosbroeck, R.; Van Roy, W.; Stakenborg, T.; Trekker, J.; D'Hollander, A.; Dresselaers, T.; Himmelreich, U.; Lammertyn, J.; Lagae, L. Synthetic Antiferromagnetic Nanoparticles as Potential Contrast Agents in MRI. ACS Nano 2014, 8, 2269–2278.
- 63. Son, T.; Kim, M.; Choi, M.; Nam, S.H.; Yoo, A.; Lee, H.; Han, E.H.; Hong, K.S.; Park, H.S. Advancing fluorescence imaging: Enhanced control of cyanine dye-doped silica nanoparticles. *J. Nanobiotechnol.* **2025**, 22, 347–361.
- 64. Doan, V.H.M.; Nguyen, V.T.; Mondal, S.; Vo, T.M.T.; Ly, C.D.; Vu, D.D.; Ataklti, G.Y.; Park, S.; Choi, J.; Oh, J. Fluorescence/photoacoustic imaging-guided nanomaterials for highly efficient cancer theragnostic agent. *Sci. Rep.* **2021**, *11*, 15943.
- 65. Walsh, E.G.; Mills, D.R.; Lim, S.; Sana, B.; Brilliant, K.E.; Park, W.K.C. MRI contrast demonstration of antigen-specific targeting with an iron-based ferritin construct. *J. Nanopart Res.* **2013**, *15*, 1409.
- 66. Hamzaini, N.N.; Ghazali, S.A.; Yusoff, A.N.; Zaki, F.M.; Sulaiman, W.N.A.W.; Dwihapsari, Y. FeCl3 and GdCl3 solutions as superfast relaxation modifiers for agarose gel: A quantitative analysis. *Magn. Reson. Mater. Phys. Biol. Med.* **2025**, *38*, 141–160.
- 67. Caspani, S.; Magalhães, R.; Araújo, J.P.; Sousa, C.T. Magnetic Nanomaterials as Contrast Agents for MRI. *Materials* **2020**, *13*, 2586.
- 68. Rohrer, M.; Bauer, H.; Mintorovitch, J.; Requardt, M.; Weinmann, H.-J. Comparison of magnetic properties of MRI contrast
- 69. Zuo, H.; Chen, W.; Li, B.; Xu, K.; Cooper, H.; Gu, Z.; Xu, Z.P. MnAl Layered Double Hydroxide Nanoparticles as a DualFunctional Platform for Magnetic Resonance Imaging and siRNA Delivery. *Chem. Eur. J.* **2017**, 23, 14299.
- 70. Chen, Y.; Ye, D.; Wu, M.; Chen, H.; Zhang, L.; Shi, J.; Wang, L. Break-up of Two-Dimensional MnO<sub>2</sub> Nanosheets Promotes Ultrasensitive pH-Triggered Theranostics of Cancer. *Adv. Mater.* **2014**, *26*, 7019–7026.
- 71. Huang, G.; Zhang, K.-L.; Chen, S.; Li, S.-H.; Wang, L.-L.; Wang, L.-P.; Liu, R.; Gao, J.; Yang, H.-H. Manganese-iron layered double hydroxide: A theranostic nanoplatform with pH-responsive MRI contrast enhancement and drug release. *J. Mater. Chem. B* **2017**, *5*, 3629–3633.
- 72. Na, H.B.; Lee, J.H.; An, K.; Park, Y.I.; Park, M.; Lee, I.S.; Nam, D.-H.; Kim, S.T.; Kim, S.-H.; Kim, S.-W.; et al. Development of a T1 Contrast Agent for Magnetic Resonance Imaging Using MnO Nanoparticles. *Angew. Chem.* **2007**, *46*, 5397–5401.
- 73. Chen, Y.; Yin, Q.; Ji, X.; Zhang, S.; Chen, H.; Zheng, Y.; Sun, Y.; Qu, H.; Wang, Z.; Li, Y.; et al. Manganese oxide-based multi-functionalized mesoporous silica nanoparticles for pH-responsive MRI, ultrasonography and circumvention of MDR in cancer cells. *Biomaterials* **2012**, *33*, 7126–7137.

74. Li, B.; Gu, Z.; Kurniawan, N.; Chen, W.; Xu, Z.P. Manganese-Based Layered Double Hydroxide Nanoparticles as a T1-MRI Contrast Agent with Utrasensitive pH Response and High Relaxivity. *Adv. Mater.* **2017**, *29*, 1700373.

75. Banerjee, A.; Blasiak, B.; Pasquier, E.; Tomanek, B.; Trudel, S. Synthesis, characterization, and evaluation of PEGylated first-row transition metal ferrite nanoparticles as T2 contrast agents for high-field MRI. RSC Adv. 2017, 7, 38125–38134.

Disclaimer/Publisher's Note: The statements, opinions and data contained in all publications are solely those of the individual author(s) and contributor(s) and not of MDPI and/or the editor(s). MDPI and/or the editor(s) disclaim responsibility for any injury to people or property resulting from any ideas, methods, instructions or products referred to in the content.





Article

## Markedly Enhanced Photoluminescence of Carbon Dots Dispersed in Deuterium Oxide

Corneliu S. Stan <sup>1</sup>, Adina Coroaba <sup>2</sup>, \*, Conchi O. Ania <sup>3</sup>, Cristina Albu <sup>1</sup> and Marcel Popa <sup>1,4</sup>, \*

- Faculty of Chemical Engineering and Environmental Protection, Gh. Asachi Technical University D, Mangeron 73 Ave., 700050 Iasi, Romania; stancs@tuiasi.ro (C.S.S.)
- Centre of Advanced Research in Bionanoconjugates and Biopolymers, "Petru Poni" Institute of Macromolecular Chemistry of Romanian Academy, Grigore Ghica Voda 41A Alley, 700487 Iasi, Romania
- Conditions Extremes Materiaux: Haute Temperature et Irradiation (CEMHTI), UPR 3079, CNRS, Université d'Orléans, 45071 Orleans, France; conchi.ania@cnrs-orleans.fr
- Academy of Romanian Scientists, Ilfov Street, 050044 Bucharest, Romania
- \* Correspondence: adina.coroaba@icmpp.ro (A.C.); marpopa2001@yahoo.fr (M.P.)

Abstract: In this work, we report some surprisingly interesting results in our pursuit to improve the photoluminescent emission of Carbon Dots (CDs) prepared from various precursors. By simply replacing the regular water with deuterium oxide (D<sub>2</sub>O) as a dispersion medium, the emission intensity and the subsequent quantum efficiency of the radiative processes could be markedly enhanced. The present study was performed on our previous reported works related to CDs; in each case, the preparation path was maintained accordingly. For each type of CD, the emission intensity and the absolute photoluminescence quantum yield (PLQY) were highly improved, with, in certain cases, more-than-doubled values being recorded and the gain in performance being easily noticeable with the naked eye even in plain daylight. For each type of CD dispersed in regular water and heavy water, respectively, the photoluminescent properties were thoroughly investigated through Steady State, lifetime, and absolute PLQY. To further elucidate the mechanism involved in the photoluminescence intensity enhancement, samples of D<sub>2</sub>O and H<sub>2</sub>O dispersed CDs were embedded in a crosslinked Poly(acrylic acid) polymer matrix. The investigations revealed the major influence of the deuterium oxide dispersion medium over the PL emission properties of the investigated CDs.

Keywords: carbon nanodots; photoluminescence; deuterated mediums



Academic Editor: Jandro L. Abot

Received: 9 December 2024 Revised: 15 January 2025 Accepted: 19 January 2025 Published: 22 January 2025

Citation: Stan, C.S.; Coroaba, A.; Ania, C.O.; Albu, C.; Popa, M. Markedly Enhanced Photoluminescence of Carbon Dots Dispersed in Deuterium Oxide. *C* 2025, 11, 10. https://doi.org/10.3390/ c11010010

Copyright: © 2025 by the authors. Licensee MDPI, Basel, Switzerland. This article is an open access article distributed under the terms and conditions of the Creative Commons Attribution (CC BY) license (https://creativecommons.org/licenses/by/4.0/).

### 1. Introduction

Photoluminescent Carbon Dots (CDs) are a newer established class of carbon materials which gained a lot of research interest in the last decade due to their high application potential in optoelectronic devices, sensors, medical investigations [1–3], and even food sciences [4]. One of their particular properties is the observed emission peaks dependence on the excitation wavelength, which triggered a lot of debate regarding the involved photoluminescence mechanisms. To date, the contribution of both the defect-rich,  $\pi$ -bond-conjugated, graphitic-like configuration of the carbon core and the radiative transitions arising from the surface-located functional groups is still a generally accepted open debate subject [5–7]. While the first study regarding the influence of deuterium substitution of hydrogen in naphthalene over its phosphorescence arising from triplet states is dated to the beginning of the 1960s [8], to date, there are still a limited number of studies regarding this matter. More recently, the benefit of deuterated water over the luminescent emission

C 2025, 11, 10 2 of 14

was studied in a wider range of fluorescent dyes [9,10], the results being impressive since the enhancement of the recorded PL intensity varies within 30-70% range. A similar effect of increasing the fluorescent intensities induced by deuterium oxide was reported for intercalated dyes, such as fluorochromes bound to DNA [11], or in the case of liquid chromatography with fluorescence detection [12]. The presence of deuterium in various dyes, proteins, and lanthanide compounds is also able to produce a notable enhancement of their luminescent emission [13]. Also, in the pursuit of improving the performance of the OLED displays in terms of efficiency and long-term operational stability, hydrogen replacement with deuterium in TADF/AlQ/Q2AlOAr emitters was found to be highly effective in achieving these goals [14,15]. In a very recent study, CDs prepared from citric acid via a hydrothermal route were dispersed both in water and deuterium oxide, and a similar markedly increased emission was recorded. Thus, the PLQY values were doubled in case of D<sub>2</sub>O-prepared CDs. The structural analysis revealed, according to the authors, the replacement to a certain extent of hydrogen with deuterium within the CDs structure [13–16], which provide, in their view, a decisive contribution in achieving the overall emission intensity improvement. As will be further presented, our investigation does not necessarily sustain the claim regarding the significant contribution of the H to D substitution within the CDs structure to the observed emission intensity improvement. While the effective deuteration of the CDs might play a significant role in achieving better PLQY, the particular conditions provided by the D<sub>2</sub>O dispersion medium environment are, in our opinion, the main trigger of the markedly enhanced emission efficiency. In this work, CDs prepared through thermal processing of some imide precursors and argan waste were dispersed in deuterium oxide and further investigated through Steady State, lifetime, and PLQY fluorescence. For gathering more information regarding the role of D<sub>2</sub>O in achieving the recorded enhancement of photoluminescent emission, the CDs dispersions were further embedded in a crosslinked Poly(acrylic acid) polymer matrix. The reported results could bring additional evidence in the pursuit of definitive elucidation of the specific PL mechanisms of CDs and also an interesting approach for their applications in optoelectronics, sensors, and medical imaging, where an as-high-as-possible emission intensity is often required. Also, given the observed markedly enhanced PL emission in D<sub>2</sub>O medium, this study may trigger further interest in research related to deuteration and deuterated mediums.

## 2. Materials and Methods and Preparation

### 2.1. Materials

N-Hydroxyphthalimide (NHF) (97%), N-Hydroxysuccinimide (NHS), anhydrous ferric chloride (FeCl<sub>3</sub>), acrylic acid (AA), N,N'-Methylenebisacrylamide (MBAM), 1-Hydroxycyclohexyl phenyl ketone (HCPK), deuterium oxide (D<sub>2</sub>O), and ethanol (EtOH) were sourced from Merck Chemicals Darmstadt, Germany. Argan cake waste obtained during argan oil preparation through cold pressing was provided by a local Moroccan co-operative. Ultra-pure distilled water (Merck-Millipore-Direct Q) was used during preparation stages.

### 2.2. Methods

Freshly prepared samples were investigated through steady-state fluorescence, the emission spectra were recorded on a Horiba Fluoromax 4P spectrofluorometer (Horiba Ltd., Kyoto, Japan). In each case of pair investigation (H<sub>2</sub>O vs. D<sub>2</sub>O), the measurement parameters (entrance/exit slits and integration time) were kept unchanged. The absolute photoluminescence quantum yield (PLQY) values were recorded with the Quanta  $\Phi$  integration sphere controlled by the Horiba spectrofluorometer according to the equip-

C 2025, 11, 10 3 of 14

ment manufacturer's procedure using FluorEssence software (ver. 3.5.1.20) for spectral acquisition and subsequent calculations of the QY and CIE1931 parameters. Excited-states lifetimes (LT) were investigated on the same equipment with the attached Horiba Lifetime module using a 370 nm LED excitation source.

A dimensional analysis (DLS) was performed on a Malvern Panalytical Zetasizer Advance Pro Red (Malvern Panalytical Ltd., Malvern, UK). Freshly prepared and one-weekaged dispersions were investigated.

## 2.3. Preparation

Each type of CD was prepared according to experimental approach detailed in our previous works. Briefly, NHF (NHF-CDs) [17], NHS (NHS-CDs) [18], argan waste CDs (AW-CDs) [19] and NHF-Fe(III) complex (Fe-CDs) [20], were prepared by thermal processing of the respective precursors, followed by dispersion in  $H_2O$  and  $D_2O$  and further centrifugation, purification and dimensional selection. In case of Fe(III) doped CDs (Fe-CDs), additional steps for preparation/purification of the intermediate Fe(III)-NHF complex is required. For the embedment of the CDs in the polymer matrix the following experimental procedure was followed: in each 1.5 mL of freshly prepared NHF-CDs dispersed in  $D_2O$  and  $H_2O$ , respectively, 140 mmol AA and 2 mmol MBAm (as crosslinker) were dissolved under stirring, followed by the addition of 0.1 mmol of HCPK (as photoinitiator). Then, the mixture is transferred in a conveniently shaped container and further photopolymerized through exposure to a UV-A (360–370 nm) source. The photopolymerization process is fast (under 60 s), depending on the UV-A source type (in our case a 365 nm LED array was used).

## 3. Results and Discussion

## 3.1. Photoluminescence Investigation

One of the most interesting and sought after features of CDs is their PL emission, which is excitation-wavelength-dependent in most reported cases. Besides the type of precursors and the chosen preparation route, their PL emission characteristics are strongly dependent on the dispersion environment, the solvent or the polymer matrix types being key factors in terms of PL emission efficiency and location of the emission peaks [17,21]. The PL mechanism of CDs is still an open debate subject with a general opinion in favor of both contribution of the defect-rich, disordered graphitic core and the radiative transitions arising from the surface-located functional groups [6]. As mentioned in Section 1, there are several studies regarding the influence of deuteration over the emission intensity of CDs or other fluorophores where the "isotope effect" is highlighted as the main reason of the observed emission enhancement [16,22]. According to our study, there are several observations worth mentioning regarding this approach: (a) spontaneous  $H \to D$  exchange might occur for a certain functional groups especially in case of organic fluorophores (-OH, NH) when solved in D<sub>2</sub>O but less probable in the case of CDs where the highly packed carbonaceous core involves bonding stability achieved through high temperature carbonization of the precursor; (b) deuteration is more likely to occur in the surfacelocated functional groups attached to the carbonaceous core of the CDs especially when the hydrothermal (with D<sub>2</sub>O instead of H<sub>2</sub>O as processing medium) route is used for the their preparation; (c) CDs obtained through the wider spread route of direct thermal exposure (pyrolytic or not) of the precursor is less capable of sustaining a H  $\rightarrow$  D exchange since the CDs are already structurally stable within the  $D_2O$  dispersion medium. In this case, a preliminary stage of  $H \to D$  exchange within the precursor might provide a certain level of structural deuteration of the resulting CDs. Generally, the efficiency of the radiative transitions could be markedly affected by the surroundings of the emissive species. In

C 2025, 11, 10 4 of 14

aqueous dispersions, the efficiency of the radiative processes is lowered by the vicinity of the OH oscillators favoring vibrational coupling which provide an efficient non-radiative deactivation path of the excited states [23,24]. Given the configuration of the CDs with their multiple emission sites located within the carbonaceous core or in the surface-attached functional groups, it is expected that the overall efficiency of the radiative processes to be strongly affected. Switching water to deuterium oxide provides a more favorable surrounding where the non-radiative deactivation paths are markedly diminished, thus favoring the radiative relaxations through photon production. Given the particularities of  $D_2O$  [25], which dissociates less than  $H_2O$ , and the new vibrational conditions due to the presence of the heavier deuterium providing a better environment for the photonic processes within the CDs. Therefore, in our view and due to the investigations results detailed here, the isotope effect plays an indirect role in enhancing the PL emission by providing a more favorable environment for the radiative transitions.

### 3.1.1. Steady-State Fluorescence Investigation

For each investigated type of CD, the spectra were recorded at three excitation wavelengths (330, 350, 370 nm), with the equipment measuring parameters (entrance/exit slits, integration time, etc.) kept unchanged. In Figure 1 are presented the recorded spectra recorded for NHF-CDs dispersions in  $H_2O$  and  $D_2O$ , respectively, while the embedded pictures (recorded using a commonly available laboratory 370 nm UV lamp) could provide a clear view regarding the visually perceived emission intensity difference between the two samples. As could be noted, the recorded spectral intensity at any excitation wavelength is at least  $2.4 \times$  higher in case of NHF-CDs dispersed in  $D_2O$ , which is consistent with the visually perceived observation. In both cases, the location of the peaks remain practically unchanged irrespective of the excitation wavelength, with the most intense peaks being recorded at 370 nm excitation.

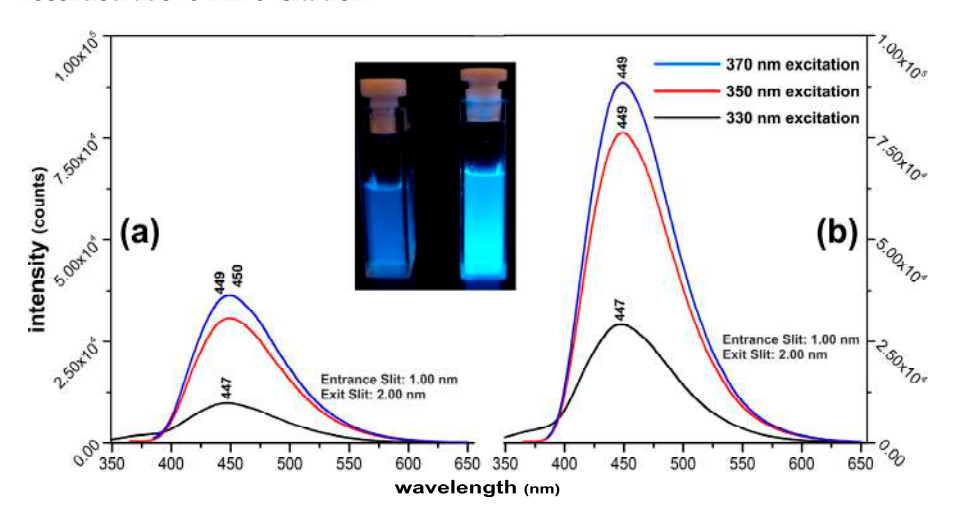


Figure 1. PL emission of the NHF-CDs dispersed in (a) water, (b) deuterium oxide.

In case of the NHS-CDs (Figure 2), the emission intensity enhancement in the  $D_2O$  environment is still significant (both instrumental and visual) but not as impressive as observed in the previous situation. Overall, the emission intensity of this type of CDs is markedly lower compared with the NHF-CDs (please note the entrance/exit slits values) but still  $1.2\times$  higher for the NHS-CDs dispersed in  $D_2O$ . The recorded emission peaks remain unchanged at 350 and 370 nm excitation, with a minor difference (414 to 417 nm) being noted at a 330 nm excitation. The maximum intensity peaks were, in both cases, recorded at 350 nm excitation.

C **2025**, 11, 10 5 of 14

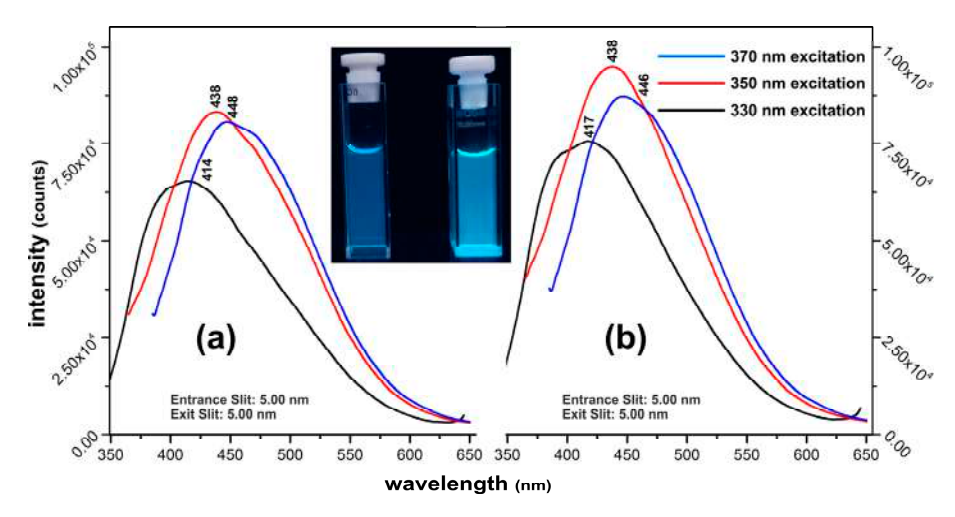


Figure 2. PL emission of the NHS-CDs dispersed in (a) water, (b) deuterium oxide.

The AW-CDs (Figure 3) displayed a similar behavior as the NHS-CDs, with a clearly enhanced emission recorded for the  $D_2O$  dispersions. In both cases ( $H_2O$  and  $D_2O$  dispersions), the most intense peaks are recorded at the 370 nm excitation wavelength, their location being unchanged at the 350 nm excitation, with a slight difference (414 to 417 nm) recorded at the 330 nm and (448 to 446 nm) at the 370 nm excitation wavelengths. In all cases, the observed unchanged location of the emission peaks (in  $H_2O$  and  $H_2O$  and  $H_2O$  dispersions) are consistent with other reported works where the emission peaks in deuterated solvents show no significant shift [6].

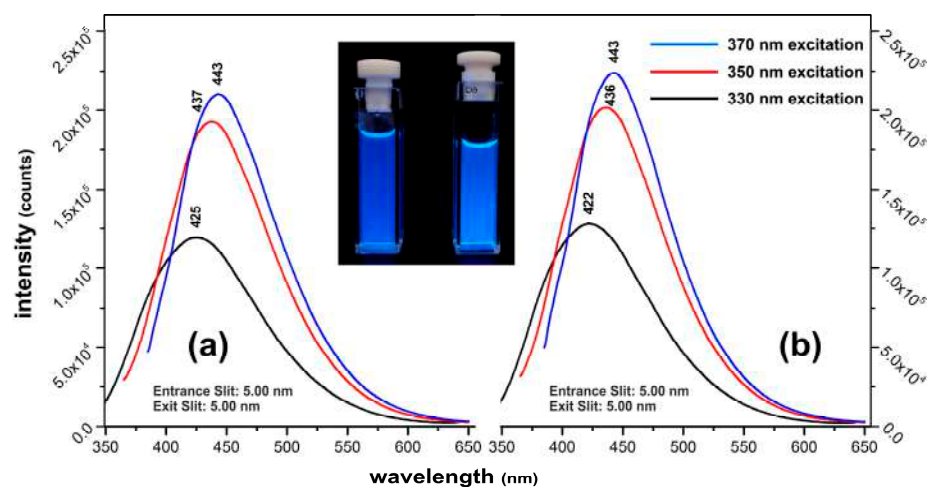
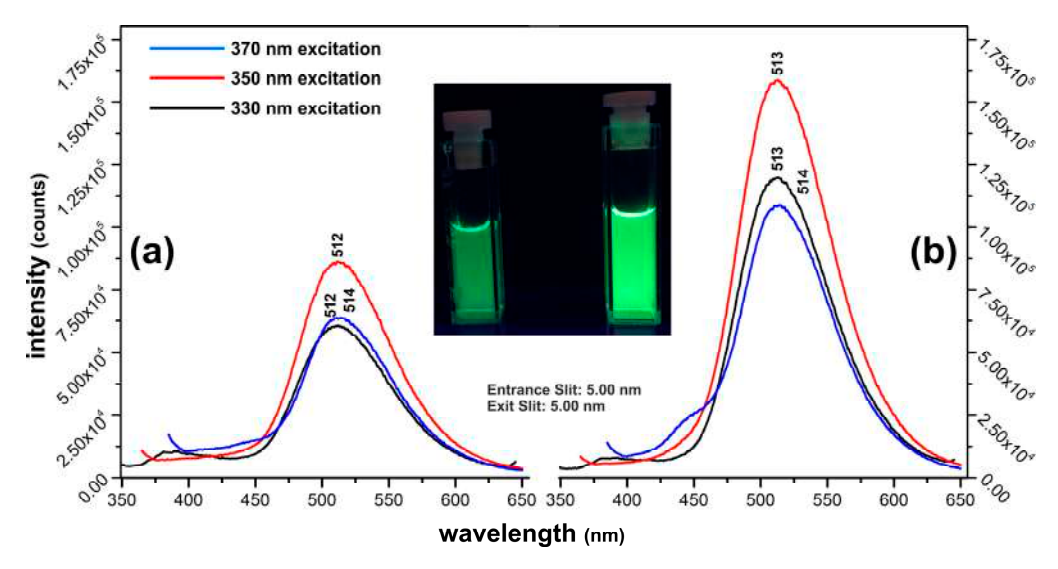


Figure 3. PL emission of the AW-CDs dispersed in (a) water, (b) deuterium oxide.

The green-emitting Fe(III)-doped CDs prepared by thermal processing of an Fe(III)-NHF complex also present a markedly enhanced emission when dispersed in  $D_2O$  (Figure 4). As could be noted, the enhanced emission intensity is highlighted both instrumentally and visually. The recorded emission intensity is at least  $1.6 \times$  higher in  $D_2O$  dispersion at all investigated excitation wavelengths, the most intense emission being achieved at 350 nm excitation. Practically, there are no differences between emission peaks, the variations (+/-1 nm) could be safely attributed to the inherent measuring and/or results interpretation errors. As mentioned above, the recorded results for all four types of prepared CDs led to the conclusion that the enhancement of the PL emission intensity is rather a result of more favorable conditions achieved in the  $D_2O$  dispersion environment, which provide significantly less non-radiative vibrational deactivation routes compared

C 2025, 11, 10 6 of 14

with H<sub>2</sub>O dispersions. In our view, the "isotope effect" could be only indirectly used to provide a convincing insight regarding the generally observed PL intensity enhancement.



**Figure 4.** PL emission of the Fe-CDs dispersed in (a) water, (b) deuterium oxide.

To further strengthen the above-mentioned observations, we also investigated the behavior of both NHF-CDs dispersions in D<sub>2</sub>O and H<sub>2</sub>O when embedded in a polymer matrix (Section 2.3). Changing the surroundings of the NHF-CDs could be a good test of the hypothetic contribution of  $H \to D$  exchange within the CDs structure. In Figure 5 are presented the observed PL intensities of the NHF-CDs/monomer/crosslinker/photoinitiator in the D<sub>2</sub>O mixture just after the commencing of the photopolymerization process (a) and post-polymerization when a solid nanocomposite of NHF-CDs trapped in the crosslinked polymer matrix is obtained (b). While within the initial 0–5 s after the UV exposure of the mixture, the characteristic blue emission of the NHF-CDs is intense, it becomes gradually fainter towards the end of the photopolymerization when the polymer matrix is completely established with the CDs trapped within. The entire process is demonstrated in the short video file (Video S1) attached to this manuscript. Due to the fast polymerization process (within a 40 s interval), the diminishing PL blue emission is clearly noticeable, most probably being a result of changing the emissive sites surrounding the conditions. At the end of the process, the initial q.ty of D<sub>2</sub>O of the mixture is mostly expelled, the crosslinked polymer matrix backbone being the new surrounding environment for the NHF-CDs.

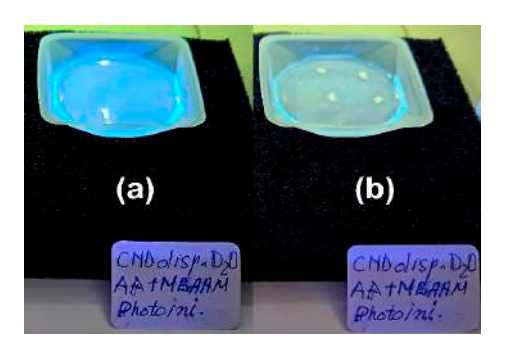


**Figure 5.** Observed PL emission intensity of the NHF-CDs/monomer/crosslinker/photoinitiator/ $D_2O$  mixture (**a**) prior and (**b**) post-polymerization.

## 3.1.2. PLQY Measurements

The PLQY investigation revealed the notable enhancement of the radiative processes involved in the CDs photoluminescence. The results are included in Table 1 along with the CIE 1931 chromaticity parameters. The most impressive results were recorded in the

C **2025**, 11, 10 7 of 14

case of D<sub>2</sub>O-dispersed NHF-CDs, where the highest QY (70.97%) was recorded at the 350 nm excitation wavelength, the value of which is more than 2.3× higher compared with the same CDs dispersed in H<sub>2</sub>O, while at the 330 nm excitation, the QY is more than  $3\times$  higher. For the NHS-CDs, the PLQY is almost two times higher when  $D_2O$  is used as a dispersion medium, a very good value (25.47%) being achieved at the 370 nm excitation. In the case of the D<sub>2</sub>O-dispersed Fe-CDs, the results are equally impressive, with the PLQY gain at the 330 nm excitation in the D<sub>2</sub>O medium being almost 2.4× higher (29.10%) compared to the same batch dispersed in  $H_2O$  (12.20%). The results recorded for 350 and 370 nm excitation are also notable:  $1.63 \times$  and  $1.9 \times$  increased QY values in the case of the D<sub>2</sub>O-dispersed Fe-CDs. The least impressive results were recorded in the case of AW-CDs, where the highest PLQY (30.17%) was recorded at the 370 nm excitation for the batch dispersed in  $D_2O$ , only a 1.27× improvement compared with the  $H_2O$  dispersion (23.67%). The values recorded at 330 and 350 nm excitation are even less noticeable, the differences between the D<sub>2</sub>O and H<sub>2</sub>O batches being within the 0.3–0.84% range. The CIE 1931 chromaticity parameters revealed, in each case, minor differences between the D<sub>2</sub>Oand H<sub>2</sub>O-dispersed CDs results, which are in very good agreement with the previously discussed configuration of the emission peaks, which also revealed insignificant variations between the same batches dispersed in D<sub>2</sub>O and H<sub>2</sub>O, respectively.

**Table 1.** Recorded values for absolute PLQY and CIE 1931 chromaticity parameters.

Absolute PLQY										
Excitati	ion (nm)	330	350	370						
CNDs NHF	PLQY (%)	13.37	30.13	34.05						
H <sub>2</sub> O dispersed	abs. error $(+/-)$	0.028	0.066	0.086						
_	CIE 1931 coord.	x = 0.14588	x = 0.15215	x = 0.15235						
	CIE 1931 COORG.	y = 0.10874	y = 0.11844	y = 0.11802						
CNDs NHF	PLQY (%)	41.48	71.27	70.97						
D <sub>2</sub> O dispersed	abs. error $(+/-)$	0.086	0.143	0.146						
	CIE 1931 coord.	x = 0.15165	x = 0.15299	x = 0.15285						
	CIE 1931 COOIG.	y = 0.11366	y = 0.11746	y = 0.11656						
CNDs NHS	PLQY (%)	11.92	12.31	12.46						
H <sub>2</sub> O dispersed	abs. error $(+/-)$	0.041	0.048	0.07						
	CIE 1931 coord.	x = 0.16148	x = 0.16749	x = 0.17203						
	CIE 1931 COOIU.	y = 0.14843	y = 0.17764	y = 0.20566						
CNDs NHS	PLQY (%)	21.41	22.26	25.47						
D <sub>2</sub> O dispersed	abs. error $(+/-)$	0.118	0.144	0.279						
	CIE 1931 coord.	x = 0.1580	x = 0.16467	x = 0.17064						
	CIE 1991 coold.	y = 0.13088	y = 0.15574	y = 0.19365						
CNDs Fe doped	PLQY (%)	12.2	10.43	5.38						
H <sub>2</sub> O dispersed	abs. error $(+/-)$	0.025	0.015	0.015						
	CIE 1931 coord.	x = 0.23316	x = 0.24067	x = 0.23791						
	CIE 1991 coold.	y = 0.55765	y = 0.6311	y = 0.58452						
CNDs Fe doped	PLQY (%)	29.1	17.09	10.29						
D <sub>2</sub> O dispersed	abs. error $(+/-)$	0.086	0.021	0.057						
	CIE 1931 coord.	x = 0.23471	x = 0.23704	x = 0.23234						
	CIE 1991 Coold.	y = 0.55098	y = 0.5814	y = 0.55199						
CNDs Argan	PLQY (%)	15.94	19.93	23.67						
H <sub>2</sub> O dispersed	abs. error $(+/-)$	0.04	0.059	0.102						
	CIE 1931 coord.	x = 0.14839	x = 0.15448	x = 0.15723						
	CIL 1701 COOIG.	y = 0.08361	y = 0.10221	y = 0.12234						

C 2025, 11, 10 8 of 14

<b>Table</b>	1	Cont
iabie	1.	Com.

Absolute PLQY										
Excitat	ion (nm)	330	350	370						
CNDs Argan	PLQY (%)	16.24	21.77	30.17						
D <sub>2</sub> O dispersed	abs. error $(+/-)$	0.04	0.069	0.164						
•	CIE 1931 coord.	x = 0.15136 y = 0.09372	x = 0.15611 y = 0.11137	x = 0.15501 y = 0.1093						

Overall, the  $D_2O$  dispersion medium allows for an impressive improvement in terms of efficiency of the CDs specific radiative processes compared with  $H_2O$ . The PLQY improvement might vary depending on the specific structural configuration of different types of CDs prepared from a certain precursor. According to our observations, a initially higher PLQY of a certain type of CDs dispersed in  $H_2O$  will produce an even higher gain in PL efficiency when  $D_2O$  is used. An already good PLQY is most probably due to the richness of the emissive sites within the CDs structure, which will highly benefit from a dispersion medium, which is less prone to provide non-radiative paths leading to premature deactivation of the excited states.

## 3.1.3. Fluorescence Lifetime (LT) Measurements

In Figure 6A–H are illustrated the typical time-resolved fluorescence decay profiles (in Figure S1A–H the residuals of the fluorescence decay fitting), while in Table 2 are presented the relevant decay characteristics. To accurately model the fluorescence decay behavior, we employed a single exponential decay model or a multi-exponential decay model, depending on the sample behavior (Equation (1)) [9,26,27]:

$$I(t) = \sum_{i=1}^{n} a_i \cdot exp\left(\frac{-t}{\tau_i}\right) \tag{1}$$

where I(t) is the fluorescence intensity, and  $a_i$  corresponds to the amplitude of each component i, which reflects the relative contribution of that specific decay process. Each component is characterized by a unique fluorescence lifetime  $\tau_i$ , and the sum of all amplitudes is normalized to 1 ( $\sum a_i = 1$ ), ensuring that the model represents the entirety of the observed decay. To further understand the contribution of each lifetime component, we calculated the fractional concentration, ( $f_i$ ) of each decay time, which quantifies the proportion of fluorescence attributable to each lifetime (Equation (2)):

$$f_i = \frac{a_i \tau_i}{\sum_{j=1}^n a_j \tau_j} \tag{2}$$

The sum of  $f_i$  values is also normalized to 1 ( $\sum_{i=1}^n f_i = 1$ ), indicating that the calculated fractions account for the total observed fluorescence. The average lifetime ( $\langle \tau \rangle$ ) was given by this Equation (3):

$$\langle \tau \rangle = f_1 \tau_1 + f_2 \tau_2 + f_3 \tau_3 \tag{3}$$

In the present study, the fluorescence decay in water was best described by a three-exponential model. However, the same three-exponential model also applied to two of the deuterated samples, NHS-CDs and AW-CDs. Interestingly, for the NHF-CDs and Fe-CDs samples in deuterated solvent, a single-exponential decay was observed. Additionally, we found that the  $D_2O$  dispersion medium increased the average lifetimes compared to the  $H_2O$  dispersed samples, a phenomenon reported by others in the literature as well [9,27].

C 2025, 11, 10 9 of 14

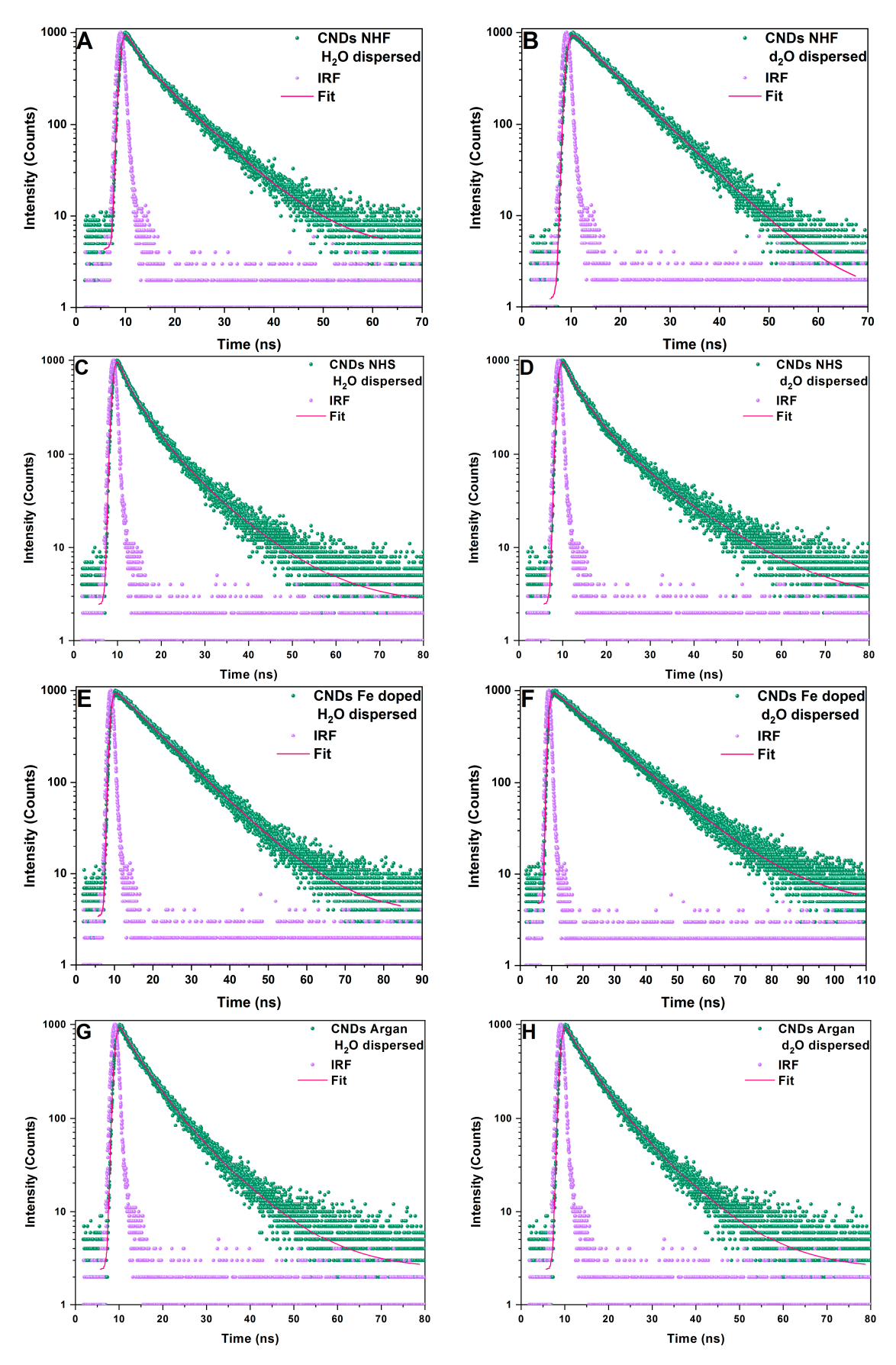


**Figure 6.** The typical time-resolved fluorescence decay profiles of the **(A)** NHF-CDs/ $H_2O$ , **(B)** NHF-CDs  $D_2O$ , **(C)** NHS-CDs/ $H_2O$ , **(D)** NHS-CDs/ $D_2O$ , **(E)** Fe-CDs/ $H_2O$ , **(F)** Fe-CDs/ $D_2O$ , **(G)** AW-CDs/ $H_2O$ , and **(H)** AW-CDs/ $D_2O$  samples.

C 2025, 11, 10 10 of 14

Sample Code	Ф (%)	k <sub>r</sub> * (ns <sup>-1</sup> )	k <sub>nr</sub> * (ns <sup>-1</sup> )	τ <sub>1</sub> (ns)	a <sub>1</sub> (%)	$f_1$	τ <sub>2</sub> (ns)	a <sub>2</sub> (%)	f <sub>2</sub>	τ <sub>3</sub> (ns)	a <sub>3</sub> (%)	f <sub>3</sub>	x <sup>2</sup>	<τ> (ns)
NHF-CDs H <sub>2</sub> O dispersed	34.05	0.042	0.082	8.38	81.43	0.952	2.09	16.33	0.048	0.11	2.24	0.000	1.04	8.07
NHF-CDs D <sub>2</sub> O dispersed	70.97	0.086	0.035	8.22	100.00	1.000	-	-	-	-	-	-	1.09	8.22
NHS-CDs H <sub>2</sub> O dispersed	12.46	0.014	0.101	10.68	44.22	0.698	4.20	46.42	0.289	0.95	9.36	0.013	1.11	8.68
NHS-CDs D <sub>2</sub> O dispersed	25.47	0.024	0.071	12.72	47.40	0.744	4.39	45.47	0.246	1.04	7.13	0.009	1.13	10.56
NHS-CDs H <sub>2</sub> O dispersed	5.38	0.005	0.089	12.98	17.83	0.222	9.99	81.00	0.778	0.09	1.17	0.000	1.10	10.66
Fe-CDs D <sub>2</sub> O dispersed	10.29	0.007	0.061	14.65	100.00	1.000	-	-	-	-	-	-	1.07	14.65
AW-CDs H <sub>2</sub> O dispersed	23.67	0.029	0.094	9.85	46.75	0.673	4.49	49.43	0.324	0.47	3.82	0.003	1.11	8.09
AW-CDs	30.17	0.028	0.066	12.88	47 32	0.713	5.09	46 97	0.280	1 12	5 17	0.007	1 14	10.62

0.713

5.09

30.17

D<sub>2</sub>O dispersed

0.028

0.066

47.32

**Table 2.** Absolute PLQY at  $\lambda_{ex} = 370$  nm, radiative and non-radiative decay rate constants, and fluorescence lifetimes of the analyzed samples.

 $\Phi$  = fluorescence quantum yield,  $\tau_{1,2,3}$  = fluorescence lifetimes,  $a_{1,2,3}$  = amplitude of the components,  $f_{1,2,3}$  = fractional concentrations,  $\langle \tau \rangle$  = average fluorescence lifetimes,  $k_r$  = radiative rate constants,  $k_{nr}$  = non-radiative rate constants. \* calculated for the  $\Phi$  at  $\lambda_{ex} = 370$  nm.

1.12

46.97

Additionally, to provide insight into the decay mechanisms, we derived both radiative  $(k_r)$  and non-radiative  $(k_{nr})$  decay constants (Table 2) from nanosecond lifetime measurements and quantum yields using the following equations:

$$k_r = \frac{\Phi}{\langle \tau \rangle} \tag{4}$$

1.14

10.62

$$k_{nr} = \frac{1 - \Phi}{\langle \tau \rangle} \tag{5}$$

Generally,  $k_{nr}$  is higher than  $k_r$  for each sample, indicating that non-radiative decay processes are more prominent, which may contribute to the observed differences in fluorescence behavior in H<sub>2</sub>O and D<sub>2</sub>O. Furthermore, the influence of the deuterated solvent led to a decrease in the non-radiative decay constant  $(k_{nr})$  and an increase in the radiative decay constant  $(k_r)$ . This shift in decay pathways aligns with the observed increase in quantum yield when the samples are dispersed in deuterated solvent compared to regular water. The reduction in  $k_{nr}$  suggests that the non-radiative relaxation processes, such as vibrational relaxation and other energy-dissipating mechanisms, are less prominent in deuterated solvent. This reduction could be attributed to the isotope effect, where deuterium atoms, with their greater mass, decrease vibrational energy dissipation, effectively reducing nonradiative losses. At the same time, the increase in  $k_r$  indicates that the radiative decay pathway (fluorescence emission) becomes more favorable in the presence of deuterated solvent, contributing to the enhanced quantum yield. These changes suggest that deuterated solvents can shift the balance between radiative and non-radiative decay processes, enhancing fluorescence efficiency by promoting radiative decay while suppressing nonradiative pathways [28]. Therefore, the LT investigation results are in very good agreement with PLQY and Steady-State fluorescence investigations, sustaining very well our opinion that the "isotope effect" induced by the D<sub>2</sub>O presence plays an indirect role in enhancing the PL emission by providing a more favorable environment for the radiative transitions.

### 3.2. Characterization of the D<sub>2</sub>O Dispersed CDs

As stated above, the experimental procedure for the preparation of each type of investigated CDs was kept unchanged, as detailed in our previous reported works [14–17], where an in-depth morpho-structural investigation was performed and discussed. Since the only difference consists of the final dispersion medium ( $D_2O$ ), the investigations presented in this work were focused on the morphological aspects which could provide new information. Therefore, the DLS (dimensional analysis) was performed for each type of CDs dispersed in  $D_2O$ .

## Dimensional (DLS) Investigation

Freshly prepared samples of each type of CDs dispersed in D2O were investigated. Also, for the evaluation of longer-term stability of the dispersions, same samples were investigated again after 1 week. In Figure 7a–d are presented the dimensional distributions for each type of CDs dispersed in D<sub>2</sub>O, freshly prepared and after 1 week of aging.

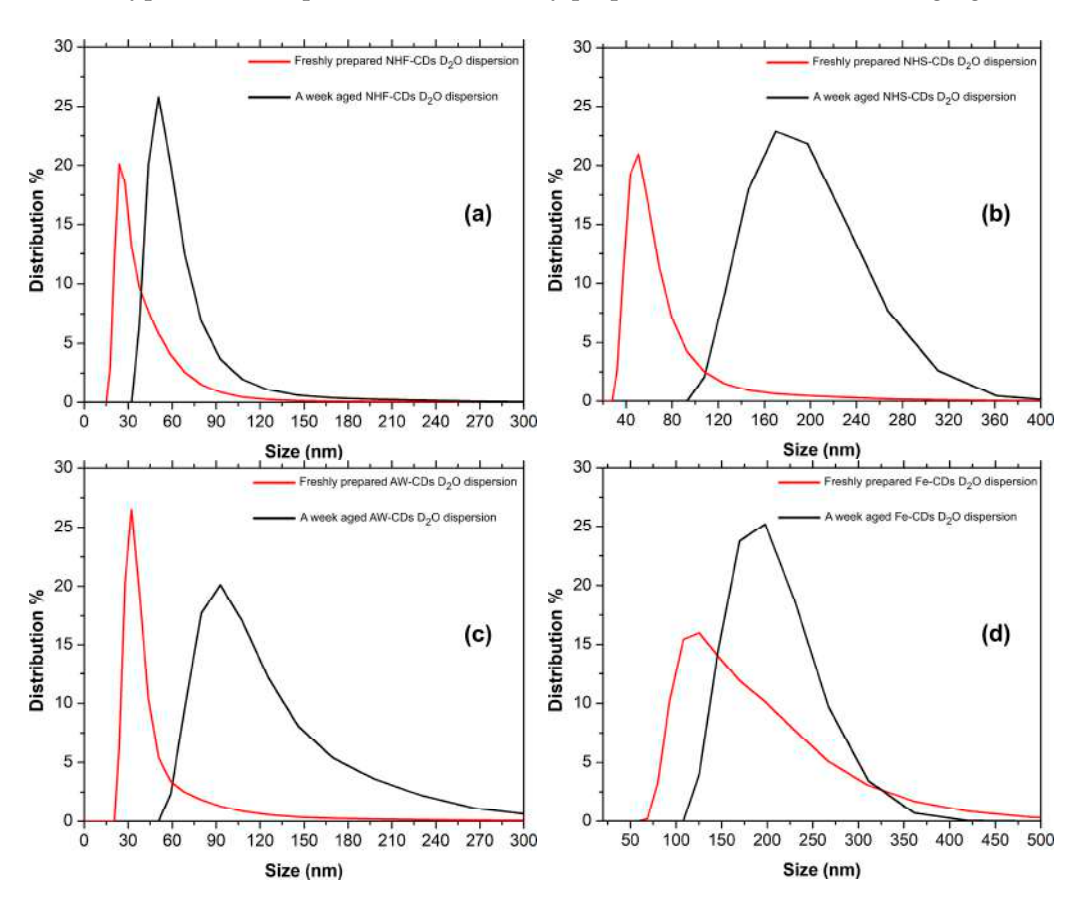


**Figure 7.** Dimensional distribution of freshly prepared/1 week aged of (a) NHF-CDs, (b) NHS-CDs, (c) AW-CDs, and (d) Fe-CDs dispersed in  $D_2O$ .

All the prepared samples present, as expected, an agglomeration tendency which was observed irrespective of the type of solvent used as dispersion medium. The freshly prepared NHF-CDs/D2O dispersion size distribution is mainly situated within 30–90 nm range. As demonstrated in our previous works, CDs present a clusterization tendency which became even more noticeable in case of the aged dispersion where the size distribution migrates within 40–140 nm range. In case of NHS-CDs, the freshly prepared dispersion presents a narrower size distribution (40–120 nm) compared with the aged dispersion where a broad 120–320 nm distribution was observed most probably due to an even more clusterization tendency. This behavior is almost the same in the case of AW-CDs where the freshly prepared dispersion presents a narrow distribution (25–90 nm), which becomes

significantly broader for the aged dispersion (60–250 nm). The Fe-CDs/ $D_2O$  dispersion behaves differently compared with the rest of the investigated samples, with an initial broad distribution (60–400 nm), which also remain large but slightly translated to higher dimensional range (100–400 nm). This particular behavior could be a result of iron presence within the CDs structure. Overall, the stability of the dispersions is slightly better compared with the same CDs types but dispersed in water.

Interestingly, in the case of NHF-CDs, AW-CDs, and Fe-CDs dispersions, the PL intensity remained unchanged after 1 week, no notable differences being noticed both visually and instrumentally, which might additionally sustain the key role of the dispersion medium in achieving a better emissive intensity. The aged NHS-CDs/D $_2$ O dispersion presents a slightly fainter emission intensity. Compared with samples of same CDs type dispersed in water, the PL emission is markedly better preserved.

### 4. Conclusions

The photoluminescence (PL) properties of several types of Carbon Dots (CDs) dispersed in deuterium oxide were thoroughly investigated. Through simple replacement of the commonly used aqueous dispersion medium with D<sub>2</sub>O, the CDs prepared from various precursors are able to achieve an impressive enhancement of their PL emission intensity. In the present work, four types of CDs were prepared, the emission intensity being markedly enhanced in each case. The recorded PL quantum yield (QY) was found to increase at least  $1.27 \times$  to  $2.3 \times$  compared with the same CDs batches dispersed in H<sub>2</sub>O, an impressive 70.97% QY being achieved in the most favorable case. The isotope effect over the PL properties of fluorophores (including CDs) is a less investigated research topic with relatively scarce reported works. Unlike many of the reported studies which hypothesize that the observed PL intensity enhancement is a result of the isotope effect induced by spontaneous  $H \to D$  exchange within the CDs structure, our investigation supports an alternative mechanism where the isotope effect might be indirectly involved. In our view, switching  $H_2O$  to  $D_2O$  as the dispersion medium allows for the ability to provide a more favorable environment, which diminishes the non-radiative deactivation paths, thus favoring the radiative relaxations through photon production. Given the particularities of  $D_2O$ , which dissociates less than H<sub>2</sub>O, and the new vibrational conditions due to the presence of the heavier deuterium in the surroundings of the emissive sites, a better environment for the photonic processes is provided within the CDs.

**Supplementary Materials:** The following supporting information can be downloaded at https://www.mdpi.com/article/10.3390/c11010010/s1: Figure S1: Recorded Lifetime residuals, Video S1.

**Author Contributions:** Conceptualization, C.S.S., C.O.A. and M.P.; methodology, C.S.S., A.C. and C.O.A.; investigation, C.S.S. and A.C.; writing—original draft preparation, C.S.S. and A.C.; experimental, C.S.S. and C.A.; writing—review and editing, C.S.S. and C.O.A. All authors have read and agreed to the published version of the manuscript.

**Funding:** This work was supported by a grant from the Romanian National Authority for Scientific Research and Innovation UEFISCDI, project: ERANET 293/2022-COFUND-LEAP-RE-NANOSOLARCELL. The authors thank the financial support of the LEAP-RE program (Long-Term Joint EUAU Research and Innovation Partnership on Renewable Energy; grant NANOSOLARCELLS).

**Data Availability Statement:** The data presented in this study are available upon request from the corresponding author.

Conflicts of Interest: The authors declare no conflicts of interest.

## References

1. Ozyurt, D.; Al Kobaisi, M.; Hocking, R.K.; Fox, B. Properties, synthesis, and applications of carbon dots: A review. *Carbon Trends* **2023**, *12*, 100276. [CrossRef]

- 2. Etefa, H.F.; Tessema, A.A.; Dejene, F.B. Carbon Dots for Future Prospects: Synthesis, Characterizations and Recent Applications: A Review (2019–2023). *C* **2024**, *10*, 60. [CrossRef]
- 3. Ullah, M.; Awan, U.A.; Ali, H.; Wahab, A.; Khan, S.U.; Naeem, M.; Ruslin, M.; Mustopa, A.Z.; Hasan, N. Carbon Dots: New Rising Stars in the Carbon Family for Diagnosis and Biomedical Applications. *J. Nanotheranostics* **2025**, *6*, 1. [CrossRef]
- 4. Majid, A.; Ahmad, K.; Tan, L.; Niaz, W.; Na, W.; Huiru, L.; Wang, J. The Advanced Role of Carbon Quantum Dots in Nano-Food Science: Applications, Bibliographic Analysis, Safety Concerns, and Perspectives. *C* **2025**, *11*, 1. [CrossRef]
- 5. Ai, L.; Yang, Y.; Wang, B.; Chang, J.; Tang, Z.; Yang, B.; Lu, S. Insights into photoluminescence mechanisms of carbon dots: Advances and perspectives. *Sci. Bull.* **2021**, *66*, 839–856. [CrossRef]
- 6. Wang, B.; Lu, S. The light of carbon dots: From mechanism to applications. Matter 2022, 5, 110–149. [CrossRef]
- 7. Carbonaro, C.M.; Corpino, R.; Salis, M.; Mocci, F.; Thakkar, S.V.; Olla, C.; Ricci, P.C. On the Emission Properties of Carbon Dots: Reviewing Data and Discussing Models. *C* **2019**, *5*, 60. [CrossRef]
- 8. Hutchison, C.A.; Mangum, B.W. Effect of deuterium substitution on the lifetime of the phosphorescent triplet state of naphthalne. *J. Chem. Phys.* **1960**, 32, 1261–1262. [CrossRef]
- 9. Kučera, J.; Peš, O.; Janovič, T.; Hofr, C.; Kubinyiová, L.; Tóth, J.; Káňa, Š.; Táborský, P. Enhancement of luminescence signal by deuterated water—Practical implications. *Sens. Actuators B Chem.* **2022**, 352, 131029. [CrossRef]
- 10. Gamage, R.; Smith, B. Fluorescence imaging using deep-red Indocyanine Blue (ICB) a complementary partner for near infrared Indocyanine Green (ICG). *Chem. Biomed. Imaging* **2024**, *2*, 384–397. [CrossRef] [PubMed]
- 11. Sailer, B.L.; Nastasi, A.J.; Valdez, J.G.; Steinkamp, J.A.; Crissman, H.A. Differential Effects of Deuterium Oxide on the Fluorescence Lifetimes and Intensities of Dyes with Different Modes of Binding to DNA. *J. Histochem. Cytochem.* 1997, 45, 165–175. [CrossRef]
- 12. Taborsky, P.; Kucera, J.; Jurica, J.; Pes, O. Heavy water enhancement of fluorescence signal in reversed-phase liquid chromatography. *J. Chromatogr. B* **2018**, 1092, 7–14. [CrossRef] [PubMed]
- 13. Filer, C.N. Luminescence enhancement by deuterium. J. Label. Compd. Radiopharm. 2023, 66, 372–383. [CrossRef]
- 14. Tong, C.C.; Hwang, K.C. Enhancement of OLED Efficiencies and High-Voltage Stabilities of Light-Emitting Materials by Deuteration. *J. Phys. Chem. C* **2007**, *111*, 3490–3494. [CrossRef]
- Jung, S.; Cheung, W.L.; Li, S.; Wang, M.; Li, W.; Wang, C.; Song, X.; Wei, G.; Song, Q.; Chen, S.S.; et al. Enhancing operational stability of OLEDs based on subatomic modified thermally activated delayed fluorescence compounds. *Nat. Commun.* 2023, 14, 6481.
- 16. Yao, Z.; Wen, X.; Hong, X.; Tao, R.; Yin, F.; Cao, S.; Yan, J.; Wang, K.; Wang, J. Deuteration-Induced Energy Level Structure Reconstruction of Carbon Dots for Enhancing Photoluminescence. *Adv. Sci.* **2024**, *11*, 2308523. [CrossRef] [PubMed]
- 17. Stan, C.S.; Horlescu, P.; Ursu, L.E.; Popa, M.; Albu, C. Facile preparation of highly luminescent composites by polymer embedding of carbon dots derived from N-hydroxyphthalimide. *J. Mater. Sci.* **2017**, *52*, 185–196. [CrossRef]
- 18. Stan, C.S.; Albu, C.; Coroaba, A.; Popa, M.; Sutiman, D. One step synthesis of fluorescent Carbon Dots through pyrolysis of N-hydroxysuccinimide. *J. Mater. Chem. C* **2015**, *3*, 789–795. [CrossRef]
- 19. Stan, C.S.; Elouakassi, N.; Albu, C.; Ania, C.O.; Coroaba, A.; Ursu, L.E.; Popa, M.; Kaddami, H.; Almaggoussi, A. Photoluminescence of Argan-Waste-Derived Carbon Nanodots Embedded in Polymer Matrices. *Nanomaterials* **2024**, *14*, 83. [CrossRef] [PubMed]
- 20. Stan, C.S.; Coroaba, A.; Ursu, E.L.; Secula, M.S.; Simionescu, B.C. Fe(III) doped carbon nanodots with intense green photoluminescence and dispersion medium dependent emission. *Sci. Rep.* **2019**, *9*, 18893. [CrossRef] [PubMed]
- 21. Papaioannou, N.; Marinovic, A.; Yoshizawa, N.; Goode, A.E.; Fay, M.; Khlobystov, A.; Titirici, M.M.; Sapelkin, A. Structure and solvents effects on the optical properties of sugar-derived carbon nanodots. *Sci. Rep.* **2018**, *8*, 6559. [CrossRef]
- 22. Ma, Z.; Zhang, L.; Cui, Z.; Ai, X. Improving the Luminescence and Stability of Carbon-Centered Radicals by Kinetic Isotope Effect. *Molecules* **2023**, *28*, 4805. [CrossRef] [PubMed]
- 23. Dobretsov, G.E.; Syrejschikova, T.I.; Smolina, N.V. On mechanisms of fluorescence quenching by water. *Biophysics* **2014**, *59*, 183–188. [CrossRef]
- 24. Maillard, J.; Klehs, K.; Rumble, C.; Vauthey, E.; Heilemann, M.; Fürstenberg, A. Universal quenching of common fluorescent probes by water and alcohols. *Chem. Sci.* **2021**, *12*, 1352–1362. [CrossRef] [PubMed]
- 25. Kumar, S.; Hoshino, M.; Kerkeni, B.; Kerkeni, B.; García, G.; Limão-Vieira, P. Isotope Effect in D2O Negative Ion Formation in Electron Transfer Experiments: DO–D Bond Dissociation Energy. *J. Phys. Chem. Lett.* **2023**, *14*, 5362–5369. [CrossRef] [PubMed]
- 26. Coroaba, A.; Al-Matarneh, C.; Vasiliu, T.; Ibanescu, S.-A.; Zonda, R.; Esanu, I.; Isac, D.-L.; Pinteala, M. Revealing the supramolecular interactions of the bis(azopyrenyl) dibenzo-18-crown-6-ether system. *J. Mol. Liq.* **2023**, *374*, 121298. [CrossRef]

27. Magde, D.; Wong, R.; Seybold, P.G. Fluorescence Quantum Yields and Their Relation to Lifetimes of Rhodamine 6G and Fluorescein in Nine Solvents: Improved Absolute Standards for Quantum Yields. *Photochem. Photobiol.* **2002**, 75, 327–334. [CrossRef] [PubMed]

28. Lakowicz, J.R. *Principles of Fluorescence Spectroscopy*, 3rd ed.; Lakowicz, J.R., Ed.; Springer Science & Business Media: New York, NY, USA, 2007.

**Disclaimer/Publisher's Note:** The statements, opinions and data contained in all publications are solely those of the individual author(s) and contributor(s) and not of MDPI and/or the editor(s). MDPI and/or the editor(s) disclaim responsibility for any injury to people or property resulting from any ideas, methods, instructions or products referred to in the content.



MDPI

Article

## Photoluminescence of Argan-Waste-Derived Carbon Nanodots Embedded in Polymer Matrices

Corneliu S. Stan <sup>1,\*</sup> , Noumane Elouakassi <sup>2</sup>, Cristina Albu <sup>1</sup>, Conchi O. Ania <sup>3</sup> , Adina Coroaba <sup>4</sup> , Laura E. Ursu <sup>4</sup>, Marcel Popa <sup>1,5,\*</sup> , Hamid Kaddami <sup>2,6</sup> and Abdemaji Almaggoussi <sup>2,7</sup>

- Faculty of Chemical Engineering and Environmental Protection, Gh. Asachi Technical University of Iasi, D. Mangeron 73 Ave., 700050 Iasi, Romania; cristina.albu@tuiasi.ro
- Innovative Materials for Energy and Sustainable Development (IMED-Lab), Faculty of Science and Technology, Cadi Ayyad University, Av. Abdelkrim Khattabi, B.P. 511, Marrakech 40000, Morocco; noumanelouaskassi0641@gmail.com (N.E.); h.kaddami@uca.ma (H.K.); a.almaggoussi@uca.ma (A.A.)
- Onditions Extremes Matériaux Haute Temperature et Irradiation (CEMHTI), UPR 3079, CNRS, Université d'Orléans, 45100 Orleans, France; conchi.ania@cnrs-orleans.fr
- <sup>4</sup> Centre of Advanced Research in Bionanoconjugates and Biopolymers, "Petru Poni" Institute of Macromolecular Chemistry, Grigore Ghica Voda 41A Alley, 700487 Iasi, Romania; adina.coroaba@icmpp.ro (A.C.); ursu.laura@icmpp.ro (L.E.U.)
- Academy of Romanian Scientists, Ilfov Street, 050054 Bucharest, Romania
- Sustainable Materials Research Center (SusMat-RC), Lot 660-Hay Moulay Rachid, Ben Guerir 43150, Morocco
- Applied Chemistry and Engineering Research Centre of Excellence (ACER CoE), Advanced Organic Optoelectronic Laboratory, Mohammed VI Polytechnic University (UM6P), Lot 660-Hay Moulay Rachid, Ben Guerir 43150, Morocco
- \* Correspondence: stancs@tuiasi.ro (C.S.S.); marpopa@ch.tuiasi.ro (M.P.)

Abstract: In this work, photoluminescent (PL) carbon nano dots (CNDs) prepared from argan waste were embedded in highly optical transparent poly(styrene-co-acrylonitrile) (PSA) and cyclo-olefin copolymer (COC) matrices, which were further processed into thin films. In the first step, the luminescent CNDs were prepared through thermal processing of fine-groundargan waste, followed, in the second step, by direct dispersion in the polymer solutions, obtained by solving PSA and COC in selected solvents. These two polymer matrices were selected due to their high optical transparency, resilience to various environmental factors, and ability to be processed as quality thin films. The structural configuration of the CNDs was investigated through EDX, XPS, and FTIR, while DLS, HR-SEM, and STEM were used for their morphology investigation. The luminescence of the prepared CNDs and resulted polymer nanocomposites was thoroughly investigated through steady-state, absolute PLQY, and lifetime fluorescence. The quality of the resulted CND–polymer nanocomposite thin films was evaluated through AFM. The prepared highly luminescent thin films with a PL conversion efficiency of 30% are intended to be applied as outer photonic conversion layers on solar PV cells for increasing their conversion efficiency through valorization of the UV component of the solar radiation.

Keywords: carbon dots; polymer nanocomposites; photonic conversion materials



Citation: Stan, C.S.; Elouakassi, N.; Albu, C.; Ania, C.O.; Coroaba, A.; Ursu, L.E.; Popa, M.; Kaddami, H.; Almaggoussi, A. Photoluminescence of Argan-Waste-Derived Carbon Nanodots Embedded in Polymer Matrices. *Nanomaterials* **2024**, *14*, 83. https://doi.org/10.3390/nano14010083

Academic Editor: Myungkwan Song

Received: 21 November 2023 Revised: 22 December 2023 Accepted: 25 December 2023 Published: 27 December 2023



Copyright: © 2023 by the authors. Licensee MDPI, Basel, Switzerland. This article is an open access article distributed under the terms and conditions of the Creative Commons Attribution (CC BY) license (https://creativecommons.org/licenses/by/4.0/).

### 1. Introduction

Photoluminescent carbon nano dots (CNDs) prepared from natural sources [1] could be a convenient approach due to the abundance of the raw materials from various vegetal and agricultural wastes available in large quantities. Besides the valorization of these readily available resources, the resultant CNDs are biocompatible [2] in most cases, and, according to the chemical composition of the precursors, the application range could vary from optoelectronic [3,4] and sensing [5,6] devices to biomedicine, including anti-tumoral activity [7–9] or medical imaging [10] such as MRI investigation techniques [11]. Typically, the CND structure consists of a surface-rich functional group-decorated graphitic core with

a disordered configuration containing various atomic species (i.e., N and O) intercalated between the sp<sup>2</sup> carbons [12,13].

One of their most interesting features is their photoluminescence, with a particular excitation-dependent emission [14,15] which is rather unique among fluorescent materials. The mechanism of the radiative processes involved in photoluminescent (PL) emission is still unclear but later studies highlight the importance of the surface functional groups and defects located within the graphitic core [16,17]. The efficiency of the radiative processes ranges from a few percent to an impressive 90% quantum yield [18] depending on the precursors, preparation approach, and certain strategies of surface chemistry modifications or doping of the graphitic core with various atomic species [19,20]. In most cases, the reported emission is located within the blue region of the visible spectrum, but green [21,22], red [23], and NIR [24] emission CNDs have been reported. In this regard, it has been reported that characteristics of the emission are markedly dependent on the dispersion medium [25].

CNDs are typically prepared following physical and chemical approaches [26]. The last ones (e.g., hydrothermal [27], pyrolytic [28], and thermal [29] processing) are usually the preferred strategic route due to their simplicity and the variety of the resulting CNDs in terms of composition (e.g., surface groups and graphitic core) adapted for an intended application. Besides the synthesis strategies, another important aspect in the preparation of CNDs is the choice of the precursor, and the use of abundant natural sources is most appealing [30,31]. In this sense, a wide variety of carbon-rich natural sources has been explored as precursors, covering a diversity of wastes such as plant wastes from agricultural and food processing [32], dried leaves [33], palm kernel [34], collagen [35], algae [36], or orange waste peels [37], among the many reported works with notable results.

Regarding applications and especially in those targeting optoelectronic devices, CNDs are hardly to be used directly, as resulted from synthesis. CND dispersions tend to gradually lose their PL emission intensity, due to a marked agglomeration of the nanosized particles into large clusters. This process depends on the dispersion solvent used, with polar solvents (i.e., water and EtOH) favoring the clustering and thus rendering a fast decay of the PL (within few days) [38]. Hence, for the applications where the long-term stability of the PL emission is required, the encapsulation of the CNDs in a suitable matrix appears an interesting approach to preserve their structural integrity and PL properties [39]. For this, the compatibility between the CNDs and the embedment medium is a critical requirement. Another important aspect is the transparency within excitation/emission wavelengths range. In this regard, optically transparent polymer matrices can provide both the long-term preservation of CNDs structural and PL emission stability. This is most outstanding for their use as photonic conversion layers in photovoltaic applications. As a few examples, CNDs have been embedded in poly(methylmethacrylate) [40], poly(vinyl-alcohol) [41], poly(dimethylsiloxane) [42], polystyrene [43], poly(vinylchloride), or polycarbonate [25].

In this work, CNDs with remarkable PL emission have been prepared through thermal processing of argan wastes, and they have been dispersed in poly(styrene-co-acrylonitrile) (PSA) and cyclo-olefin copolymer (COC) solutions and further processed in thin layers. The argan waste was selected as a precursor due to its availability as a low-cost material resulting from the argan oil production [44] through cold pressing of the argan kernels. Indeed, the production of argan oil represents an important socioecoenomic resource for Morocco, with over 3000 tons of oil produced per year, representing a percentage of argan cake wastes generated. On the other hand, the polymer matrices were selected due to their high optical transparency, resilience to various environmental factors, and ability to yield high quality thin films. Our data have shown that, through the embedment of the CNDs in those polymer matrices, the quantum efficiency of their photoluminescent emission is markedly increased. The prepared CND–COC/PSA nanocomposites were tested with notable results as thin photonic down-conversion layers aiming to improve the overall efficiency of the conventional photovoltaic (PV) solar cells by taking advantage of the UV radiation contained in the solar spectrum (~8% at the earth level).

Nanomaterials **2024**, 14, 83 3 of 14

### 2. Materials and Methods

### 2.1. Materials

Argan cake waste obtained during argan oil preparation through cold pressing (provided by a local Moroccan co-operative) was used as precursor of the CNDs. Ultra-pure distilled water (Millipore-Direct Q, Millipore, San Salvador, Salvador), ethanol (EtOH), chloroform (CLF), and tetrahydrofuran (THF) (Merck-Sigma-Aldrich, Bucharest, Romania) were used as dispersion media and solvents of the polymer matrices. Poly(styrene-co-acrylonitrile) (PSA) (Mw = 165,000) and cyclo-olefin copolymer (COC) pellets (Mw = 180,000) were also supplied by Merck-Sigma-Aldrich, Bucharest, Romania.

### 2.2. Methods

The infrared (FT-IR) spectra were recorded in the 400–4000 cm<sup>-1</sup> range using a Shimadzu IR Affinity 1S spectrometer (Shimadzu Corp., Kyoto, Japan) according to the KBr method. The EDX investigation was performed on a Verios G4 UC Scanning Electron Microscope equipped with an EDS, EDAX Octane Elite energy-dispersive spectrometer (Thermo Fisher Scientific, Waltham, MA, USA). XPS analysis was performed on a K-Alpha Thermo Scientific spectrometer using Al-Kα (1486.6 eV) radiation. Processing of the XPS spectra was performed using the Avantage software (ver. 5.9922), with energy values referenced against the C1s peak of adventitious carbon at 284.6 eV, and using a Shirley background. Dimensional analysis (DLS) was performed on a Malvern Panalytical Zetasizer Advance Pro Red (Malvern Panalytical Ltd., Malvern, UK). The AFM imaging was performed using an Ntegra Spectra-NT-MDT instrument (NT-MDT BV, Apeldoorn, The Netherlands) operated in tapping mode. Silicon cantilever tips (NSG 10) with a resonance frequency of 140-390 kHz, a force constant of 5.5-22.5 Nm<sup>-1</sup>, and 10 nm tip curvature radius were used. The HR-SEM micrographs were recorded with a Carl Zeiss NEON 40EsB Cross Beam System (Zeiss Microscopy, Jena, Germany) with thermal Schottky field emission emitter and accelerated Ga ions column. The samples were deposited on the analysis pad from a freshly prepared aqueous and chloroform dispersions of CNDs. The HR-STEM micrographs were recorded with a Thermo Fisher Verios G4 equipped with BF/DF/HAADF-STEM detectors. The EtOH-dispersed CND samples were deposited on the analysis grids and allowed to dry prior to investigation. Freshly prepared samples were investigated through steady-state fluorescence emission spectra and were recorded on a Horiba Fluoromax 4P spectrofluorometer (Horiba Ltd., Kyoto, Japan). The absolute photoluminescence quantum yield (PLQY) values were recorded with the Quanta Fi integration sphere controlled by the Horiba spectrofluorometer using FluorEssence software (ver. 3.5.1.20), according to the equipment manufacturer's procedure. Excited states' lifetimes were investigated on the same equipment with the attached Horiba Lifetime module, using a 370 nm LED excitation source.

### 2.3. Preparation of the Argan-Waste-Derived CNDs and Polymer-CND Nanocomposites

Argan cake waste (coarse grinded and dried at 120  $^{\circ}$ C for 48 h) generated during argan oil preparation through cold pressing was used as precursor. The as-received argan cake waste pellets were ground to a fine powder with an average 100–150  $\mu$ m size, and further dried prior to thermal processing.

For the preparation of the CNDs, a partial carbonization of the argan waste powders was performed under normal atmospheric conditions. In a typical experimental procedure, ca. 0.5 g of argan waste powders are introduced in an open quartz tube reactor provided with a glass heating jacket and exposed at 280 °C for 15 min using a temperature/flow regulated hot air gun (the temperature is reached in ca. 5 s) (Figure S1, Supplementary Information). After the 15 min, the remaining mass in quartz tube is suddenly flooded with cold (3–4 °C) water or cold THF/PSA solutions (0.8 g PSA in 25 mL THF), CLF/COC (0.5 g COC in 20 mL CLF; COC is dissolved under reflux at 62–63 °C and vigorous stirring for at least 1–2 h, given its high resistance to solvents). Approximately 10 mL of the solvents (water/CLF/THF or PSA/THF, COC/CLF) are used to flood the hot carbonized mass

Nanomaterials **2024**, 14, 83 4 of 14

resulted after thermal exposure. In our previous works [11,21,43], it was found that the rapid flooding of the hot carbonized mass is critically important in order to obtain CNDs with intense PL emission, most probably due to the sudden cooling of the hot reaction mass when a favorable configuration of the carbonaceous core is achieved. The resulting dispersions are centrifuged at 15,000 rpm for about 15 min. After centrifugation, the final dispersions are optically clear under environmental illumination and present an intense blue PL emission under UV-A/UV-B excitation (Figure 1). The yield of CNDs obtained in the synthesis (evaluated upon evaporation of the solvent in an oven) was ca. 0.1 g CNDs. The COC–CND and PSA–CND thin films were obtained by using a commercially available airbrush with a 0.2 mm nozzle supplied with compressed air. The spray coating operations were performed in a dust free environment. The samples were deposited according to their destination on test PV cells or glass and mica slides for further investigation of the quality of the thin films.

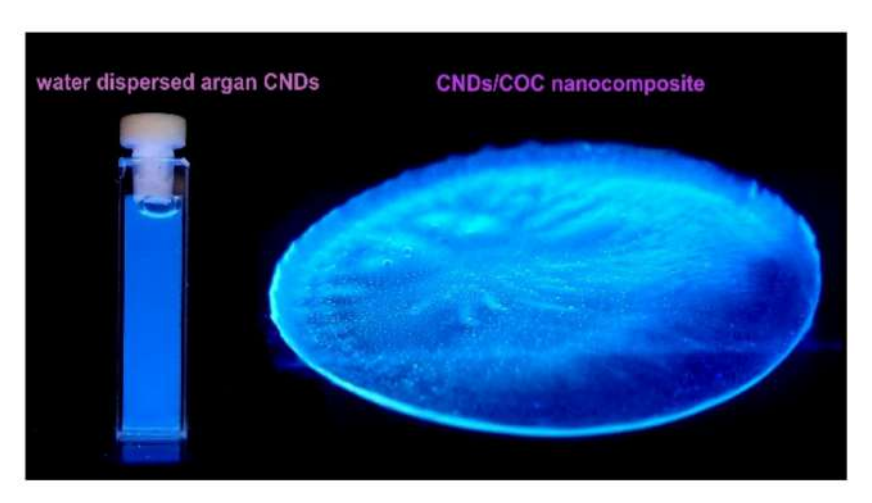


**Figure 1.** Prepared argan-derived-CNDs dispersed in water and a thick film of CND/COC nanocomposite under UV-A excitation.

### 3. Results and Discussion

As mentioned above, the structural configuration of CNDs has an essential role in their photoluminescence emission properties. Hence, we have performed a thorough morpho-structural characterization of the CNDs from argan wastes, so as to link their physicochemical properties with the observed PL emission, both in aqueous suspensions and embedded in polymer nanocomposites.

### 3.1. Physicochemical Characterization of the Prepared CNDs

The overall composition of the argan cake waste used as a precursor is presented in Table 1, along with that of the obtained CNDs. The wide XPS survey spectra and deconvoluted data of the C1s, O1s, and N1s regions are shown in the Supplementary Information (Figures S2–S4).

<b>Table 1.</b> Elementa	I composition o	t the argan waste and	the prepared CNDs.
--------------------------	-----------------	-----------------------	--------------------

	XPS							
Element	Argan Ca	ke Waste	CNDs		Argan Ca	ke Waste	CNDs	
	wt.%	at.%	wt.%	at.%	wt.%	at.%	wt.%	at.%
Carbon	74.4	78.7	81.5	84.6	78.7	82.9	83.8	86.5
Nitrogen	8.8	8	9.4	8.3	2.6	2.3	7.2	8
Oxygen	16.8	13.3	9.1	7.1	18.7	14.8	9	5.5

Nanomaterials **2024**, 14, 83 5 of 14

It should be noted that there is a rather good agreement between the composition evaluated by EDX and XPS (with the exception of nitrogen for the precursor), indicating a homogeneous composition of the materials. As seen, the thermal treatment of the argan waste resulted in an overall increase in the carbon content from 74.4 to 81.5 wt.% and a marked decrease in the oxygen content (16.8 to 9.1 wt.%), while the nitrogen content remained rather similar. The carbon enrichment of a biomass precursor upon the thermal treatment is expected, due to the removal of volatile matter (mainly oxygen containing groups) during the treatment. Interestingly, the temperature is low enough to preserve most of the nitrogen content. The XPS spectra of the C1s region (Figures S3 and S4) were deconvoluted into various contributions at binding energies of 284.6 eV (Csp²), 286.2 eV (C-O bonds), and 286.7 eV (C=O bonds). The large contributions of the peaks at 284.6 eV (78 at.%) and 285.7 eV (8 at.%) for the C1s region confirmed the predominant aromatic structure of the CNDs. The XPS spectra of the O1s region show the presence of quinone and hydroxyl moieties.

FTIR analysis was performed for both the argan cake waste precursor and the vacuumdried CND powders obtained upon thermal processing and cooling in water as a dispersion medium (Figure 2a,b). As seen, the precursor presents a wide signal located between  $3359-3259 \text{ cm}^{-1}$ , related to the bending and stretching vibrations of -OH bonds and attributed to hydroxyl groups and intercalated water [45]. As expected, the contribution of this signal decreased significantly upon the thermal treatment of the precursor to render the CNDs. The bands at 2927/2858 cm<sup>-1</sup>, characteristic of the stretching vibrations of C-H in sp<sup>3</sup> bonds, were detected in both samples, although they were slightly displaced to lower wavenumbers (2921/2852 cm<sup>-1</sup>) in the CNDs, suggesting some re-arrangements of the carbon within the graphitic core. The presence of various types of fatty acids in the argan waste is highlighted by the bands related to carbonyl groups (1737–1647 cm<sup>-1</sup>). The precursor also displayed a band located at 1546 cm<sup>-1</sup> associated to N-O stretching. Both former bands are less evident for the CNDs. The 1457  $\mathrm{cm}^{-1}$  (-C-H bending) low-intensity peak is slightly down shifted at 1452 cm<sup>-1</sup> in the case of CNDs. The low-intensity bands located at 1241 and 1153  $\,\mathrm{cm}^{-1}$  are attributed to -C-N and -C-O stretching vibrations, and they are observed in both samples. The band associated with the C=C stretching vibrations of hybridized sp<sup>2</sup> carbons (~1580–1602 cm<sup>-1</sup>) and the band located at 740 cm<sup>-1</sup> associated to the -C=C- bending vibrations were only observed for the CNDs; this confirms the aromatization of the carbon matrix during the thermal treatment.

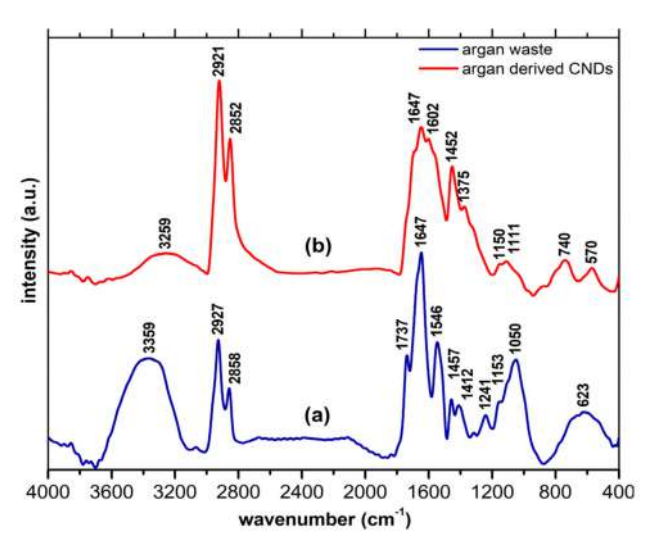


**Figure 2.** Record FT–IR spectra of the (a) argan cake waste and (b) derived CNDs.

Dynamic light scattering (DLS) was employed to analyze the particle size of the CNDs dispersed in water and chloroform (Figure 3). As seen, the average hydrodynamic diameter of the CND particles dispersed in water is mostly located within the 6–21 nm

Nanomaterials **2024**, 14, 83 6 of 14

range, with the largest fraction (19.17%) at 10 nm. On the other hand, the CND particles dispersed in chloroform displayed a narrower distribution of particle sizes, with the average hydrodynamic diameter in the 6–32 nm range, and the largest fraction (58.3%) within the 9–13 nm range. Furthermore, the zeta potential recorded for the CNDs dispersed in water is -44.9 mV, which indicates a moderate to good stability of the dispersion. The narrower size distribution recorded for chloroform-dispersed CNDs indicates the lower agglomeration tendency of the CNDs in this solvent, compared to water. This is attributed to polar surface moieties present in the CNDs, as inferred by the XPS and FTIR analysis. The average particle size is in rather good agreement with the particle size analysis obtained from SEM/TEM images (see below).

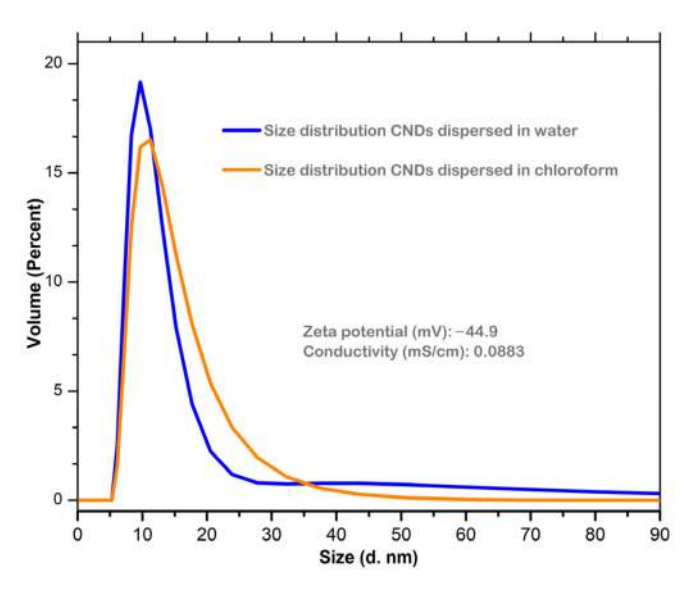


**Figure 3.** Average hydrodynamic diameter distribution of CND particles dispersed in water and chloroform, obtained by dynamic light scattering.

High-resolution SEM micrographs of the CNDs dispersed in water and in chloroform are presented in Figure 4a,b, respectively. Average particle sizes of 25–30 nm were observed for the sample dispersed in water, with some higher-dimension clusters (70–80 nm) clearly visible. This wider distribution of particle sizes is due to the agglomeration tendency in water. For the CNDs dispersed in chloroform, the particle size distribution is markedly lower, with an average size within 15–25 nm and less observation of bigger clusters.

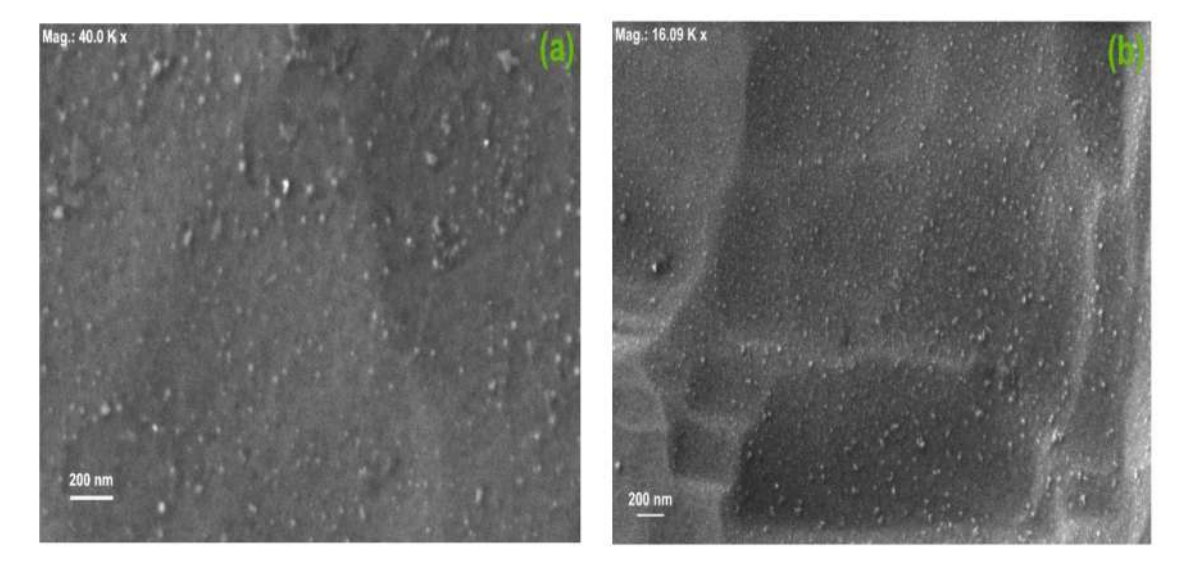


Figure 4. HR-SEM micrographs of the CNDs dispersed in (a) water and (b) chloroform.

Nanomaterials **2024**, 14, 83 7 of 14

Figure 5a,b presents the TEM micrographs of the prepared CNDs. The samples were prepared by dispersing the CNDs in ethanol, and further allowed to dry on the grids. As seen, nanostructures with dimensions within the 5–20 nm range and a reasonable narrow size distribution were obtained (Figure 5a). Figure 5b provides an interesting close up view of singular nanostructures, which clearly sustains the cluster organization of much smaller individual entities (approx. 5 nm).

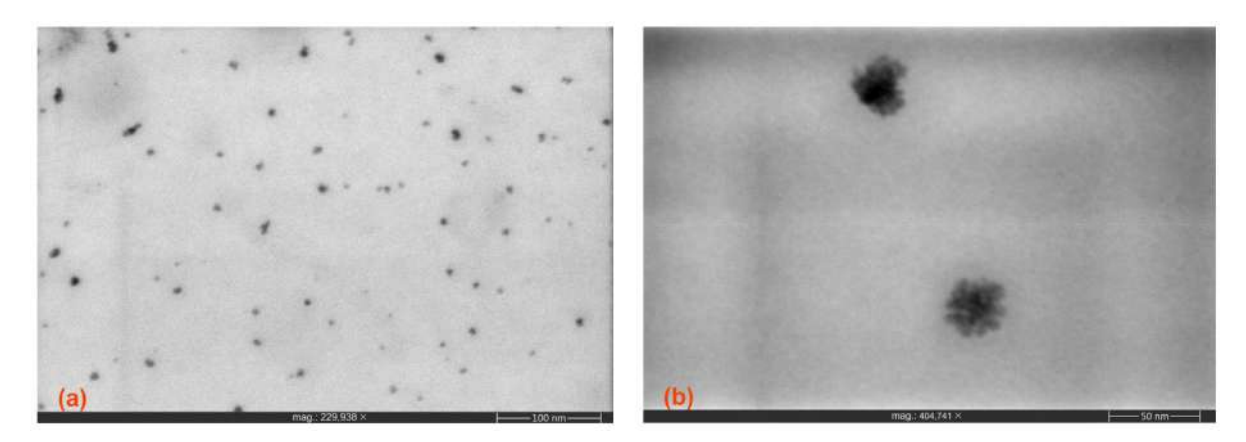


Figure 5. TEM micrographs of the CNDs recorded at (a) 230 k and (b) 405 k magnifications.

### 3.2. Characterization of the CND/Polymer Nanocomposites

Figure 6a,b displays the AFM images recorded for the prepared CND/polymer nanocomposites: CND/PSA and CND/COC. The films were deposited on mica through spray coating. The films prepared from CND/COC (Figure 6a) are smooth and homogenous in appearance, with a relatively low density of height irregularities (these are most likely due to small variations of compressed air pressure during the spray coating). In case of the CND/PSA (Figure 6b), the density of height variations is slightly higher, with several regular patterns observed that affect the smoothness of the surface. We attribute these patterns to the rapid drying of the nanocomposite on the mica slide. Anyhow, these small height variations observed in both nanocomposites do not modify the optical transparency of the deposited layers (see below).

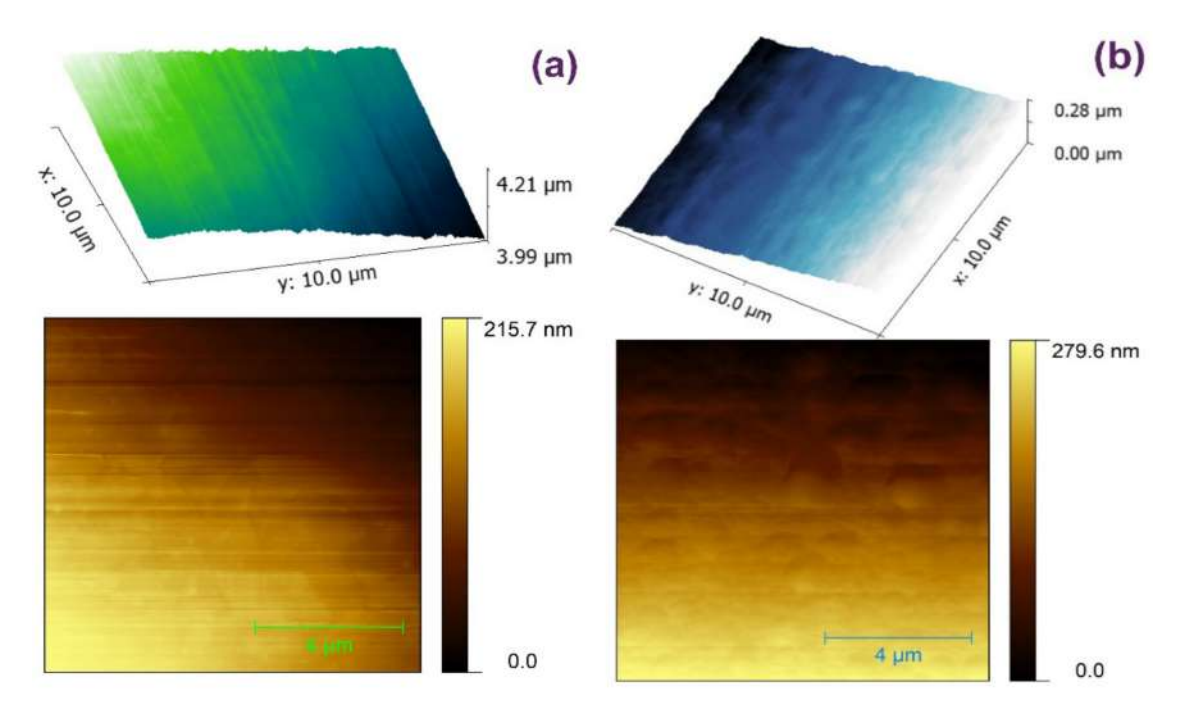
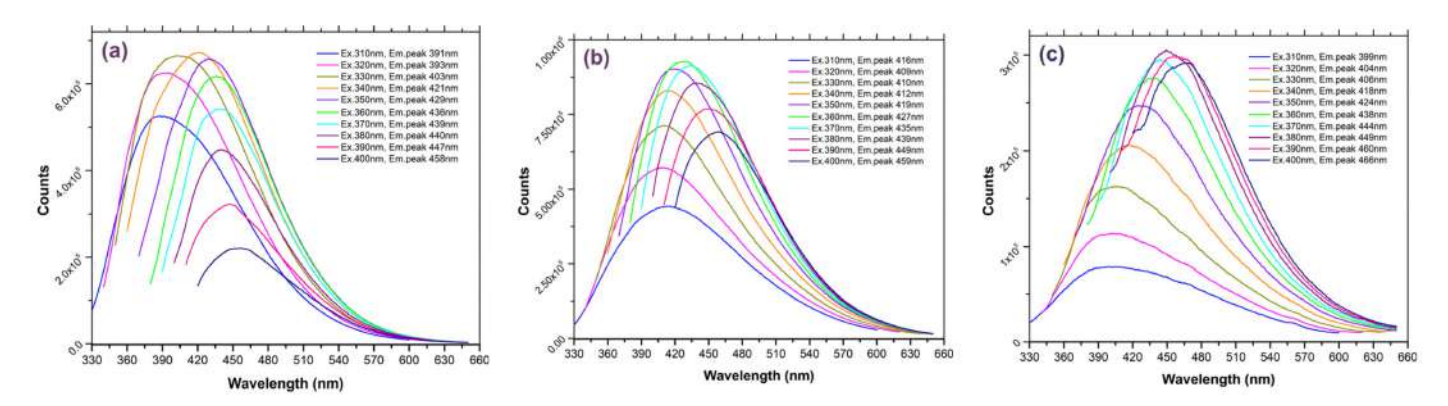


Figure 6. AFM images of the CND/polymer nanocomposites: (a) CND/COC and (b) CND/PSA.

Nanomaterials **2024**, 14, 83 8 of 14

### 3.3. Photoluminescence Features of the CNDs and the CND/Polymer Nanocomposites

The photoluminescence (PL) features of the prepared carbon nanostructures were investigated both in the suspensions (water and chloroform) and after immobilization in the polymers (CND/polymer nanocomposites). Figure 7a–c presents the steady-state emission spectra of the argan-derived CNDs dispersed in water, chloroform (CLF), and tetrahydrofuran (THF), respectively. As indicated above, the solvents were chosen based on their ability to dissolve the polymers (see experimental section). All the emission spectra were recorded within a 310–400 nm excitation range (10 nm step).



**Figure 7.** Steady-state PL emission of the argan-prepared CNDs dispersed in (a) water, (b) chloroform, and (c) tetrahydrofuran.

As seen, wide-range emission bands were obtained in all the solvents (average FWHM 50 nm). For the CNDs dispersed in water, the emission bands are centered between 391–458 nm, with the most intense emission at 421 nm under 340 nm excitation. For the CNDs dispersed in CLF, the emission bands were located in the 416–459 nm range, while the most intense emission signal is located at 427 nm under 360 nm excitation. Finally, for the CNDs dispersed in THF, the emission bands are located between the 399–466 nm range and the most intense emission signal at 449 nm was achieved under 380 nm excitation.

For the water-dispersed CNDs, the Stokes shift (i.e., difference between the spectral position of the maximum of the absorption band and the maximum of the emission band) is slightly higher (ca. 79 nm at 350 nm excitation) than that of the CNDs dispersed in CLF (ca. 69 nm at 350 nm excitation) and the CNDs dispersed in THF (ca. 74 nm at 350 nm excitation). For the CNDs dispersed in water, the emission of low-energy photon results are attributed to the presence of -OH moieties in the vicinity of the emissive sites [46]. This is supported by the XPS analysis.

Figure 8a,b displays the emission spectra recorded for the CNDs immobilized in the different polymers: COC/CND and PSA/CND nanocomposites, recorded within the same 310–400 nm excitation range. It should be noted that both nanocomposites presented an intense PL emission (ca. 2 times more intense than that of the CNDs dispersed in water and 3–4 times compared with CND–CLF/THF dispersions). According to our tests, the PL emission remained unchanged and stable for several months (tested over four months).

As shown in Figure 1, upon excitation with a regular UV-A source, the dominant emission of both nanocomposites is located in the blue area of the visible spectrum. In particular, the COC/CND nanocomposite PL emission band ranged between 383 and 455 nm, the most intense contribution being located at 407 nm under 350 nm excitation (Figure 8a). In contrast, the emission of PSA/CND is located within the 367–463 nm range, with the most intense emission contribution at 388 nm under a 340 nm excitation wavelength (Figure 8b). The most notable difference compared to the emission features of the CNDs dispersed in the different solvents is the markedly smaller Stokes shift of the immobilized CNDs, particularly for COC/CND (ca. 57 nm for COC/CND, and 79 nm for PSA/CND, under 350 nm excitation). Besides the improved PL emission stability, the rigid environment provided by the polymer backbone seems to also improve the efficiency of

Nanomaterials **2024**, 14, 83 9 of 14

the radiative processes. This is inferred from the absolute PLQY yield values recorded for the immobilized and non-immobilized CNDs (Table 2).

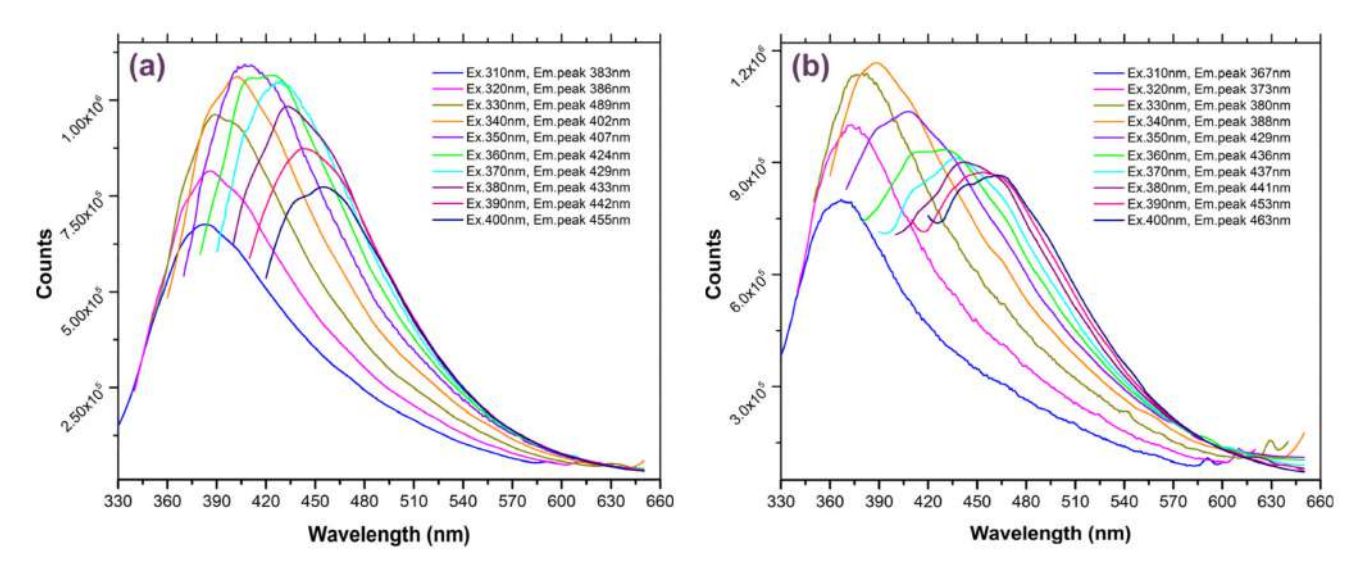


Figure 8. Steady-state PL emission of the (a) COC/CND and (b) PSA/CND nanocomposites.

Table 2. Absolute PLQY values at different excitation wavelengths of the solvent dispersed CNDs
and the CND/polymer nanocomposites (maximum values are highlighted in bold).

Excitation (nm)	310	320	330	340	350	360	370	380	390	400
CNDs dispersed in H <sub>2</sub> O	CIE 1931 parameter X= 0.167, Y= 0.130 @350 nm									
Absolute PLQY (%)	2.6	12.3	14	13.8	15.1	11.3	9.3	7.5	5.3	3.4
CNDs dispersed in THF	CIE 1931 parameter X= 0.168, Y= 0.153 @350 nm									
Absolute PLQY (%)	1.4	3.4	4.1	5.5	5.9	5.5	5.2	5	4.9	4.7
CNDs dispersed in CLF	CIE 1931 parameter X = 0.168, Y = 0.148 @350 nm									
Absolute PLQY (%)	8.1	8.1	8.5	8.8	8.9	8.7	8.2	8	7.5	6.9
CND/PSA nanocomposite	CIE 1931 parameter X = 0.187, Y = 0.175 @350 nm									
Absolute PLQY (%)	18	12.4	12.6	12.1	12	10	8	7.7	8.6	10.1
CND/COC nanocomposite	CIE 1931 parameter X = 0.176, Y = 0.157 @350 nm									
Absolute PLQY (%)	29.6	22.4	21.7	23.9	21.8	17.1	14.9	14.9	16.6	18.3

For the dispersed CNDs, the highest PLQY values were recorded at a 350 nm excitation wavelength and followed the trend of water > CLF > THF, with a value when using water as the dispersion medium (ca. 15.1%) of almost twice and three times higher than those obtained upon dispersion in CLF and THF, respectively. Interestingly, this trend does not follow a clear correlation with the polarity of the solvents (e.g., dielectric constants of 80 for water; 7.4 for THF; and 4.7 for CLF), suggesting the important role of the surface charges. For the CND/polymer nanocomposites, the PLQY followed the trend of CND/COC (29.6%) > CND/PSA (18%), even though both values are higher than those of the dispersed carbon nanostructures. In this case, the maximum PLQY was obtained upon excitation at 310 nm. The values upon excitation at 350 nm were still higher or comparable to those of the dispersed CNDs. This confirms the improved efficiency of the radiative process upon the embedment in the polymer matrix.

Figure 9a,b shows a comparison of the chromatic parameters (according to the CIE 1931 chromaticity co-ordinates) between the solvent-dispersed CNDs and those of the CND/polymer nanocomposites recorded under 350 nm excitation. As seen, the chro-

maticity co-ordinates of the immobilized CNDs were slightly shifted to higher luminance (brightness, y co-ordinate) and chromaticity (color, x co-ordinate), thus demonstrating the improved stability of the PL features of the former.

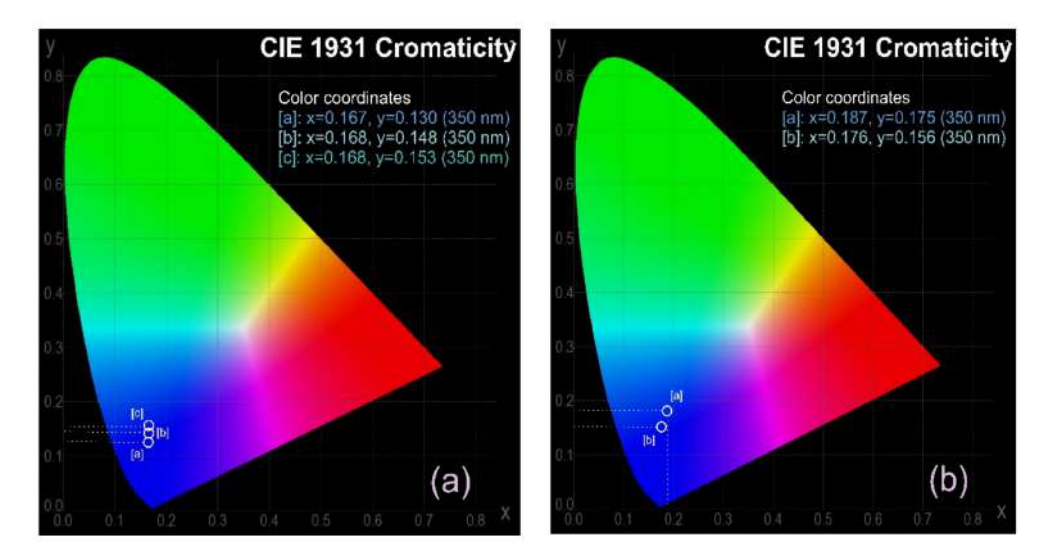


**Figure 9.** PL emission chromaticity parameters (CIE1931) of the **(a)** solvent-dispersed CNDs and the **(b)** CND/polymer nanocomposites.

The excited states' lifetime recorded for both CLF-dispersed CNDs and COC-CND nanocomposites revealed radiative processes within the nanosecond range, as presented in Figure 10 and detailed in Table 3.

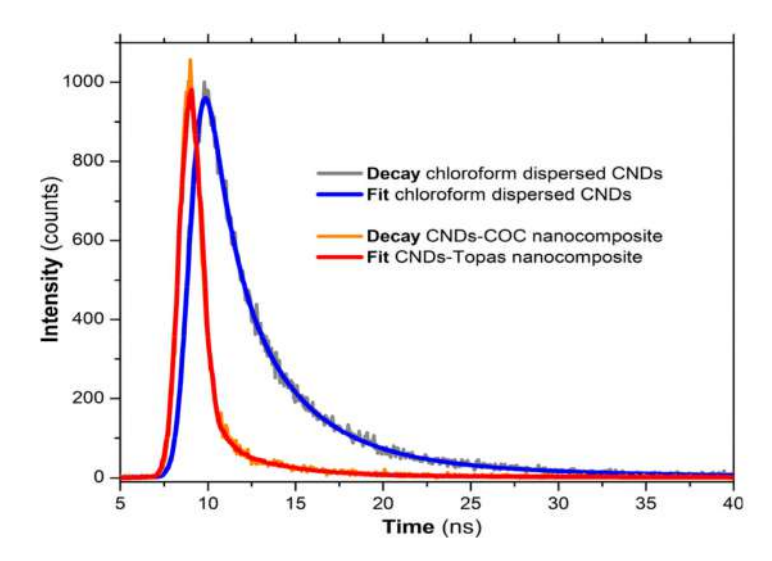


Figure 10. PL lifetime decay recorded for the CLF-dispersed CNDs and COC-CND nanocomposites.

Table 3. Recorded excited states' lifetimes.

CLF Dispo	ersed CNDs	COC-CND Nanocomposites			
Lifetimes (ns) Contribution (%)		Lifetimes (ns)	Contribution (%)		
$\tau 1 = 1.01$	20	$\tau 1 = 1.05$	84		
$\tau 2 = 3.38$	55	$\tau 1 = 3.03$	12		
$\tau 3 = 9.18$	25	$\tau 1 = 10.60$	4		

Furthermore, the lifetime of the excited states of the CND/polymer nanocomposites was within the nanosecond range (Table 3), typical values for CNDs as reported in the literature [47]. It should be noted that the lifetime of the radiative processes for the CND/polymer nanocomposites was lower than that of the dispersed nanostructures (ca. predominant contribution at 1.05 ns). This agrees with the higher PLQY values. Through embedment in the polymer matrix, the excitation energy transferred to the emissive sites within the CNDs and the resulted photon emission become more efficient.

# 4. Testing the Prepared CND/Polymer Nanocomposites as Photonic Conversion Layers on PV Cells

As mentioned above, the prepared nanocomposites could be easily implemented as photonic conversion layers in a new approach aiming to increase the conversion efficiency of commercially available PV solar cells by taking advantage of the UV radiation contained in the solar spectrum. Most of the available PV solar cells are less sensitive in the upper spectral region of the solar spectrum, the incident UV photons having a low impact on the overall conversion efficiency. Through conversion of the solar UV photons located in the UV-A/UV-B range into the Vis range where the PV cells are mostly sensitive, the overall conversion efficiency could be improved. Typically, the solar radiation UV content at earth level is ~8% depending on the geographical position, elevation, season, time of the day, and specific atmospheric conditions [48]. By harvesting the solar UV photons, which are rather unused in the conversion processes of the commonly available PV cells, an improvement in the overall efficiency could be achieved. Even a small 4–5% conversion efficiency improvement in the UV region could be significant for energy generation where the output power/surface ratio is very important.

In order to test the newly prepared CND/polymer nanocomposites, some commonly available polycrystalline PV cells (model ZW85X115, 12 V, 1.5 W) were provided with an outer photonic conversion layer consisting of the prepared COC–CND nanocomposites. The thin polymeric nanocomposite layer was obtained through spray coating using the methodology and equipment described in Section 2.3. The results are presented in Figure 11a,b.

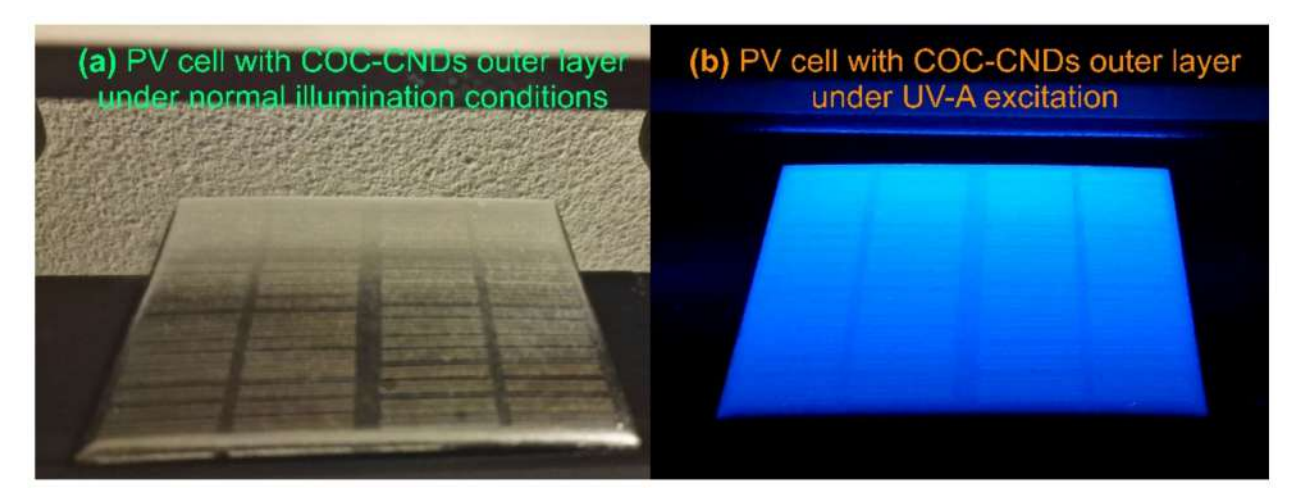


**Figure 11.** PV cell provided with the COC–CND nanocomposite outer thin layer: (**a**) under normal illumination conditions and (**b**) under UV-A excitation.

As could be noted, the deposited COC–CND nanocomposite thin layer present a strong PL emission under UV-A excitation (provided by a 6 W laboratory 365 nm UV lamp) in the blue region of the visible spectrum, thus down-converting the UV photons in a region where the PV cells are more sensitive. Details of the experimental testing layout and measurement setup are presented in Figure S5 (Supplemental Information).

The measurements were performed using a custom-made UV source consisting of an UV LED array powered by an I/V regulated power supply. In order to minimize the measurements errors due to the inherent production batch variance of the PV cells, the same PV cells were measured prior to the application of the COC–CND thin layer with the exactly the same power supply parameters (V/I) of the UV LED array. In each case, the intensity of the LED array UV emission was fine-tuned with a UVAB light meter (RS Pro IM-213) to a value of 5 mW/cm² (roughly corresponding to a 5% UV content of the solar radiation). The output of the tested PV cells was measured without a load resistor using a Tenma 72-7732 data-logging multimeter. The results clearly indicate the conversion efficiency improvement provided by the thin COC–CND photonic conversion layer. Thus, prior to the addition of the outer photonic conversion layer, the PV cell output measured 10.62 V, while the same PV cell provided with the COC–CND conversion layer achieved 11.14 V.

### 5. Conclusions

Blue-emitting polymer/carbon nanodot nanocomposites were prepared through embedding carbon nanodots prepared upon thermal processing of argan cake waste in optically transparent polymer matrices. The as-prepared CNDs dispersed in various solvents presented characteristic excitation wavelength-dependent emission features, with the maximum of the emission located in the blue region of the visible spectrum. The immobilization of the CNDs in optically transparent matrices (e.g., poly(styrene-co-acrylonitrile and cycloolefin copolymer) preserved the long-term (blue) emission properties of the CNDs, and improved the quantum efficiency of the radiative processes by twice and three times (achieving a 29.6% PLQY).

The facile processability of the CNDs in thin films of optically transparent polymers is a promising alternative for the implementation of these carbon nanostructures as photonic down-conversion layers in optoelectronics devices. Our preliminary tests of their implementation on commercially available PV cells revealed a notable improvement in the conversion efficiency in the UV range. Current studies are ongoing, aiming to further improve the conversion efficiency of conventional photovoltaic solar cells with these conversion layers by taking advantage of the UV radiation contained in the solar spectrum.

Supplementary Materials: The following supporting information can be downloaded at: https://www.mdpi.com/article/10.3390/nano14010083/s1, Figure S1: Laboratory experimental setup used for CNDs preparation; Figure S2: XPS survey spectra recorded for (a) argan waste cake and (b) prepared CNDs; Figure S3: Deconvolution of the (a) C1s, (b) O1s and (c) N1s regions in the XPS spectra recorded for argan waste cake; Figure S4: Deconvolution of the (a) C1s, (b) O1s and (c) N1s regions in the XPS spectra recorded the prepared CNDs; Figure S5: Experimental testing layout and measurement setup for testing the PV cells provided with the prepared nanocomposites as photonic conversion layers.

**Author Contributions:** Conceptualization, C.S.S., M.P., C.O.A., H.K. and A.A.; methodology, C.S.S., M.P. and C.O.A.; investigation, A.C., L.E.U. and C.O.A.; writing—original draft preparation, C.S.S., C.A. and A.C.; experimental, C.S.S., N.E. and C.A.; writing—review and editing, C.S.S., M.P. and C.A. All authors have read and agreed to the published version of the manuscript.

**Funding:** This work was supported by a grant from the Romanian National Authority for Scientific Research and Innovation UEFISCDI, project: ERANET 293/2022-COFUND-LEAP-RE-NANOSOLARCELL. The authors thank the financial support of the LEAP-RE program (Long-Term Joint EU-AU Research and Innovation Partnership on Renewable Energy; grant NANOSOLARCELLS).

**Data Availability Statement:** The data presented in this study are available upon request from the corresponding author.

Conflicts of Interest: The authors declare no conflict of interest.

### References

1. Humaera, N.A.; Fahri, A.N.; Armynah, B.; Tahir, D. Natural source of carbon dots from part of a plant and its applications: A review. *Luminescence* **2021**, *36*, 1354–1364. [CrossRef] [PubMed]

- 2. Rodríguez-Varillas, S.; Fontanil, T.; Obaya, Á.J.; Fernández-González, A.; Murru, C.; Badía-Laíño, R. Biocompatibility and Antioxidant Capabilities of Carbon Dots Obtained from Tomato (*Solanum lycopersicum*). *Appl. Sci.* **2022**, *12*, 773. [CrossRef]
- 3. Stepanidenko, E.A.; Ushakova, E.V.; Fedorov, A.V.; Rogach, A.L. Applications of Carbon Dots in Optoelectronics. *Nanomaterials* **2021**, *11*, 364. [CrossRef] [PubMed]
- 4. Yuan, T.; Meng, T.; He, P.; Shi, Y.; Li, Y.; Li, X.; Fan, L.; Yang, S. Carbon quantum dots: An emerging material for optoelectronic applications. *J. Mater. Chem. C* **2019**, *7*, 6820–6835. [CrossRef]
- 5. Barrientos, K.; Arango, J.P.; Moncada, M.S.; Placido, J.; Patiño, J.; Macías, S.L.; Maldonado, C.; Torijano, S.; Bustamante, S.; Londoño, M.E.; et al. Carbon dot-based biosensors for the detection of communicable and non -communicable diseases. *Talanta* **2023**, 251, 123791. [CrossRef] [PubMed]
- 6. Das, S.; Ngashangva, L.; Goswami, P. Carbon Dots: An Emerging Smart Material for Analytical Applications. *Micromachines* **2021**, 12, 84. [CrossRef]
- 7. Bhattacharya, T.; Shin, G.H.; Kim, J.T. Carbon Dots: Opportunities and Challenges in Cancer Therapy. *Pharmaceutics* **2023**, *15*, 1019. [CrossRef]
- 8. Geng, B.; Hu, J.; Li, Y.; Feng, S.; Pan, D.; Feng, L.; Shen, L. Near-infrared phosphorescent carbon dots for sonodynamic precision tumor therapy. *Nat. Commun.* **2022**, *13*, 5735. [CrossRef]
- 9. Naik, K.; Chaudhary, S.; Ye, L.; Parmar, A.S. A Strategic Review on Carbon Quantum Dots for Cancer-Diagnostics and Treatment. *Front. Bioeng. Biotechnol.* **2022**, *10*, 882100. [CrossRef]
- 10. Latha, B.D.; Soumya, K.; More, N.; Choppadandi, M.; Guduru, A.T.; Singh, G.; Kapusetti, G. Fluorescent carbon quantum dots for effective tumor diagnosis: A comprehensive review. *Adv. Biomed. Eng.* **2023**, *5*, 100072.
- 11. Tiron, A.; Stan, C.S.; Luta, G.; Uritu, C.M.; Vacarean-Trandafir, I.-C.; Stanciu, G.D.; Coroaba, A.; Tiron, C.E. Manganese-Doped N-Hydroxyphthalimide-Derived Carbon Dots—Theranostics Applications in Experimental Breast Cancer Models. *Pharmaceutics* **2021**, *13*, 1982. [CrossRef] [PubMed]
- 12. Liu, J.; Li, R.; Yang, B. Carbon Dots: A New Type of Carbon-Based Nanomaterial with Wide Applications. *ACS Cent. Sci.* **2020**, *6*, 2179–2195. [CrossRef] [PubMed]
- 13. Yadav, P.K.; Chandra, S.; Kumar, V.; Kumar, D.; Hasan, S.H. Carbon Quantum Dots: Synthesis, Structure, Properties, and Catalytic Applications for Organic Synthesis. *Catalysts* **2023**, *13*, 422. [CrossRef]
- 14. Dam, B.D.; Nie, H.; Ju, B.; Marino, E.; Paulusse, J.M.J.; Schall, P.; Li, M.; Dohnalová, K. Excitation-Dependent Photoluminescence from Single-Carbon Dots. *Small* **2017**, *13*, 1770251.
- 15. Singhal, P.; Vats, B.G.; Pulhani, V. Origin of solvent and excitation dependent emission in newly synthesized amphiphilic carbon dots. *J. Lumin.* **2022**, 244, 118742. [CrossRef]
- 16. Ding, H.; Li, X.H.; Chen, X.B.; Wei, J.S.; Li, X.B.; Xiong, H.M. Surface states of carbon dots and their influences on luminescence. *J. Appl. Phys.* **2020**, 127, 231101. [CrossRef]
- 17. Wang, B.; Lu, S. The light of carbon dots: From mechanism to applications. *Matter* 2022, 5, 110–149. [CrossRef]
- 18. Tiwari, A.; Walia, S.; Sharma, S.; Chauhan, S.; Kumar, M.; Gadlyd, T.; Randhawa, T.K. High quantum yield carbon dots and nitrogen-doped carbon dots as fluorescent probes for spectroscopic dopamine detection in human serum. *J. Mater. Chem. B* **2023**, 11, 1029–1043. [CrossRef]
- 19. Yan, F.; Jiang, Y.; Sun, X.; Bai, Z.; Zhang, Y.; Zhou, X. Surface modification and chemical functionalization of carbon dots: A review. *Microchim. Acta* **2018**, *185*, 424. [CrossRef]
- 20. Koç, O.K.; Üzer, A.; Apak, R. High Quantum Yield Nitrogen-Doped Carbon Quantum Dot-Based Fluorescent Probes for Selective Sensing of 2,4,6-Trinitrotoluene. ACS Appl. Nano Mater. 2022, 5, 5868–5881. [CrossRef]
- 21. Stan, C.S.; Coroabă, A.; Ursu, E.L.; Secula, M.S.; Simionescu, B.C. Fe(III) doped carbon nanodots with intense green photoluminescence and dispersion medium dependent emission. *Sci. Rep.* **2019**, *9*, 18893. [CrossRef] [PubMed]
- 22. Singh, A.; Qu, Z.; Sharma, A.; Singh, M.; Tse, B.; Ostrikov, K.; Popat, A.; Sonar, P.; Kumeria, T. Ultra-bright green carbon dots with excitation-independent fluorescence for bioimaging. *J. Nanostruct. Chem.* **2023**, *13*, 377–387. [CrossRef]
- 23. Li, P.; Xue, S.; Sun, L.; Zong, X.; An, L.; Qu, D.; Wang, X.; Sun, Z. Formation and fluorescent mechanism of red emissive carbon dots from o-phenylenediamine and catechol system. *Light Sci. Appl.* **2022**, *11*, 298. [CrossRef] [PubMed]
- 24. Ding, H.; Zhou, X.X.; Wei, J.S.; Li, X.B.; Qin, B.T.; Chen, X.B.; Xiong, H.M. Carbon dots with red/near-infrared emissions and their intrinsic merits for biomedical applications. *Carbon* **2020**, *167*, 322–344. [CrossRef]
- 25. Stan, C.S.; Gospei Horlescu, P.; Ursu, L.E.; Popa, M.; Albu, C. Facile preparation of highly luminescent composites by polymer embedding of carbon dots derived from N-hydroxyphthalimide. *J. Mater. Sci.* **2017**, *52*, 185–196. [CrossRef]
- 26. Cui, L.; Ren, X.; Sun, M.; Liu, H.; Xia, L. Carbon Dots: Synthesis, Properties and Applications. *Nanomaterials* **2021**, *11*, 3419. [CrossRef] [PubMed]
- 27. Nammahachak, N.; Aup-Ngoen, K.K.; Asanithi, P.; Horpratum, M.; Chuangchote, S.; Ratanaphan, S.; Surareungchai, W. Hydrothermal synthesis of carbon quantum dots with size tunability via heterogeneous nucleation. *RSC Adv.* **2022**, *12*, 31729–31733. [CrossRef]

28. Luo, H.; Lari, L.; Kim, H.; Hérou, S.; Tanase, L.C.; Lazarovc, V.K.; Titirici, M.M. Structural evolution of carbon dots during low temperature pyrolysis. *Nanoscale* **2022**, *14*, 910–918. [CrossRef]

- 29. Khayal, A.; Dawane, V.; Amin, M.A.; Tirth, V.; Yadav, V.K.; Algahtani, A.; Khan, S.H.; Islam, S.; Yadav, K.K.; Jeon, B.H. Advances in the Methods for the Synthesis of Carbon Dots and Their Emerging Applications. *Polymers* **2021**, *13*, 3190. [CrossRef]
- 30. Adejumo, I.O.; Adebiyi, O.A. Agricultural Solid Wastes: Causes, Effects, and Effective Management. In *Strategies of Sustainable Solid Waste Management*; C Solid Waste Management; Saleh, H.M., Ed.; IntechOpen: Cairo, Egypt, 2021.
- 31. Raza, M.H.; Abid, M.; Faisal, M.; Yan, T.; Akhtar, S.; Adnan, K.M.M. Environmental and Health Impacts of Crop Residue Burning: Scope of Sustainable Crop Residue Management Practices. *Int. J. Environ. Res. Public Health* **2022**, *19*, 4753. [CrossRef]
- 32. Kang, C.; Huang, Y.; Yang, H.; Yan, X.F.; Chen, Z.P. A Review of Carbon Dots Produced from Biomass Wastes. *Nanomaterials* **2020**, 10, 2316. [CrossRef] [PubMed]
- 33. Gedda, G.; Sankaranarayanan, S.A.; Putta, C.L.; Gudimella, K.K.; Rengan, A.K.; Girma, W.M. Green synthesis of multi-functional carbon dots from medicinal plant leaves for antimicrobial, antioxidant, and bioimaging applications. *Sci. Rep.* **2023**, *13*, 6371. [CrossRef] [PubMed]
- 34. Newman Monday, Y.; Abdullah, J.; Yusof, N.A.; Abdul Rashid, S.; Shueb, R.H. Facile Hydrothermal and Solvothermal Synthesis and Characterization of Nitrogen-Doped Carbon Dots from Palm Kernel Shell Precursor. *Appl. Sci.* **2021**, *11*, 1630. [CrossRef]
- 35. Xiaoyun, Q.; Cuicui, F.; Jin, Z.; Wenlong, S.; Xiaomei, Q.; Yanghai, G.; Lan, W.; Huishi, G.; Fenghua, C.; Liying, J.; et al. Direct preparation of solid carbon dots by pyrolysis of collagen waste and their applications in fluorescent sensing and imaging. *Front. Chem.* **2022**, *10*, 1006389.
- 36. Zhang, J.; Xia, A.; Chen, H.; Nizami, A.S.; Huang, Y.; Zhu, X.; Zhu, X.; Liao, Q. Biobased carbon dots production via hydrothermal conversion of microalgae Chlorella pyrenoidosa. *Sci. Total Environ.* **2022**, *839*, 156144. [CrossRef]
- 37. Prasannan, A.; Imae, T. One-Pot Synthesis of Fluorescent Carbon Dots from Orange Waste Peels. *Ind. Eng. Chem. Res.* **2013**, 52, 15673–15678. [CrossRef]
- 38. González-González, R.B.; González, L.T.; Madou, M.; Leyva-Porras, C.; Martinez-Chapa, S.O.; Mendoza, A. Synthesis, Purification, and Characterization of Carbon Dots from Non-Activated and Activated Pyrolytic Carbon Black. *Nanomaterials* **2022**, *12*, 298. [CrossRef]
- Ganguly, S.; Das, P.; Banerjee, S.; Das, N.C. Advancement in science and technology of carbon dot-polymer hybrid composites: A review. Funct. Compos. Struct. 2019, 1, 022001. [CrossRef]
- 40. Maxim, A.A.; Sadyk, S.N.; Aidarkhanov, D.; Surya, C.; Ng, A.; Hwang, Y.-H.; Atabaev, T.S.; Jumabekov, A.N. PMMA Thin Film with Embedded Carbon Quantum Dots for Post-Fabrication Improvement of Light Harvesting in Perovskite Solar Cells. *Nanomaterials* **2020**, *10*, 291. [CrossRef]
- 41. Liu, Y.; Wang, P.; Shiral Fernando, K.A.; LeCroy, G.E.; Maimaiti, H.; Harruff-Miller, B.A.; Lewis, W.K.; Bunker, C.E.; Hou, Z.L.; Sun, P.Y. Enhanced fluorescence properties of carbon dots in polymer films. *J. Mater. Chem. C* **2016**, *4*, 6967–6974. [CrossRef]
- 42. Bhunia, S.K.; Nandi, S.; Shiklerb, R.; Jelinek, R. Tuneable light-emitting carbon-dot/polymer flexible films prepared through one-pot synthesis. *Nanoscale* **2016**, *8*, 3400–3406. [CrossRef] [PubMed]
- 43. Shebeeb, C.M.; Joseph, A.; Chalikkara, F.; Dinesh, R.; Sajith, V. Fluorescent carbon dot embedded polystyrene particle: An alternative to fluorescently tagged polystyrene for fate of microplastic studies: A preliminary investigation. *Appl. Nanosci.* **2022**, 12, 2725–2731. [CrossRef]
- 44. Gharby, S.; Charrouf, Z. Argan Oil: Chemical Composition, Extraction Process, and Quality Control. *Front. Nutr.* **2022**, *8*, 804587. [CrossRef] [PubMed]
- 45. Zhang, C.; Dabbs, D.M.; Liu, L.M.; Ilhan, A.; Aksay, I.A.; Car, R.; Selloni, A. Combined Effects of Functional Groups, Lattice Defects, and Edges in the Infrared Spectra of Graphene Oxide. *J. Phys. Chem. C* **2015**, *119*, 18167–18176. [CrossRef]
- 46. Kamel, B.; El-Daher, M.S.; Bachir, W.; Ibrahim, A.; Aljalali, S. Effect of Solvents on the Fluorescent Spectroscopy of BODIPY-520 Derivative. *J. Spectrosc.* **2022**, 2022, 1172183. [CrossRef]
- 47. Barman, M.K.; Patra, A. Current status and prospects on chemical structure driven photo luminescence behaviour of carbon dots. *J. Photochem. Photobio. C* **2018**, *37*, 1–22. [CrossRef]
- 48. Chadyšienė, R.; Girgždiene, R.; Girgždys, A. Ultraviolet radiation and ground level ozone variation in Lithuania. *J. Environ. Eng. Landsc. Manag.* **2005**, *13*, 31–36. [CrossRef]

**Disclaimer/Publisher's Note:** The statements, opinions and data contained in all publications are solely those of the individual author(s) and contributor(s) and not of MDPI and/or the editor(s). MDPI and/or the editor(s) disclaim responsibility for any injury to people or property resulting from any ideas, methods, instructions or products referred to in the content.





Article

# Manganese-Doped N-Hydroxyphthalimide-Derived Carbon Dots—Theranostics Applications in Experimental Breast Cancer Models

Adrian Tiron <sup>1</sup>, Corneliu S. Stan <sup>2</sup>, Gabriel Luta <sup>1</sup>, Cristina M. Uritu <sup>3,\*</sup>, Irina-Cezara Vacarean-Trandafir <sup>1</sup>, Gabriela D. Stanciu <sup>3</sup>, Adina Coroaba <sup>4</sup> and Crina E. Tiron <sup>1,\*</sup>

- TRANSCEND Centre, Regional Institute of Oncology, 2-4 General Henri Mathias Berthelot Street, 700483 Iasi, Romania; adrian.tiron@iroiasi.ro (A.T.); gabriel.luta@iroiasi.ro (G.L.); irina.trandafir@iroiasi.ro (I.-C.V.-T.)
- Department of Natural and Synthetic Polymers, "Gheorghe Asachi" Technical University of Iasi, 71 Prof. dr. docent Dimitrie Mangeron Street, 700050 Iasi, Romania; stancs@tuiasi.ro
- Centre for Advanced Research and Development in Experimental Medicine (CEMEX), "Grigore T. Popa" University of Medicine and Pharmacy, 16 Universitatii Street, 700115 Iasi, Romania; gabriela-dumitrita.s@umfiasi.ro
- <sup>4</sup> Centre of Advanced Research in Bionanoconjugates and Biopolymers, "Petru Poni" Institute of Macromolecular Chemistry, 41A Grigore Ghica Voda Alley, 700487 Iasi, Romania; adina.coroaba@icmpp.ro
- \* Correspondence: cristina-mariana.uritu@umfiasi.ro (C.M.U.); transcendctiron@iroiasi.ro (C.E.T.)

Abstract: Background: Theranostics, a novel concept in medicine, is based on the use of an agent for simultaneous diagnosis and treatment. Nanomaterials provide promising novel approaches to theranostics. Carbon Dots have been shown to exhibit anti-tumoral properties in various cancer models. The aim of the present study is to develop gadolinium, Fe<sup>3+</sup>, and Mn<sup>2+</sup>-doped N-hydroxyphthalimide-derived Carbon Dots. The resulted doped Carbon Dots should preserve the anti-tumoral properties while gaining magnetic resonance imaging properties. Methods: Normal and cancer cell lines have been treated with doped Carbon Dots, and the cell viability has been measured. The doped Carbon Dots that exhibited the most prominent anti-tumoral effect accompanied by the lowest toxicity have been further in vivo tested. Magnetic resonance imaging evaluates both in vitro and in vivo the possibility of using doped Carbon Dots as a contrast agent. Results: According to the results obtained from both the in vitro and in vivo experimental models used in our study, Mn<sup>2+</sup>-doped Carbon Dots (Mn-CDs-NHF) exhibit anti-tumoral properties, do not significantly impair the cell viability of normal cells, and reduce lung metastasis and the volume of mammary primary tumors while allowing magnetic resonance imaging. Conclusions: Our findings prove that Mn-CDs-NHF can be used as theranostics agents in pre-clinical models.

Keywords: carbon dots; anti-cancer; MRI; nanomedicine; theranostic



Citation: Tiron, A.; Stan, C.S.; Luta, G.; Uritu, C.M.; Vacarean-Trandafir, I.-C.; Stanciu, G.D.; Coroaba, A.; Tiron, C.E. Manganese-Doped N-Hydroxyphthalimide-Derived Carbon Dots—Theranostics Applications in Experimental Breast Cancer Models. *Pharmaceutics* 2021, 13, 1982. https://doi.org/10.3390/pharmaceutics13111982

Academic Editor: Tomáš Etrych

Received: 21 October 2021 Accepted: 19 November 2021 Published: 22 November 2021

**Publisher's Note:** MDPI stays neutral with regard to jurisdictional claims in published maps and institutional affiliations.



Copyright: © 2021 by the authors. Licensee MDPI, Basel, Switzerland. This article is an open access article distributed under the terms and conditions of the Creative Commons Attribution (CC BY) license (https://creativecommons.org/licenses/by/4.0/).

### 1. Introduction

Due to the fact that cancer still remains a major worldwide health problem despite the latest advances in understanding cancer biology and developing new tools for early detection and treatments, researchers are looking for new ways to improve drug delivery and treatments toward being less invasive as well as having fewer side effects and higher efficiency [1].

Different technologies, such as nanomedicine, have opened up new opportunities for the treatments in different diseases. Nanocomposites play an important role in drug release and biodistribution in various types of diseases. For example, they could improve the release of chemotherapeutic drugs in the therapy of certain cancer types [2]. Nanoparticles (NPs) have been widely employed in the past few years in order to deliver therapeutic drugs more effectively to different targeted tissues [3,4]. Several studies indicate that nanomaterials-based delivery systems suppress in vivo tumor growth [5–7].

In this context, Carbon Dots-based materials have gained attention in the scientific community due to their physical and chemical properties, which make them one of the most promising tools for drug delivery and imaging [8,9]. Cytotoxicity studies on different cell lines demonstrate the lower toxicity of Carbon Dots even at high concentrations. Moreover, Carbon Dots have recently been proven in vitro and in vivo to exhibit antitumoral properties in various cancer models [10–14]. Our previous work demonstrated in vitro and in vivo the anti-tumoral properties of N-Hydroxyphthalimide-derived Carbon Dots (CDs-NHF) in a breast cancer model [15]. In another paper, we have shown that although CDs-NHF alone do not impair U87 glioblastoma cell line viability, combining lower doses of key pathways inhibitors with lower CDs-NHF doses significantly reduced cell viability [16].

Despite the outstanding advances in medical imaging for diagnosis, magnetic resonance imaging (MRI) remains one of the most valuable techniques for in vivo investigations, due to its non-invasive nature in the absence of ionizing radiation, which may provide both anatomical and functional data [17]. The majority of MRI contrast probes are based on gadolinium (Gd<sup>3+</sup>). However, due to the fact that Gd<sup>3+</sup> is associated with different side effects such as nephrogenic system fibrosis, new alternatives are necessary [18,19].

Manganese-based nanoparticles (Mn-based NPs) represent promising alternatives due to their lower toxicity compared with  $Gd^{3+}$  [20,21]. Additionally, there are no data to report any pre-clinical data regarding the in vitro and in vivo toxicity of Mn-based NPs, making them a viable alternative to  $Gd^{3+}$  [22,23].

Apoptosis or programed cell death is a regulatory system having a crucial role in controlling cell proliferation, tissue homeostasis, and removing cells that are no longer needed. The dysregulation of apoptosis mechanisms contributes to human diseases such as cancer. Molecules responsible for apoptosis have offered new ways to develop solutions in order to increase cancer cell death. Mitochondria play an important role in apoptotic cell death. Mitochondria dysfunction leads to apoptosis [24,25].

The cytokine interleukin-6 (IL-6) plays a crucial role in both normal human physiology and diseases. The findings demonstrate that IL-6 promotes the development of breast [26], colorectal [27], pancreatic [28], and skin [29] cancers. IL-6 signaling has been shown to play an important role in tumor progression and metastasis dissemination in a different tumor type [30]. High circulating levels of IL-6 have been reported in patients with different types of cancers such as breast [31], colorectal [32], ovarian [33], renal [34], non-small-cell lung cancer (NSCLC) [35], and head and neck [36], and circulating IL-6 levels are reported to be increased in patients with recurrent tumors [37].

In the present study, we aim to develop a theranostics agent that combines the antitumoral properties of CDs-NHF with enhanced imaging properties, which are doubled by low toxicity of Mn. For this, we have developed doped CDs-NHF with Gd<sup>3+</sup>, Mn<sup>2+</sup>, or Fe<sup>3+</sup>. Using an MRI in vitro model, we have investigated the anti-tumoral effects of doped CDs-NHF as well as the imaging properties. The most promising candidate, Mn-CDs-NHF, has been further investigated in an in vivo 4T1 murine breast cancer model in order to evaluate its theranostics potential. Additionally, we have also aimed to explore the effect of the Mn-CDs-NHF on lung metastases due to the fact that lungs represent the primary metastasis site of the 4T1 cell line.

### 2. Materials and Methods

### 2.1. Preparation and Investigation of the Doped CDs-NHF

The preparation of the doped CDs-NHF was performed according to the procedure and the experimental setup mentioned in our previous work [38]. N-Hydroxyphthalimide (97%) (NHF) and anhydrous MnCl<sub>2</sub> were sourced from Merck Chemicals. High-purity water and reagent grade ethanol (EtOH) were used for all preparation stages. Briefly, the first stage involves the preparation of a Mn(II)–NHF complex at a  $\frac{1}{2}$  metal/ligand ratio, according to the following reaction:

Pharmaceutics **2021**, 13, 1982 3 of 17

The complexation reaction undergoes at  $35\text{--}40\,^{\circ}\text{C}$ , under stirring for about 24 h in a water/EtOH (60/40% volume ratio) medium. The precipitate is collected, washed twice with water, and further freeze dried. In the second stage, the prepared complex is thermally processed through pyrolysis in the same conditions and process parameters using the previously mentioned experimental setup [38]. The resulted aqueous dispersion of Mn-CDs-NHF was purified and dimensionally selected through centrifugation and further freeze dried to obtain a fine powder which was re-dispersed in a convenient solvent according to the testing requirements.

The mean zeta potential of the samples was evaluated by DelsaNano C Submicron Particle Size Analyzer from Beckman Coulter Inc. Light source: Dual 30 mW laser diodes as 658 nm. For zeta potential, the instrument uses electrophoretic light scattering (ELS) to measure the zeta potential, which determines the electrophoretic movement of charged particles under an applied electric field.

### 2.2. Cell Cultures and Cell Viability Assay

Murine breast cancer 4T1cells (American Type Culture Collection, Rockville, MD, USA, ATCC), a generous gift from James Lorens (Bergen Bio AS, Bergen, Norway), were cultured in RPMI-1640 media supplemented with 10% fetal bovine serum (Sigma-Aldrich®, St. Louis, MO, USA). Normal human mammary epithelial (HMLE) cells (ATCC), a generous gift from James Lorens (Bergen Bio AS, Bergen, Norway), were cultured in DMEM/F12 supplemented with 5% horse serum, 20 ng/mL EGF, 10 ug/mL insulin, 0.5 ng/mL hydrocortisone, 10 ng/mL cholera toxin, and 1% Pen/Strep. Cells were seeded into a 96-well flat-bottom tissue culture plate at a density of 3000 cells/well and allowed to adhere to the plate by incubating at 37 °C under 5% CO2 overnight. Following overnight cell attachment, the cells were incubated with the tested doped CDs-NHF at 5% concentrations (50 μg CDs-NHF/mL) for 72 h. For each doped CDs-NHF, we have tested the amount of compound of that contained 50 μg CDs-NHF/mL.

For cell viability assessment, we used the CellTiter-Blue<sup>®</sup> Cell Viability Assay (Promega). After each of the 72 h treatment time periods,  $50~\mu L$  of cell viability solution was added to each well, and the plate was reincubated for 4 h before luminescence recording using a multiplate microplate reader (FilterMax F5, Sunnyvale, CA, USA).

### 2.3. Mouse Strain and Animal Care

The experiments were approved by Ethical Committee of the "Grigore T. Popa" University of Medicine and Pharmacy of Iasi and were performed in accordance with the European legislation on the protection of animals used for scientific purpose and with authorization from the National Sanitary Veterinary and Food Safety Authority (no. 17/09.04.2020). Female BALB/c mice (6–8 weeks old; Cantacuzino Institute, Bucharest, Romania) were used. The mice were housed in the animal facility of the CEMEX, "Grigore T. Popa" University of Medicine and Pharmacy, Iasi; in individually ventilated cages (IVCs) in a climate-controlled:  $20 \pm 4^\circ$  Celsius,  $50 \pm 5\%$  relative humidity, and 12 h light/dark cycles containing shaving bedding material with regular rodent chow and water ad libitum.

### 2.4. Mammary Fat Pad Spontaneous Metastasis Model

4T1 mouse breast carcinoma cells were suspended in RPMI medium/Matrigel (1:1) (1  $\times$  10<sup>6</sup> in 50  $\mu$ L) and injected into the mammary pad of female BALB/c mice under depth anesthesia, as previously described [15]. At two weeks post tumor cells inoculation, mice had been started to be treated via intraperitoneal injection (twice per week) with 10% (100  $\mu$ g/mL) Mn-CDs-NHF (n = 6) or Gadovist (n = 6) for 3 weeks. CD-NHF concentration is relative to mice blood volume and represents one of the previously tested concentrations [15].

At the end of the testing period, the animals were euthanized (neck dislocation under deep anesthesia), and primary tumors and various organs (liver, kidneys, lungs, spleen) were collected. Half of each primary tumor and half of each lung were immediately

Pharmaceutics **2021**, 13, 1982 4 of 17

suspended in RNA Save (Biological Industries, New Haven, CT, USA) and stored at  $-80\,^{\circ}$ C until use. The other half from each primary tumor and each lung were preserved in 10% paraformaldehyde (Sigma-Aldrich) for further analysis.

### 2.5. In Vitro MRI Investigations

The in vitro experiments were planned to evaluate the potential of the new prepared doped CDs-NHF as MRI contrast agents by determining the values of longitudinal and transversal relaxivities, r1 and r2, respectively, which were calculated from the corresponding T1 and T2 relaxation times. From each compound, a 5 mg/mL stock solution was prepared by dissolving 20 mg of powder in 4 mL of PBS 0.01 M, at physiological pH (7.4). The samples for MRI scanning were prepared by dispersing  $10 \div 60~\mu L$  stock solutions in 10 mL of 1% agarose gel freshly prepared, at about 50 °C to obtain six concentrations for each tested compound, as follows: 0.005, 0.01, 0.015, 0.02, 0.025, and 0.03 mg/mL.

The T1 and T2 measurements were performed using a 1 Tesla instrument for small animals (nanoScan PET-MRI, Mediso LTD), having B0 magnetic field shimming and coil calibration at a water proton frequency. The glass vials comprising the samples to be analyzed were positioned horizontally on the rat body acquisition bed in the center of the coil field of view. T1 relaxation times were determined by a two-point estimation method [39] through a 2D spoiled gradient echo sequence (T1 GRE), while for T2 measurements, we have used a multiecho 2D standard spin echo sequence (T2 SE).

### 2.6. In Vivo MRI Investigations

Two groups of tumor-bearing mice (females), comprising 6 mice per group, were investigated once per week by MRI scanning: one group named "Treated", which has received Mn-CDs-NHF as a teranostic agent via i.p. administration and another group named "Control", receiving only Gadovist, which is a commercial contrast agent. Both Mn-CDs-NHF and Gadovist were administered by i.p. injection 2 h prior to the MRI examination.

Fasted mice (not more than 6 h) were anesthetized using an isoflurane delivery system connected to a transparent chamber at a concentration of 3.5–4% isoflurane in a mixture of air and oxygen. After induction, the mice were transferred to the scanner bed of the nanoScan PET/MRI (Mediso®, Budapest, Hungary), and maintenance anesthesia was adjusted to 2%. The animals were subjected to MRI scanning using T1GRE sequence, coronal, and axial planes. This sequence was selected due to the short investigation time: 22 min for both planes. The parameters were as follows: TR = 13.1; TE = 3.8/2.2; FA =  $30^{\circ}$ ; NSA = 4; slice thickness = 1 mm. The raw imaging data were processed using Carimas software (v. 2.10), which allowed the calculation including the tumor volume, apart from 2D images for each section.

### 2.7. RNA Extraction, cDNA Synthesis, and Quantitative RT-PCR (qRT-PCR) Analysis

For in vitro investigations, total RNA was isolated from the control and treated samples (experimental design) using TRIzol reagent (Thermo Fisher Scientific, Waltham, MA, USA) according to the manufacturer's protocol. Briefly, approximately  $10^7$  cells per sample were mixed with 1 mL of Trizol before RNA was separated from DNA and proteins by adding 200  $\mu$ L chloroform. Then, the total RNA was precipitated using 500  $\mu$ L of isopropanol. The RNA pellet was washed afterwards with 1 mL of 75% ethanol solution and finally eluted in 11.5  $\mu$ L ultrapure sterile water (Biomol, United States Biological).

For in vivo investigations, small fragments ( $\approx 1$  mm/1.5 mm) of tissue were cut/scraped and diced with a sterile scalpel and homogenized prior to the RNA extraction. Briefly, tissue was homogenized in 1 mL of Trizol (Thermo Fisher Scientific) before the RNA was separated from DNA and proteins by adding 200  $\mu$ L chloroform. Then, the total RNA was precipitated using 500  $\mu$ L of isopropanol. The RNA pellet was washed afterwards with 1 mL of 75% ethanol solution and finally eluted in 11.5  $\mu$ L ultrapure sterile water (Biomol, United States Biological).

Pharmaceutics **2021**. 13, 1982 5 of 17

A list of the primers used in this study, as well as the species, gene symbol, gene name, UniGene ID, and primer sequences is in Supplementary Table S1.

### 2.8. Immunofluorescence (IF)

IF was performed on 4  $\mu m$  thick sections of formalin-fixed and paraffin-embedded tissues. Sections were deparaffinized and rehydrated; then, they were stained for detecting mitochondria in the fixed cells (IraZolve-Mito, Rezolve Scientific, Adelaide, Australia) or the apoptotic cells (DeadEnd Fluorometric TUNEL System, Promega) according to the manufacturer's recommendations.

### 2.9. Statistics

GraphPad Prism 6 (San Diego, CA, USA) software was used for statistical analysis. Grouped analyses were performed using one-way ANOVA for cell viability investigations and paired Student's t-test for other statistical analysis. Quantitative data for statistical analysis were expressed as mean  $\pm$  SEM (shown as error bar). Significance was established for p < 0.05.

### 3. Results

### 3.1. Characterization of Mn-CDs-NHF

The structural analysis showed a typical Mn<sup>2+</sup>-doped CDs-NHF (Mn-CDs-NHF) structure, which consists mostly of a carbonaceous core with a surface decorated with different remnant functional groups. The thermal destruction of the Mn(II)-NHF complex through the controlled pyrolytic process resulted in the formation of this graphitic-like core with a variety of functional groups attached on its surface, as previously studied [40,41]. XPS analysis revealed the formation of the carbonaceous core along with the relative concentrations of the various functional groups. Therefore, the recorded wide scan spectrum of Mn-CDs-NHF revealed the overall atomic and mass concentrations as presented in the Supplementary Table S2. As it could be noted, the preponderant carbon presence sustains the formation of the carbonaceous core, while the presence of O, N, and Mn indicates the presence of the various remnant functional groups. The high-resolution spectra recorded for the Mn-CDs-NHF are presented in Supplementary Figure S1a–d together with the relative concentrations of the attached remnant groups.

Mn-CDs-NHF dispersed in water exhibit the same agglomeration tendency as observed in the case of non-doped CDs-NHF presented in our previous work [40], which was most likely as a result of the interactions between the functional groups from the surface that favor clustering. As it could be observed in Supplementary Figure S2, the cluster sizes are mainly located within the 250–400 nm range. These results are sustained by the SEM investigation (Supplementary Figure S3), where it is clearly visible that the Mn-CDs-NHF organize in clusters within the range of 100–300 nm.

The surface charge was determined by measuring the zeta potential of the synthetized CDs. The zeta potential value is determined by the stability of particles. Particles with a high zeta potential (either negative or positive) are electrostatically stable, while the particles with low zeta potentials tend to aggregate within a short period of time. The positive values of the zeta potential reflect the presence of a positively charged environment around the CDs. Having in mind the previously presented facts, the analyzed samples, CDs-NHF and Mn-CDs-NHF, which have positive values of zeta potential, confirm that both un-doped and doped CDs have positively charged surroundings. Moreover, it is obvious that the CDs-NHF sample possesses higher colloidal stability, having a mean zeta potential value of +16.59 mV, whereas the Mn-CDs-NHF sample possesses lower colloidal stability. The mean zeta potential value in this case is +6.87 mV, meaning that this sample tends to aggregate. The zeta potential measurement for each sample was acquired in triplicate, and the obtained values (Supplementary Table S3) are plotted in Supplementary Figure S4 as the mean zeta potential with SD.

Pharmaceutics **2021**, 13, 1982 6 of 17

### 3.2. Cell Viability Assay

Our previous results [15] demonstrated that 5% CDs-NHF (50 µg CDs-NHF/mL) treatment resulted in the decreased migration, invasion, and viability/proliferation of tested cancer cell lines without significantly affecting the tested normal cell line. As a result of doping, it may be possible that the obtained doped CDs-NHF exhibits altered antitumoral properties than the previously tested, non-doped CDs-NHF. Therefore, assessing cell viability is the first step in investigating the theranostics application of doped CDs-NHF (Figure 1).

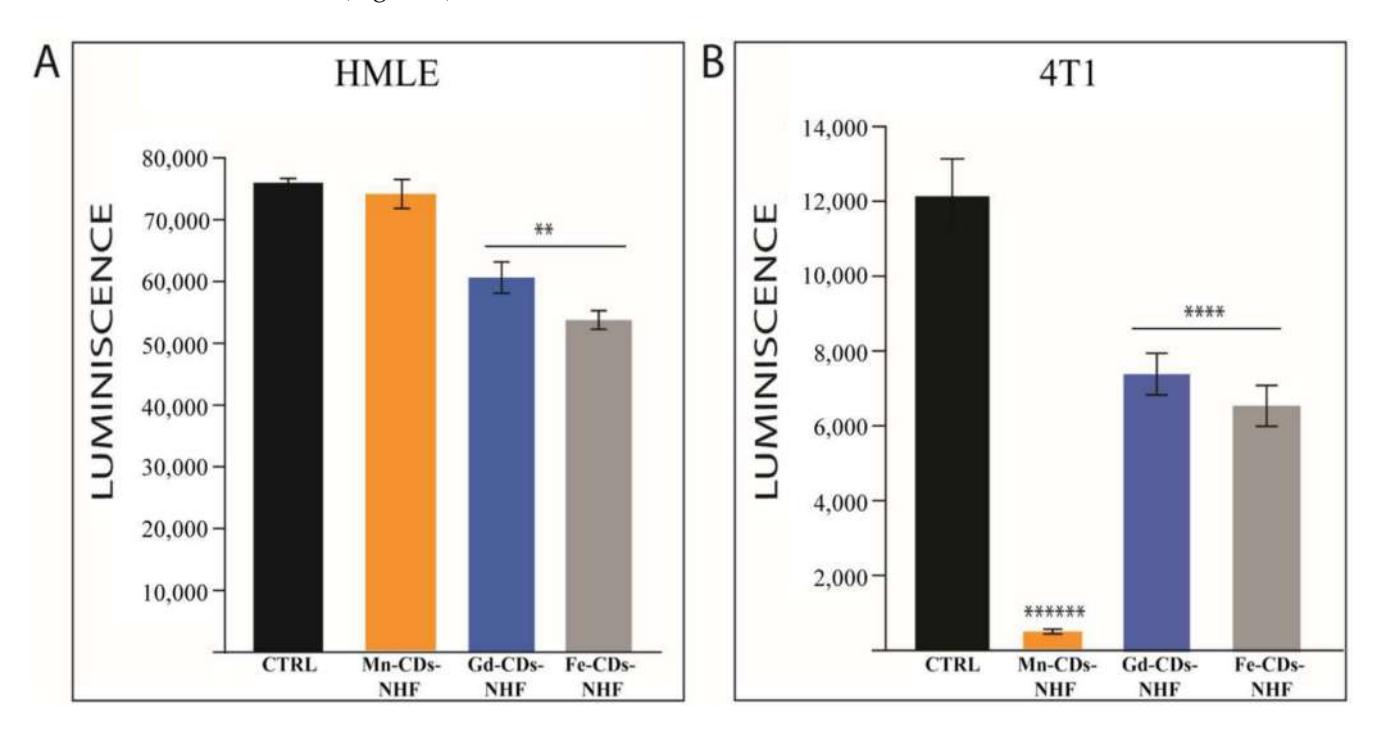


**Figure 1.** Effects of doped CDs-NHF on cell viability. (**A**). Normal cell line HMLE; (**B**). Cancer cell line 4T1. \*\* p < 0.05, \*\*\*\* p < 0.0005, \*\*\*\*\* p < 0.0005.

The cell viability data demonstrate that gadolinium (Gd<sup>3+</sup>)-doped CDs-NHF (Gd-CDs-NHF) and Fe<sup>3+</sup>-doped CDs-NHF (Fe-CDs-NHF) significantly reduced the cell viability in both tested normal (HMLE) (Figure 1A) and cancer (4T1) cell lines (Figure 1B). Mn-CDs-NHF had the strongest effect on cancer cell line when compared to the control (untreated group) and the other two doped CDs-NHF, without significantly impairing the normal cell line viability.

### 3.3. In Vitro MRI Imaging

In order to develop theranostics-doped CDs-NHF, in addition to their anti-tumoral properties, the imaging capabilities must be investigated. In our work, we have tested doped CDs-NHF as contrast agents in MRI (Figure 2).

Pharmaceutics **2021**, 13, 1982 7 of 17

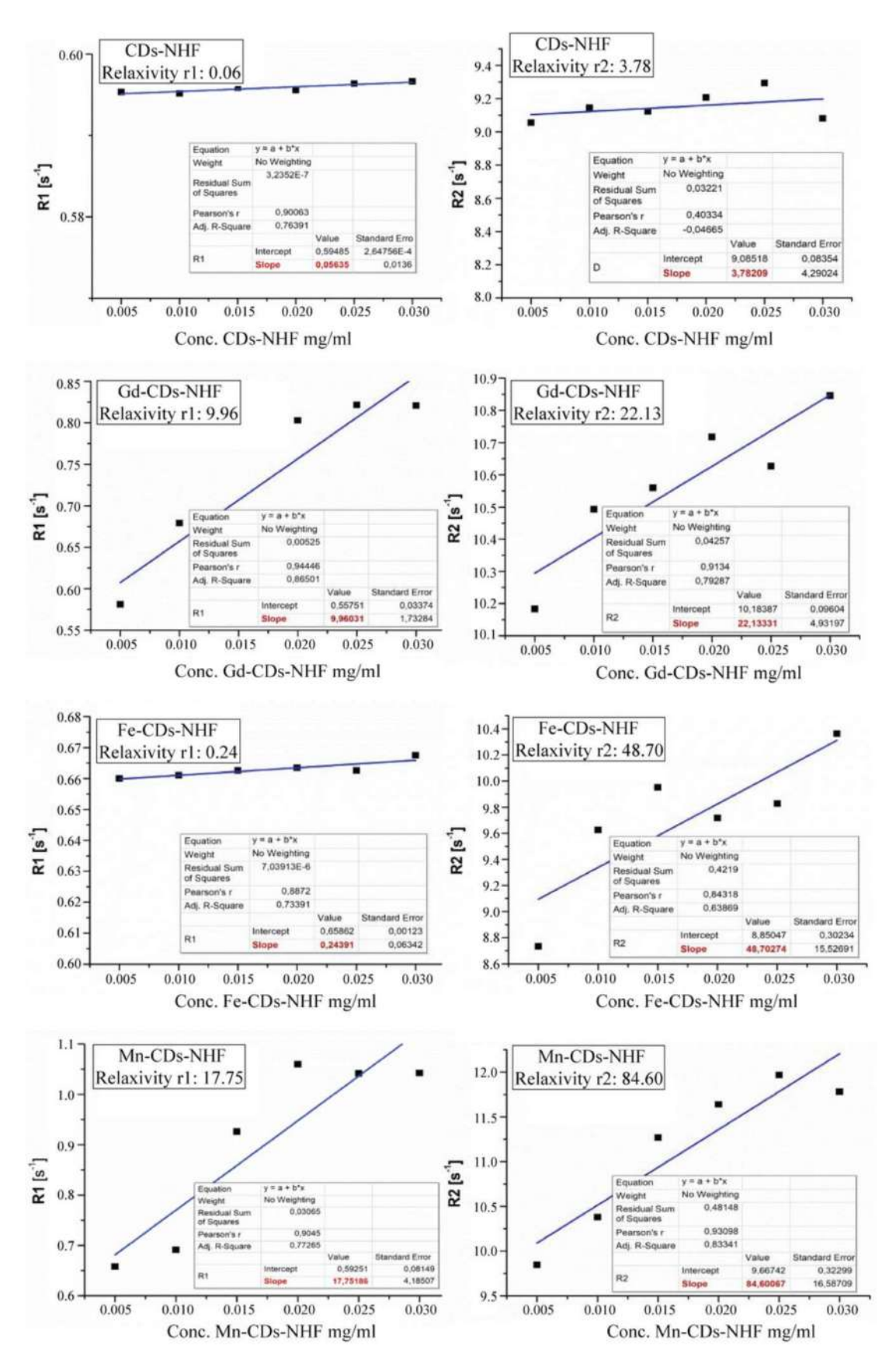


**Figure 2.** The r1 and r2 relaxivities of CD-NHF (negative control), Gd-CD-NHF (positive control), Fe-CD-NHF, and Mn-CDs-NHF.

Pharmaceutics **2021**, 13, 1982 8 of 17

The r1 and r2 relaxivity values represent the slope of the linear regression of T1 and T2 relaxation rates (1/T1 and 1/T2, respectively) in the range of the product concentrations we have considered. The relaxivity values indicate the T1/T2 shortening ability of the tested compounds with a direct impact on the MRI contrast. According to the r1/r2 values obtained, as it can be observed from Figure 2, the Mn-CDs-NHF best meets the feature of an MRI contrast agent. In addition, in the case of Fe-CDs-NHF, the ability of the trivalent ion to provide NMR contrast in T2 sequences is confirmed by a high r2 value of 48.70 mg<sup>-1</sup>·mL·s<sup>-1</sup>, while r1 is insignificant to provide MRI contrast, of only  $0.24 \text{ mg}^{-1} \cdot \text{mL} \cdot \text{s}^{-1}$ . Since gadolinium is the only ion with clinical applicability to enhance the MRI contrast, it was considered in this study as a positive control, which was bound into the Gd-CDs-NHF in a similar manner to the rest of metal included in the prepared compounds. In such an environment, the Gd<sup>3+</sup> ion caused relaxivity values of r1 and r2 of 9.96 and 22.13 mg $^{-1}$ ·mL·s $^{-1}$ , respectively, suggesting a good ability to enhance the MRI contrast, especially in T2 sequences. Quite different is the case of Mn-CDs-NHF product, which although it has a relaxivity r2 significantly higher than all other materials tested, of 88.60 mg<sup>-1</sup>·mL·s<sup>-1</sup>, it also presents a noticeable value for r1, of 17.75 mg<sup>-1</sup>·mL·s<sup>-1</sup>, which is close to the r2 value of Gd-CDs-NHF. In such circumstances, we can infer that the Mn-CDs-NHF product is able to be successfully applied as a contrast agent in both T1 and T2 sequences, depending on what is pursued in that study. The in vitro imaging data using T1 and T2 MRI sequences are presented in Supplementary Figure S5.

Due to the fact that Mn-CDs-NHF exhibited the lowest impact on normal cell viability and the most effective impact on cancer cell viability, doubled by the fact that it can be successfully used as MRI contrast agent, we further investigate the Mn-CDs-NHF theranostics applications.

### 3.4. In Vivo MRI Imaging

Prior to accomplishing the MRI scans on breast cancer animal models, the effect of the selected compound (Mn-CDs-NHF) as a contrast agent on healthy mice was studied by comparing the resulting images with those obtained using Gadovist MRI images (Figure 3). The same conditions and scanning parameters were met as in the groups of tumor-bearing animals.

An MRI signal is much more intense in the case of the group that received the suspension of Mn-CDs-NHF in comparison with the group receiving Gadovist. There is also a very obvious uptake of the Mn<sup>2+</sup>-based compound, which is predominantly in the liver, kidneys, peritoneal cavity, and heart and much less in the brain or other regions located distant from the injection site. The images are displayed in rainbow color visualization to show as suggestive as possible the difference in MRI contrast between different tissues, while the color intensities in all the recorded images were normalized using the same brightness level in all images so that they could be compared.

Representative weekly MRI images of tumor-bearing mice are presented in Figure 4, while the weekly evaluations of each tumor-bearing animal from both groups are presented in Supplementary Figures S6 and S7.

Pharmaceutics **2021**, 13, 1982 9 of 17

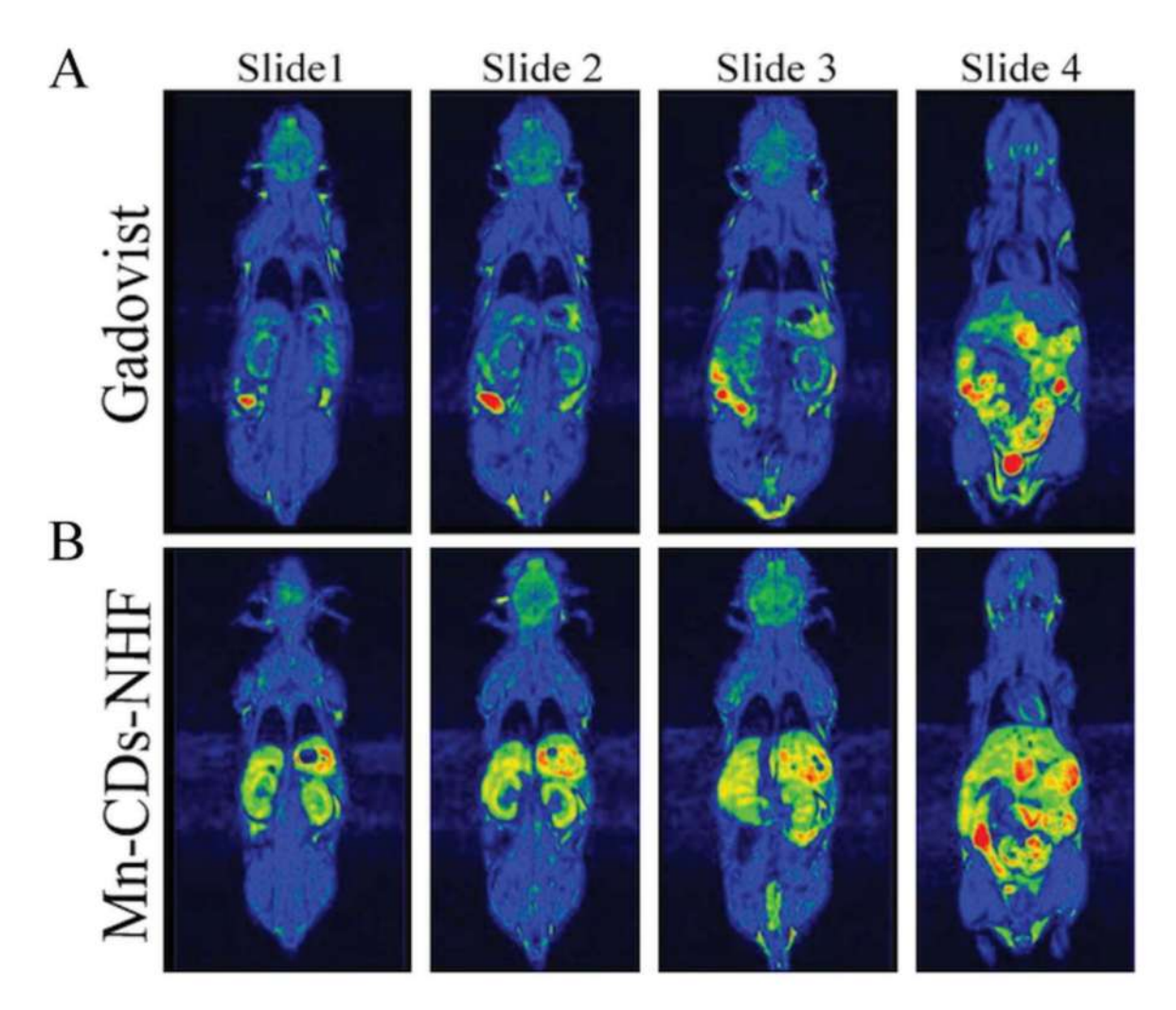


**Figure 3.** MRI comparative images of healthy mice highlighting the ability of the new compound, Mn-CDs-NHF as an MRI contrast agent (**B**) as compared to Gadovist, which is a commercial MRI contrast agent (**A**). Images are obtained using the same sequences, which were performed at 2 h after i.p. administration.

In addition to the improved MRI contrast capabilities of Mn-CDs-NHF relatively to the commercial agent Gadovist, it is also essential to notice that when compared with the control group (Figure 4A\_Gadovist), the volume of the primary tumors is reduced in Mn-CDs-NHF treated group (Figure 4\_Mn-CDs-NHF), as summarized in Figure 4B. These data demonstrate that the proposed teranostic agent, Mn-CDs-NHF, fulfill at the same time the role of increasing the MRI contrast as well the anti-tumor features.

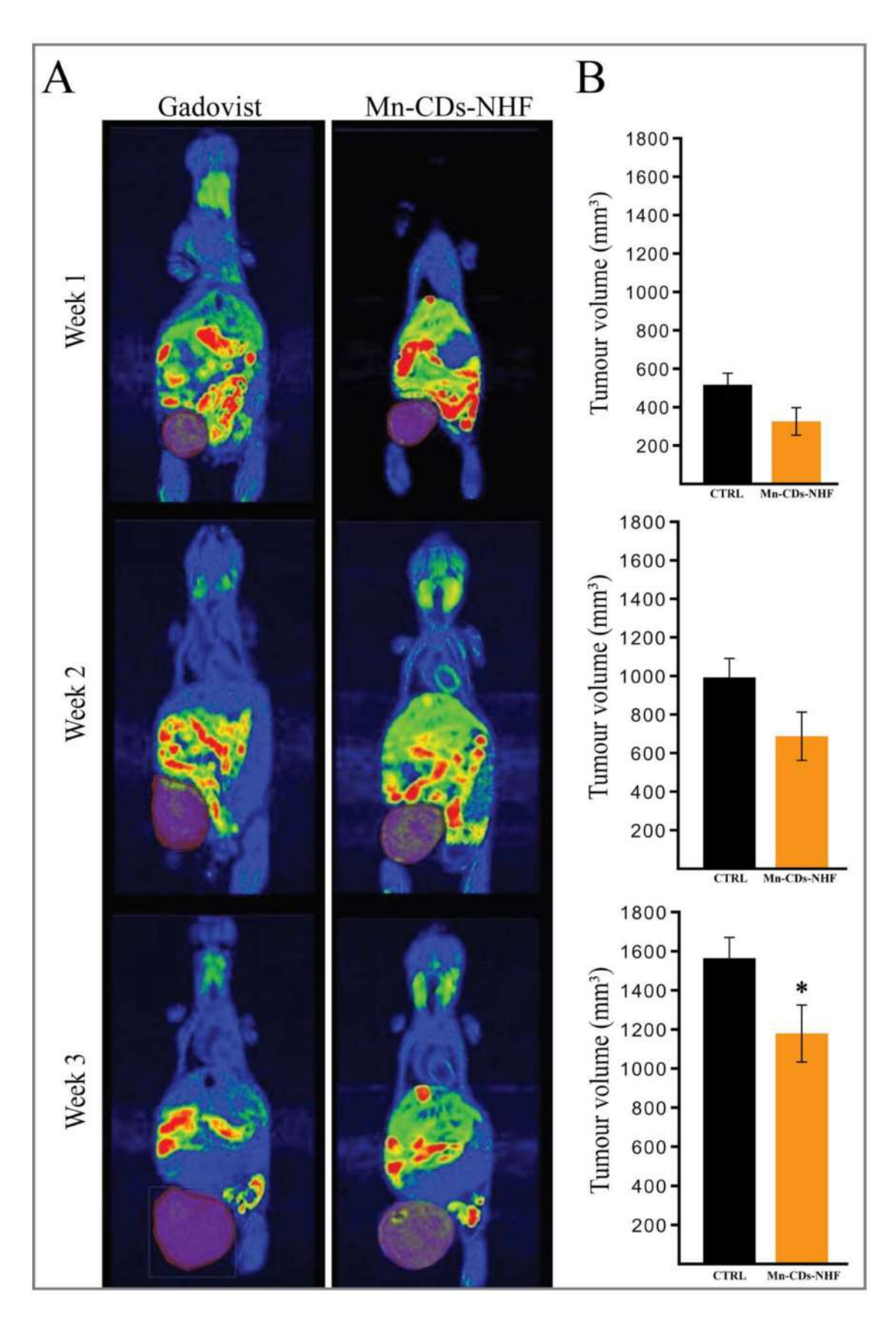


**Figure 4.** Representative MRI images and scorization of primary tumor volume. (**A**). Weekly images of tumor-bearing mice treated with Gadovist or Mn-CDs-NH. (**B**): Scorization of primary tumor volume for each treated group. \* p < 0.05.

### 3.5. Evaluation of Lung Metastases

In clinical practice, the primary tumor is surgically removed, and metastases and local recurrence are usually responsible for the cancer recurrence. As the lung metastases are very common in the case of the 4T1 tumor cells, which could be highlighted by MRI, we also imaged the animals for the presence of lung metastases (Figure 5).

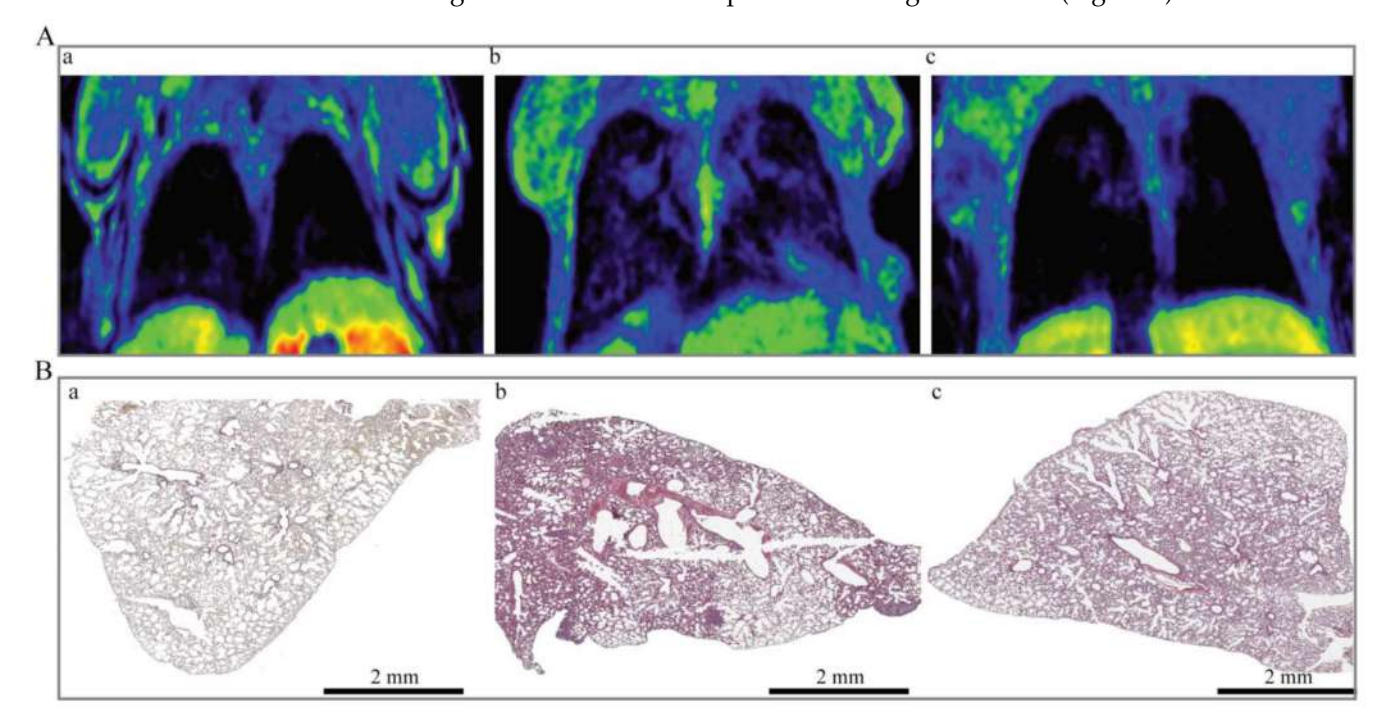


**Figure 5.** Metastatic investigation of lungs. (**A**) MRI images, (**B**) HE staining. (**a**) Healthy mice; (**b**) Tumor-bearing mice treated with Gadovist; (**c**) Tumor-bearing mice treated with Mn-CDs-NHF. Individual pictures acquired at  $10 \times$  were used to rebuild the image of the lung specimens.

MRI imaging of thoracic cavity in the third week shows newly formed tissue, suggesting the presence of lung metastases. According to the MRI data, the prevalence of lung metastases was higher in the control group (Figure 5(Ab)) relatively to the Mn-CDs-NHF-treated group (Figure 5(Ac)). These data correlate with the results of hematoxylin and eosin (HE) staining of lung paraffin-embedded specimens (Figure 5B). The HE data of Mn-CDs-NHF (Figure 5(Bc))-treated group show a reduced number and size of lung metastases relative to the control group (Figure 5(Bb)) and an overall more normal resembling architecture of lung tissue, with less thickened alveolar walls (Figure 5(Ba)).

### 3.6. Mitochondria Evaluation in Paraffin-Embedded Lung Tissue

Our previous in vitro data showed reduced mitochondrial activity upon CDs-NHF treatment [42]. The new data (Figure 6) demonstrate that doping the CDs-NHF with Mn<sup>2+</sup> do not affect the ability of CDs-NHF to reduce the number of mitochondria in cancer cells as assessed in paraffin-embedded lung tissue.

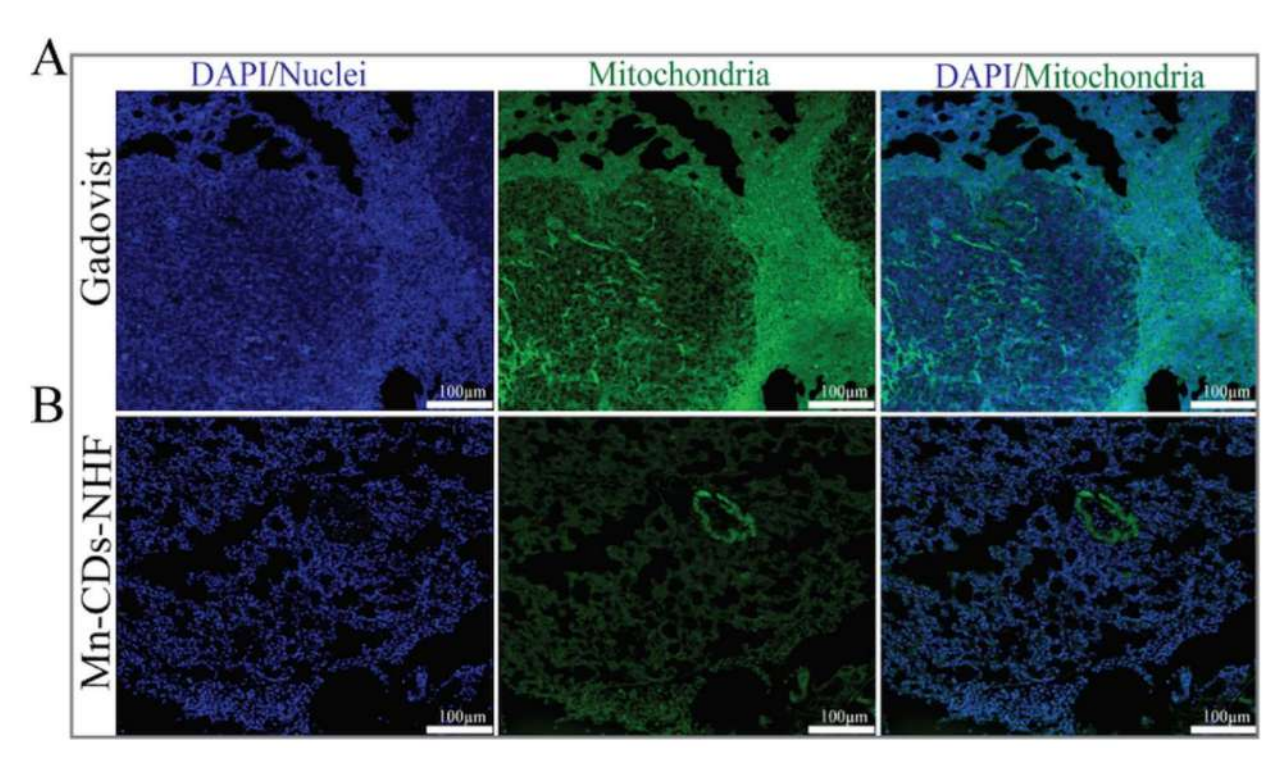


**Figure 6.** Immunofluorescence staining of mitochondria in paraffin-embedded murine lung specimens. Pictures acquired at  $20\times$ .

### 3.7. TUNEL Visualization of Apoptotic Cells in Lung Metastases

The growth of the primary tumor, as well of metastases, is driven by cell proliferation and cell death. In our previous in vivo investigations [15], we have found that Ki67, a marker of cell proliferation, is decreased after CDs-NHF treatment. However, we did not investigate the apoptosis in the mouse tissue. In current work, we deployed TUNEL investigation for showing the apoptotic cells (Figure 7).

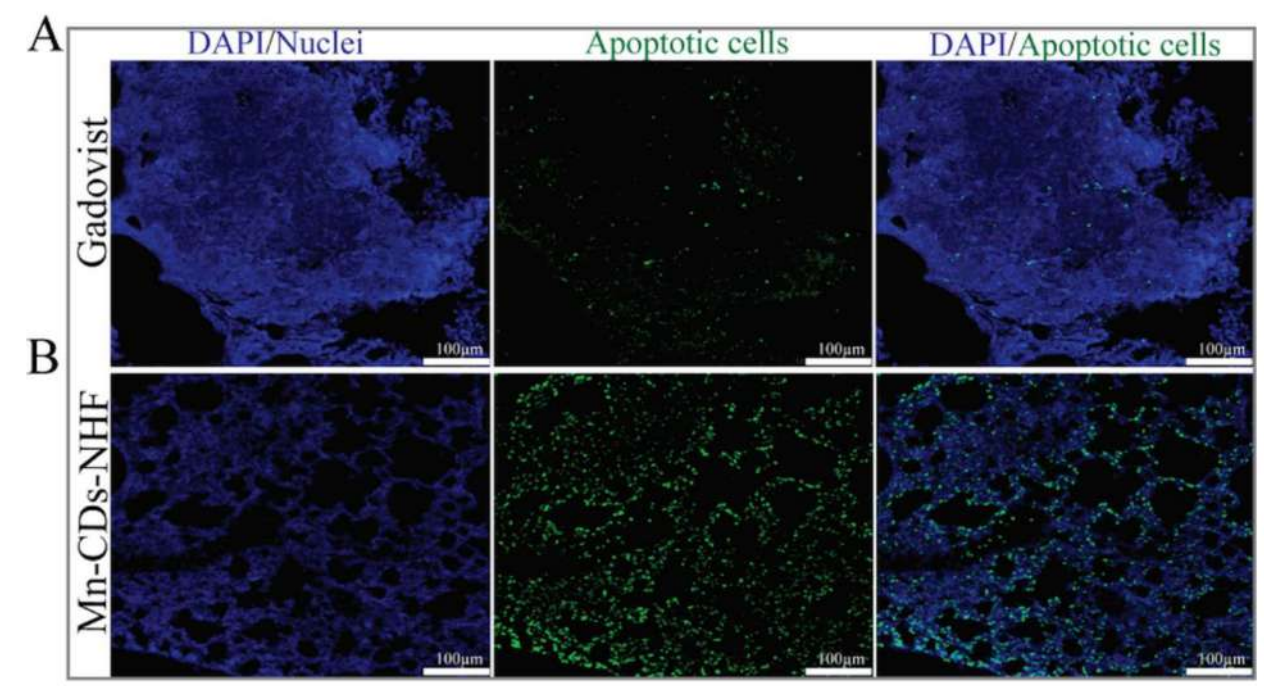


**Figure 7.** Immunofluorescence staining of apoptotic cells in paraffin embedded murine lung specimens. Pictures acquired at  $20\times$ .

Our new data show only a few apoptotic cells in the control group (Figure 7A). The number of apoptotic cells is massively increased in the lung metastases of the Mn-CDs-NHF treated group (Figure 7B). These data sustain the in vitro cell viability data, which demonstrated reduced cell viability in the Mn-CDs-NHF-treated group relative to the Gadovist-treated group.

### 3.8. IL-6 qRT-PCR Investigations

Interleukin 6 (IL-6), a pro-inflammatory cytokine, mediates pro-survival signals in cancer and inflammations. Our in vitro investigation shows that the levels of IL-6 mRNA in cancer cell treated with Mn-CDs-NHF are significantly reduced relative to Gadovist-treated cells (Figure 8A).

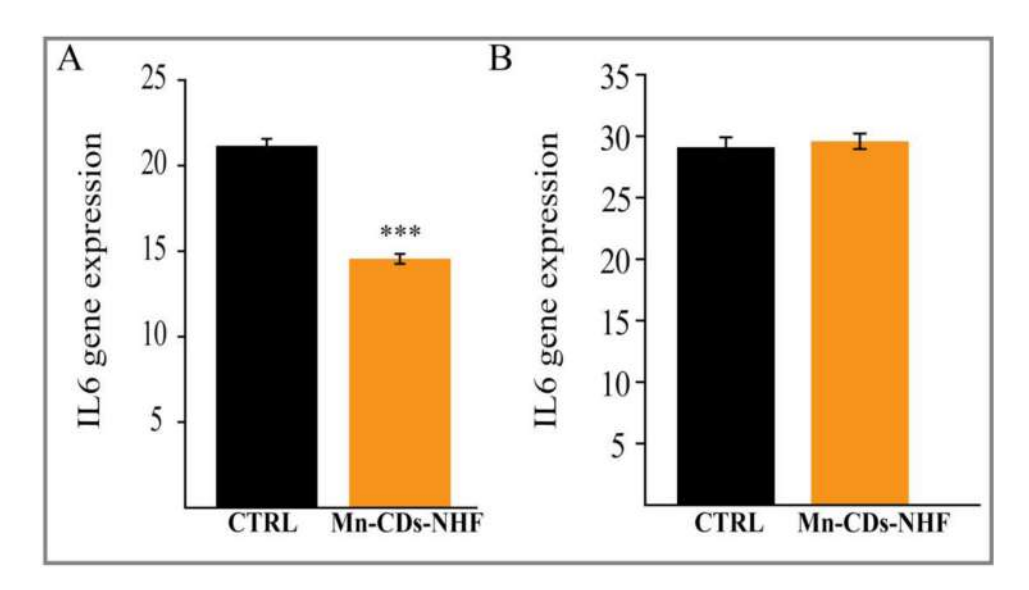


**Figure 8.** IL-6 mRNA expression in cell culture (**A**) and murine lung samples (**B**) \*\*\* p < 0.005.

However, we failed to observe these changes in lung specimens (Figure 8B), which was probably due to the dilution of IL-6 mRNA expressed by cancer cells from metastases with IL-6 mRNA expression from various normal cells.

### 4. Discussion

The increase in the morbidity and mortality of cancer cases put pressure on the scientists to find new tools for diagnostic and treatments. The detection of cancer at early stages can have a massive impact on cancer treatment and patient status. Developing agents with theranostics properties, both therapy and imaging, will improve early cancer detection and overall cancer management. The importance of theranostic agents in the diagnosis and therapy of cancer has been recently reviewed [43–45]. Since the widely used contrast agent, gadolinium, presents various side effects, we aimed to develop theranostic agents by doping CDs-NHF with ions that present lower toxicity. Previously, we have demonstrated the anti-tumoral properties of non-doped CDs-NHF in various models [15,16,42]. In our new experimental investigations, we decide to combine the anti-tumoral properties of CDs-NHF with MRI imaging capabilities of Gd<sup>3+</sup>, Fe<sup>3+</sup>, or Mn<sup>2+</sup>.

In a recent investigation [46], 24 h incubation of Fe(III)-doped Carbon Dots significantly reduces the cell viability of A549 lung cancer cells at concentrations ranging between 12.5 and 200  $\mu$ g/mL. Our results indicate that after 72 h exposure of 50  $\mu$ g/mL Fe-CDs-NHF, in addition to cancer cells, the viability of normal cells is impaired. Moreover, the cellular uptake of Carbon Dots reached its peak at 4 h and decreased after 12 h of incubation [46].

In another recent study [47], Carbon Dots decorated with quaternary ammonium groups were incorporated into the cytosol of mouse NIH/3T3 fibroblast cells from the concentration of  $50 \,\mu\text{g/mL}$  and accumulated in the perinuclear area up to  $200 \,\mu\text{g/mL}$ . The

first sign of Carbon Dots inside the nucleus occurred at 300  $\mu g/mL$ , and all NIH/3T3 cells had filled nuclei and nucleoli after exposure to 400  $\mu g/mL$ . Moreover, the authors reported that tested concentrations (50–400  $\mu g/mL$ ) do not evoke notable DNA damage and do not impair NIH/3T3 cell viability. This was not the situation in the case of L929 mouse fibroblast cells where concentrations of 50–100  $\mu g/mL$  did not cause viability impairment but higher concentrations induce cell dead without to target the nucleus. These data endorse the variety of impact on normal and cancer cells of the 50  $\mu g/mL$  doped CDs-NHF we have tested.

Our in vitro findings showed that Mn-CDs-NHF exert a significant pro-apoptotic effect on cancer cell line without exhibiting a substantial impact on the normal cell line that we have tested. The other two doped CDs-NHF we have tested, Gd-CDs-NHF and Fe-CDs-NHF, significantly decreased the cell viability of the normal cell line. Moreover, the impact of Gd-CDs-NHF and Fe-CDs-NHF on cancer cell viability was lower relative to Mn-CDs-NHF, which indicates that doping CDs-NHF with Gd<sup>3+</sup> or Fe<sup>3+</sup> may reduce the anti-tumoral properties of CDs-NHF. The effect of Gd-CDs-NHF and Fe-CDs-NHF on both cell lines indicates that these two doped CDs-NHF exert a certain degree of toxicity. In addition to the in vitro data, the number of apoptotic cells is increased in the lung metastases in the Mn-CDs-NHF-treated group when compared with the classical MRI contrast agent, Gadovist. Even more, the decreased expression of the mitochondria staining in the Mn-CDs-NHF-treated group further sustains the anti-tumoral properties of Mn<sup>2+</sup>-doped CDs-NHF.

As we demonstrated that doping CDs-NHF with Mn<sup>2+</sup> preserves the anti-tumoral properties of CDs-NHF, we have investigated next the MRI imaging application, which is the second characteristic of a theranostics agent. Both the in vitro cell line investigations and in vivo data from healthy mice demonstrate that the MRI signals of Mn<sup>2+</sup> from Mn-CDs-NHF fulfill the second condition required for Mn-CDs-NHF to be used as a theranostics agent in experimental models. In tumor-bearing animal investigations, the lung metastases from the control group are well developed, and MRI imaging of the Mn-CDs-NHF group demonstrates that treatment with Mn<sup>2+</sup>-doped CDs-NHF reduces the primary tumor volume. These data are in line with our newly reported in vitro pro-apoptotic effect of Mn<sup>2+</sup>-doped CDs-NHF and with our previous reported data that showed that non-doped CDs-NHF treatment reduces the Ki67cell proliferation marker at the level of lung metastases [15]. The reduction of tumor volume requires time, becoming significant after three weeks of treatment administration and is a consequence of both the impairment of cell proliferation and the pro-apoptotic effect of Mn-CDs-NHF.

The MRI signal intensity of the liver, kidney and lung is enhanced in the Mn-CDs-NHF treated group relatively to healthy untreated mice, while the signal intensity of the brain and heart are at similar levels (Supplementary Figure S8). In week two, the MRI signal is relatively homogenously distributed in the entire primary tumors. In the third week, the MRI signal appears to be unevenly distributed; some areas have higher intensity, while other have lower intensity. The MRI signal distribution in the third week suggests the presence of larger necrotic areas in the primary tumors. MRI signal intensity is not different between the tumor core and tumor periphery in week two, but it becomes significant in week three (Supplementary Figure S9).

Altogether, our experimental findings demonstrate the theranostics properties of Mn-CDs-NHF. In comparison to Gd<sup>3+</sup>-based compounds (Gd-CDs-NHF and Gadovist), Mn-CDs-NHF exhibited lower toxic effects on normal cells, anti-tumoral properties, and a stronger MRI signal.

Supplementary Materials: The following are available online at https://www.mdpi.com/article/10.3390/pharmaceutics13111982/s1, Table S1: List of the primers used in this study, species, gene symbol, gene name, NCBI accession number, mRNA reference sequence and primer sequences, Table S2: Overall atomic and mass concentrations recorded for the Mn-CDs-NHF, Table S3: Zeta potential results for CDs-NHF and Mn-CDs-NHF, Figure S1: High-resolution XPS spectra recorded for the Mn-CDs-NHF, Figure S2: Size distribution of the prepared Mn-CDs-NHF, Figure S3: SEM

Pharmaceutics **2021**, 13, 1982 15 of 17

image recorded for the prepared Mn-CDs-NHF, Figure S4. Graphical representation of mean zeta potential with SD for CDs-NHF and Mn-CDs-NHF, Figure S5: The imaging data obtained by in vitro MRI scanning, Figure S6: Weekly evaluations by MRI of each tumor-bearing animal treated with Gadovist, Figure S7: Weekly evaluations by MRI of each tumor-bearing animal treated with Mn-CDs-NHF, Figure S8: In vivo tissue distribution of Mn-CDs-NHF, Figure S9: Quantification of MRI signal intensity in primary tumors.

**Author Contributions:** Conceptualization, C.E.T. and C.S.S.; methodology, A.T., C.M.U., C.S.S. and C.E.T.; investigation, A.T., G.L., C.M.U., A.C., C.S.S. and C.E.T.; data curation, A.T.; writing—original draft preparation, A.T., C.M.U., I.-C.V.-T., C.S.S. and C.E.T.; writing—review and editing, A.T., C.M.U., A.C. and C.E.T.; visualization, C.M.U., A.C. and C.E.T.; supervision, G.D.S. and C.E.T.; project administration, C.E.T.; funding acquisition, C.E.T. All authors have read and agreed to the published version of the manuscript.

**Funding:** This work was supported by a grant within the frame of the Complex Projects Partnership Program–PCCDI, under authority of the Romanian National Authority for Scientific Research-UEFISCDI, project code PN-III-P1-1.2-PCCDI-2017-0083 (37PCCDI/2018).

**Institutional Review Board Statement:** The experiments were approved by Ethical Committee of the "Grigore T. Popa" University of Medicine and Pharmacy of Iasi and were performed in accordance with the European legislation on the protection of animals used for scientific purpose and with authorization from National Sanitary Veterinary and Food Safety Authority (no. 17/09.04.2020).

**Informed Consent Statement:** Not applicable.

**Data Availability Statement:** The data presented in this study will be openly available upon publication.

**Acknowledgments:** The authors would like to express their gratitude to Bogdan Florin Craciun for taking the time to conduct the zeta potential measurements and for providing insightful comments on the results.

Conflicts of Interest: The authors declare no conflict of interest. The funders had no role in the design of the study; in the collection, analyses, or interpretation of data; in the writing of the manuscript, or in the decision to publish the results.

### References

- Siegel, R.L.; Miller, K.D.; Jemal, A. Cancer statistics, 2020. CA Cancer J. Clin. 2020, 70, 7–30. [CrossRef]
- 2. Van Der Meel, R.; Sulheim, E.; Shi, Y.; Kiessling, F.; Mulder, W.J.M.; Lammers, T. Smart cancer nanomedicine. *Nat. Nanotechnol.* **2019**, *14*, 1007–1017. [CrossRef] [PubMed]
- Zhang, M.; Sheng, B.; Ashley, J.; Zheng, T.; Wang, W.; Zhang, Q.; Zhang, J.; Zhou, N.; Shen, J.; Sun, Y. Manganese ion chelated FeOCl@PB@PDA@BPQDs nanocomposites as a tumor microenvironment-mediated nanoplatform for enhanced tumor imaging and therapy. Sens. Actuators B Chem. 2020, 307, 127491. [CrossRef]
- 4. Bertrand, N.; Wu, J.; Xu, X.; Kamaly, N.; Farokhzad, O.C. Cancer nanotechnology: The impact of passive and active targeting in the era of modern cancer biology. *Adv. Drug Deliv. Rev.* **2014**, *66*, 2–25. [CrossRef]
- 5. Dong, W.; Luo, Y.; Zhang, G.; Zhang, H.; Liang, Y.; Zhuo, Y.; Liang, Y.; Zou, F.; Zhong, W. Carbon Nanospheres Exert Antitumor Effects Associated with Downregulation of 4E-BP1 Expression on Prostate Cancer. *Int. J. Nanomed.* **2020**, *15*, 5545–5559.
- 6. Li, X.; Wu, M.; Pan, L.; Shi, J. Tumor vascular-targeted co-delivery of anti-angiogenesis and chemotherapeutic agents by mesoporous silica nanoparticle-based drug delivery system for synergetic therapy of tumor. *Int. J. Nanomed.* **2015**, *11*, 93–105. [CrossRef] [PubMed]
- Kesharwani, P.; Iyer, A.K. Recent advances in dendrimer-based nanovectors for tumor-targeted drug and gene delivery. *Drug Discov. Today* 2015, 20, 536–547. [CrossRef]
- 8. Teradal, N.L.; Jelinek, R. Carbon Nanomaterials in Biological Studies and Biomedicine. Adv. Health Mater. 2017, 6. [CrossRef]
- 9. Alagarsamy, K.N.; Mathan, S.; Yan, W.; Rafieerad, A.; Sekaran, S.; Manego, H.; Dhingra, S. Carbon nanomaterials for cardiovascular theranostics: Promises and challenges. *Bioact. Mater.* **2021**, *6*, 2261–2280. [CrossRef] [PubMed]
- 10. Sun, S.; Zhang, L.; Jiang, K.; Wu, A.; Lin, H. Toward High-Efficient Red Emissive Carbon Dots: Facile Preparation, Unique Properties, and Applications as Multifunctional Theranostic Agents. *Chem. Mater.* **2016**, *28*, 8659–8668. [CrossRef]
- 11. Hua, X.-W.; Bao, Y.-W.; Wu, F.-G. Fluorescent Carbon Quantum Dots with Intrinsic Nucleolus-Targeting Capability for Nucleolus Imaging and Enhanced Cytosolic and Nuclear Drug Delivery. *ACS Appl. Mater. Interfaces* **2018**, *10*, 10664–10677. [CrossRef] [PubMed]

12. Le Broc-Ryckewaert, D.; Carpentier, R.; Lipka, E.; Daher, S.; Vaccher, C.; Betbeder, D.; Furman, C. Development of innovative paclitaxel-loaded small PLGA nanoparticles: Study of their antiproliferative activity and their molecular interactions on prostatic cancer cells. *Int. J. Pharm.* 2013, 454, 712–719. [CrossRef] [PubMed]

- 13. Bao, S.; Zheng, H.; Ye, J.; Huang, H.; Zhou, B.; Yao, Q.; Lin, G.; Zhang, H.; Kou, L.; Chen, R. Dual Targeting EGFR and STAT3 With Erlotinib and Alantolactone Co-Loaded PLGA Nanoparticles for Pancreatic Cancer Treatment. *Front. Pharmacol.* **2021**, 12. [CrossRef] [PubMed]
- 14. Li, J.; Yang, S.; Deng, Y.; Chai, P.; Yang, Y.; He, X.; Xie, X.; Kang, Z.; Ding, G.; Zhou, H.; et al. Emancipating Target-Functionalized Carbon Dots from Autophagy Vesicles for a Novel Visualized Tumor Therapy. *Adv. Funct. Mater.* **2018**, 28. [CrossRef]
- 15. Tiron, C.E.; Luta, G.; Butura, M.; Zugun-Eloae, F.; Stan, C.S.; Coroaba, A.; Ursu, E.-L.; Stanciu, G.D.; Tiron, A. NHF-derived carbon dots: Prevalidation approach in breast cancer treatment. *Sci. Rep.* **2020**, *10*, 12662. [CrossRef]
- Luta, G.; Butura, M.; Tiron, A.; Tiron, C. Enhancing Anti-Tumoral Potential of CD-NHF by Modulating PI3K/Akt Axis in U87 Ex Vivo Glioma Model. *Int. J. Mol. Sci.* 2021, 22, 3873. [CrossRef] [PubMed]
- Hoult, D.I.; Bahkar, B. NMR Signal Reception: Virtual Photons and Coherent Spontaneous Emission. Concepts Magn. Reson. 1998, 9, 277–297. [CrossRef]
- 18. Idée, J.M.; Fretellier, N.; Robic, C.; Corot, C. Involvement of Gadolinium Chelates in the Mechanism of Nephrogenic Systemic Fibrosis: An Update. *Radiol. Clin. N. Am.* **2009**, 47, 855–869. [CrossRef] [PubMed]
- 19. Abujudeh, H.H.; Kosaraju, V.K.; Kaewlai, R. Acute Adverse Reactions to Gadopentetate Dimeglumine and Gadobenate Dimeglumine: Experience With 32,659 Injections. *Am. J. Roentgenol.* **2010**, 194, 430–434. [CrossRef]
- 20. Yu, X.; Wadghiri, Y.Z.; Sanes, D.H.; Turnbull, D.H. In vivo auditory brain mapping in mice with Mn-enhanced MRI. *Nat. Neurosci.* **2005**, *8*, 961–968. [CrossRef]
- 21. Bin Na, H.; Lee, J.H.; An, K.; Park, Y.I.; Park, M.; Lee, I.S.; Nam, D.-H.; Kim, S.T.; Kim, S.-H.; Kim, S.-W.; et al. Development of aT1 Contrast Agent for Magnetic Resonance Imaging Using MnO Nanoparticles. *Angew. Chem. Int. Ed.* **2007**, *46*, 5397–5401.
- 22. Shin, J.; Anisur, R.M.; Ko, M.K.; Im, G.H.; Lee, J.H.; Lee, I.S. Hollow Manganese Oxide Nanoparticles as Multifunctional Agents for Magnetic Resonance Imaging and Drug Delivery. *Angew. Chem. Int. Ed.* **2009**, *48*, 321–324. [CrossRef]
- 23. Kim, T.; Momin, E.; Choi, J.; Yuan, K.; Zaidi, H.; Kim, J.; Park, M.; Lee, N.; McMahon, M.T.; Quinones-Hinojosa, A.; et al. Mesoporous Silica-Coated Hollow Manganese Oxide Nanoparticles as Positive T1 Contrast Agents for Labeling and MRI Tracking of Adipose-Derived Mesenchymal Stem Cells. *J. Am. Chem. Soc.* 2011, 133, 2955–2961. [CrossRef] [PubMed]
- 24. Wong, R.S.Y. Apoptosis in cancer: From pathogenesis to treatment. J. Exp. Clin. Cancer Res. 2011, 30, 87. [CrossRef] [PubMed]
- 25. Kaczanowski, S. Apoptosis: Its origin, history, maintenance and the medical implications for cancer and aging. *Phys. Biol.* **2016**, 13, 031001. [CrossRef]
- 26. Sansone, P.; Storci, G.; Tavolari, S.; Guarnieri, T.; Giovannini, C.; Taffurelli, M.; Ceccarelli, C.; Santini, D.; Paterini, P.; Marcu, K.B.; et al. IL-6 triggers malignant features in mammospheres from human ductal breast carcinoma and normal mammary gland. *J. Clin. Investig.* 2007, 117, 3988–4002. [CrossRef] [PubMed]
- 27. Becker, C.; Fantini, M.C.; Schramm, C.; Lehr, H.A.; Wirtz, S.; Nikolaev, A.; Burg, J.; Strand, S.; Kiesslich, R.; Huber, S.; et al. TGF-β Suppresses Tumor Progression in Colon Cancer by Inhibition of IL-6 trans-Signaling. *Immunity* **2004**, *21*, 491–501. [CrossRef] [PubMed]
- 28. Lesina, M.; Kurkowski, M.U.; Ludes, K.; Rose-John, S.; Treiber, M.; Klöppel, G.; Yoshimura, A.; Reindl, W.; Sipos, B.; Akira, S.; et al. Stat3/Socs3 Activation by IL-6 Transsignaling Promotes Progression of Pancreatic Intraepithelial Neoplasia and Development of Pancreatic Cancer. *Cancer Cell* 2011, 19, 456–469. [CrossRef]
- 29. Lederle, W.; Depner, S.; Schnur, S.; Obermueller, E.; Catone, N.; Just, A.; Fusenig, N.E.; Mueller, M.M. IL-6 promotes malignant growth of skin SCCs by regulating a network of autocrine and paracrine cytokines. *Int. J. Cancer* **2011**, *128*, 2803–2814. [CrossRef] [PubMed]
- 30. Siersbæk, R.; Scabia, V.; Nagarajan, S.; Chernukhin, I.; Papachristou, E.K.; Broome, R.; Johnston, S.J.; Joosten, S.E.; Green, A.R.; Kumar, S.; et al. IL6/STAT3 Signaling Hijacks Estrogen Receptor α Enhancers to Drive Breast Cancer Metastasis. *Cancer Cell* **2020**, 38, 412–423. [CrossRef] [PubMed]
- 31. Dethlefsen, C.; Højfeldt, G.; Hojman, P. The role of intratumoral and systemic IL-6 in breast cancer. *Breast Cancer Res. Treat.* **2013**, 138, 657–664. [CrossRef] [PubMed]
- 32. Chung, Y.-C.; Chang, Y.-F. Serum interleukin-6 levels reflect the disease status of colorectal cancer. *J. Surg. Oncol.* **2003**, *83*, 222–226. [CrossRef] [PubMed]
- 33. Sanguinete, M.M.M.; De Oliveira, P.H.; Martins-Filho, A.; Micheli, D.C.; Tavares-Murta, B.M.; Murta, E.F.C.; Nomelini, R.S. Serum IL-6 and IL-8 Correlate with Prognostic Factors in Ovarian Cancer. *Immunol. Investig.* **2017**, *46*, 677–688. [CrossRef]
- 34. Altundag, O.; Altundag, K.; Gunduz, E. Interleukin-6 and C-Reactive Protein in Metastatic Renal Cell Carcinoma. *J. Clin. Oncol.* **2005**, 23, 1044. [CrossRef] [PubMed]
- 35. Chang, C.H.; Hsiao, C.F.; Yeh, Y.M.; Chang, G.C.; Tsai, Y.H.; Chen, Y.M.; Huang, M.S.; Chen, H.L.; Li, Y.J.; Yang, P.C.; et al. Circulating interleukin-6 level is a prognostic marker for survival in advanced nonsmall cell lung cancer patients treated with chemotherapy. *Int. J. Cancer* **2013**, *132*, 1977–1985. [CrossRef]
- 36. Jinno, T.; Kawano, S.; Maruse, Y.; Matsubara, R.; Goto, Y.; Sakamoto, T.; Hashiguchi, Y.; Kaneko, N.; Tanaka, H.; Kitamura, R.; et al. Increased expression of interleukin-6 predicts poor response to chemoradiotherapy and unfavorable prognosis in oral squamous cell carcinoma. *Oncol. Rep.* **2015**, *33*, 2161–2168. [CrossRef] [PubMed]

Pharmaceutics **2021**, 13, 1982 17 of 17

37. Kumari, N.; Dwarakanath, B.S.; Das, A.; Bhatt, A.N. Role of interleukin-6 in cancer progression and therapeutic resistance. *Tumor Biol.* **2016**, *37*, 11553–11572. [CrossRef] [PubMed]

- 38. Stan, C.S.; Coroaba, A.; Ursu, E.L.; Secula, M.S.; Simionescu, B.C. Fe(III) doped carbon nanodots with intense green photoluminescence and dispersion medium dependent emission. *Sci. Rep.* **2019**, *9*, 18893. [CrossRef] [PubMed]
- 39. Homer, J.; Beevers, M.S. Driven-equilibrium single-pulse observation of T1 relaxation. A reevaluation of a rapid "new" method for determining NMR spin-lattice relaxation times. *J. Magn. Reason.* **1985**, *63*, 287–297. [CrossRef]
- 40. Stan, C.S.; Horlescu, P.G.; Ursu, L.E.; Popa, M.; Albu, C. Facile preparation of highly luminescent composites by polymer embedding of carbon dots derived from N-hydroxyphthalimide. *J. Mater. Sci.* **2017**, *52*, 185–196. [CrossRef]
- 41. Stan, C.S.; Albu, C.; Coroaba, A.; Popa, M.; Sutiman, D. One step synthesis of fluorescent carbon dots through pyrolysis of N-hydroxysuccinimide. *J. Mater. Chem. C* **2015**, *3*, 789–795. [CrossRef]
- 42. Savin, C.-L.; Tiron, C.; Carasevici, E.; Stan, C.S.; Ibanescu, S.A.; Simionescu, B.C.; Peptu, C.A. Entrapment of N-Hydroxyphthalimide Carbon Dots in Different Topical Gel Formulations: New Composites with Anticancer Activity. *Pharmaceutics* **2019**, *11*, 303. [CrossRef] [PubMed]
- 43. Liu, P.; Shi, X.; Zhong, S.; Peng, Y.; Qi, Y.; Ding, J.; Zhou, W. Metal-phenolic networks for cancer theranostics. *Biomater. Sci.* **2021**, 9, 2825–2849. [CrossRef] [PubMed]
- 44. Jeyamogan, S.; Khan, N.A.; Siddiqui, R. Application and Importance of Theranostics in the Diagnosis and Treatment of Cancer. *Arch. Med. Res.* **2021**, 52, 131–142. [CrossRef] [PubMed]
- 45. Robertson, A.G.; Rendina, L.M. Gadolinium theranostics for the diagnosis and treatment of cancer. *Chem. Soc. Rev.* **2021**, *50*, 4231–4244. [CrossRef]
- 46. Li, J.; Hu, Z.-E.; We, Y.-J.; Liu, Y.-H.; Wang, N.; Yu, X.-Q. Multifunctional carbon quantum dots as a theranostic nanomedicine for fluorescence imaging-guided glutathione depletion to improve chemodynamic therapy. *J. Colloid Interface Sci.* **2021**, 606, 1219–1228. [CrossRef] [PubMed]
- 47. Havrdová, M.; Urbančič, I.; Tománková, K.B.; Malina, L.; Štrancar, J.; Bourlinos, A. Self-Targeting of Carbon Dots into the Cell Nucleus: Diverse Mechanisms of Toxicity in NIH/3T3 and L929 Cells. *Int. J. Mol. Sci.* **2021**, 22, 5608. [CrossRef]



### **OPEN**

# Fe(III) doped carbon nanodots with intense green photoluminescence and dispersion medium dependent emission

Corneliu Sergiu Stan<sup>1\*</sup>, Adina Coroabă<sup>2</sup>, Elena Laura Ursu<sup>2</sup>, Marius Sebastian Secula<sup>1</sup> & Bogdan C. Simionescu<sup>1,2</sup>

The preparation and investigation of Fe(III) doped carbon nanodots (CNDs) with intense green photoluminescence and emission dependence on the dispersion medium are reported. Their unusual photoluminescence is especially highlighted in water where the initial blue emission is gradually shifted to intense deep green, while in other common solvents (chloroform, acetone etc.) this behavior has not been observed. Through embedding in a polymer matrix (e.g., PVA) the color transition becomes reversible and dependent on water content, ranging from a full blue emission, when completely dried, to an intense green emission, when wetted. The preparation path of the Fe(III) doped CNDs undergoes two main stages involving the initial obtaining of Fe(III)–N–Hydroxyphthalimide complex and then a thermal processing through controlled pyrolysis. Morphostructural investigations of the prepared Fe(III) doped CNDs were performed through TG, FT-IR, XPS, DLS, TEM and AFM techniques whereas absolute PLQY, steady state and lifetime fluorescence were used to highlight their luminescence properties. The results issued from structural and fluorescence investigations bring new insights on the particular mechanisms involved in CNDs photoluminescence, a topic still open to debate.

CNDs are a new class of nanostructured materials which gathered an increasing attention during the last decade due to their particular features such as excitation dependent photoluminescence, resistance to photobleaching, biocompatibility and lack of toxicity, facile surface functionalization or dispersibility in various solvents etc<sup>1,2</sup>. By definition, the CNDs structure consists of a carbonaceous core with a defect rich graphitic configuration which is surface decorated with various functional groups3. Although many studies focused on their implementation in different application areas including sensors<sup>4</sup>, bioimaging<sup>5</sup>, drug delivery<sup>6</sup>, catalysis<sup>7</sup>, optoelectronics<sup>8</sup>, controversies on their structural configuration or photoluminescence mechanisms still exist<sup>9,10</sup>. Their excitation dependent photoluminescence is a particular feature, which triggered much debate as concerns the mechanisms involved in the radiative processes. A first approach is based on a behavior similar to that of semiconductor Quantum Dots, where the emission peaks are size dependent and rely on quantum confinement<sup>11</sup> while the second one highlights the radiative transitions occurring within or between the surface attached functional groups, with the graphitic core defects playing a key role over the entire process<sup>12</sup>. The latter approach seems to gain more evidence as very recent studies revealed the importance of carbonyl or nitrogen containing groups and also the influence of the dispersion medium on the emission characteristics of the CNDs<sup>13,14</sup>. In most cases, the photoluminescence (PL) emission is located in the blue region of the visible spectrum irrespective of the starting precursors. However, an increasing number of papers reported green, yellow or even red emission 15-17. Usually, the emission located in the inferior regions of the visible spectrum is achieved through surface modifications yet, with few exceptions 18,19, for the price of a lower intensity. CNDs preparation methods could be roughly divided into two main categories: top-down approaches, where bulk carbon materials like graphite, graphite oxide or carbon soot are processed through combustion, arc discharge, laser ablation or electrochemical routes<sup>20</sup> and bottom-up approaches, where various organic compounds are used as precursors in pyrolytic, hydrothermal and microwave/ultrasonic assisted processes<sup>21</sup>. The doping of CNDs<sup>22</sup> with various elements including nitrogen<sup>23</sup>, phosphorus<sup>24</sup>, sulfur<sup>25</sup>,

<sup>1</sup>Gheorghe Asachi Technical University of Iasi, Faculty of Chemical Engineering and Environmental Protection, Iasi, 700050, Romania. <sup>2</sup>Petru Poni Institute of Macromolecular Chemistry, Department of Chemistry, Iasi, 700487, Romania. \*email: stancs@tuiasi.ro

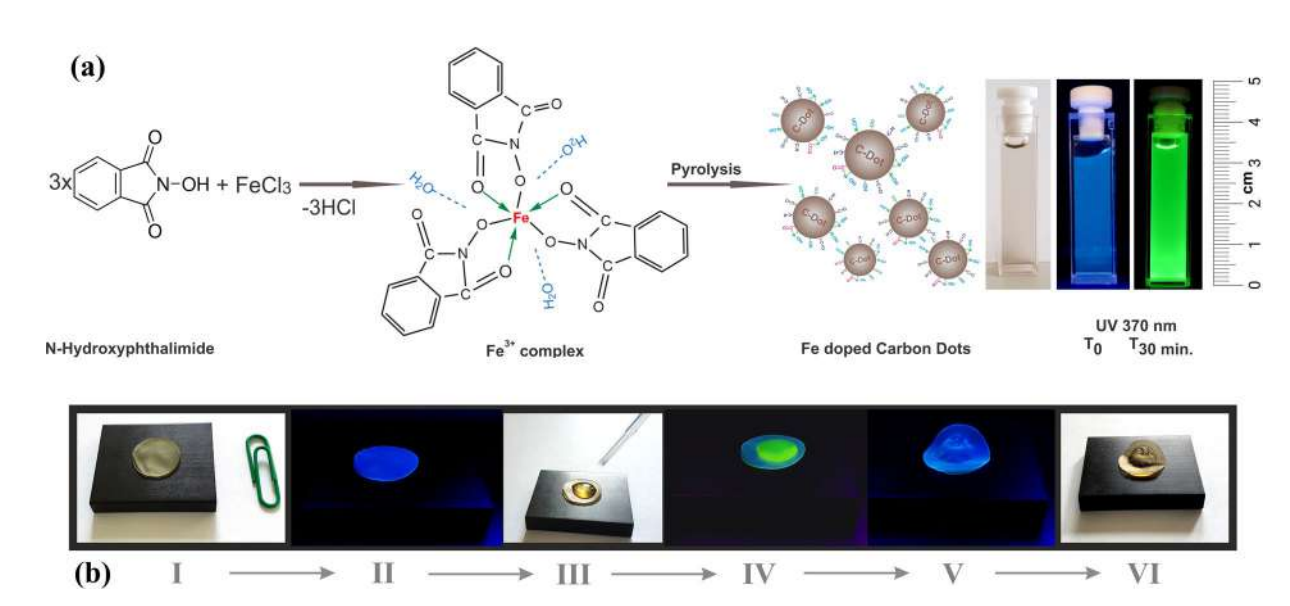


**Figure 1.** (a) Preparation stages of the Fe doped CNDs: intermediary prepared complex, resulted CNDs under ambient light and UV (370 nm) radiation, respectively; (b) Sequence of the reversible emission shift from blue to green of the PVA-Fe doped CNDs composite.

Stage 1	Stage 1 Stage 2		Stage 3		Stage 4	Residue		
ΔT, (°C)	Δm, (%)	ΔT, (°C)	Δm, (%)	ΔT, (°C) Δm, (%)		ΔT, (°C)	Δm, (%)	(%)
25-122	14.56 ± 0.18	168.6-250	$44.81 \pm 0.19$	250-331	$19.01 \pm 0.15$	357-402	$6.46 \pm 0.19$	15.16±0.21

**Table 1.** Decomposition stages recorded for the Fe(III)–N–Hydroxyphthalimide complex.

boron $^{26}$  or transition metals (Zn, Mn) $^{27,28}$  can alter the emission spectra while the overall efficiency of the radiative processes can be markedly enhanced. In the present paper, new highly green emissive Fe(III) doped CNDs are reported. Fe(III)-doped CNDs were prepared through a straightforward pyrolytic $^{29}$  processing of a Fe(III)-N-Hydroxyphthalimide intermediate complex. The achieved CNDs present an unusual reversible emission transition when dispersed in water, the emission turning gradually from deep blue to intense green in the presence of ambient light or exposed to UV (370 nm). Their unique feature of emission transition reversibility was tested by embedding the Fe(III) doped CNDs in a polymer matrix (PVA in this case, though not limited to) leading to color transition depending on water content, turning from a full blue emission when completely dried to intense green when wetted. To our knowledge, the reported CNDs are the first to exhibit this type of behavior, opening several new perspectives in terms of potential applications and providing several new insights regarding their specific structure and luminescent mechanisms.

### **Results and Discussion**

Figure 1a presents the preparation stages of the Fe(III) doped CNDs. As can be seen, in the first stage Fe(III) is complexed with N–Hydroxyphthalimide at 1:3 metal to ligand ratio, resulting in a complex with the suggested structure sustained by TG, FT-IR and XPS investigations. The [ $Fe(C_8H_4NO_3)_3(H_2O)_x$ ] complex is the result of the bidentate behavior of the N–Hydroxyphthalimide ligand. The coordination number is 6, which is typical for Fe(III)<sup>30</sup>, the covalent bonding being established between the Fe(III) cation and the oxygen in the –O–N< group while a coordinative bonding occurs between the cation and the oxygen in the carbonyl group –O=C<<sup>31</sup>. Water molecules are also present in the inner/outer coordination sphere. In the second stage the prepared complexes processed by pyrolysis result in water-dispersed CNDs as described in Preparation subsection. Further, the Fe(III) doped CNDs were introduced in a PVA matrix. Figure 1b shows the sequence of the emission shift from blue to green of the Fe doped CND embedded in PVA (I- prepared composite under ambient lighting, II- initial blue region located emission under 370 nm UV radiation, III-H<sub>2</sub>O wetting of the composite, IV- shifted blue to green emission of the wetted area after 20–30 min, V- oven re-dried composite reversed blue emission, VI- aspect of the re-dried composite under ambient lighting).

**Thermal analysis.** Thermal analysis of the intermediate complex provided useful information on its structural configuration and expected thermal behavior during the second stage pyrolytic processing leading to CNDs formation. The recorded decomposition stages are detailed in Table 1 while Fig. S1 presents the mass loss variation within the investigated interval. In the first stage, as suggested by the recorded value, water molecules located within the inner or outer coordination sphere are lost. The steep mass loss recorded in the second decomposition stage is most probably due to the advanced destructuration of the complex which is accompanied by volatiles exhaustion. This stage is particularly important from the perspective of the pyrolytic process leading to CNDs.

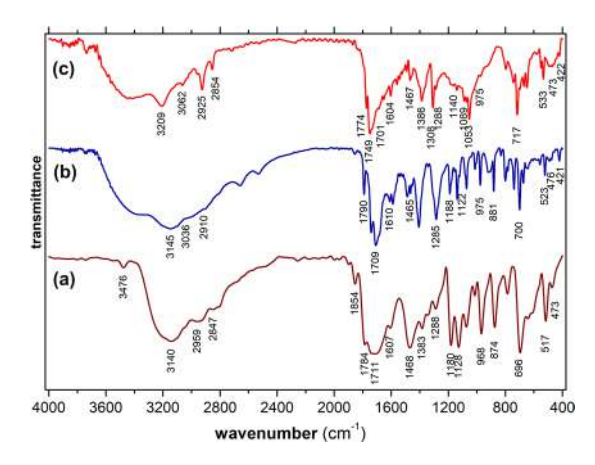


**Figure 2.** IR spectra recorded for (a) N-Hydroxyphthalimide ligand, (b) Fe(III)-N-Hydroxyphthalimide complex and (c) Fe(III) doped CNDs.

The experimentally established pyrolysis parameters ( $210\,^{\circ}$ C, 6 min) allow the formation of the graphitic core yet, also through partial destructuration, various functional groups still remain available within the final configuration of the Fe(III) doped CNDs. In the  $3^{rd}$  and  $4^{th}$  stages, the decomposition processes are still present, but to a smaller extent, while between  $402-900\,^{\circ}$ C no mass loss was recorded, the final decomposition residue being attained.

**FT-IR analysis.** IR spectra (Fig. 2) were acquired in case of both the intermediary Fe(III)–N–Hydroxyphthalimide complex and the resulted Fe(III) doped CNDs. To highlight the modifications occurring through complexation, the spectrum of N–Hydroxyphthalimide ligand was also recorded.

Table S1 lists several significant specific vibrations of various groups<sup>32</sup> and highlights the modifications occurring through complexation and further pyrolytic processing of the complex, leading to Fe(III) doped CNDs. The formation of the complex (Fig. 2, line (b)) is illustrated by a series of modifications, as follows: the intense characteristic band with a maximum peak at 1784 cm<sup>-1</sup> corresponding to the sym. carbonyl (O=C<) stretch appearing for the ligand is shifted to 1740 cm<sup>-1</sup> in case of the complex, as a result of the coordinative bonding established between the central Fe<sup>3+</sup> cation and the oxygen atoms; the new peak occurs at 421 cm<sup>-1</sup> due to the stretching vibration of the newly established Fe-O-N< bonding while the -OH stretch peak is no more present. Due to the rearrangements determined by the complexation, other vibrations corresponding to the aromatic and succinic rings are shifted toward higher wavenumbers as a result of the influence of the central Fe(III) cation. As for the Fe(III) doped CNDs (Fig. 2, line (c)), the structural modifications resulted following the partial pyrolysis are clearly visible in the recorded spectrum. Thus, in the upper region (3300-2800 cm<sup>-1</sup>) the recorded peaks corresponding to C-H, C-C and C=C groups are displaced and more intense, while in the mid and lower regions a series of peaks corresponding to various groups are less intense, displaced or missing compared to the Fe(III)-N-Hydroxyphthalimide complex. These modifications occur due to the formation of the carbonaceous core and the re-arrangements of the functional groups within the defect rich graphitic structure or surface attached as terminal groups. The characteristic band at 421 cm<sup>-1</sup>, corresponding to the Fe–O– stretch vibration is still present in the recorded spectrum but its intensity is markedly lower. The thermal processing parameters (temperature and duration of the thermal exposure) play a key role in achieving the favorable configuration of the resulted Fe(III) doped CNDs. During the experimental study on the optimal pyrolytic processing temperature and duration of the main sequence of the partial decomposition process, it was observed that higher temperature values or longer thermal exposure lead to a severe diminution in the emission most probably due to an enhanced depletion of the attached functional groups.

**XPS analysis.** XPS investigation revealed the relative concentrations of various functional groups in both the prepared Fe(III) complex and Fe doped CNDs. Figure 3a-c provide the high resolution spectra (C1s, O1s, N1s) recorded for the Fe(III) complex, while the relative concentrations of main functional groups are detailed in the attached tables. The results are in good agreement with the proposed structure of the Fe(III) complex. The Fe-O bonding achieved through complexation is clearly visible and in agreement with the FT-IR investigation. Figure 3d-f present the high resolution spectra recorded for the Fe(III) doped CNDs along with the relative concentrations of remnant functional groups. As could be noted from the C1s spectrum, the increased values of the C=C groups are the result of the carbonaceous core issued through the pyrolytic processing. The presence of C-C/C-H bonds suggest a highly disordered, defect rich graphitic structure. The relatively high concentrations of C=O, C-N, N-O groups is also an indication of various remnant groups still attached to the carbonaceous core, which most probable are responsible for the radiative transitions leading to the observed PL properties. The Fe-O bonding is still present in even higher concentrations as compared to the complex as a result of the volatiles depletion occurring during the pyrolytic processing. Fit residual plots are detailed in Fig. S2.

**Dimensional investigation.** For the dimensional investigation, Fe(III) doped CNDs were dispersed in three solvents. Thus, water (polar protic), acetone (polar aprotic) and chloroform (non-polar)<sup>33</sup> dispersions were

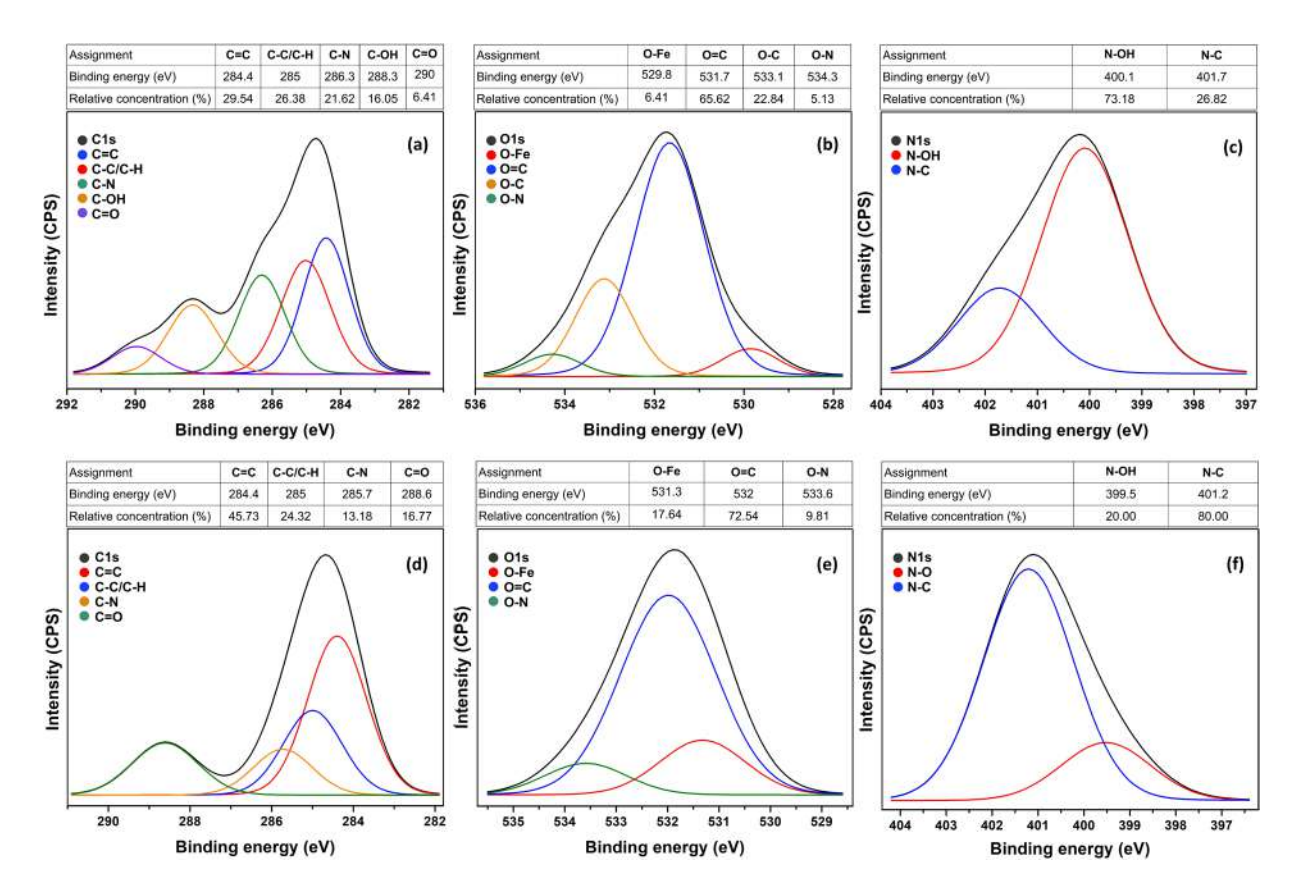


**Figure 3.** High resolution spectra and relative concentrations of various groups recorded for Fe(III) complex (a) C1s, (b) O1s and (c) N1s, and for Fe(III) doped CNDs (d) C1s, (e) O1s and (f) N1s.

prepared by suspending 1 mg of Fe(III) doped CNDs in each 10 mL of the ante-mentioned solvents, the mixtures being further sonicated and then centrifuged at 15000 RPM for 10 min. The recorded results are presented in Fig. 4a. In aqueous medium the Fe(III) doped CNDs are well dispersed, with 20–25 nm average size of individual dots or clusters representing about 60%, while the rest are up to 35 nm. The situation is slightly different in acetone, the dimensional distribution between 35–50 nm in a proportion of 75%, the rest being at a max. 60–120 nm range. For chloroform dispersed Fe(III) doped CNDs the agglomeration tendency is very high, with clusters exceeding 1.5  $\mu$ m. The average recorded measurement errors for the Fe(III) doped CNDs dispersed in water, acetone and chloroform, respectively, are: 2%; 1.5%; 1.1%. The results confirm the significant influence of the dispersion medium on the agglomeration tendency of the CNDs<sup>7,34</sup>. In the particular case of aqueous dispersion, the Fe<sup>3+</sup> cation seems to favor the hydration of the individual CND. The presence of water molecules in the outer coordination sphere or interacting with the surface located functional groups seems to avoid the agglomeration tendency to a certain extent. As will be later shown, the presence of water molecules is responsible for both unusual color shift and deep green photoluminescent emission, while for the other solvents this behavior is absent.

**TEM investigation.** The recorded TEM micrographs also revealed comprehensive information regarding the size and clustering tendency of the Fe(III) doped CNDs. As could be noted from Fig. 4b, the size of the nanostructures ranges from 2–3 nm to hundreds of nm. The larger entities are the result of an agglomeration process, a granular structure being clearly visible. The smaller entities in 2–3 nm range could be individual CNDs, yet a clustered structure is also possible. Figure 4c clearly reveals the granular structure of a larger aggregate (120–140 nm), smaller clustered entities (15–25 nm) being also visible.

**AFM investigation.** AFM imaging provided useful information regarding the different agglomeration tendency as a function of the solvent used as dispersion medium. Images were recorded for water and chloroform solutions (prepared as described in the prior section) deposited through evaporation on mica substrates. Figure 4d shows the image recorded for the Fe(III) doped CNDs dispersed in water. As can be observed, the average particle size is in the 20–40 nm range, which is in a very good agreement with DLS results. The dimensional distribution is narrow and the dried nanostructures are evenly spread on mica substrate. As for sample prepared from Fe(III) doped CNDs dispersed in chloroform (Fig. 4e), the average particle size is in 2–3  $\mu$ m range, also in very good agreement with DLS results. The size distribution is markedly larger as compared to the aqueous dispersion, while the cluster shapes are irregular.

**Fluorescence investigations.** Photoluminescence (PL) of the CNDs is one of their most interesting and debated properties. Usually, they exhibit a blue, excitation dependent emission when dispersed in various media

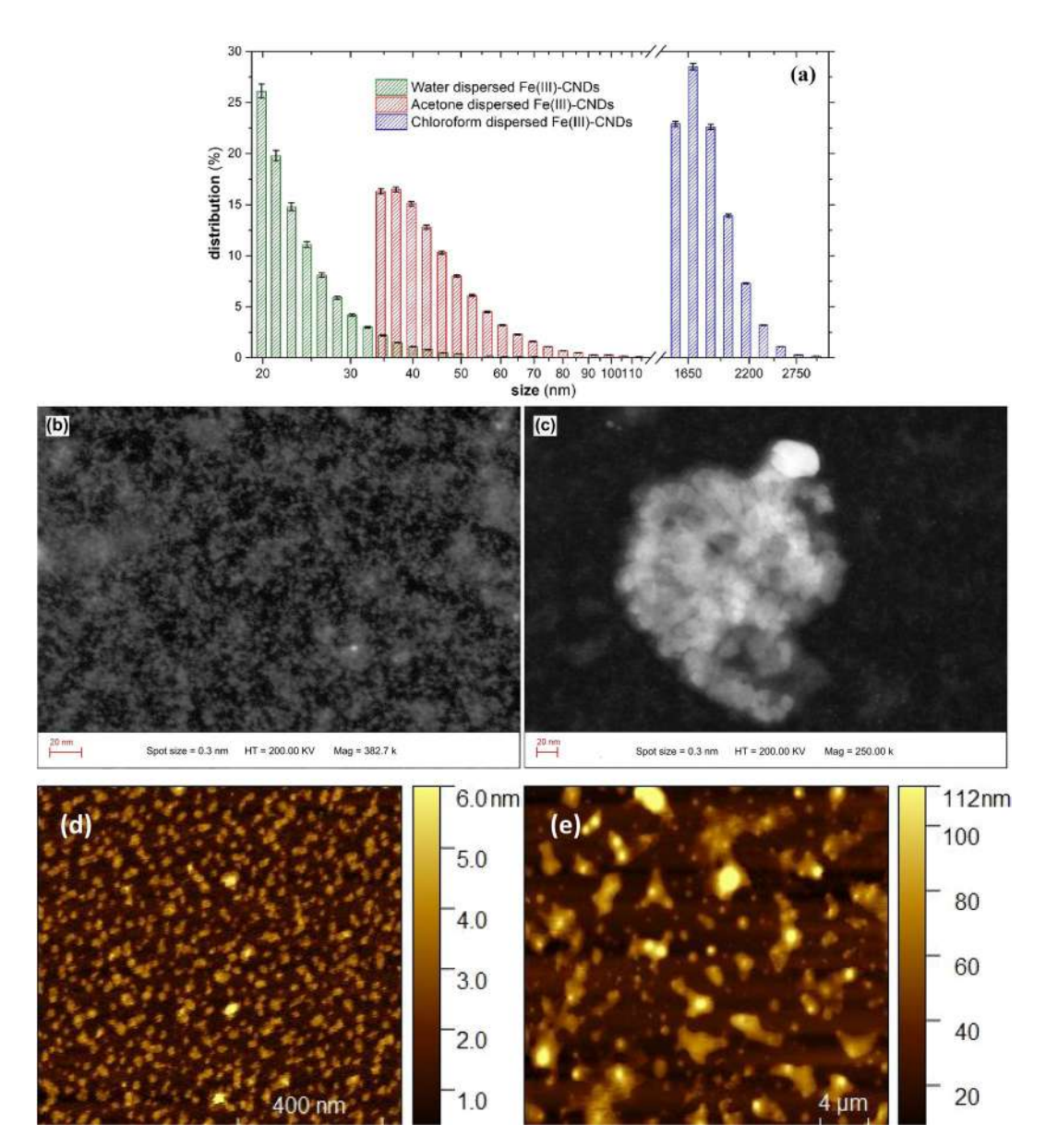


**Figure 4.** Dimensional distribution of the prepared Fe(III) doped CNDs (**a**) dispersed in water, acetone and chloroform; TEM micrographs (**b,c**) of Fe(III) doped CNDs; and AFM imaging recorded for Fe(III) doped CNDs dispersed in (**d**) water, (**e**) chloroform.

(solvents, polymer matrices etc.). The intensity and emission peak positions are also closely dependent on the type of the dispersion medium<sup>35</sup>. As mentioned in the first section, the PL mechanism is still an actively debated subject, with an approach which emphasizes a size-depending emission under quantum confinement conditions and alternatively, the preponderant role of structural defects within the carbonaceous core/surface attached functional groups and interactions occurring between or within various constituent atomic species<sup>36,37</sup>.

Steady state fluorescence investigation. As previously mentioned, the water dispersed Fe(III) doped CNDs present some interesting particularities of their emission. Following the preparation and dispersion in water, the emission is initially located in the blue region of the visible spectrum but, under UV exposure (as well as under ambient solar light), it gradually turns to intense green, which further remains indefinitely stable. The color transition occurs within 30–35 min after initial water dispersion and sunlight/UV radiation exposure. Figure 5a presents the PL emission spectra recorded immediately after water dispersion/UV exposure while the spectra in Fig. 5b were recorded after 30 min.

As can be noted, in both cases the luminescent emission is excitation dependent within the investigated interval (300–390 nm in 10 nm steps) with emission peaks occurring in 435–450 nm range and 509–513 nm, respectively. The maximum emission intensity peaks were observed at 447 nm (360 nm excitation) and at 510 nm (350 nm excitation), respectively. Visually, the intensity emission is markedly higher in case of green emission achieved after 30 min. compared to initial blue emission observed prior to light exposure. Figure 5c,d present the

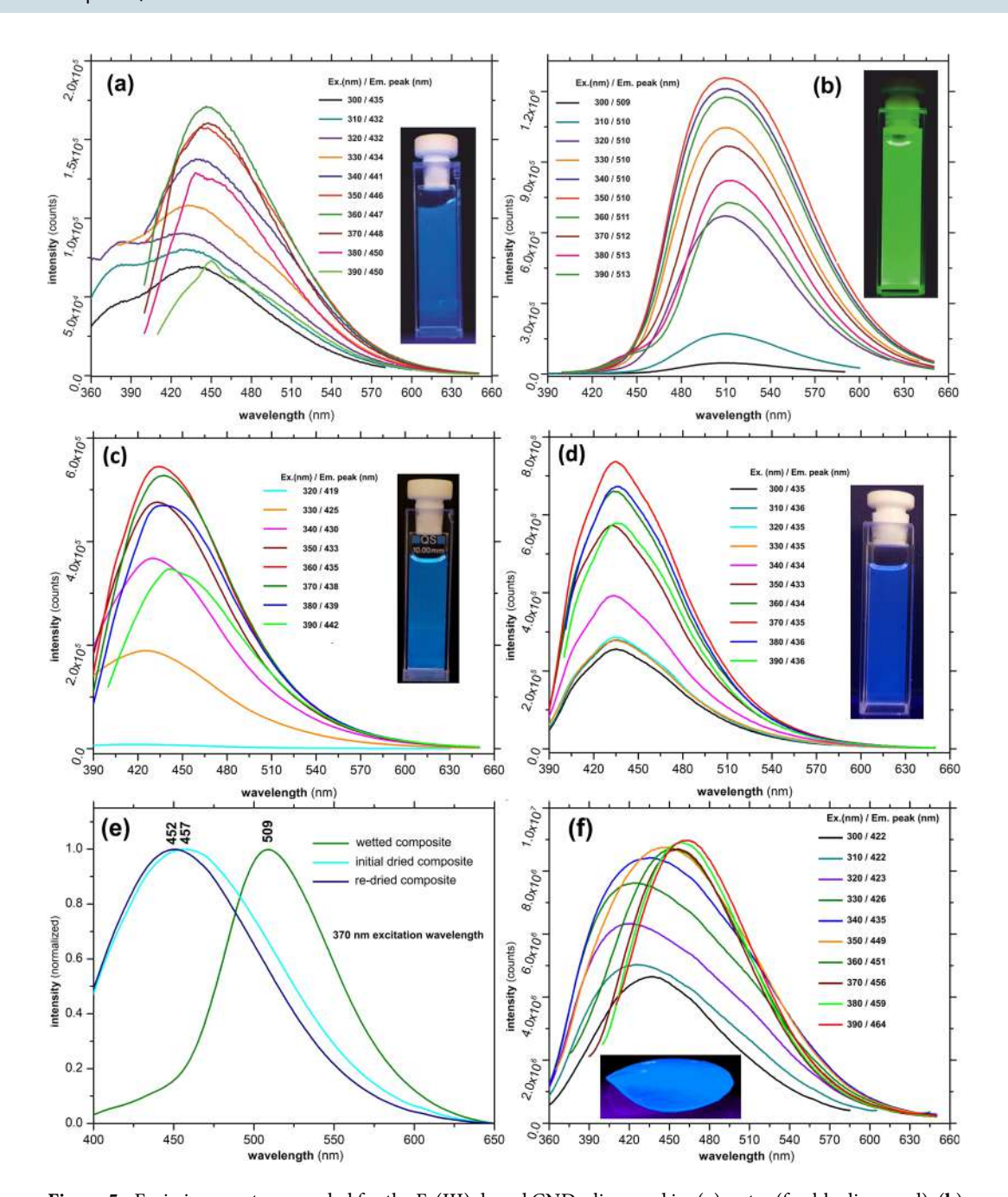


**Figure 5.** Emission spectra recorded for the Fe(III) doped CNDs dispersed in: (a) water (freshly dispersed); (b) water - after 30 min of UV exposure; (c) acetone; (d) chloroform; (e) emission shifting of the PVA- Fe(III) doped CNDs composite and (f) for the PVA- Fe(III) doped CNDs composite.

recorded spectra of the Fe(III) doped CNDs dispersed in acetone and chloroform. In both cases the PL emission is located in the blue region of the visible spectrum and remains unchanged (both peaks location and intensity) for an indefinitely long exposure to UV. Thus, in case of acetone dispersion, the peaks were recorded within 419–442 nm range (320–390 nm excitation, 10 nm steps) while for the chloroform dispersion, the peaks are almost excitation independent (434–436 nm within 300–390 nm excitation range). In both solvents the emission intensities are comparable, yet slightly lower than those recorded for the freshly water dispersed/UV exposed Fe(III) doped CNDs (Fig. 5a). The recorded results lead to several interesting conclusions concerning the mechanism involved in the transition from blue to intense green emission. Water molecules seem to play a key role along with the particular structural configuration resulting due to the presence of Fe(III) cations. While a series of other prepared N–Hydroxyphthalimide transition metals (Mn, Co, Ni) complexes were also tested during the preliminary experiments, no comparable results were obtained. The presence of the Fe(III) cations attached to the remnant surface located groups or entrapped as defects within the carbonaceous core affect the radiative transitions occurring within various functional groups or within the traps created in the defect rich structure of the core. Not to be neglected, the Fe(III) cation could favorably influence the local emissive sites through its particularities such

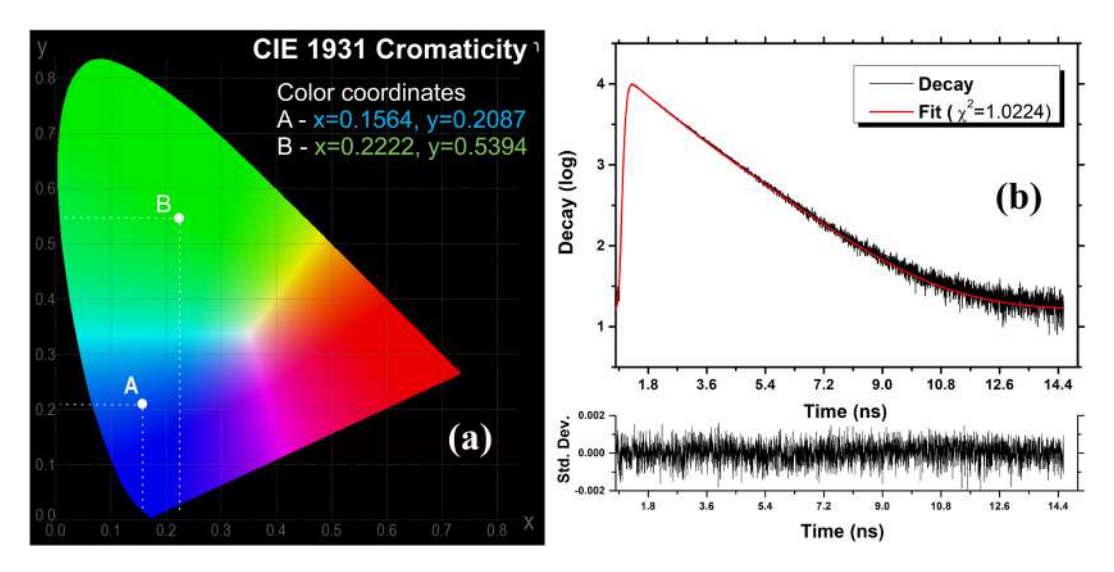


**Figure 6.** CIE 1931 chromaticity of water dispersed Fe(III) doped CNDs (a) and fluorescence lifetime of water dispersed Fe(III) doped CNDs (b).

as ionic radius for instance, to influence positively the local emissive sites. Also, through hydration, the present OH groups tend to alter the excited states and the resulted photonic emission 38,39. Most probably, during the mentioned 30 min interval, water molecules gradually migrate toward outer coordination sphere of the Fe(III) cations, arriving in the vicinity of the groups responsible for the radiative transitions. The presence of the OH oscillators seems to favor the local interactions occurring within or between various functional groups or atomic species essentially involved in achieving the excited states responsible for the photonic emission. The blue to green emission shift is also a possible consequence of the OH oscillators presence near the emission sites, the resulted photons having a lower energy (higher Stokes shift). To test the assumption that the blue to green emission shifting is mainly a result of water molecules presence, the Fe(III) doped CNDs were introduced in a PVA matrix according to the procedure described in preparation subsection. The transparent, light yellow tinted aspect of the resulted polymer composite film, under ambient lighting conditions is presented in Fig. S2. When completely dried, the film presents a relatively intense blue emission under UV. As expected, when wetted or placed in a high humidity environment, the composite PL gradually turns to a green emission which further returns to a blue emission after drying, the process being reversible as presented in the recorded photo sequence detailed in Fig. 6a. The reversible emission shifting is highlighted by the recorded emission spectra presented in Fig. 5e. Figure 5f presents the emission spectra of freshly prepared and dried PVA-Fe(III) doped CNDs composite. As can be noted, the recorded emission spectra also presents the specific excitation dependent emission, with peaks located within 422-464 nm range (300-390 nm excitation, 10 nm steps). Compared to the freshly dispersed Fe(III) doped CNDs (Fig. 5a) the emission peaks are slightly displaced to lower wavelengths, most probably due to the influence of the polymer matrix<sup>40,41</sup> or presence of remnant water content within the composite. As a conclusion, the above mentioned results inherently support the PL mechanism which emphasizes the preponderant role of the surface attached functional groups and/or defects located within the carbonaceous core. As issued from the experimental, the dimensional characteristics of the CNDs are hardly to be linked to the observed behavior.

*PLQY*, chromaticity and lifetime investigations. The absolute PLQY investigations were performed in the 310–390 nm excitation range (10 nm steps) for the Fe(III) doped CNDs dispersed in three types of solvents (water - polar protic, acetone - polar aprotic and chloroform - non-polar), the results being presented in Table 2. The highest PLQY value (33.12%) is achieved at 330 nm excitation in case of water/after 30 min interval, while for the freshly water dispersed/unexposed sample a 26.81% value (350 nm excitation) was recorded. The acetone dispersed Fe(III) doped CNDs achieved a 28.04% PLQY at 320 nm excitation. For the chloroform dispersion, the max. PLQY (29.47%) was recorded at 390 nm excitation.

As can be seen, for both types of polar solvents the highest values were recorded in 320–350 nm (within UV-B) excitation range while for the non-polar solvent the maximum PLQY was achieved in upper UV range (UV-A). The recorded results suggest interactions occurring between solvent and emissive centers, in case of polar solvents, higher energy UV excitation photons being required to trigger the radiative transitions. Figure 6a presents the chromatic parameters according to CIE 1931 color space, recorded for water dispersed Fe(III) doped CNDs with initial bluish emission (A) and shifted greenish emission achieved after 30 min. (B).

Fluorescence lifetime of the radiative processes occurring in water dispersed Fe(III) doped CNDs is presented in Fig. 6b. While the overall lifetime is located in nanoseconds range, several interesting details were highlighted during investigation. Similar to what have been found for other CNDs, the fluorescence lifetime decays could not be deconvoluted with a mono-exponential function<sup>42,43</sup>. The deconvolution fits became satisfactory with the use of a tri-exponential function, for which the corresponding pre-exponential factors (A<sub>1</sub>, A<sub>2</sub> and A<sub>3</sub>) and lifetimes  $(\tau_1, \tau_2 \text{ and } \tau_3)$  are shown in Table S2. These values were used to calculate the average fluorescence lifetime according

Fe(III) doped CNDs	Excitation wave	elength (nm)													
	310	320	330	340	350	360	370	380	390						
dispersed in:	PLQY (%)														
water (freshly dispersed)	$16.14 \pm 0.06$	20.18 ± 0.06	23.44 ± 0.06	25.96 ± 0.06	<b>26.81</b> ± 0.08	25.62 ± 0.09	24.01 ± 0.08	21.06 ± 0.07	$18.73 \pm 0.06$						
water (after 30 min UV exp.)	25.73 ± 0.02	25.08 ± 0.02	<b>33.12</b> ± 0.03	32.66 ± 0.02	30.94±0.02	25.58 ± 0.01	20.19±0.01	17.14±0.01	$16.55 \pm 0.01$						
acetone	$26.57 \pm 0.20$	28.04 ± 0.24	27.10±0.16	$25.31 \pm 0.20$	$22.66 \pm 0.16$	$19.14 \pm 0.20$	$16.23 \pm 0.20$	$13.09 \pm 0.10$	$10.38 \pm 0.10$						
chloroform	$20.01 \pm 0.03$	21.16±0.03	$21.37 \pm 0.04$	$22.52 \pm 0.04$	$25.56 \pm 0.08$	$26.75 \pm 0.09$	$28.84 \pm 0.13$	$28.76 \pm 0.13$	<b>29.47</b> ± 0.22						

Table 2. Recorded PLQY for the Fe(III) doped CNDs, and their corresponding absolute error values.

to the equation  $<\tau_F>=[(A_1(\tau_1)^2+(A_2(\tau_2)^2+(A_3(\tau_3)^2]/(A_1\tau_1+A_2\tau_2+A_3\tau_3)^{44}]$ . The recorded data supports the PL mechanism which is related to the radiative transitions occurring within/between surface attached groups or within the traps located in the defect rich graphitic structure of the carbonaceous core.

# **Experimental**

**Materials.** N-Hydroxyphthalimide (97%), anhydrous FeCl<sub>3</sub> and Poly(vinyl alcohol) (PVA) Mw = 58000 were sourced from Merck Chemicals. High purity water and reagent grade ethanol (EtOH) were used for preparation of the Fe(III)-N-Hydroxyphthalimide complex, intermediate purification stages and dispersion, while reagent grade acetone, chloroform, EtOH provided by the same supplier were used as re-dispersion mediums for the prepared CNDs.

**Preparation.** In the first stage a Fe(III) - N-Hydroxyphthalimide complex was prepared at 1:3 metal to ligand ratio. In a typical procedure 0.5 g anhydrous FeCl<sub>3</sub> was dissolved in 10 mL of water while in a separate glass beaker 1.5 g N-Hydroxyphthalimide was dissolved under magnetic stirring in a mixture of 20 mL water and 25 mL EtOH at a moderate 45-50 °C temperature. The two resulted solutions were mixed under continuous stirring and kept overnight at 35-40 °C for reaction completion. The resulted dark brown precipitate was washed at least three times with water and further dried under vacuum. In the second stage the powder of fine milled complex was processed in the experimental setup presented in Fig. S3. The flowchart of the preparation stages are detailed in Fig. S4. The experimental set-up consists of a quartz tube, a heating mantle, a temperature/flow controlled hot air source along with a water container, an evacuation pump and the required piping. Thus, 0.3 g of Fe(III) - N-Hydroxyphthalimide complex was added in the quartz tube and heated at 210 °C for 6 min in N<sub>2</sub> atmosphere. Following the completion of the pyrolytic process, the reaction product was flooded with cold water (3-5°C). The resulted CNDs aqueous dispersion was evacuated and further centrifuged at 15000 RPM for about 10 min. The aqueous supernatant is again centrifuged in the same conditions, the collected supernatant containing dimensionally selected Fe(III) doped CNDs was used as obtained or freeze dried for re-dispersion in other solvents (ex. acetone, chloroform). The aqueous dispersion of the prepared Fe(III) doped CNDs presents a slightly yellow tinted transparent aspect under normal illumination conditions. When exposed to solar light or UV radiation (370 nm) immediately after preparation, the dispersion initially emits in deep blue which gradually (within 30 min) turns to intense green emission (Fig. 1b). The polymer film composite is prepared by dissolution under stirring of 1 g PVA in 15 mL of previously obtained aqueous dispersed Fe(III) doped CNDs and further drying in ambient conditions in a conveniently shaped mold. The transparent, light yellow tinted aspect of the resulted polymer composite film, under ambient lighting conditions is presented in Fig. S5.

**Characterization methods.** Structural investigations were performed for both the prepared Fe(III)-N-Hydroxyphthalimide complex and Fe(III) doped CNDs. Quantitative data are expressed as the mean value +/- standard deviation. Prior to analysis, the samples were vacuum oven dried at 60 °C for 12 h. The thermal analysis of the prepared complex was performed in triplicate using a Mettler Toledo TGASDTA851e instrument working in N<sub>2</sub> atmosphere with 10 °C/min heating rate within the 25-900 °C range. The FT-IR spectra were recorded in duplicate in the 400-4000 cm<sup>-1</sup> range using a Shimadzu IRAffinity 1S spectrometer according to KBr method. Dimensional analysis and size distribution (performed in triplicate) of the Fe(III) doped CNDs dispersed in water, acetone and chloroform were carried out on a Beckman-Coulter Delsa Nano. Prior to investigation the solutions were twice centrifuged at 15000 RPM for 10 min. The AFM investigations were performed using a Ntegra Spectra (NT-MDT, Russia) instrument provided with silicon cantilever tips (NSG 10) operated in tapping mode under ambient conditions. The Fe(III) doped CNDs samples were deposited on mica substrates from high diluted water and chloroform solutions. TEM images were recorded on a Zeiss Libra 200MC UHR-TEM working at 200 KV acceleration voltage and a 0.3 nm spot size. The samples were deposited on carbon grids from a diluted EtOH solution. The XPS spectra were obtained on a ULVAC-PHI, 5000 VersaProbe spectrometer (Physical Electronics), equipped with a monochromatic Al K $\alpha$  X-ray source (h $\nu$  = 1.486 keV). During measurements, the pressure in the analysis chamber was maintained at  $5.9 \times 10^{-8}$  Pa and the photoelectron take-off angle relative to the sample surface was 45°. The binding energy was calibrated by the peak energy of C 1 s (284.6 eV) as reference and the resolution of the XPS analyzer is 0.85 eV for organic materials. The XPS data were analyzed using XPSPeak41 software for peak deconvolution. The Steady-State Fluorescence, Time-Correlated Single-Photon-Counting (life-time), absolute PLQY and chromaticity parameters measurements were conducted on a Horiba FluoroMax-4 equipped with Quanta Φ integration sphere for absolute PLQY measurements, TCSPC lifetime module and adapter for solid state sample investigations. The steady state fluorescence, PLQY and chromaticity parameters were acquired with the FluorEssence software according to the manufacturer recommended procedures. Lifetime measurements were performed according to the manufacturer procedures using the provided DAS6 Decay Analysis Software. The investigation was performed in freshly prepared diluted samples according to the measurements requirements.

# **Conclusions**

Fe(III) doped CNDs with intense green photoluminescence and unusual emission dependence according to the dispersion medium were prepared through controlled pyrolytic processing of a Fe(III)-N-Hydroxyphthalimide complex. Their unusual photoluminescence is especially highlighted in water where the initial blue emission is gradually shifted to intense deep green. When embedding the prepared CNDs in a PVA polymer matrix, the color transition was found to be reversible and dependent on water content. The structural investigation performed through TG, FT-IR, XPS revealed a typical configuration consisting of a carbonaceous core which is highly surface decorated with various functional groups. DLS, TEM and AFM were used to investigate their morphology. The dimensional distribution is solvent dependent and due to the interactions occurring between surface located groups a clustering tendency was observed. The emission spectra and absolute PLQY were studied in detail in several dispersion media bringing notable arguments in favor of the PL mechanism based on the preponderant role of the surface attached functional groups and/or defects located within the carbonaceous core. Their unusual photoluminescence is especially highlighted in water where the initial blue emission is gradually shifted to intense deep green. Interestingly, when embedding the prepared CNDs in a PVA polymer matrix, the color transition was found to be reversible and dependent on water content, which is a unique feature first to be reported up to date. The recorded PLQY of 33% could recommend them for applications ranging from UV protective layers to biomedical imaging or optoelectronic devices. Also, their reversible blue to green shifting emission could be of particular interest for humidity sensors.

Received: 26 August 2019; Accepted: 21 November 2019;

# Published online: 11 December 2019

- References
   Tuerhong, M., Xu, Y. & Yin, X. B. Review on carbon dots and their applications. *Chin. J. Anal. Chem.* 45, 139–150, https://doi.org/10.1016/S1872-2040(16)60990-8 (2017).
- Yao, B., Huang, H., Liu, Y. & Kang, Z. Carbon dots: A small conundrum. Trends Chem. 1, 235–246, https://doi.org/10.1016/j. trechm.2019.02.003 (2019).
- 3. Song, Y. et al. Investigation from chemical structure to photoluminescent mechanism: a type of carbon dots from the pyrolysis of citric acid and an amine. J. Mater. Chem. C. 3, 5976–5984, https://doi.org/10.1039/C5TC00813A (2015).
- 4. Sun, X. & Lei, Y. Fluorescent carbon dots and their sensing application. *TrAC Trends Anal. Chem.* 89, 163–180, https://doi.org/10.1016/j.trac.2017.02.001 (2017).
- Boakye-Yiadom, K. O. et al. Carbon dots: Applications in bioimaging and theranostics. Int. J. Pharm. 564, 308–317, https://doi.org/10.1016/j.ijpharm.2019.04.055 (2019).
- 6. Kong, T., Hao, L., Wei, Y., Cai, X. & Zhu, B. Doxorubicin conjugated carbon dots as a drug delivery system for human breast cancer therapy. *Cell Prolif.* 51, e12488, https://doi.org/10.1111/cpr.12488 (2018).
- 7. Kang, Z. & Liu, Y. Catalytic Applications of Carbon Dots. In: Carbon Nanoparticles and Nanostructures. Carbon Nanostructures, 257–298 (Springer International Publishing, Cham, 2016).
- 8. Yuan, T. *et al.* Carbon quantum dots: an emerging material for optoelectronic applications. *J. Mater. Chem. C.* 7, 6820–6835, https://doi.org/10.1039/C9TC01730E (2019).
- 9. Zhu, S. et al. The photoluminescence mechanism in carbon dots (graphene quantum dots, carbon nanodots, and polymer dots): current state and future perspective. Nano Res. 8, 355–381, https://doi.org/10.1007/s12274-014-0644-3 (2015).
- Mintz, K. J., Zhoua, Y. & Leblanc, R. M. Recent development of carbon quantum dots regarding their optical properties, photoluminescence mechanism, and core structure. Nanoscale 11, 4634–4652, https://doi.org/10.1039/C8NR10059D (2019).
- 11. Liu, M. L., Chen, B. B., Lib, C. M. & Huang, C. Z. carbon dots: synthesis, formation mechanism, fluorescence origin and sensing applications. *Green Chem.* 21, 449–471, https://doi.org/10.1039/c8gc02736f (2019).
- 12. Sciortino, A., Cannizzo, A. & Messina, F. Carbon nanodots: A review—from the current understanding of the fundamental photophysics to the full control of the optical response. *J. Carbon Res. C.* 4, 67, https://doi.org/10.3390/c4040067 (2018).
- 13. Paloncyova, M., Langer, M. & Otyepka, M. Structural dynamics of carbon dots in water and n,n-dimethylformamide probed by allatom molecular dynamics simulations. *J. Chem. Theory Comput.* 14, 2076–2083, https://doi.org/10.1021/acs.jctc.7b01149 (2018).
- 14. Stan, C. S., Gospei (Horlescu), P., Ursu, L. E., Popa, M. & Albu, C. Facile preparation of highly luminescent composites by polymer embedding of carbon dots derived from n-hydroxyphthalimide. *J. Mater. Sci.* 52, 185–196, https://doi.org/10.1007/s10853-016-0320-y (2017).
- 15. Kundu, A. et al. Facile approach to synthesize highly fluorescent multicolor emissive carbon dots via surface functionalization for cellular imaging. J. Colloid Interface Sci. 513, 505–514, https://doi.org/10.1016/j.jcis.2017.10.09 (2018).
- Fan, Y., Yang, X., Yin, C., Ma, C. & Zhou, X. Blue- and green-emitting hydrophobic carbon dots: preparation, optical transition, and carbon dot-loading. *Nanotechnology* 30, 265704, https://doi.org/10.1088/1361-6528/ab0b14 (2019).
- 17. Zheng, J. et al. Facile and rapid synthesis of yellow-emission carbon dots for white light-emitting diodes. J. Electron. Mater. 47, 7497–7504, https://doi.org/10.1007/s11664-018-6691-x (2018).
- 18. Khare, P., Bhatī, A., Raj, S., Gunture, A. & Sonkar, S. K. Brightly fluorescent zinc-doped red-emitting carbon dots for the sunlight-induced photoreduction of cr(vi) to cr(iii). ACS Omega 3, 5187–5194, https://doi.org/10.1021/acsomega.8b00047 (2018).
- 19. Liu, C. et al. Orange, yellow and blue luminescent carbon dots controlled by surface state for multicolor cellular imaging, light emission and illumination. Microchim Acta. 185, 539, https://doi.org/10.1007/s00604-018-3072-3 (2018).
- Kargbo, O., Jin, Y. & Ding, S. N. Recent advances in luminescent carbon dots. Curr. Anal. Chem. 11, 4–21, https://doi.org/10.2174/1 573411010666141010160217 (2015).
- 21. Choi, Y., Choi, Y., Kwon, O. H. & Kim, B. S. Carbon dots: Bottom-up syntheses, properties, and light-harvesting applications. *Chem Asian J.* 13, 586–598, https://doi.org/10.1002/asia.201701736 (2018).
- 22. Atabaev, T. S. Doped carbon dots for sensing and bioimaging applications: A minireview. *Nanomater. (Basel)* **8**, 342, https://doi.org/10.3390/nano8050342 (2018).
- 23. Liu, X. et al. Doped carbon dots: green and efficient synthesis on a large-scale and their application in fluorescent ph sensing. New J. Chem. 41, 10607–10612, https://doi.org/10.1039/C7NJ01889D (2017).
- 24. Chen, Z., Wang, S. & Yang, X. Phosphorus-doped carbon dots for sensing both au (iii) and l-methionine. *J. Photochem. Photobiol. A: Chem.* 365, 178–184, https://doi.org/10.1016/j.jphotochem.2018.08.001 (2018).

- 25. Naik, V. M. et al. Quick and low cost synthesis of sulphur doped carbon dots by simple acidic carbonization of sucrose for the detection of fe3+ ions in highly acidic environment. Diam. Relat. Mater. 88, 262–268, https://doi.org/10.1016/j.diamond.2018.07.018 (2018).
- Zhao, X. et al. A magnetofluorescent boron-doped carbon dots as a metal-free bimodal probe. Talanta 200, 9–14, https://doi. org/10.1016/j.talanta.2019.03.022 (2019).
- Xu, Q. et al. Photoluminescence mechanism and applications of zn-doped carbon dots. RSC Adv. 8, 17254–17262, https://doi. org/10.1039/C8RA02756K (2018).
- Sun, S. et al. Highly luminescence manganese doped carbon dots. Chin. Chem. Lett. 30, 1051–1054, https://doi.org/10.1016/j. cclet.2019.01.014 (2019).
- Stan, C. S., Albu, C., Coroaba, A., Popa, M. & Sutiman, D. One step synthesis of fluorescent carbon dots through pyrolysis of n-hydroxysuccinimide. J. Mater. Chem. C 3, 789–795, https://doi.org/10.1039/C4TC02382J (2015).
- 30. Sanchez, M., Sabio, L., Galvez, N., Capdevila, M. & Dominguez-Vera, J. M. Iron chemistry at the service of life. *IUBMB Life* 69, 382–388, https://doi.org/10.1002/iub.1602 (2017).
- 31. Crudu, M., Sibiescu, D., Gurau, D. & Vasilescu, A. M. New coordination compounds of fe(iii) with ligand from nhydroxysuccinimide, with applications in ecologic leather tanning technologies. *Revista de Chimie Buchar.* 66, 958–962 (2015).
- 32. Krishnakumar, V., Sivasubramanian, M. & Muthunatesan, S. Density functional theory study and vibrational analysis of ft-ir and ft-raman spectra of n-hydroxyphthalimide. *J. Raman Spectrosc.* 40, 987–991, https://doi.org/10.1002/jrs.2214 (2009).
- 33. Sadek, P. C. The HPLC Solvent Guide. Second Edition (American Chemical Society, 2002).
- 34. Hill, S. & Galan, M. C. Fluorescent carbon dots from mono- and polysaccharides: synthesis, properties and applications. *Beilstein J. Org. Chem.* 13, 675–693, https://doi.org/10.3762/bjoc.13.67 (2017).
- 35. Papaioannou, N. et al. Structure and solvents effects on the optical properties of sugar-derived carbon nanodots. Sci. Reports 8, 6559, https://doi.org/10.1038/s41598-018-25012-8 (2018).
- 36. Jiang, Z. et al. Understanding the photoluminescence mechanism of carbon dots. MRS Adv. 2, 2927–2934, https://doi.org/10.1557/adv.2017.461 (2017).
- van Dam, B. et al. Excitation-dependent photoluminescence from single-carbon dots. Small 13, 48, https://doi.org/10.1002/smll.201702098 (2017).
- Singh, A. K., Das, S., Karmakar, A., Kumar, A. & Datta, A. Solvation and hydrogen bonding aided efficient nonradiative deactivation of polar excited state of 5-aminoquinoline. Phys. Chem. Chem. Phys. 20, 22320–22330, https://doi.org/10.1039/C8CP03590C (2018).
- Dobretsov, G. E., Syrejschikova, T. I. & Smolina, N. V. On mechanisms of fluorescence quenching by water. *Biophysics* 59, 231–237, https://doi.org/10.1134/S0006350914020079 (2014).
- 40. Fedorenko, E. V. et al. The influence of the polymer matrix on luminescent properties of compositions doped with boron chelates. Opt. Spectrosc. 127, 459–462, https://doi.org/10.1134/S0030400X19090091 (2019).
- Amato, F. et al. Nitrogen-doped carbon nanodots/pmma nanocomposites for solar cells applications. Chem. Eng. Transactions 74, 459–462, https://doi.org/10.3303/CET1974185 (2019).
- 42. Wang, X. et al. Photoinduced electron transfers with carbon dots. Chem. Commun. 25, 3774–3776, https://doi.org/10.1039/B906252A (2009).
- 43. Li, D. *et al.* Adverse effects of fluorescent carbon dots from canned yellow croaker on cellular respiration and glycolysis. *Food Funct.* **10**, 1123–1131, https://doi.org/10.1039/C8FO02602E (2019).
- 44. Lakowicz, J. R. Principles of Fluorescence Spectroscopy, 97-155 (Springer, Boston, M. A, 2006).

# **Acknowledgements**

This work was supported by a grant within the frame of the Complex Projects Partnership Program - PCCDI, under authority of Romanian National Authority for Scientific Research - UEFISCDI, project code PN-III-P1-1.2-PCCDI-2017-0083 (37PCCDI/2018). The authors are grateful to Dr. Marius Dobromir and Prof. Dumitru Luca from the "Alexandru Ioan Cuza" University, Iasi, for recording the XPS spectra.

# **Author contributions**

C.S.S. conceived the idea, designed the study, carried out experiments and analyzed data, conceived, prepared and submitted the manuscript. A.C. performed XPS analysis and fluorescence life-time measurements and interpretation. E.L.U. carried out AFM recordings and DLS measurements. M.S.S. performed statistical data analysis. C.S.S., M.S.S. and B.C.S. contributed to manuscript preparation and revisions. B.C.S. supervised the project. All authors reviewed the manuscript.

# Competing interests

The authors declare no competing interests.

# Additional information

**Supplementary information** is available for this paper at https://doi.org/10.1038/s41598-019-55264-x.

Correspondence and requests for materials should be addressed to C.S.S.

Reprints and permissions information is available at www.nature.com/reprints.

**Publisher's note** Springer Nature remains neutral with regard to jurisdictional claims in published maps and institutional affiliations.

Open Access This article is licensed under a Creative Commons Attribution 4.0 International License, which permits use, sharing, adaptation, distribution and reproduction in any medium or format, as long as you give appropriate credit to the original author(s) and the source, provide a link to the Creative Commons license, and indicate if changes were made. The images or other third party material in this article are included in the article's Creative Commons license, unless indicated otherwise in a credit line to the material. If material is not included in the article's Creative Commons license and your intended use is not permitted by statutory regulation or exceeds the permitted use, you will need to obtain permission directly from the copyright holder. To view a copy of this license, visit <a href="https://creativecommons.org/licenses/by/4.0/">https://creativecommons.org/licenses/by/4.0/</a>.

© The Author(s) 2019

Received: 19 July 2019

Revised: 18 September 2019

Accepted article published: 3 October 2019

Published online in Wiley Online Library:

(wileyonlinelibrary.com) DOI 10.1002/pi.5926

# Highly photoemissive polymer-transition metal complexes based on poly(2-hydroxyethyl) methacrylate

Corneliu S Stan,<sup>a\*</sup> Adina Coroaba,<sup>b</sup> Marcel Popa<sup>a,c</sup> and Laura E Ursu<sup>b</sup>

# **Abstract**

The paper presents several new polymer complexes based on poly(2-hydroxyethyl) methacrylate (P-HEMA) and transition metals including Y³+, Eu³+, Tb³+ and Dy³+. Red-, green-, blue- and yellow-emitting polymer complexes with remarkable photoluminescent (PL) properties, high degree of transparency and excellent processability both in bulk and in thin film were prepared and investigated. In the case of the prepared P-HEMA-Eu³+ and P-HEMA-Tb³+ polymer complexes, divinylbenzene was used as a crosslinker resulting a markedly enhanced PL emission, most probably due to the presence of the benzene rings which improve the efficiency of the energy transfer to the cation emissive centres. The prepared polymer complexes were structurally investigated through Fourier transform infrared and X-ray photoelectron spectroscopies while atomic force microscopy was used to study the morphology of the prepared thin films. Steady-state fluorescence spectroscopy and absolute PL quantum yield were used for the investigation of the luminescent properties. The impressive PL emission and the convenience of preparation in bulk or thin films could be important arguments for a wide area of applications ranging from photonic conversion materials in optoelectronic devices (light-emitting diodes, flat-panel displays) to full-colour watermarks on special-purpose papers or PL inks and coatings.

© 2019 Society of Chemical Industry

Keywords: lanthanide complexes; photoemissive polymer complexes; luminescent polymers

# INTRODUCTION

Photoluminescent (PL) materials continue to be the focus of scientific research due to their wide application areas ranging from optoelectronics and medical investigation techniques to special coatings and varnishes. Generally, the past and current research studies are targeting the improvement of emissive properties, long-term stability of initial properties and/or facile synthesis and implementation in various applications.

Among various classes of PL compounds, lanthanide and transition metal complexes 1,2 are arguably some of the most studied as a result of their particular emission features and facile preparation paths. Eu<sup>3+</sup> and Tb<sup>3+</sup> complexes<sup>3,4</sup> are well known for their narrow emission bands arising from their radiative transitions within 4f orbitals,<sup>5</sup> located, respectively, in the red and green regions of the visible spectrum. The sharp emission bands located at 620-623 nm featured by the Eu<sup>3+</sup> cation and 540 nm in case of Tb<sup>3+</sup> are especially useful for optoelectronic devices (e.g. colour displays). In this case, accurate colour reproduction is obtained by additive combination of the three fundamental colours (R, G, B) or in the case of light-emitting diodes (LEDs) for lighting purposes where warm tinted white light is usually preferred. Although the luminescence properties of transition metal complexes may be impressive in certain past or newer reported studies, there are several limitations affecting their implementation potential in the abovementioned application areas. One of them, though not quite the most important, is the difficulty in obtaining a blue emission complex. The reported studies regarding this matter are scarce

and, even in the most promising cases, the emission intensity is too low for practical implementation.<sup>6</sup> Another limiting factor is the difficulty of their use in applications (e.g. optoelectronic devices, special-purpose inks or coatings) where thin films or regular shapes are required. The complexes are usually obtained as powders with high susceptibility for water retention (which, among other drawbacks, severely limits the PL emission); in many cases even short-term exposure to environmental conditions could irreversible alter both their structure and properties. Although these problems could be addressed by embedding the complexes in polymer or silica matrices, the resulted photoemissive composites<sup>7,8</sup> may still have problems in terms of emission efficiency, processability, transparency or long-term stability.

- \* Correspondence to: CS Stan, Department of Natural and Synthetic Polymers, 'Gheorghe Asachi' Technical University of lasi, Faculty of Chemical Engineering and Environmental Protection Cristofor Simionescu, Prof.dr.docent Dimitrie Mangeron 73 Ave., 700050, lasi, Romania. E-mail: stancs@tuiasi.ro
- a Department of Natural and Synthetic Polymers, 'Gheorghe Asachi' Technical University of lasi, Faculty of Chemical Engineering and Environmental Protection Cristofor Simionescu, Iasi, Romania
- b Centre of Advanced Research in Bionanoconjugates and Biopolymers, 'Petru Poni' Institute of Macromolecular Chemistry of Romanian Academy Grigore Ghica, Iasi, Romania
- c Academy of Romanian Scientists, Bucharest, Romania



www.soci.org



Photoemissive polymers have been extensively investigated for their significant application potential in printed organic electronics, especially for the development of polymer LED displays and solar cells. Facile processability from solution yielding quality thin films and high emission intensities are, among others, the most important advantages from the targeted applications perspective. Conjugated polymers with sp<sup>2</sup> carbons in the main chain such as polyphenylenevinylene,<sup>10</sup> polyfluorene<sup>11</sup> and  $poly(p-phenylene)^{12}$  are typical examples of emissive polymers. Non-conjugated polymers such as poly(vinyl carbazole) (PVK)<sup>13</sup> are also intensively studied. In the case of PVK, various functional groups are attached to the polymer backbone or functional compounds are doped within the PVK matrix. Intense PL emission was achieved by doping PVK films with C<sub>60</sub> and C<sub>70</sub> fullerenes through solution casting, under 488 nm laser radiation.<sup>14</sup> Various transition metal complexes were doped in host PVK matrices in order to obtain light-emitting layers in organic LED devices. For instance, intense red emission was achieved by doping a PVK matrix with Eu(FTA)<sub>3</sub>Phen complex.<sup>15</sup> Another approach was the attachment of Ir complexes to the polymeric side chain in order to prepare fluorescent/phosphorescent emitting layers in organic LED devices.<sup>16</sup> One interesting study reported the use organometallic bismuth (e.g. triphenylbismuth) embedded in a PVK matrix as a low-cost scintillator for gamma-ray spectroscopy.<sup>17</sup> Polymer composites using conjugated polymers as host (e.g. MEH-PPV) and semiconductor quantum dots (e.g. CdSe, CdS) are expected to play a key role in future developments of light-emitting and light-harvesting devices. 18 2-Hydroxyethyl methacrylate (HEMA) was used to prepare crosslinked Eu(III)-HEMA hydrogels<sup>19</sup> while carbon dots were embedded in a poly(HEMA) – acrylic acid matrix leading to highly fluorescent hydrogels.<sup>20</sup>

Luminescent polymer complexes with transition metal cations have been less investigated compared with the classes of luminescent materials mentioned above. One possible explanation is the limited number of available monomers as ligands with a favourable chemical configuration for complexation of transition metals, especially the lanthanide series that could yield remarkable luminescent emission if proper complexation and sensitization are achieved. Nonetheless, successful preparation paths and polymer complex formulations have been reported, many of them with notable results. In an earlier approach, PL polycarboxylate complexes of Tb<sup>3+</sup> and Eu<sup>3+</sup> were prepared in aqueous solution. The prepared polymer complexes present an interesting proportional enhancement of their luminescent emission in the presence of hydroxyl functionality, thus providing a convenient modality for the determination of hydroxyl group concentration in certain aqueous solutions.<sup>21</sup> In a more recent study, an amphiphilic block copolymer with diketone as chelating agent for Gd<sup>3+</sup> and Eu<sup>3+</sup> was prepared and investigated as a promising magnetic resonance imaging/fluorescent agent aimed at medical investigations.<sup>22</sup> A near-infrared-emitting polymer complex was prepared through coordination of Nd3+ with 2-methyl-5-phenylpent-1-en-3,5-dione and allyl-3-oxobutanoate which was further copolymerized by free radical polymerization with styrene and N-vinylcarbazole.<sup>23</sup>

In the work reported here, red (R), green (G), blue (B) and yellow (Y) emissive polymer complexes were prepared and investigated. HEMA was used for the initial preparation of  $Eu^{3+}$ ,  $Tb^{3+}$ ,  $Dy^{3+}$  and  $Y^{3+}$  complexes which were further photopolymerized in bulk or thin films. In the case of the  $Eu^{3+}$  and  $Tb^{3+}$  polymer complexes, additional experiments were performed using p-divinylbenzene

(*p*-DVB) as crosslinker resulting in markedly enhanced PL emission. The prepared polymer complexes are transparent in environmental lighting conditions becoming highly luminescent under UV light. As will be further discussed, the red-emitting Eu<sup>3+</sup> polymer complex, green-emitting Tb<sup>3+</sup> polymer complex and yellow-emitting Dy<sup>3+</sup> polymer complex present narrow emission bands specific for radiative transitions within 4f orbitals, while in the case of the blue-emitting Y<sup>3+</sup> polymer complex the wide band emission involves a different PL mechanism. Through simply mixing in certain proportions R-, G- and B-emitting polymer complexes, any colour emission or warm/cold tinted white light are achievable.

# **EXPERIMENTAL**

# **Materials**

HEMA as ligand/monomer, 2-hydroxy-1-[4-(2-hydroxyethoxy)phen yl]-2-methyl-1-propanone (Irgacure 2959) as polymerization photoinitiator, p-DVB (85%), and europium chloride (EuCl $_3$ ·H $_2$ O, 99.9%), terbium chloride (TbCl $_3$ ·6H $_2$ O, 99.99%), dysprosium chloride (DyCl $_3$ ·H $_2$ O, 99.9%) and yttrium chloride (YCl $_3$ ·H $_2$ O, 99.99%) as cation sources were purchased from Sigma-Aldrich. High-purity MilliQ water and anhydrous N,N-dimethylformamide (DMF; 99.8%) were used as reaction and polymerization mediums.

### Preparation of luminescent polymer complexes

In the first step the complexes of HEMA with the selected trivalent cations (Eu<sup>3+</sup>, Tb<sup>3+</sup>, Dy<sup>3+</sup>, Y<sup>3+</sup>) were prepared at a 1/3 metal-to-ligand ratio. The metal chlorides are easily soluble in both water and DMF along with HEMA ligand and photopolymerization initiator. DMF was used only in case of the DVB-crosslinked polymer complexes. The complexation reaction was carried out in a glass beaker provided with magnetic stirrer, under heating (40-45 °C) for about 5-6 h. Typically, 1 mmol of lanthanide salt was mixed with 3 mmol of HEMA in about 5 mL of water, resulting in complexes with the general formula  $[M(L)_3(H_2O)_3]$   $(M = Eu^{3+}, Tb^{3+}, Dy^{3+}, Y^{3+}; L = HEMA).$ Further, 0.005 g of Irgacure 2959 was added under stirring and dim lighting conditions until complete dissolution of the photoinitiator (about 15-25 min). Other photoinitiators were tested (including 1-hydroxycyclohexylphenylketone (Irgacure 184) and  $\alpha, \alpha$ -dimethoxy- $\alpha$ -phenylacetophenone (Irgacure 651)). However, the quality of the resulting polymer complexes was less satisfactory in terms of both PL and morphological properties, most probably due to certain unwanted interactions (for instance, the structural configuration of Irgacure 184 was found to be favourable for Ln<sup>3+</sup> complexation). For the preparation of bulk regular-shaped polymer complexes, the resulting mixture was poured in a mould (e.g. a cut plastic syringe) and exposed to irradiation using a 320–360 nm laboratory UV lamp for ca 20–40 min. The resulting bulk polymer complexes are presented in Fig. 1. As can be seen, with the exception of poly(DyHEMA) the other three polymer complexes are highly PL. The overall PL intensity could be easily varied by dilution of the prepared complexes with additional quantities of HEMA prior to the polymerization phase.

For the crosslinked polymer complexes, 0.2 mmol of *p*-DVB was added under stirring prior to the photopolymerization phase, the reaction medium being DMF. As can be seen from Fig. 2, the PL emission intensity is markedly enhanced in the case of poly(EuHEMA) and poly(TbHEMA), whereas in the case of poly(YHEMA) no PL intensity enhancement was observed. The



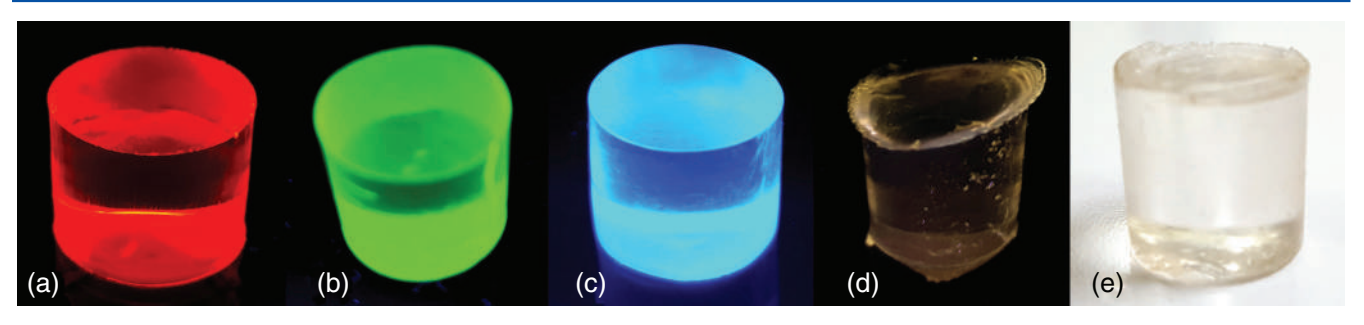


Figure 1. Prepared PL bulk polymer complexes (a) poly(EuHEMA), (b) poly(TbHEMA), (c) poly(YHEMA) and (d) poly(DyHEMA) under 330 nm UV excitation and (e) under ambient lighting conditions.

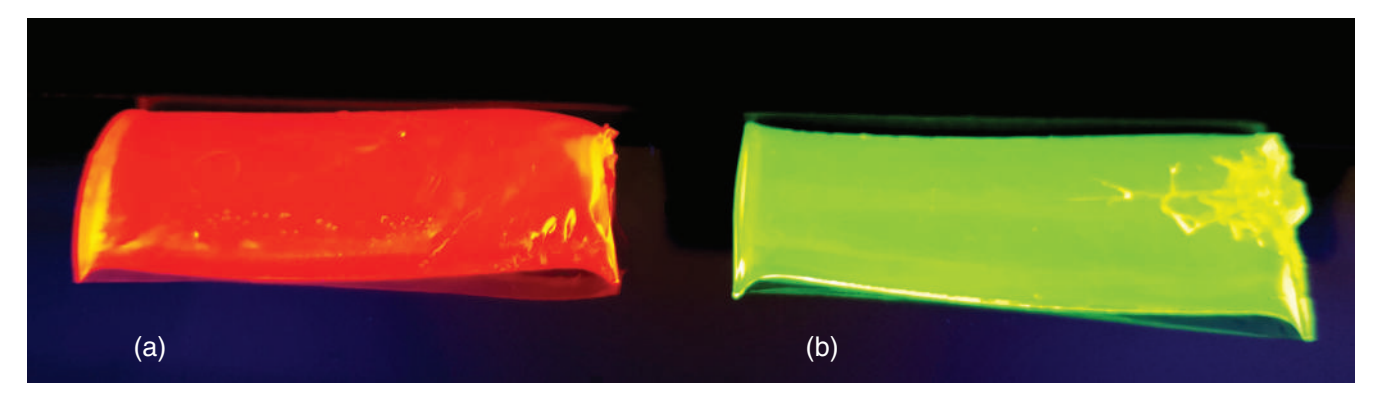


Figure 2. p-DVB-crosslinked (a) poly(EuHEMA) and (b) poly(Tb(HEMA) under 330 nm UV excitation.

crosslinked polymer complexes are also transparent but with a slight yellowish tint.

To obtain thin polymer films, a solution containing the photoinitiator was spray/spin-coated on the substrate and exposed to UV light for about 15–25 min depending on the thickness of the layer. Figure 3 presents crosslinked poly[(EuHEMA)DVB] sprayed as a thin film on a flexible poly(ethylene terephthalate) sheet which was further dried under ambient conditions. As can be seen, the PL emission remains very intense and the film is homogenous despite the simple method used for spraying on the substrate.

### Methods

X-ray photoelectron spectroscopy (XPS) was performed with a KRATOS Axis Nova, using Al K $\alpha$  radiation, with 20 mA current and 15 kV voltage. The incident X-ray beam was focused on a 0.7 mm × 0.3 mm area of the surface. The wide-scan XPS spectra were collected in the range 10-1200 eV with a resolution of 1 eV and a pass energy of 160 eV. The high-resolution spectra for all the elements identified from the survey spectra were collected using a pass energy of 20 eV and a step size of 0.1 eV. Fourier transform infrared (FTIR) spectra were recorded in the range 400-4000 cm<sup>-1</sup>, using a Bruker Vertex 70 spectrometer. The steady-state fluorescence, chromaticity and absolute PL quantum yields (PLQY) were recorded using a Horiba Fluoromax 4P provided with a Quanta- $\phi$  integration sphere. AFM imaging was performed using a Ntegra Spectra NT-MDT (Russia) instrument operated in tapping mode. Silicon cantilever tips (NSG 10) with a resonance frequency of 140-390 kHz, a force constant of 5.5-22.5 Nm<sup>-1</sup> and 10 nm tip curvature radius were used. The samples were prepared by spin-coating on glass slides using Laurell WS-400-6NPP equipment.

# **RESULTS AND DISCUSSION**

Figure 4 presents the two stages of the preparation path and the suggested structure of the polymer complexes. The coordination number of the central cation within the  $[M(L)_3(H_2O)_3]$  complexes is nine through the bidentate behaviour of the HEMA ligand and also through the presence of three water molecules in the first coordination sphere.<sup>24</sup> Covalent bonding is established between the central cation and the oxygen atom in the hydroxyl group located on the side of the HEMA monomer chain, while coordinative bonding is established with the oxygen atom in the carbonyl group. As will be further discussed, the favourable configuration achieved through complexation allows an efficient sensitization of the Eu<sup>3+</sup>, Tb<sup>3+</sup> and Dy<sup>3+</sup> central cations thus triggering their specific narrow radiative transitions within 4f orbitals; in the case of the blue-emitting polymer complex the wider band emission is due to the influence of the Y3+ central cation on the excited states of the surrounding ligands.

# **XPS investigation**

XPS investigation revealed the bonding established for various atomic species and the structure of the polymer complexes as described above. The recorded wide-scan spectra revealed the relative atomic and mass concentrations (Table 1) for the poly(EuHEMA), poly(TbHEMA) and poly(YHEMA) polymer complexes. The high-resolution C 1s (Fig. 5) and O 1s (Fig. 6) spectra revealed the relative atomic and mass concentrations of various types of bonding within the polymer complexes (Tables 2 and 3).

The recorded results are in good agreement with the proposed structures of the polymer complexes. The high-resolution O 1s spectra revealed the establishment of covalent bonding between



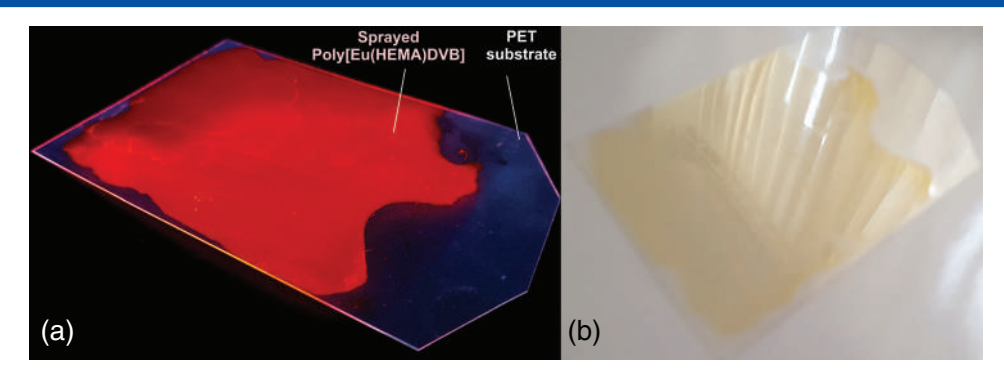


Figure 3. Thin poly[(EuHEMA)DVB] film deposited on poly(ethylene terephthalate) foil (a) under 330 nm UV excitation and (b) under ambient lighting conditions.

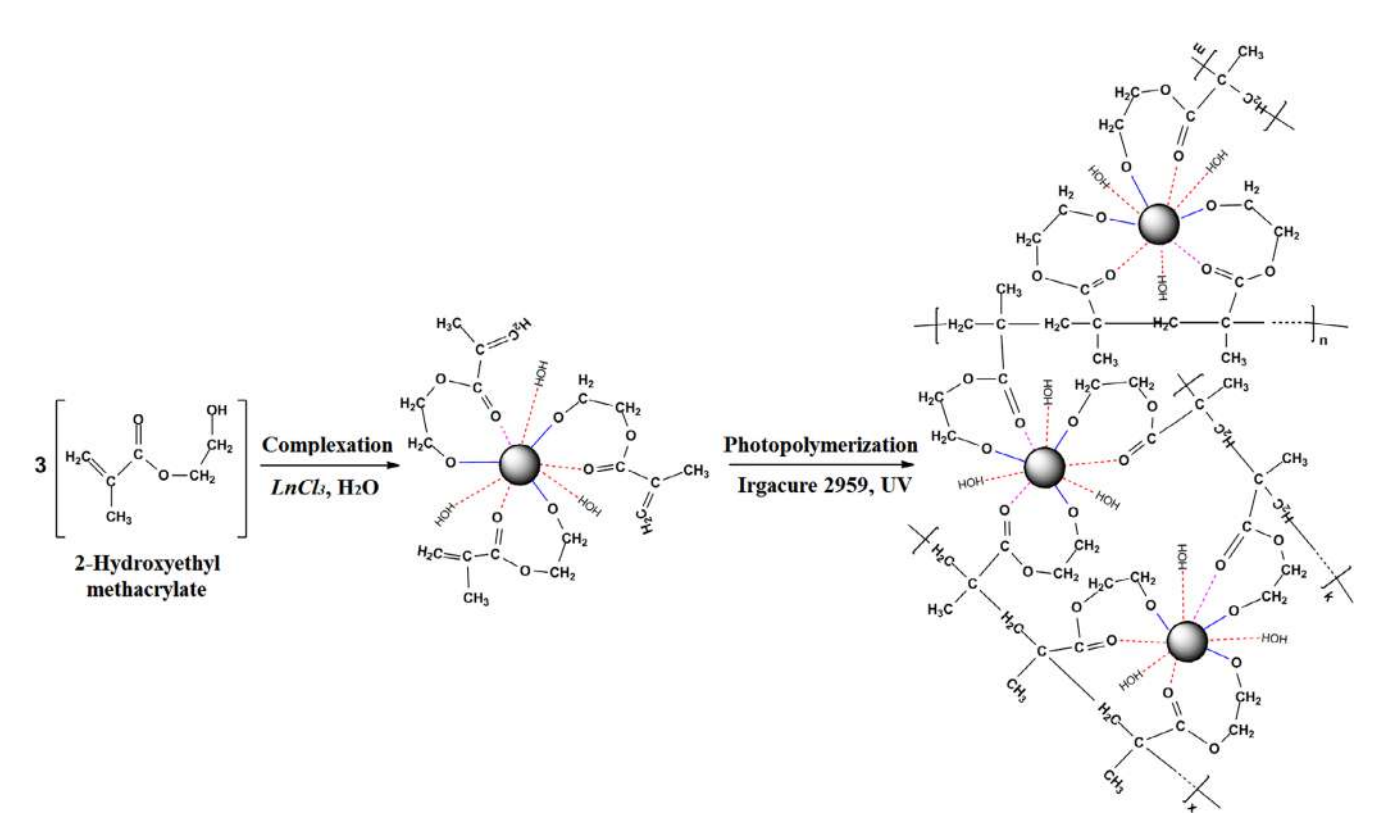


Figure 4. Preparation path and suggested structure of the polymer complexes.

the central cation ( $Eu^{3+}$ ,  $Tb^{3+}$ ,  $Y^{3+}$ ) and oxygen atom and also coordinative bonding between the same central cations and the oxygen atoms within the carbonyl groups.

# **FTIR** investigation

Investigation of the recorded FTIR spectra revealed the interactions occurring between the HEMA ligand and the selected trivalent cations. Figure 7 presents the recorded spectra for the non-complexed poly(HEMA) and the prepared polymer complexes, in each case the significant absorption peaks being included. The initial investigation of the free ligand was required to emphasize the modifications occurring during the complexation process.

In the higher wavenumber region of the recorded spectra the characteristic peaks of C—H, C—C and C—C bonds (2850–3150 cm<sup>-1</sup>) are unchanged or slightly displaced most

probably due to the rearrangements occurring as a result of complexation. The broad peaks recorded in the range 3522-3451 cm<sup>-1</sup> are typical for the presence of —OH groups due to the remnant water retained during the preparation process. Also, water is usually present in the inner/outer coordination sphere of the central trivalent lanthanide cations.<sup>24</sup> Significant changes arising from the complexation process could be easily noticed in the lower wavenumber region of the recorded spectrum for each prepared complex. Besides displacements of various peaks due to the rearrangements of various groups, new absorption peaks appear due the establishment of covalent bonds between the central trivalent cation and oxygen atom from the former -OH group located in the side chain of the free HEMA ligand. These new established covalent bonds are supported by the presence of moderate intensity peak located in the range 482-474 cm<sup>-1</sup>, 25 which is clearly visible in each spectrum of the prepared complexes, while in the case of non-complexed



Table 1. Overall C, O, M (Eu,	Tb, Y) concen	trations recor	ded for the pr	repared polym	ner complexes	;				
		Poly(EuHEMA	)		Poly(TbHEMA)			Poly(YHEMA)		
Element	С	0	Eu	С	0	Tb	C	0	Y	
Atomic concentration (%)	79.41	8.11	2.47	80.52	18.16	1.32	78.08	19.88	2.04	
Mass concentration (%)	58.90	17.89	23.21	65.93	19.81	14.26	65.25	22.13	12.61	

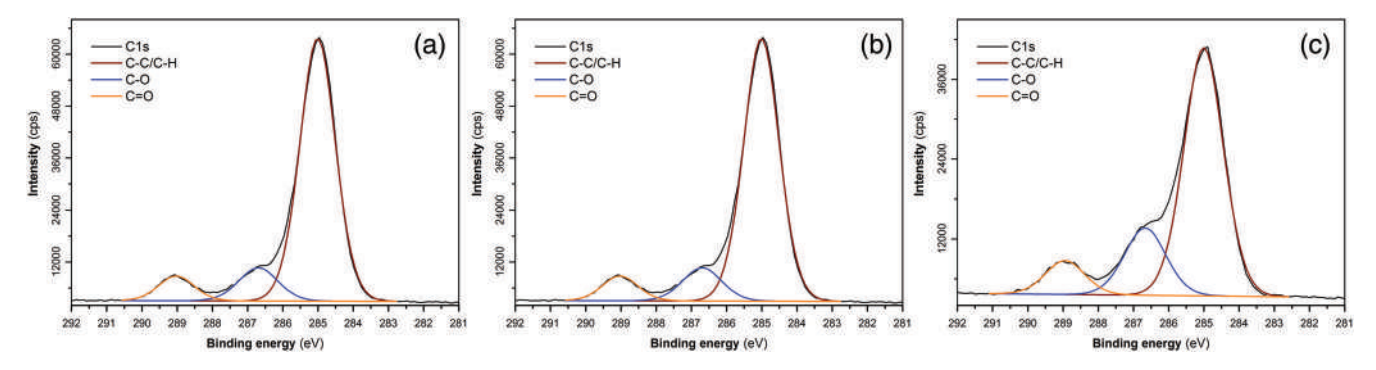


Figure 5. High-resolution C 1s spectra recorded for (a) poly(EuHEMA), (b) poly(TbHEMA) and (c) poly(YHEMA) polymer complexes.

poly(HEMA) is absent. The stretching vibrations (valence) of carbonyls (O=C<) having an intense characteristic band with a maximum peak at 1728 cm<sup>-1</sup> are shifted to 1724–1690 cm<sup>-1</sup> in the case of the prepared complexes. The specific carbonyl peak at 1728 cm<sup>-1</sup> for the non-complexed poly(HEMA) appears split in two in the case of the polymer complexes in the form of a shoulder peak located at 1639–1657 cm<sup>-1</sup> explained by the coordination bonds occurring between the central cation and oxygen atoms.<sup>26</sup> The results are in strong agreement with those provided by the XPS investigation, revealing the coordination of the trivalent cations and the formation of the polymer complexes.

# Fluorescence analysis

While the PL emission of all the prepared polymer complexes is quite remarkable, the mechanisms that govern their radiative transitions may be divided into two main categories. Poly(EuHEMA), poly(TbHEMA) and poly(DyHEMA) polymer complexes fall in one category since their emission occurs as a 'classic' metal-centred luminescence with characteristic narrow emission bands arising from inner transitions within 4f orbitals. Lanthanide luminescence is possible only in that the

energy levels supplied by the excited states of the surrounding ligands to the emissive centre are beyond the resonance levels specific for a certain trivalent lanthanide cation. For example, in the case of Eu<sup>3+</sup> the main resonance level is <sup>5</sup>D<sub>0</sub>  $(17.250 \,\mathrm{cm}^{-1})$  while in the case of Tb<sup>3+</sup> it is  $^5D_4$   $(20.430 \,\mathrm{cm}^{-1}).^{27}$ The luminescence is due to a ligand-to-metal charge transfer mechanism, the sensitization induced by the HEMA ligand proving to be effective for all three lanthanide cations. The presence of water molecules in the first coordination sphere seems to have little effect on the efficiency of the energy transfer to the central cation. Although it is well known that the vicinity of OH oscillators favours vibrational coupling leading to non-radiative deactivation, these processes are especially efficient in aqueous solutions. Since the luminescence of the prepared polymer complexes is achieved in bulk or thin layers, the influence of the OH oscillators is diminished to a degree which will not significantly alter the efficiency of the radiative processes.

In the second main category is included the poly(YHEMA) polymer complex whose PL properties cannot be attributed to transition within the central cation. While its recorded luminescence is strong, the characteristic emission spectrum differs significantly when compared to those recorded for the polymer complexes

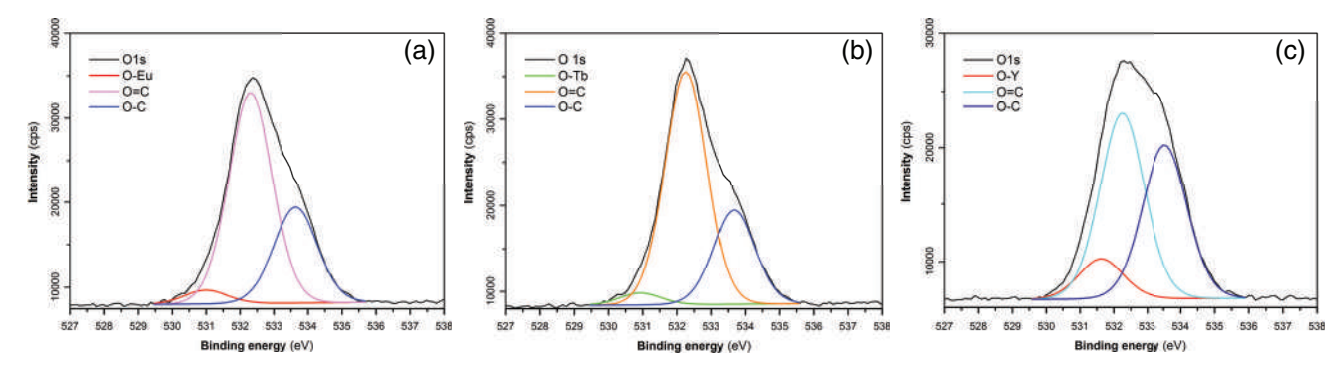


Figure 6. High-resolution O 1s spectra recorded for (a) poly(EuHEMA), (b) poly(TbHEMA) and (c) poly(YHEMA) polymer complexes.



SCI www.soci.org CS Stan et al.

**Table 2.** Concentrations of various groups/bonding within the prepared polymer complexes according to high-resolution C 1s spectra

Poly(EuHEMA)				Poly(TbHEM	A)		Poly(YHEMA)		
Group/bonding	O-C	O=C	C-C/C-H	O-C	O=C	C-C/C-H	O-C	O=C	C-C/C-H
Mass concentration (%)	13.84	6.64	79.52	11.2	7.65	81.06	20.07	9.59	70.34

**Table 3.** Concentrations of various groups/bonding within the prepared polymer complexes according to high-resolution O 1s spectra

		Poly(EuHEMA)			Poly(TbHEMA)			Poly(YHEMA)	ıA)			
Group/bonding	O-C	O=C	O-Eu	O-C	O=C	O-Tb	O-C	O=C	O-Y			
Mass concentration (%)	29.79	65.91	4.31	27.81	68.64	3.54	40.49	48.91	10.60			

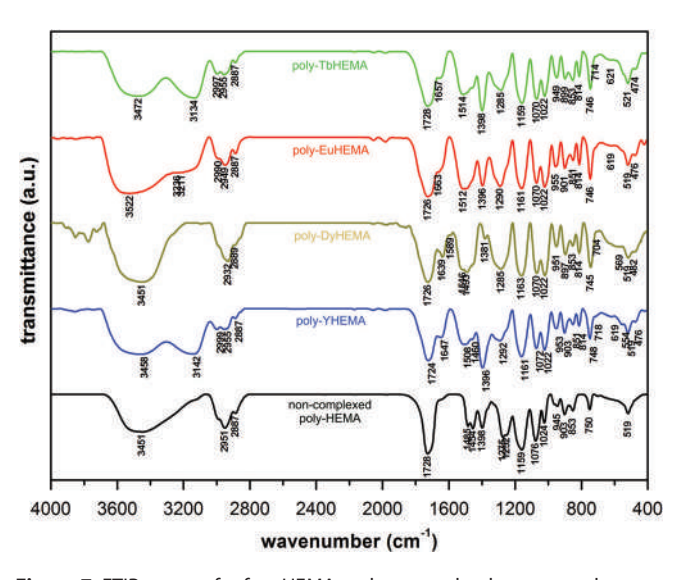


**Figure 7.** FTIR spectra for free HEMA and prepared polymer complexes.

in the first category. Its PL emission is rather a result of the influence of the heavy cation  $(Y^{3+})$  on the excited states of the ligand.<sup>28</sup>

In Fig. 8(a) the recorded excitation/emission spectra of poly(EuHEMA) and poly[(EuHEMA)DVB] are presented. As mentioned above, the presence of the benzene rings in the DVB-crosslinked polymer complexes provides an even better sensitization of the central trivalent cation, the emission peaks being more intense as can be noted from the recorded spectra. The most significant emission peaks are located at 590 and 614 nm due the  ${}^5D_0 \rightarrow {}^7F_1$  and  ${}^5D_0 \rightarrow {}^7F_2$  transitions. The  $^{5}D_{0} \rightarrow ^{7}F_{1}$  parity-allowed magnetic dipole transition is unaffected by the surrounding symmetry, but the most intense  ${}^5D_0 \rightarrow {}^7F_2$ electrical-dipole-allowed hypersensitive transition is known to be highly affected by surrounding degree of symmetry. It is widely accepted that the ratio between the emission intensities of  ${}^5D_0 \rightarrow {}^7F_2$  and  ${}^5D_0 \rightarrow {}^7F_1$  is an asymmetry parameter for the Eu<sup>3+</sup> surrounding sites.<sup>29</sup> All the excitation peaks were recorded in the UVB-UVA regions, with the most intense peak located at 332-334 nm.

In the case of the poly(TbHEMA) and the poly[(TbHEMA)DVB] polymer complexes (Fig. 8(b)), the most intense emission peak

is located at 542 nm due to the  ${}^5D_4 \rightarrow {}^7F_5$  transition while a medium intensity peak is recorded at 487 nm due the  ${}^5D_4 \rightarrow {}^7F_6$  transition. The less intense 582 and 619 nm peaks are due to the  ${}^5D_4 \rightarrow {}^7F_4$  and  ${}^5D_4 \rightarrow {}^7F_3$  transitions. As can be noted for the DVB-crosslinked polymer complex, the peak intensity is markedly enhanced. The recorded excitation spectra revealed an intense broader peak located also in the UVB region at 317–332 nm.

For poly(DyHEMA) (Fig. 8(c)), the two significant emission peaks are due to  $^4\mathrm{F}_{9/2} \rightarrow ^6\mathrm{H}_{13/2}$  (571 nm) and  $^4\mathrm{F}_{9/2} \rightarrow ^6\mathrm{H}_{15/2}$  (477 nm). The recorded excitation spectrum revealed a less broad peak located also in the UVB region at 317–323 nm. In this case, the emission intensity is much lower compared with the other prepared polymer complexes.

An interesting situation was encountered in the case of poly(YHEMA) where, as mentioned above, the wider intense emission peak located at 427–450 nm (Fig. 8(d)) is due to the influence of the presence of a heavy cation on the excited states of the surrounding ligands. In the case of this polymer complex a particular behaviour was highlighted since the location of the emission peak is dependent on the excitation wavelength. Thus, at 345 nm excitation the wide range emission peak is located at 427 nm, while at 360 and 370 nm excitation the peaks are located at 441 and 450 nm, respectively. The situation is less usual in the case of a 'classic' fluorophore, being often encountered in the case of certain nanostructures such as carbon dots or graphene quantum dots. The maximal excitation peak is located at 382 nm, having also a broad shape due to the observed excitation-dependent emission.

Table 4 lists the recorded absolute PLQY for each prepared polymer complex. As can be seen, the values are quite notable for poly[(TbHEMA)DVB] and poly[(EuHEMA)DVB] being in accordance with the steady-state fluorescence investigations. The PLQY values, with the exception of that for poly(DyHEMA), are high enough to be interesting for practical applications.

# **AFM** investigation

As already mentioned, the polymer complexes could be easily processed into thin films. This capability is highly important for a wide range of applications, especially in optoelectronic devices where thin photonic conversion layers are required. Figure 9 shows the AFM images recorded for two of the prepared polymer complexes: poly[(EuHEMA)DVB] and poly(YHEMA). As can be



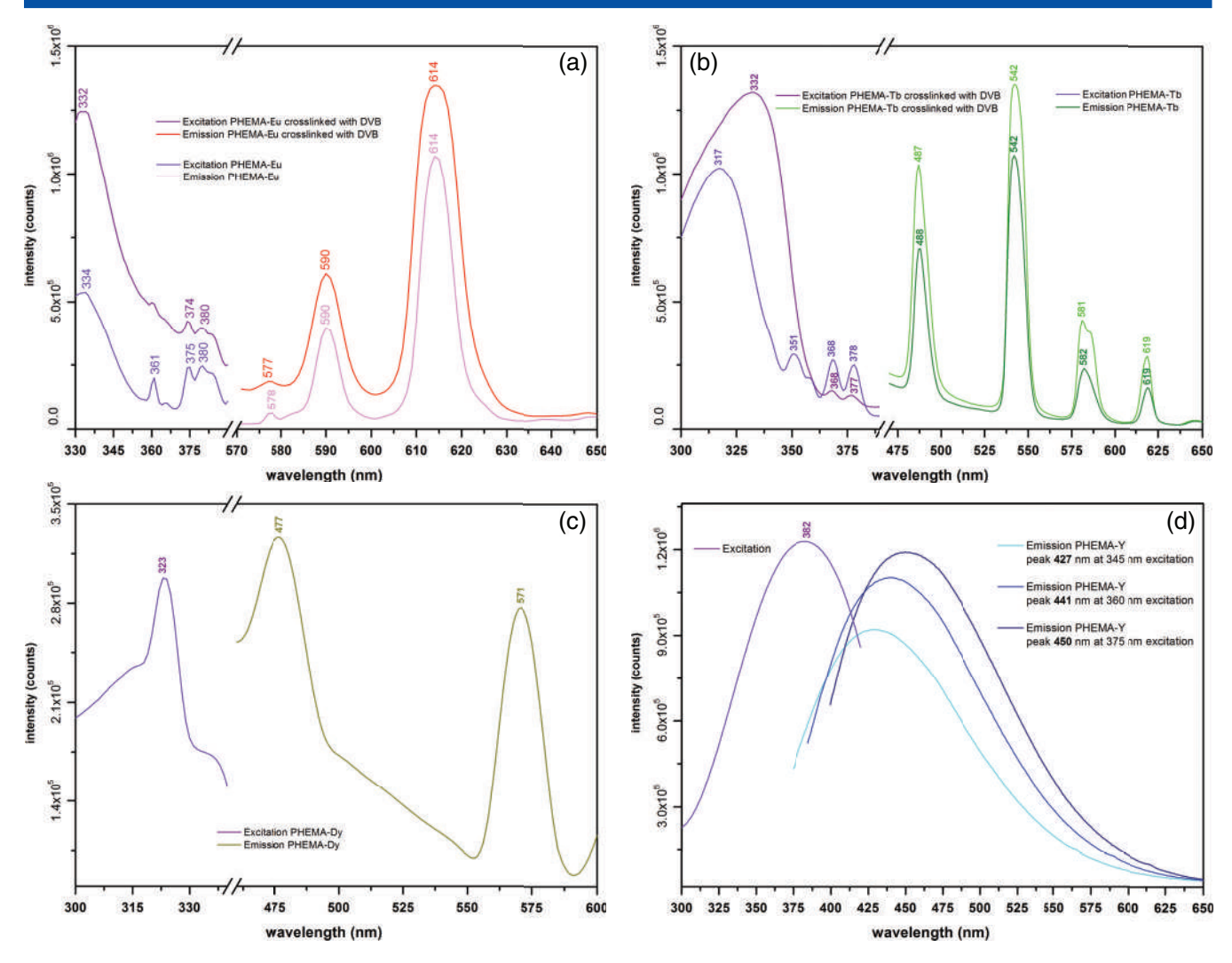


Figure 8. Excitation/emission spectra recorded for (a) poly(EuHEMA)/poly[(EuHEMA)DVB], (b) poly(TbHEMA)/poly[(TbHEMA)DVB], (c) poly(DyHEMA) and (d) poly(YHEMA)xu

<b>Table 4.</b> Absolute PLQY recorded complexes	for the investigated polymer
Polymer complex	Absolute PLQY (%)/ excitation wavelength (nm)
Poly[(TbHEMA)DVB] Poly[(EuHEMA)DVB] Poly(TbHEMA) Poly(EuHEMA) Poly(YHEMA) Poly(DyHEMA)	69.07/330 58.35/330 51.17/320 44.00/330 38.05/375 4.7/320

seen, the thin films prepared from poly[(EuHEMA)DVB] are very smooth and homogenous, most of the observed height differences being due to the inherent irregularities of the poly(ethylene terephthalate) substrate. In the case of poly(YHEMA), the results are notably good, but several aggregated entities are present most probably due to an agglomeration occurring during the drying phase.

# **CONCLUSIONS**

The paper reports six new highly luminescent polymer complexes based on poly(HEMA) and transition metals Y<sup>3+</sup>, Eu<sup>3+</sup>, Tb<sup>3+</sup> and Dy<sup>3+</sup>. All the prepared polymer complexes present remarkable PL properties, high degree of transparency and excellent processability both in bulk and thin films. The DVB-crosslinked Eu<sup>3+</sup> and Tb<sup>3+</sup> polymer complexes present enhanced emission intensity due to the presence of benzene rings, which further enhance the radiative transitions within the trivalent lanthanide cations as luminescent centres. The coordination of the central cations is clearly evidenced using the selected structural investigation techniques while the investigated morphology revealed the excellent ability to be processed into thin films. Another notable advantage is their emission in the three fundamental colours (R, G, B) with high spectral purity emission bands in the case of poly(EuHEMA)/poly[(EuHEMA)DVB] and poly(TbHEMA)/poly[(TbHEMA)DVB]. The blue-emitting poly(YHEMA) presents an unusual feature of excitation-dependent emission which is less encountered in case of classic PL materials. Their impressive PL emission and the convenience of preparation in bulk or thin films could be important arguments for a wide area of applications ranging from photonic conversion materials in optoelectronic devices (LEDs, flat-panel displays) to



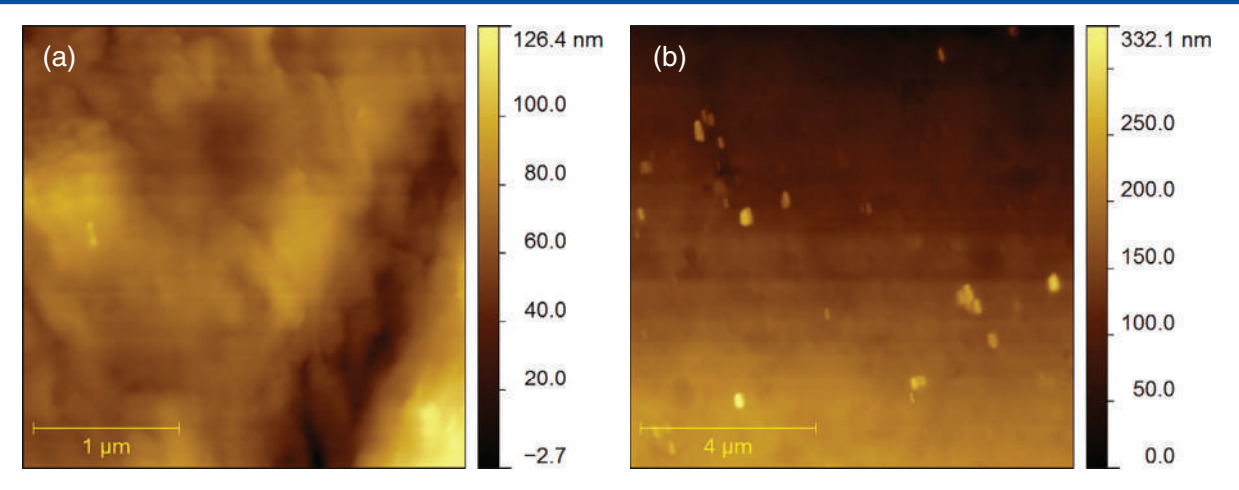


Figure 9. AFM images recorded for (a) poly[(EuHEMA)DVB] and (b) poly(YHEMA).

full-colour watermarks on special-purpose papers or PL inks and coatings.

# **ACKNOWLEDGEMENTS**

This work was supported by a grant of the Romanian National Authority for Scientific Research and Innovation, CNCS/CCCDI-UEFISCDI, PNCDI III., project no. PN-III-P2-2.1-PED-2016-0760, 77PED/2017.

# REFERENCES

- 1 Cotton SA, *Lanthanide and Actinide Chemistry*. John Wiley, Chichester, England (2006).
- 2 Armelao L, Quici S, Barigelletti F, Accorsi G, Bottaro G, Cavazzini M et al., Coord Chem Rev 254:487 – 505 (2010).
- 3 Leonard JP and Gunnlaugsson T, J Fluoresc 15:585-595 (2005).
- 4 Grushin V, Herron N, Petrov VA, Radu NS and Wang Y. Photoactive lanthanide complexes with phosphine oxides, phosphine oxide sulfides, pyridine N-oxides and phosphine oxide pyridine N-oxides and devices made with such complexes. US Patent 7063903B2 (2006).
- 5 Lattuada L, Barge A, Cravotto G, Giovenzana GB and Tei L, *Chem Soc Rev* **40**:3019 3049 (2011).
- 6 Canaj AB, Tsikalas GK and Philippidis A, *Dalton Trans* **43**:12486 12494 (2014)
- 7 Kalyani NT, Dhoble SJ and Pode RB, Adv Mater Lett 2:65-70 (2011).
- 8 Singh AK, Singh SK, Mishra H, Prakash R and Rai SB, *J Phys Chem B* **114**:13042 13051 (2010).
- 9 Sekine C, Tsubata Y, Yamada T, Kitano M and Doi S, Sci Technol Adv Mater 15:034203 (2014).
- 10 Pichler K, Halliday DA, Bradley DDC, Burn PL, Friend RH and Holmes AB, J Phys Condens Matter 5:7155 (1993).

- 11 Craig MR, de Kok MM, Hofstraat JW, Schenning APHJ and Meijer EW, J Mater Chem 13:2861–2862 (2003).
- 12 Remmers M, Müller B, Martin K and Räder HJ, Macromolecules 32:1073–1079 (1999).
- 13 Upadhyay P, Ramrakhiani M and Bisen DP, JOL **128**:1595 1600 (2008).
- 14 Li GZ and Minami N, Chem Phys Lett 331:26-30 (2000).
- 15 Zhang Y, Li C, Shi H, Du B, Yang W and Cao Y, *New J Chem* **31**:569–574 (2007).
- 16 Wang XY, Kimyonok A and Weck M, Chem Commun:3933 3935 (2006). http://dx.doi.org/10.1039/B609382E
- 17 Rupert BL, Cherepy NJ, Sturm BW, Sanner RD and Payne SA, Europhys Lett 97:22002 (2002).
- 18 Guzelturk B and Demir HV, J Phys Chem Lett 6:2206-2215 (2015).
- 19 Bradberry SJ, Dee G, Kotova O, McCoy CP and Gunnlaugsson T, Chem Commun 55:1754–1757 (2019).
- 20 Wang J, Ma X, Wei L, Zhu X, Zhu Y, Wang G et al., Colloid Polym Sci 296:745-752 (2018).
- 21 Okamoto Y, Makromol Chem Macromol Symp 59:83-98 (1992).
- 22 Cao F, Huang T, Wang Y, Liu F, Chen L, Ling J *et al.*, *Polym Chem* **6**:7949–7957 (2015).
- 23 Berezhnytska O, Savchenko I, Ivakha N, Trunova O, Rusakova N, Smola S et al., Nanoscale Res Lett 12:338 (2017).
- 24 Kowall T, Foglia F, Helm L and Merbach AE, *J Am Chem Soc* **117**:3790–3799 (1995).
- 25 Nengwu Z, Long P, Maiming L and Robinson WR, *Spectrosc Lett* **30**:61–70 (1997).
- 26 Iravani E, Nami N, Nabizadeh F, Bayani E and Neumüller B, *Bull. Korean Chem. Soc.* **34**:3420–3424 (2013).
- 27 Binnemans K, Chem Rev 109:4283-4374 (2009).
- 28 Vogler A and Kunkely H, Inorg Chim Acta 359:4130-4138 (2006).
- 29 Henrie DE, Fellows RL and Choppin GR, Coord Chem Rev 18:199–224 (1976).
- 30 Liu G and Jacquier B, Spectroscopic Properties of Rare Earth in Optical Materials. Springer, New York (2005).



# Facile preparation of highly luminescent composites by polymer embedding of carbon dots derived from N-hydroxyphthalimide

Corneliu Sergiu Stan<sup>1,\*</sup> , Petronela Gospei Horlescu<sup>1</sup>, Laura Elena Ursu<sup>2</sup>, Marcel Popa<sup>1</sup>, and Cristina Albu<sup>1</sup>

**Received:** 5 May 2016 **Accepted:** 19 August 2016

© Springer Science+Business Media New York 2016

# **ABSTRACT**

Highly luminescent composites were prepared through embedding newly developed carbon dots (C-Dots) derived from N-hydroxyphthalimide in PS, PVC and PC polymer matrices. N-hydroxyphthalimide was found to be an excellent precursor for obtaining C-Dots through a simple pyrolytic process. The C-Dots prepared by the described method are highly luminescent with an absolute quantum yield of 79.95 % which is among the highest values reported up to date. The resulted composites preserve the remarkable photoluminescent properties of the embedded C-Dots. The composites were processed in thin films or various shaped monoliths. Prior to embedment, the composition and morphology of the prepared C-Dots were investigated by XPS, FT-IR, P-XRD, DLS TEM and fluorescence spectroscopy whereas the prepared composites were investigated by AFM. Due to their truly remarkable photoluminescent properties and facile fabrication, the prepared C-Dots and related composites could be of interest for applications ranging from sensors to solar energy conversion and light-emitting devices. As will be described later, one suggested straightforward application is the UV protection of various sensitive surfaces provided by thin layers of prepared composites.

# Introduction

Carbon dots with their tunable photoluminescence (PL) located in the lower-mid region of the visible spectrum, chemical inertness, lack of toxicity and

facile preparation [1] should provide an interesting starting point for applications ranging from optoelectronics, sensors to new formulations of assays for bioimaging. Despite their most interesting feature, the excitation wavelength-dependent PL emission, the mechanism underneath this behaviour is still a

Address correspondence to E-mail: stancs@ch.tuiasi.ro

DOI 10.1007/s10853-016-0320-y

Published online: 30 August 2016



<sup>&</sup>lt;sup>1</sup> Faculty of Chemical Engineering and Environmental Protection, Gh. Asachi Technical University, D. Mangeron 73 Ave., 700050 Iasi, Romania

<sup>&</sup>lt;sup>2</sup>Centre of Advanced Research in Bionanoconjugates and Biopolymers, "Petru Poni" Institute of Macromolecular Chemistry of Romanian Academy, Grigore Ghica Voda 41A Alley, 700487 Iasi, Romania

subject of investigation. One of the accounted mechanisms emphasizes the role of quantum confinement effect similar to semiconductor QD's [2] while another proposed approaches rely on radiative transitions occurring in various functional groups located on the surface of the C-Dots [3]. Some very recent studies attribute the origin of the carbon dot photoluminescence to certain organic fluorophores created during the thermal destruction of the primary precursor. Thus, through investigation of the reaction products resulted from the one pot thermal processing of the citric acid and ethylenediamine it was found that [(imidazo)1,2-a] pyridine-7-carboxylic acid is mainly responsible for the intense blue luminescence [4]. During the synthesis, carbonaceous nanostructured species are also produced but their PL emission is less intense. While the emission peak of the organic fluorophore is independent of the excitation wavelength, the carbon dots resulted from the thermal process behave in a "classic" manner with excitation-dependent emission peaks. In an even more radical view, carbon dots are seen as a blend of polycyclic aromatic hydrocarbons (PAH) with their PL properties resulting from the inner emissive states of each species [5]. This model, according to the author's view, could explain both the large Stokes shifts and the excitation-dependent emission of the carbon dots which is a result of slightly different energy gaps of each of the PAHs. If proven, this approach could provide an interesting path to the fine tuning of the carbon dot emission by trimming the PAH blend composition. Another interesting feature is the up-conversion photoluminescence from NIR to the upper region of the visible spectrum which is sustained by several works [6, 7] while certain studies [8] dismiss it by questioning the investigation conditions. Although an important number of C-Dots related studies are focused on bioimaging applications [9, 10], they seem to gather more interest in applications ranging from sensors to optoelectronic devices such are high-efficiency solar cells or light-emitting devices [11, 12].

Photoluminescent composites prepared through embedding nanoparticulate compounds in polymer matrices are interesting for many of the above-mentioned applications [13]. Thus, polymer–semi-conductor quantum dots (QD) such as CdX, ZnX, MnX (X = S, Se) composites are considered to be used as large area backlighting or light-emitting layers in next-generation flat panel displays [14, 15],

whereas CdSe QD's embedded in PMMA are already used as colour-converting layers to obtain warm white tinted light-emitting diodes [16, 17]. Carbon-related materials such as graphene, carbon nanotubes and graphene QD's with their unique properties are among the most notable candidates to obtain polymer composites able to provide new approaches in electronics-related materials [18, 19], solar and fuel cells [20, 21], supercapacitors [22] or light-emitting devices [23, 24]. C-Dots-polymer composites are equally interesting for developing new challenging materials intended to be applied in state-of-the-art applications ranging from bioimaging to optoelectronics. Thus, poly-ethyleneglycol-C-Dots nanocomposites [25] were found to markedly increase the NIR emission in bioimaging applications while C-Dots-polysiloxane photoluminescent composite deposited in thin films was able to increase by 12 % the conversion efficiency of fullerene-based solar cells [26].

In a previous work [27] we reported a similar approach for the preparation of C-Dots using N-hydroxysuccinimide as precursor in a facile pyrolytic process. Up to date investigations which are reported in the present work revealed that N-hydroxyphthalimide (NHF) is even better suited as precursor in a similar pyrolytic process, leading to excitation wavelength-dependent photoluminescent carbon dots but, with an impressive 80 % PLQY which is among the highest values reported up to date. The fluorescence properties were investigated in detail using a selection of commonly used solvents as dispersion mediums. The prepared C-Dots were further introduced in polystyrene (PS), poly(vinyl chloride) (PVC) and polycarbonate polymer matrices, the resulted highly luminescent composites being obtained in regular-shaped monoliths and thin films. Through the protection provided by the polymer matrix, their remarkable photoluminescent properties are long-term preserved and better adapted to various applications. The described composites could be easily prepared with commonly available laboratory equipment, using low-cost starting materials and compounds. The choice of polymer matrices was focused on these commonly used polymers but, there are no limitations on using other polymer matrices (PMMA, polycarbonate, polyHEMA, etc.); the only restriction being the optical transparency of the matrix in order to efficiently transfer the excitation radiation to the embedded C-Dots.



# **Experimental**

# **Materials**

N-Hydroxyphthalimide (97 %) and poly(vinylchloride) (PVC) (powder, Mw ~48000) were purchased from Sigma-Aldrich. General purpose polystyrene (PS) (pellets) and optical grade polycarbonate (pellets) were supplied from BASF Chemicals. Milli-Q water was used during preparation, purification and dimensional selection procedures. Reagent grade chloroform, tetrahydrofuran (THF), acetone, ethyl alcohol (EtOH), dymethylsulfoxide (DMSO) ethyl ether, benzene and N-hexane from Merck Chemicals were used as re-dispersion mediums for the prepared C-Dots and further for the preparation of composites.

# **Preparation**

In a typical synthesis procedure, C-Dots were prepared by adding 5 g of NHF in a 50 mL three neck Schlenk flask provided with a magnetic stirrer and a temperature-controlled heating mantle. The temperature is gradually raised (about 10 °C/min) to the melting point of NHF (~233 °C) when the magnetic stirring is started. The reaction undergoes in N<sub>2</sub> atmosphere. After melting the entire NHF quantity, the temperature is raised up to 245-248 °C and maintained at this value for about 20 min. During this stage the mass reaction colour gradually changes from yellowish-white to brownish-red. Then, the entire content of the flask is fast transferred in 50 mL cold water and allowed to reach the room temperature and further sonicated for about 10 min. The mixture is centrifuged at 5000 RPM for 20 min. The resulted pale yellow supernatant is collected and additionally centrifuged at 15000 RPM for 10 min. The almost transparent resulted aqueous supernatant containing dimensionally selected C-Dots is collected and further freeze dried. The prepared C-Dots dried or re-dispersed in the selected solvents are kept as such for preparation of the polymer composites and investigation purposes. For the preparation of the composites, each 1.5 mg dried C-Dots are dispersed in 5 mL chloroform and 5 mL THF, respectively. Subsequently, 0.5 g of PS pellets and PVC powder are each dissolved accordingly in the chloroform and THF-containing C-Dots and vigorously stirred for about 2 h and then poured in recipients with the desired shape to obtain monolithic composites. In case of polycarbonate-embedded C-Dots a similar preparation path was performed using THF as dispersion solvent. For obtaining thin films, additional quantities of solvents are added to the composite solution to reduce the viscosity and then spin coated at 800–1200 RPM on substrate.

# Characterization

XPS analysis was performed by means of KRATOS Axis Nova, using AlKa radiation, with 20 mA current, 15 kV voltage. The incident X-ray beam was focused on a  $0.7 \text{ mm} \times 0.3 \text{ mm}$  surface area. The wide XPS spectra was recorded in the range of 10–1200 eV with a resolution of 1 eV and a pass energy of 160 eV. The high-resolution spectra for all the elements identified from the survey spectra were collected using a pass energy of 20 eV and a step size of 0.1 eV. The FT-IR spectra were recorded in the 400-4000 cm<sup>-1</sup> range, using a Bruker Vector 22 spectrometer, according to KBr pellet method. HR-TEM investigation of the prepared C-Dots prior to the embedment in polymer matrices was performed on a Hitachi HT-7700 equipment, operated at 100 kV accelerating voltage, in high contrast mode. The C-dot samples were deposited from a highly diluted chloroform solution on a 300 mesh carbon-plated copper grids. Dimensional analysis (DLS) of the prepared C-Dots was performed prior to embedment on Shimadzu SALD-7001 equipment. The steady-state fluorescence, absolute quantum yields (PLQY) and fluorescence lifetime were recorded on Horiba Fluoromax 4P provided with the Quanta-φ integration sphere and lifetime module. The UV absorption spectrum of the THF-dispersed C-Dots was performed on a Hitachi U-5100 UV-Vis equipment. The AFM measurements were performed using Ntegra Spectra-NT-MDT, Russia instrument operated in tapping mode under ambient conditions. Silicon cantilever tips (NSG 10) with a resonance frequency of 140-390 kHz, a force constant of 5.5–22.5 Nm<sup>-1</sup> and 10 nm tip curvature radius were used. The samples were prepared by spin coating at 1300 RPM of the composite solutions on glass slides by means of a Laurell WS-400-6NPP spin coater. Visual testing of photoluminescent properties was performed using a Philips UVA TL4WBLB lamp with the emission maximum located in the 370-390 nm range.



# Results and discussion

Figure 1a summarizes the C-Dots synthesis process taking place during the pyrolysis of NHF. In the attempt of obtaining the highest photoluminescence of the C-Dots, a set of experiments were performed at higher temperatures (260-290 °C) or longer thermal processing (45-90 min) time which yielded to significantly lower PL emission C-Dots. Similar unsatisfactory results were obtained in case of shorter processing time. In the first case the situation is most probably due to advanced destructuration of NHF accompanied by volatiles exhausting, which drastically depletes the amount of functional groups located on the surface, whereas in the second case lower processing temperatures do not allow the formation of the carbonaceous core. In the optimized process (245 °C, 20 min), highest PLQY was reached, which indicates the proper formation of the carbonaceous core along with the presence of various functional groups which play a key role in achieving the PL properties. Figure 1b-d presents the visually tested emission of the prepared C-Dots dispersed in chloroform and the composites under excitation with a UVA laboratory lamp.

# Structural investigation of the prepared C-Dots

XPS investigation revealed the relative concentrations of various functional groups (Fig. 2a–c).

Table 1 presents the overall O, N, C concentrations as resulted from the XPS survey spectrum. The graphitic core of the prepared C-Dots is revealed by the high-resolution C 1s spectrum (Fig. 2a) which indicates a 45.58 % relative concentration of sp<sup>2</sup>-bonded

**Table 1** Overall C, N, O concentrations recorded for the prepared C-Dots

Element	О	N	С
Atomic concentration (%)	22.81	4.90	72.29
Mass concentration (%)	28.03	5.27	66.70

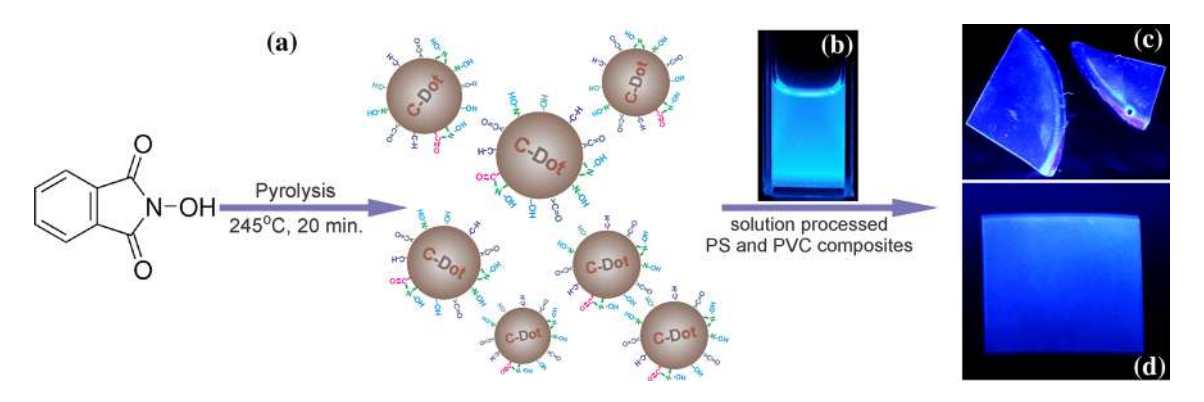


**Figure. 1** a NHF pyrolysis scheme leading to C-Dots. **b** chloroform-dispersed C-Dots and resulted composites in **c** PS matrix, and **d** PVC matrix, under UVA excitation.

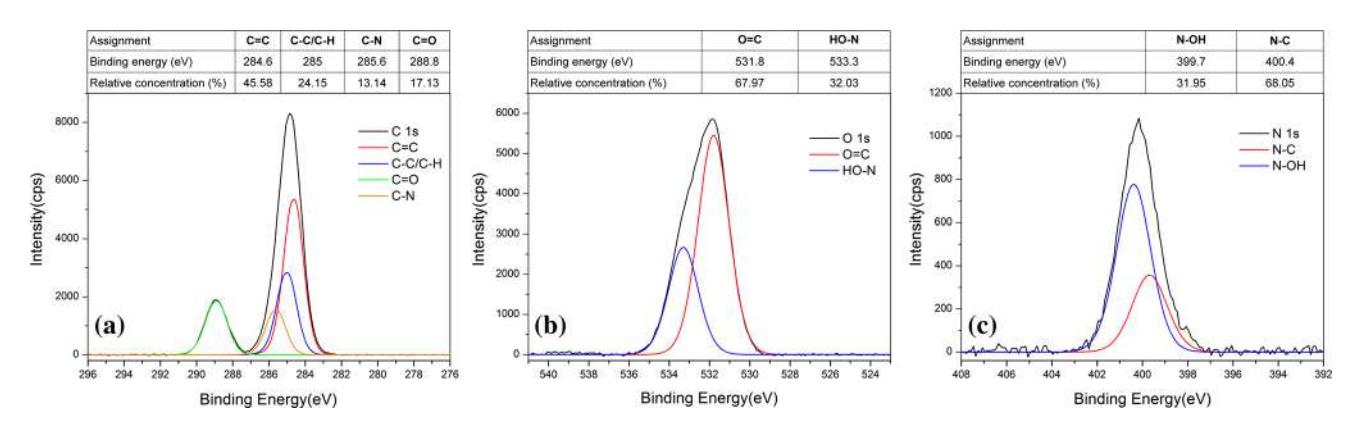
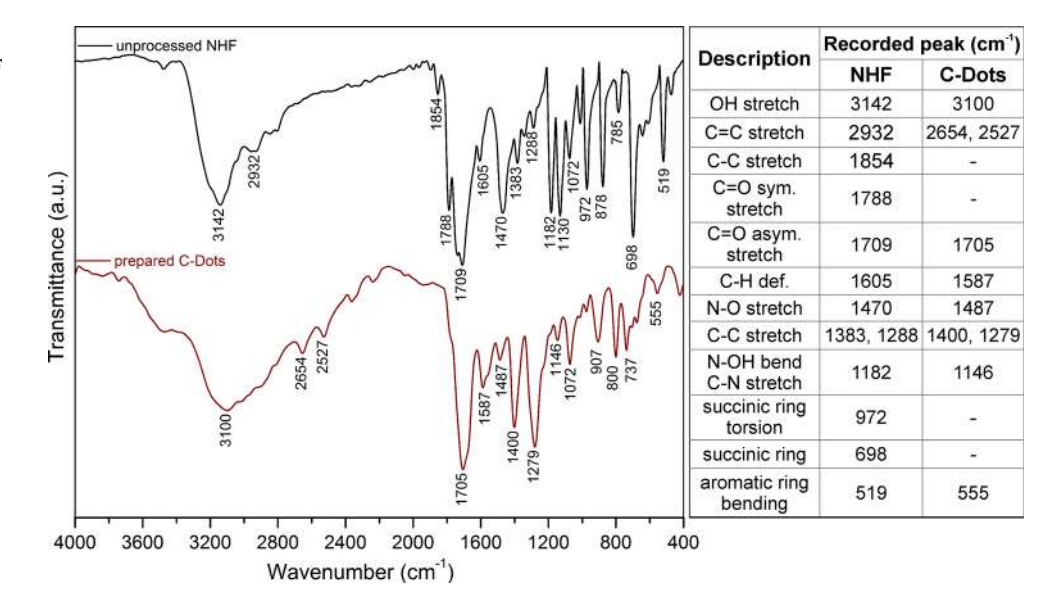


Figure. 2 High-resolution XPS spectra of a C 1s, b O 1s, c N 1s and relative concentrations of various functional groups.



**Figure. 3** FT-IR spectra recorded for unprocessed NHF and prepared C-Dots.



carbons. The relative high concentration of the carbonyl groups (17 %) is significant since they could play a key role in achieving the unique photoluminescent properties of the C-Dots. The concentration of single-bonded carbons (24 %) indicates a significant amount of structural defects in the graphitic core, leading to a surface disordered structure most probably due to the presence of edge-located functional groups. The surface-rich functional groups are also sustained by the high-resolution (Fig. 2b, c) O 1s and N 1s spectra, as will be presented further being in close agreement with the results provided by the FT-IR analysis.

Data provided by the recorded FT-IR spectrum of the prepared C-Dots confirmed both the presence of the various functional groups and also the modifications occurring during the thermal processing of NHF. Figure 3 presents both recorded spectra of unprocessed NHF and prepared C-Dots. Specific vibrations of various groups within the NHF and C-Dots are detailed in Fig. 3 attached table, the results being in close accordance with other related studies [28].

The spectrum of NH was recorded in the range of 3200–2200 cm<sup>-1</sup>. Having a broad peak located at 3142 cm<sup>-1</sup>, the spectrum configuration is mostly the result of the simultaneous presence of the OH stretching vibrations and multiple low intensity stretching vibration bands attributed to the CH bonds (2932 cm<sup>-1</sup>) within the aromatic ring. The situation is slightly different in case of C-Dots where a broader peak was recorded but, displaced to

3100 cm<sup>-1</sup> accompanied by a series of more visible peaks located in the 2700-2200 cm<sup>-1</sup> range most probably as a result of the re-configuration of C=C, CH bonds. Carbonyl groups are present in both spectra, slightly displaced to lower wavenumbers in case of asym. stretch vibrations (1709–1705 cm<sup>-1</sup>). Clearly observable in case of unprocessed NHF, the sym. stretch (1788 cm<sup>-1</sup>) cannot be identified in case of C-Dots. Barely noticeable in NHF spectrum, the low intensity peaks of C-C stretching vibrations  $(1383, 1288 \text{ cm}^{-1})$  are displaced at 1400 and 1279 cm<sup>-1</sup>, respectively, with significantly higher intensity, in case of C-dots, which indicates the reconfiguration occurred during the formation of the carbonaceous core. Various vibrations that are due to the nitrogen-containing groups are highlighted by a series of peaks in the region of 1200–1100 cm<sup>-1</sup>. The stretching (v<sub>CN</sub>) and bending (b<sub>NO</sub>) vibrations that peak at 1130 cm<sup>-1</sup> are still present in case of C-Dots. However, it has a lower intensity that is displaced to  $1146 \text{ cm}^{-1}$ .

In the lower region of the spectra, certain modifications are clearly visible. The most evident is the disappearance of the 698 cm<sup>-1</sup> peak from the C-Dots spectrum. This peak is attributed to the bending vibrations of the succinic ring and related C-C stretching vibrations. Also, the medium intensity peak recorded at 519 cm<sup>-1</sup> in the NHF spectrum and attributed to the combined skeletal vibrations of the aromatic and succinic rings is displaced to 555 cm<sup>-1</sup> with a markedly reduced intensity in case of C-Dots recorded spectrum. Both modifications further



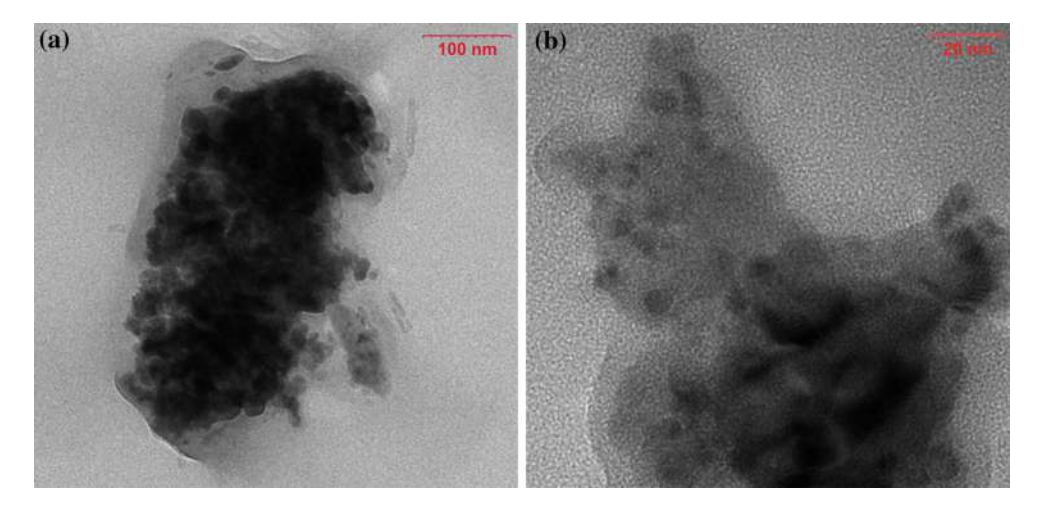


Figure. 4 Recorded HR-TEM images of the prepared C-Dots prior to embedment in the polymer matrices.

sustain the re-configuration achieved through thermal processing.

# Morphology of the prepared C-Dots and related polymer composites

HR-TEM microscopy revealed the most comprehensive information regarding the size and tendency of clustering of the prepared C-Dots. Figure 4a, b presents the recorded micrographs at two different resolutions. Figure 4a confirmed the clustering tendency of the prepared C-Dots with an average size of the clusters in 100-300 nm range. The most important aspect which is clearly highlighted by the recorded images, is the existence of smaller (20-30 nm), almost spherical-shaped entities within the cluster. While their aspect could suggest individual C-Dots, it is also possible to be attributed to even smaller clusters further organized in larger ones. The second image recorded at higher resolution (Fig. 4b) revealed the existence of even smaller entities in 2-4 nm range which could highlight the individual C-Dots.

Figure 5 presents the size distribution of C-Dots dispersed in chloroform and THF before the embedment in the polymer matrices. Both prepared suspensions have a noticeable agglomeration tendency and must be freshly prepared and thoroughly sonicated prior to DLS investigation and addition of PS pellets and PVC powder during composite preparation.

The average particle size is located in 18–30 nm range. Also, higher dimensions (50–90 nm) were

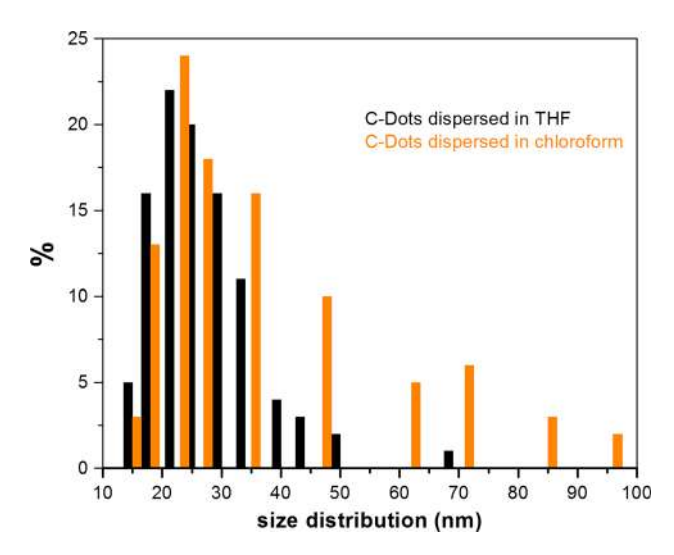


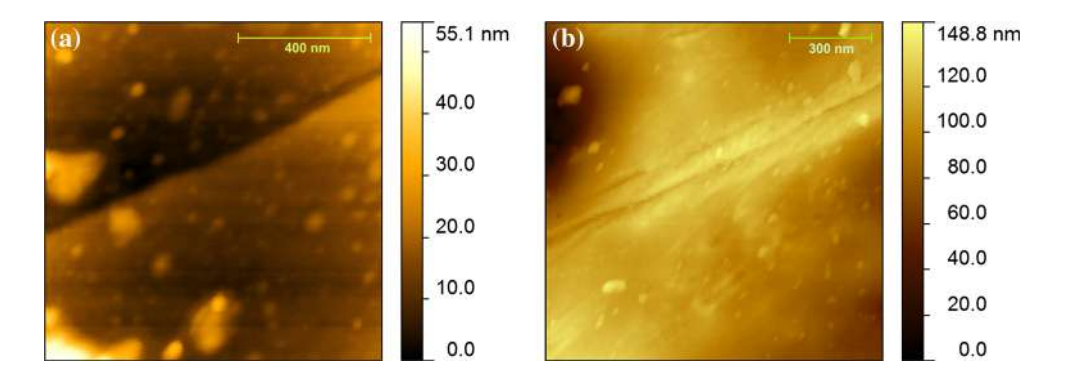
**Figure. 5** DLS recorded size distribution of the C-Dots dispersed in chloroform and THF, respectively.

recorded. Based on the results recorded by HR-TEM investigation, the recorded size distribution did not reveal individual C-Dots but the presence of various-sized C-Dots clusters. This situation is most probably due to the resolution of the equipment used for the DLS investigation which is limited to 15 nm. The results are mostly a result of the agglomeration tendency. As can be noted, the agglomeration tendency is slightly higher in chloroform-dispersed C-Dots.

A comparable situation was noted in case of AFM investigation (Fig. 6a, b) of the prepared composites processed in thin films on glass substrates according to the procedure mentioned above. The size



**Figure. 6** Recorded AFM images **a** PS–C-Dots composite, and **b** PVC–C-Dots composite.

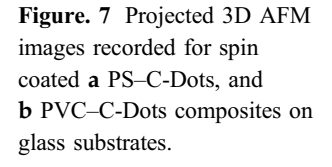


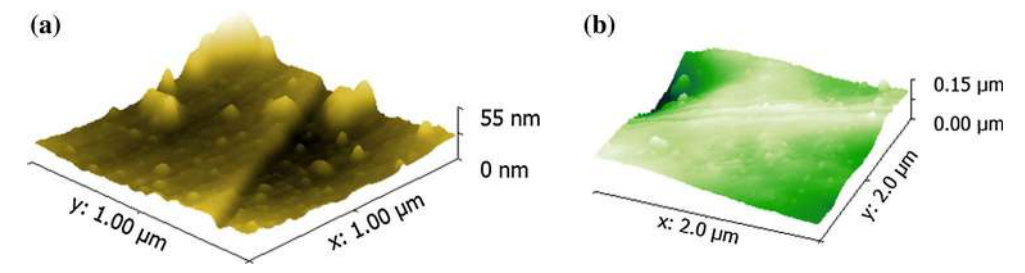
distribution is wider, with larger particles clearly noticeable in case of PS-embedded C-Dots (Fig. 6a). Therefore, it can be concluded that size distribution recorded in case of chloroform-dispersed C-Dots before the embedment in polymer matrix is preserved after the preparation of PS composite.

The same situation was encountered in case of PVC-embedded C-Dots. As could be observed (Fig. 5b), the size distribution of the entrapped C-Dots is narrower, with dominant smaller particles being present in the polymer matrix. Figure 7a, b presents the projected 3D AFM images recorded for the prepared thin PS– and PVC–C-Dots composite films.

# Fluorescence spectroscopy

Figure 8a, b presents the emission spectra recorded at different excitation wavelengths for the prepared C-Dots dispersed in chloroform (Fig. 7a) and THF (Fig. 7b) prior to embedment in the polymer matrices. As could be noted, the emission peaks were recorded within 402–472 nm range being both excitation wavelength and solvent dependent. The Stokes shifts are also solvent dependent, higher energy photons being produced in the radiative processes of chloroform-dispersed C-Dots where the emission peaks are located in 402–461 nm range (Fig. 7a) whereas for





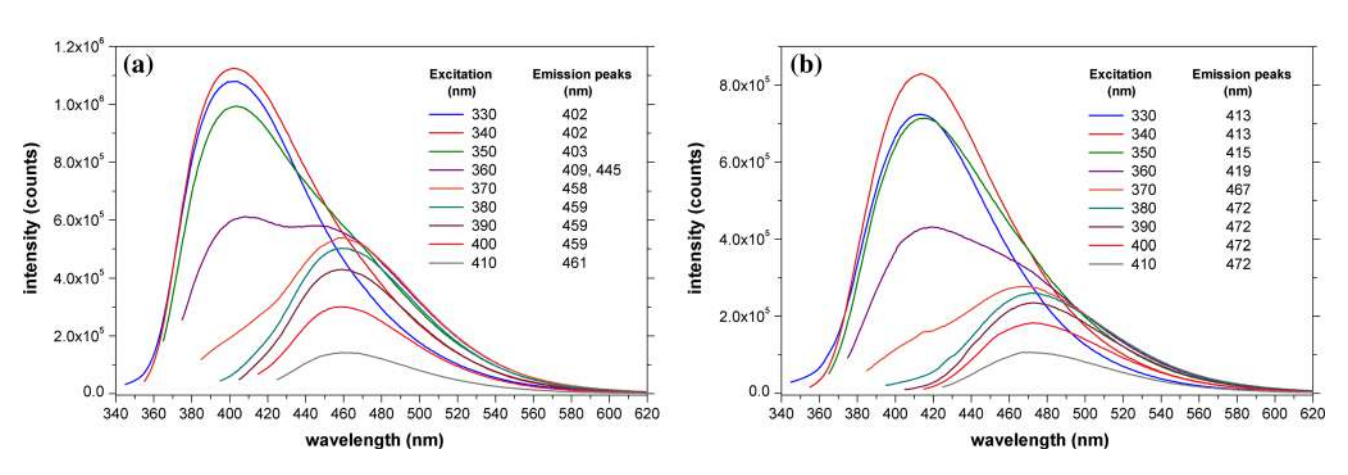


**Figure. 8** PL emission recorded for excitation wavelengths from 330 to 410 nm in 10 nm increments of the prepared C-Dots dispersed in a chloroform, and **b** THF.

Table 2 Absolute PLQY of the C-Dots dispersed in various solvents

NHF C-Dots/	Solvent	Solvent	Excita	tion (nm)	)										
dispersion solvent	type <sup>a</sup>	polarity index <sup>a</sup>	330 PLQY	340 (%)	350	360	370	380	390	400	410	420 - - 37.6 - 12.0			
C-Dots/H <sub>2</sub> O	Polar protic	9.0	_	_	8.7	8.6	8.2	9.3	11.1	10.7	_				
C-Dots/EtOH		5.2	_	_	28.6	29.5	27.8	30.6	28.8	29.5	_	_			
C-Dots/DMSO	Polar aprotic	7.2	32.6	46.7	54.7	54.3	47.9	53.8	59.5	57.3	48.9	37.6			
C-Dots/acetone		5.1	_	_	30.3	36.2	28.4	39.8	50.6	_	_	_			
C-Dots/THF		4.0	35.3	43.7	38.6	37.1	34.6	42.2	44.6	37.5	22.7	12.0			
C-Dots/chloroform	Non-polar	4.1	34.3	43.7	49.6	51.8	56.2	60.2	79.9	69.9	47.8	25.0			
C-Dots/ethyl ether		2.8	29.3	37.7		43.6	43.7	49.8	54.5	39.9	24.8	16.3			
C-Dots/benzene		2.7	_	_	5.5	7.3	9.4	12.2	12.6	8.6	3.9	_			
C-Dots/N-hexane		0.0	5.43	10.7	8.2	5.3	4.4	6.6	5.3	3.5	3.9	3.6			

<sup>&</sup>lt;sup>a</sup> According to [29]

THF-dispersed C-Dots (Fig. 7b) larger Stokes shifts were recorded (413-472 nm). These results are in close agreement with the absolute PLQY measurements (Table 2), where the highest QY (79.9 %) was recorded in case of chloroform-dispersed C-Dots which is almost double compared to that of THFdispersed C-Dots (44.55 %). This solvent dependence of the emission peaks and PLQY was also observed in case of C-Dots prepared in our previous work where N-hydroxysuccinimide was used as precursor [27] and may provide an additional support in favour of the PL mechanism relying mainly on radiative transitions occurring within or between the functional groups located on the C-Dots surface and only indirectly related to the size of the carbonaceous core. However, in certain studies [2, 3] the excitation wavelength-dependent emission peaks are explained by the simultaneous presence of C-Dots with various dimensional characteristics of the carbonaceous core, each responsible for a particular emission peak. In the view provided by the results presented in the present work, this approach is less capable to explain the notable differences in terms of recorded PLQY between various solvents used to disperse the C-Dots. For a better understanding of the influence of the dispersion solvent over the emission efficiency of the radiative processes, the prepared C-Dots reported in this work were dispersed in a series of commonly used solvents [29], as detailed in Table 2.

Several interesting conclusions could be drawn from the recorded results as follows: the efficiency of the radiative processes is smallest in case of polar protic solvents (water, EtOH) while in case of polar aprotic solvents the recorded values are almost double. A possible explanation is the vicinity of the -OH oscillators which favours vibrational coupling leading to non-radiative deactivation paths which drastically decrease the efficiency of the radiative processes. This situation was especially noticed in water where the recorded PLQY was the second lowest from the entire solvent group. One interesting detail is provided by the steady-state fluorescence investigations performed in water, EtOH and acetone-dispersed C-Dots (Supplementary Fig. S1a-c). The Stokes shifts are higher (e.g. 330-415 nm, 330–411 nm, 330–402 nm) in  $H_2O \rightarrow EtOH \rightarrow ace$ tone order, which suggests more excitation energy loss in the radiative processes according to the -OH oscillators presence, thus supporting the conclusions regarding their role in providing radiationless deactivation paths which decrease the overall emission efficiency. In the most favourable case (acetone) the surface-located function seems to be less disturbed since the conditions favourable to non-radiative deactivation path being no more present.

The highest recorded PLQY value (79.9 %) is noted for C-Dots dispersed in chloroform in the non-polar solvents group. In case of polar aprotic and non-polar solvents, the emission efficiency is in a direct relation with the polarity index. The smallest value was recorded in *N*-hexane but, this could be a result of the observed poorer dispersion of the C-Dots in this solvent. In all cases, with the exception of *N*-hexane-dispersed C-Dots, the highest PLQY values were recorded at 380–390 nm excitation wavelengths. Therefore, the recorded results seem to bring strong



arguments for the PL mechanism based on functional groups which is able to better explain it on the basis of the excited states achieved within or between surface-located functional groups responsible for various trapping states with different energy levels leading to the excitation-dependent emission [30] strongly influenced by the surrounding solvents. Such great difference of the recorded PLQY values is better supported by the interactions occurring between the solvent and the surface-located functional groups which in a particular case may favorize the radiative transitions responsible for the PL emission or may provide conditions for non-radiative deactivation paths leading to a less intense PL emission.

The greatly improved PLQY of the C-Dots prepared using NHF as precursor is reported in this work, compared to previous study of C-Dots derived from N-hydroxysuccinimide could be explained by the presence of the aromatic ring in the precursor structure, which through thermal processing may favorize a better configuration of the surface-located functional groups or a more efficient harvesting of the excitation energy which is subsequently transferred to excited states responsible for the radiative processes. Interestingly, the presence of aromatic ring in the precursor which is due to the structural rearrangements occuring through thermal processing could also provide support for the above-mentioned proposed PL mechanism where PL properties of the C-Dots are seen as a result of the presence of polycyclic aromatic hydrocarbons (PAH) [5].

The recorded fluorescence lifetime (Fig. 9) of the prepared C-Dots dispersed in chloroform was found in the 4.5–6 ns range which is in accordance with other studies related to fluorescent carbon nanostructures [31, 32].

The steady-state fluorescence investigation of the polymer composites processed in thin films or monoliths (Fig. 10a, b) revealed the same excellent emission properties due to the proper preservation of the embedded C-Dots PL properties. Obviously, the emission intensity is proportional to the concentration of C-Dots in the polymer matrix which is limited only by their agglomeration tendency (>4 mg in the above-mentioned preparation recipe) which tends to reduce the overall emission intensity and the consistency of the composites.

Certain changes in the recorded emission spectra were recorded and the most notable are the Stokes

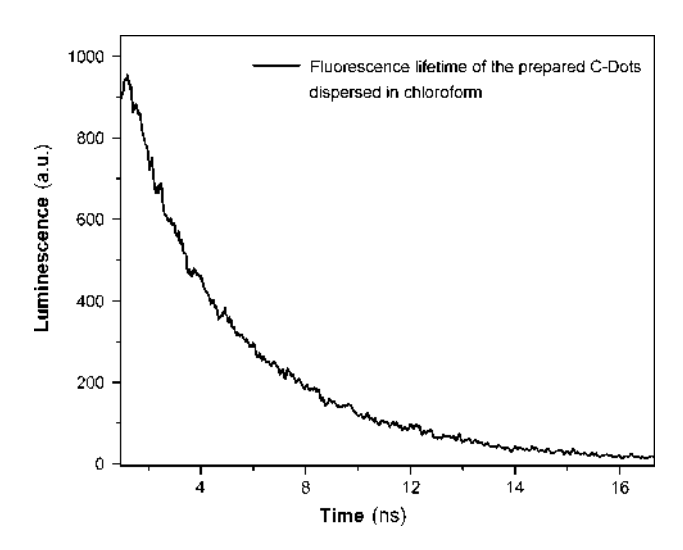


**Figure. 9** Fluorescence lifetime recorded for the prepared C-Dots dispersed in chloroform.

shifts. In both the prepared composites they are smaller compared with that of the free C-Dots dispersed in chloroform or THF. The peak emission range is shifted to smaller wavelengths (385-447 nm for PS and 386-455 nm for PVC composites), and higher energy photons are produced in the radiative processes due to a more efficient energy transfer to the excited states. In solution, non-radiative deactivation paths are more efficient due to the vicinity of solvent molecules, whereas in case of solid composites these processes are minimized. A similar situation was noted in case of polycarbonate-embedded C-Dots where a comparable emission shift was recorded (Supplementary Fig. S1d). The C-Dots dispersed in THF and chloroform and all the prepared composites were continuously exposed for 4 weeks to a combined UV-B and UV-A source in order to test their long-term stability and then re-investigated by fluorescence spectroscopy. In case of C-Dots there were no traceable changes in terms of emission peaks or PL intensity. In case of PS and PVC composites prepared in thick films, besides a barely noticeable yellowing of the samples, the recorded PL spectra were essentially the same with only a shift of 1–2 nm of the emission peaks. In case of the PC composite the exposed sample aspect was the same and the recorded PL spectra were identical with the investigation performed prior to long-term UV exposure. Therefore, in case of the PS and PVC composites the barely noticeable differences are due to the polymer matrices which are more sensitive to UV destructive action compared with the PC polymer matrix.



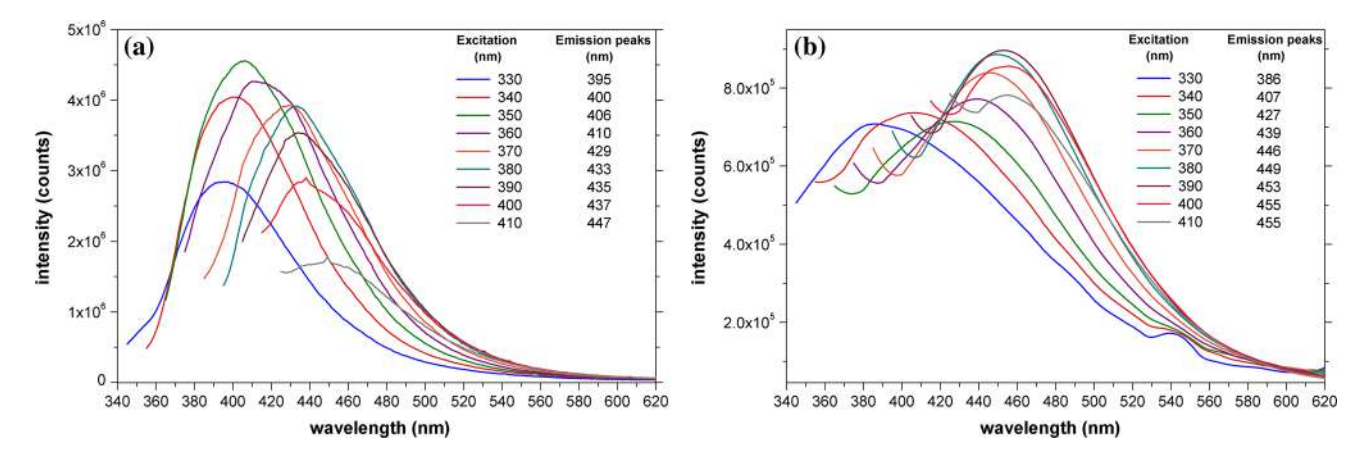


**Figure. 10** PL emission recorded for excitation wavelengths from 330 to 410 nm in 10 nm increments of the prepared **a** PS–C-Dots and **b** PVC–C-Dots composites.

Besides their commonly targeted applications in the above-mentioned state-of-the-art domains such are bioimaging or optoelectronics, we suggest another one where the prepared C-Dots and related polymer composites may offer a straightforward and cheap solution for solar UV protection of various sensitive surfaces provided by thin layers of prepared composites. One example is the protection of the painted surfaces or other sensitive parts (e.g. automotive applications) long term exposed to direct sunlight by thin layers of composites containing PL efficient C-Dots. The protection is simply provided by the translation of solar UV radiation as excitation of the embedded C-Dots towards lower wavelengths, and the lower energy photons (Stokes shift) produced in the radiative processes being markedly less harmful for the intended surface to be protected. The UV absorption interval (Fig. S2-Supporting information) is located conveniently in 300-390 nm range covering the UV-B and UV-A regions where most of the solar UV component at sea level, is located. From such a perspective, the C-Dots are particularly suited due to their wide range UV excitation of the radiative processes, physico-chemical stability, inertness, lack of toxicity and ease of fabrication.

# **Conclusions**

Highly photoluminescent composites were prepared by embedding newly developed carbon dots derived from NHF in PS, PVC and PC polymer matrices. *N*-Hydroxyphthalimide was found to be an excellent precursor for obtaining C-Dots through a simple pyrolytic process. The prepared C-Dots present excitation wavelength-dependent PL emission which is also influenced by the dispersion medium. The absolute PLQY measurements revealed an impressive 79.95 % efficiency, being among the highest values reported up to date. Composites were prepared by embedding the C-Dots in PS and PVC polymer matrices, thus their remarkable PL properties can be preserved and better adapted to various applications. The solution-processed polymeric composites were obtained in thin or thicker films and monoliths according to the intended applications. Due to their truly remarkable photoluminescent properties and facile fabrication, these new composites could be interesting for applications ranging from sensors to solar energy conversion and light-emitting devices while in another proposed application, the prepared C-Dots and composites may provide an interesting alternative for protection of various surfaces against the action of the solar UV long-term exposure.

# Acknowledgements

This work was supported by a grant of the Romanian National Authority for Scientific Research, CNCS – UEFISCDI, Project No. PN-II-ID-PCE 2011-3-0708, PN-II IDEI 335/2011.

**Electronic supplementary material:** The online version of this article (doi:10.1007/s10853-016-0320-y) contains supplementary material, which is available to authorized users.



# References

- [1] Li H, Kang Z, Liu Y, Lee ST (2012) Carbon nanodots: synthesis, properties and application. J Mater Chem 22:24230–24253
- [2] Xu Y, Wu M, Liu Y, Feng XZ, Yin XB, He XW, Zhang YK (2013) Nitrogen-doped carbon dots: a facile and general preparation method photoluminescence investigation, and imaging applications. Chem Eur J 19:2276–2283
- [3] Deng Y, Chen X, Wang F, Zhang X, Zhao D, Shen D (2014) Environment-dependent photon emission from solid state carbon dots and its mechanism. Nanoscale 17:10388–10393
- [4] Song Y, Zhu S, Zhang S, Fu Y, Wang L, Zhao X, Yang B (2015) Investigation from chemical structure to photoluminescent mechanism: a type of carbon dots from the pyrolysis of citric acid and an amine. J Mater Chem C 3:5976–5984
- [5] Fu M, Ehrat F, Wang Y, Milowska KZ, Reckmeier C, Rogach AL, Stolarczyk JK, Urban AS, Feldmann J (2015) Carbon dots: a unique fluorescent cocktail of polycyclic aromatic hydrocarbons. Nano Lett 15:6030–6035
- [6] Li M, Wu W, Ren W, Cheng HM, Tang N (2012) Synthesis and upconversion luminescence of N-doped graphene quantum dots. Appl Phys Lett 101:103107
- [7] Yin B, Deng J, Peng X, Long Q, Zhao J, Lu Q, Chen H, Li HT, Zhang Y, Yao S (2013) Green synthesis of carbon dots with down-and up-conversion fluorescent properties for sensitive detection of hypochlorite with a dual-readout assay. Analyst 138:6551–6557
- [8] Wen X, Yu P, Toh YR, Ma X, Tang J (2014) On the upconversion fluorescence in carbon nanodots and graphene quantum dots. Chem Commun 50:4703–4706
- [9] Song Y, Zhu S, Yang B (2014) Bioimaging based on fluorescent carbon dots. RSC Adv 52:27184–27200
- [10] Wei W, Lu C, Guang LW (2014) Biological applications of carbon dots. Sci China Chem 57:522–539
- [11] Mirtchev P, Henderson EJ, Soheilnia N, Yip CM, Ozin GA (2012) Solution phase synthesis of carbon quantum dots as sensitizers for nanocrystalline TiO<sub>2</sub> solar cells. J Mater Chem 22:1265–1269
- [12] Zhang X, Zhang Y, Wang Y, Kalytchuk S, Kershaw SV, Wang Y, Wang P, Zhang T, Zhao Y, Zhang H, Wang TC, Zhao J, Yu WW, Rogach AL (2013) Color-switchable electroluminescence of carbon dot light-emitting diodes. ACS Nano 7:11234–11241
- [13] Shen L (2011) Biocompatible polymer/quantum dots hybrid materials: current status and future developments. J Funct Biomater 2:355–372
- [14] Kim TH, Cho KS, Lee EK, Lee SJ, Chae J, Kim JW, Kim DH et al (2011) Full-colour quantum dot displays fabricated by transfer printing. Nat Photon 5:176–182

- [15] Wood V, Panzer MJ, Chen J, Bradley MS, Halpert JE, Bawendi MG, Bulovic V (2009) inkjet-printed quantum dotpolymer composites for full-color AC-driven displays. Adv Mater 2(1):2151–2155
- [16] Chung W, Park K, Yu HJ, Kim B, Kim SH (2010) White emission using mixtures of CdSe quantum dots and PMMA as a phosphor. Opt Mater 32:515–521
- [17] Nizamoglu S, Zengin G, Demir HV (2008) Color-converting combinations of nanocrystal emitters for warm-white light generation with high color rendering index. Appl Phys Lett 92:031102
- [18] Xu Y, Wang Y, Liang J, Huang Y, Ma Y, Wan X, Chen Y (2009) A hybrid material of graphene and poly (3,4-ethyldioxythiophene) with high conductivity, flexibility, and transparency. Nano Res 2:343–348
- [19] Zhang X, Pint CL, Lee MH, Schubert BE, Jamshidi A, Takei K, Ko H, Gillies A, Bardhan R, Urban JJ, Wu M, Fearing R, Javey A (2011) Optically- and thermally-responsive programmable materials based on carbon nanotube-hydrogel polymer composites. Nano Lett 11:3239–3244
- [20] Hong W, Xu Y, Lu G, Li C, Shi G (2008) Transparent graphene/PEDOT-PSS composite films as counter electrodes of dye-sensitized solar cells. Electrochem Commun 10:1555-1558
- [21] Xu C, Cao Y, Kumar R, Wu X, Wang X, Scott K (2011) A polybenzimidazole/sulfonated graphite oxide composite membrane for high temperature polymer electrolyte membrane fuel cells. J Mater Chem 21:11359–11364
- [22] Xiao J, Wang X, Yang XQ, Xun S, Liu G, Koech PK, Liu J, Lemmon JP (2011) Electrochemically induced high capacity displacement reaction of PEO/MoS<sub>2</sub>/graphene nanocomposites with lithium. Adv Funct Mater 21:2840–2846
- [23] Bonaccorso F, Sun Z, Hasan T, Ferrari AC (2010) Graphene photonics and optoelectronics. Nat Photon 4:611–622
- [24] Luk CM, Chen BL, Teng KS, Tang LB, Lau SP (2014) Optically and electrically tunable graphene quantum dot polyaniline composite films. J Mater Chem C 2:4526–4532
- [25] Wu L, Luderer M, Yang X, Swain C, Zhang H, Nelson K, Stacy AJ, Shen B, Lanza GM, Pan D (2013) surface passivation of carbon nanoparticles with branched macromolecules influences near infrared bioimaging. Theranostics 3:677–686
- [26] Huang JJ, Zhong ZF, Rong MZ, Zhou X, Chen XD, Zhang MQ (2014) An easy approach of preparing strongly luminescent carbon dots and their polymer based composites for enhancing solar cell efficiency. Carbon 70:190–198
- [27] Stan CS, Coroaba A, Popa M, Albu C, Sutiman D (2014) One step synthesis of fluorescent carbon dots through pyrolysis of N-hydroxysuccinimide. J Mat Chem C 3:789–795



- [28] Krishnakumar V, Sivasubramanian M, Muthunatesan S (2009) Density functional theory study and vibrational analysis of FT-IR and FT-Raman spectra of N-hydroxyphthalimide. J Raman Spectrosc 40:987–991
- [29] Sadek PC (2002) The HPLC solvent guide, 2nd edn. Wiley, New York
- [30] Tian R, Hu S, Wu L, Chang Q, Yang J, Liu J (2014) Tailoring surface groups of carbon quantum dots to improve photoluminescence behaviors. Appl Surf Sci 301:156–160
- [31] Gu J, Hu D, Wang W, Zhang Q, Meng Z, Jia X, Xi K (2015) Carbon dot cluster as an efficient "off–on" fluorescent probe to detect Au(III) and glutathione. Biosens Bioelectron 68:27–33
- [32] Zhi Y, Minghan X, Yun L, Fengjiao H, Feng G, Yanjie S, Hao W, Yafei Z (2014) Nitrogen-doped, carbon-rich, highly photoluminescent carbon dots from ammonium citrate. Nanoscale 6(3):1890–1895



# **NJC**



**View Article Online PAPER** 



Cite this: New J. Chem., 2016, 40, 6505

# Photoluminescent polymer composites with R, G, B emission and their potential applications in LCD displays

Corneliu S. Stan,\*a Petronela Horlescu, Marcel Popa, Adina Coroaba and Laura F. Ursu<sup>b</sup>

In this work, red, green and blue emitting composites with remarkable photoluminescence properties were obtained through embedding Eu<sup>3+</sup>, Tb<sup>3+</sup> and Y<sup>3+</sup> complexes with 2-(1H-1,2,4-triazol-3-yl)pyridine in poly(vinyl alcohol) and poly(n-vinyl pyrrolidone) matrices which were processed in thin or thick films. Interestingly, through embedding in the polymer matrices, their luminescence properties are markedly enhanced compared to the free complexes. PLQY values were enhanced from an average 25-30% to 52-69%, while the emission purity, especially in the case of Eu<sup>3+</sup> containing composites, was greatly improved. The prepared composites were investigated through FT-IR analysis while the emphasis on fluorescence spectroscopy provided important details regarding the impact of embedding the complexes in the polymer matrices; luminescence lifetime, absolute PLQY and chromaticity parameters were investigated in detail. The morphology of the composite films was investigated through AFM and SEM. Based on their remarkable photoluminescence properties we are suggesting their implementation in AMLCD displays in a new approach which could replace the RGB colour filters, thus bringing several potential advantages over the current approach. The facile preparation and emission characteristics should be important arguments for their implementation as photonic conversion media in various optoelectronic devices. Other applications like full colour watermarks in special purpose papers could easily take advantage of the prepared composites.

Received (in Montpellier France) 4th February 2016, Accepted 18th May 2016

DOI: 10.1039/c6nj00386a

www.rsc.org/njc

# 1. Introduction

Photoluminescent materials have constantly been the focus of the scientific research due to their wide range of applications ranging from optoelectronics to medical investigation techniques. Among various classes of photoluminescent compounds, lanthanide and transition metal complexes are arguably one of the most promising materials due to their luminescence properties and facile preparation paths. Eu<sup>3+</sup> and Tb<sup>3+</sup> cations are well known for their narrow emission bands located in the red, 1,2 respectively green<sup>3,4</sup> areas of the visible spectrum due to their radiative transitions within 4f orbitals partially shielded by the 5s and 5p orbitals.5,6 In particular, sharp emission bands located around 620 nm of Eu<sup>3+</sup> and 540 nm specific to Tb<sup>3+</sup> cations are highly considered in applications where warm/cold tinted white light

emission or accurate color reproduction is obtained by mixing the three fundamental colors (R, G, B), for example, LED or color displays. When properly sensitized with an appropriate ligand capable of energy absorption, which is subsequently transferred to the lanthanide center, the results are impressive in terms of efficiency of the radiative processes and spectral characteristics of their photoluminescence emission. Unfortunately, only a few lanthanide complexes with blue emission are reported<sup>7</sup> thus limiting a practical implementation entirely based on photoluminescent complexes. In most cases Eu and Tb complexes are used for red and green emission layers while the limited availability of a blue emitting complex is overcome by using an organic fluorophore.8 The situation could be further complicated when various ligands are used to obtain complexes with RGB emission due to the inherent differences between their excitation energy absorption efficiency or proper sensitization of the central cation. Therefore a "unified" solution based on the same ligand is advantageous for applications where RGB photoemissive layers are required. In a previous work<sup>9</sup> we reported the preparation and investigation of several new luminescent complexes with the same 2-(1H-1,2,4-triazol-3-yl)pyridine ligand. Among them, the Eu3+, Tb3+ and Y3+ complexes are especially interesting due to

<sup>&</sup>lt;sup>a</sup> Faculty of Chemical Engineering and Environmental Protection, Gh. Asachi Technical University, D. Mangeron 73 Ave., 700050, Iasi, Romania. E-mail: stancs@tuiasi.ro

<sup>&</sup>lt;sup>b</sup> Centre of Advanced Research in Bionanoconjugates and Biopolymers, "Petru Poni" Institute of Macromolecular Chemistry of Romanian Academy Grigore Ghica Voda 41A Allev. 700487 Iasi. Romania

NJC Paper

their intense photoluminescence emission located in the red, green and blue regions of the visible spectrum and also having comparable efficiency of the radiative processes.

Generally, a direct implementation of certain photoluminescent complexes in the above mentioned applications could hardly be seen as a suitable practical approach since they are usually sensitive to environmental factors which markedly affect their emissive properties and/or because they are obtained in the form of crystalline powders which are not suitable for thin or thick film processing required to obtain photonic conversion layers. Therefore, the embedment of the photoluminescent complexes in various media, especially in polymer matrices, should provide a practical approach to overcome these limitations. In a very recent approach, thin layers of RGB photoemissive polymeric composites were prepared by embedding complexes of Eu<sup>3+</sup> and Tb<sup>3+</sup> with dibenzoylmethide, general formula Ln(DBM)<sub>3</sub>, and C-dots as blue emitters in the PMMA matrix. These films show white emission through combining of the three primary colours and are meant as photonic conversion media in PC-LEDs. 10 In other studies, PMMA was also used as a polymer matrix to obtain green and red emitting composites by embedding various Eu<sup>3+</sup> and Tb<sup>3+</sup> complexes. 11,12 The embedment of lanthanide complexes in PVA matrices has been reported by several studies also targeting the preparation of photoluminescent composites. Thus, complexes of Sm3+ and Tb3+ with salicylic acid and 1,10-phenanthroline (Ln(Sal)<sub>3</sub>Phen) were embedded in PVA matrices resulting in composites with green and orange emission while white light was obtained by mixing both complexes in the same matrix.<sup>13</sup> High values of absolute PLQY (70-90%) were reported in the case of some new complexes of Eu3+ and Tb3+ with triazolepyridine-bistetrazolate embedded in PVA matrices. 14 An interesting approach allows the achievement of optically polarized photoluminescence by stretching ultrathin composite films obtained by embedding a [Tb(phen)2(NO3)3] complex in a PVA matrix.15 In another study, PVP was used to prepare photoluminescent composite fibers of about 500 nm in diameter by electrospinning. The starting composite was prepared by embedding the Eu3+ complex with thenoyl-trifluoroacetone and triphenylphosphine oxide, [Eu(TTA)<sub>3</sub>(TPPO)<sub>2</sub>] in the PVP matrix.<sup>16</sup>

In this work, R, G, B emissive polymer composites were obtained by embedding Eu<sup>3+</sup>, Tb<sup>3+</sup> and Y<sup>3+</sup> complexes with the 2-(1H-1,2,4-triazol-3-yl)pyridine ligand in PVA and PVP matrices. The choice for these polymer matrices was based on the following aspects: both PVA and PVP are water soluble polymers, which provide a suitable compatibility with the Eu<sup>3+</sup>, Tb<sup>3+</sup> and Y<sup>3+</sup> complex preparation path; optical transparence of the embedded complexes in the excitation/emission range; low cost, wide availability and the potential to be easily processed in high quality thin or thick films through various common available techniques.

As will be further discussed, through embedding in these selected polymer matrices, the emission characteristics such as PLQY and spectral purity are markedly enhanced, most probably due to the interactions occurring between polymer matrices and embedded complexes. Besides the protective role of the polymer matrices, the composites provide a convenient practical approach for obtaining thin or thick layers, easily processed by spin/spray coating or jet printing in targeted applications. As will be briefly described, one possible implementation is the replacement of the color filters in AMLCD displays<sup>17</sup> in a suggested configuration that may present several potential advantages over the current approach.

# 2. Experimental

# 2.1. Materials

2-(1H-1,2,4-Triazol-3-yl)pyridine (denoted as HL) (97%), poly(vinyl alcohol) (PVA)  $M_{\rm w} = 45\,000$  and poly(n-vinyl-2-pyrrolidone) (PVP)  $M_{\rm w}$  = 45 000 were purchased from Sigma-Aldrich while yttrium chloride (YCl<sub>3</sub>·xH<sub>2</sub>O, 99.99%), europium chloride (EuCl<sub>3</sub>·xH<sub>2</sub>O, 99.9%), and terbium chloride (TbCl<sub>3</sub>·6H<sub>2</sub>O, 99.9%) were purchased from Alfa-Aesar. Absolute ethanol and high purity Milli-Q water were used for preparation and washing operations.

# 2.2. Preparation of the photoluminescent composites

In the first step the complexes with the general formulae  $[M(L)_3(H_2O)_3]$  (M = Eu<sup>3+</sup>, Tb<sup>3+</sup>, Y<sup>3+</sup>) were prepared following a similar procedure detailed in a previous work. Briefly, aqueous solutions of Y3+, Tb3+, and Eu3+ chlorides are obtained by dissolving 1 mmol of each in 2 mL high purity MiliQ water, in separate glass beakers provided with magnetic stirrers. Then, six similar solutions each containing 3 mmol of 2-(1H-1,2,4triazol-3-yl)pyridine (HL) are prepared by dissolving the ligand in a mixture of 3 mL of MiliQ water and 1 mL of ethanol. The complexes were obtained by mixing each prepared ligand solution with the corresponding Y3+, Tb3+, Eu3+ chloride solutions; the reactions were performed under mild heating (40-45 °C) and stirring for about 180 minutes. In the next step, the polymer matrices are prepared through the dissolution of 3 g of PVA and 3 g of PVP, each in 30 mL of MiliO water. Then aqueous/ethanol solutions containing the prepared complexes are each mixed under stirring with 10 mL of previously prepared PVA and PVP solutions. Thick films of composites could be obtained by ambient drying in a conveniently shaped mould, while spin/spray coating techniques could be used to obtain thin films deposited on various substrates. In Fig. 1 the PVA- $[M(L)_3(H_2O)_3]$  and PVP- $[M(L)_3(H_2O)_3]$ composites obtained in thick films under excitation of a UV-A laboratory source are presented.

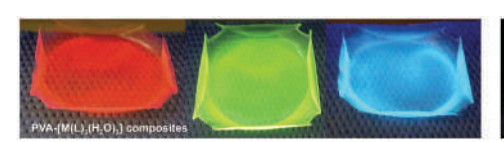




Fig. 1  $PVA-[M(L)_3(H_2O)_3]$  and  $PVP-[M(L)_3(H_2O)_3]$  thick composite films under excitation of a UV laboratory source.

NJC Paper

### 2.3. Methods

The FT-IR-ATR spectra were recorded in the 600-4000 cm<sup>-1</sup> range, using a Bruker Vertex 70 spectrometer. Steady state fluorescence, chromaticity and absolute quantum yields (PLQY) were recorded on a Horiba Fluoromax 4P with the Quanta-φ integration sphere. The lifetime measurements were performed using an Edinburgh Instruments FLS980 spectrometer equipped with the TCSPC module. For the nanosecond range lifetime of the prepared PVA-[Y(L)<sub>3</sub>(H<sub>2</sub>O)<sub>3</sub>] and PVP-[Y(L)<sub>3</sub>(H<sub>2</sub>O)<sub>3</sub>] composites, excitation was provided using a picosecond pulsed EPL-375 laser source while for the rest of the composites the measurements were made using a 50 KHz pulsed, 60 W xenon lamp (model μF920). AFM imaging was performed using a Ntegra Spectra -NT-MDT, Russia instrument operated in the tapping mode. Silicon cantilever tips (NSG 10), with a resonance frequency of 140-390 kHz, a force constant of 5.5-22.5 N m<sup>-1</sup> and a 10 nm tip curvature radius, were used. The samples were prepared by spincoating the composite solutions on glass slides using Laurell WS-400-6NPP equipment. SEM images were recorded on Hitachi SU-1510 equipment, working at a 15 kV accelerating voltage.

# 3. Results and discussion

# 3.1. Remarks over the structure of the free complexes

In Fig. 2 the generic structure of the embedded complexes  $[M(L)_3(H_2O)_3]$  (M = Eu<sup>3+</sup>, Tb<sup>3+</sup>, Y<sup>3+</sup>) is presented, and their in-depth structural investigation has been detailed in a previous work.9 Briefly, the coordination number of the central Eu<sup>3+</sup>, Tb<sup>3+</sup> and Y<sup>3+</sup> cations is 9 through the bidentate behavior of the 2-(1H-1,2,4triazol-3-yl)pyridine (HL) ligand and also by the presence of 3 water molecules in the first coordination sphere.

Covalent bonding is established between the central cation and the nitrogen atom in the triazole ring while coordinative bonding is established with the nitrogen atom in the pyridine ring. The favorable structure of the ligand and the configuration achieved through complexation allow the efficient sensitization of the Eu<sup>3+</sup> and Tb<sup>3+</sup> central cations, thus triggering intense and narrow radiative transitions located in the red and green areas of the visible spectrum. The blue emitting complex is particularly interesting due to its wider band emission owing to the influence of the Y<sup>3+</sup> central cation over the excited states of the surrounding ligands.

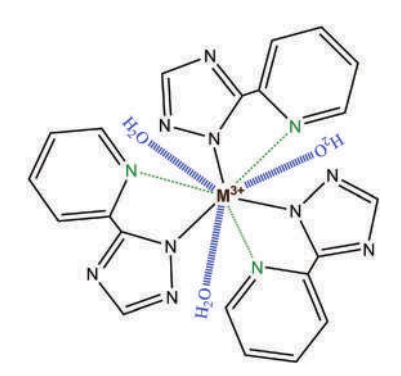


Fig. 2 Generic structure of the embedded complexes.

Through embedding in the selected polymer matrices, the emission characteristics of the complexes were enhanced in terms of PLQY and spectral purity. As will be further discussed, the spectral purity enhancement was especially noticed in the case of the Eu3+ complex where the ratio between the intensities of the two main characteristic emission peaks was markedly influenced by the new environment provided by the polymer matrices.

# 3.2. FT-IR investigation

The FT-IR spectra recorded for all prepared composites (Fig. 3) revealed several modifications compared with the starting compounds. The recorded spectra of the composites are dominated by the characteristic absorption peaks of the polymer matrices but certain specific peaks of the embedded complexes could be clearly noted. In the case of PVA composites (Fig. 3(1a-c)) the following peaks were assigned to the functional groups specific to the polymer matrix $^{18,19}$  and embedded complexes: $^{9,20}$  3285–3300 cm $^{-1}$  –OH; 2920-2922 cm<sup>-1</sup> -CH/CH<sub>2</sub> stretching (both PVA and complex); 1726–1730 cm<sup>-1</sup> - C=O (acetyl) stretching; 1647–1659 cm<sup>-1</sup> -C-C- stretching;  $1601-1609 \text{ cm}^{-1}$  - C=N stretch (pyridine ring); 1371 and 1327-1329  $cm^{-1}$  - CH deformation (both PVA and complex); 1471 and 1425 cm<sup>-1</sup> - CH<sub>2</sub> deformation and wagging; 1086–1092 cm<sup>-1</sup> – C–O (–C–C– coupled) stretching; 943–945 cm<sup>-1</sup> – syndiotactic configuration degree of PVA; 717-723 and 623-627 cm<sup>-1</sup> - triazole ring out of plane bending.

Most of the specific peaks of the embedded complexes located especially in the 1600-1000 cm<sup>-1</sup> region are masked by the higher intensity peaks of the PVA matrix. Yet, those which are still visible in the lower end of the recorded spectra appear slightly displaced. Thus, the peaks corresponding to the triazole ring bending appear to be displaced from 629-633 and  $721-727 \text{ cm}^{-1}$  in the case of the free complexes to 623–627 and 717–723 cm<sup>-1</sup> after embedment. Another important modification occurring for all prepared composites is the stretching vibration of the -C=O (acetyl) groups which not only appear displaced from 1713 cm<sup>-1</sup> to 1726-1730 cm<sup>-1</sup> but also with a higher intensity when compared with the spectrum recorded for the PVA matrix sample.

These modifications suggest possible interactions between functional groups of the PVA matrix and embedded complexes, and the structural rearrangements leading to more favorable conditions for the emission efficiency enhancement of the radiative processes.

In the case of the PVP composites the specific vibrations of the embedded complexes are even less visible in the recorded spectra (Fig. 3(2a-c)), as in the previous case, masked by the peaks related to the various groups of the polymer matrix. Thus, the PVP carbonyl groups with their highest intensity peak and other specific medium-high intensity peaks located in the lower end along with the small amount of embedded complexes impede the presence of discernable peaks of the complexes in the recorded composite spectra. Therefore, the recorded peaks are attributed to: 2883-2951 cm<sup>-1</sup> -CH/CH<sub>2</sub> stretching; 1647-1651 cm<sup>-1</sup> -C=O stretching; 1495, 1427-1429 and 1373-1375 cm<sup>-1</sup> -CH deformation; 1279–1281 cm<sup>-1</sup> -C-N stretching; 737-739 and 646 cm<sup>-1</sup> -R-CO-N- stretching.<sup>21,22</sup>

Paper NJC

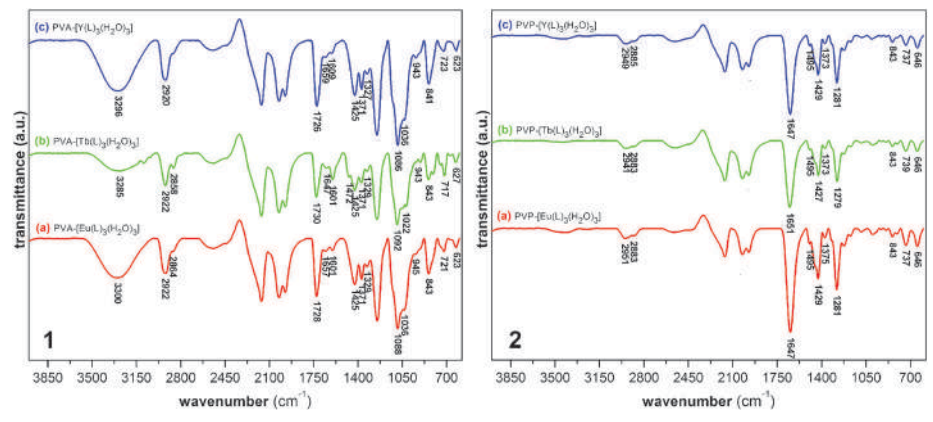


Fig. 3 FT-IR spectra of the composites: (1a) PVA- $[Eu(L)_3(H_2O)_3]$ , (1b) PVA- $[Tb(L)_3(H_2O)_3]$ , (1c) PVA- $[Y(L)_3(H_2O)_3]$ , (2a) PVP- $[Eu(L)_3(H_2O)_3]$ , (2b) PVP- $[Tb(L)_3(H_2O)_3]$ , (2c) PVP- $[Y(L)_3(H_2O)_3]$ .

Several modifications compared with the spectrum recorded for a PVP sample were also noticed, the most important being the displacement of the peak related to the carbonyl group initially located at 1662 cm<sup>-1</sup> which suggests interactions, and the most probable being with the central cation of the embedded complexes. Other notable displacements were noted in case of -C-N stretching vibration from 1288 to 1279–1281 cm<sup>-1</sup> and for the -R-CO-N- stretching vibration from 745 to 737–739 cm<sup>-1</sup>. As in the case of PVP composites, these rearrangements and possible interactions between functional groups of the PVP matrix and embedded complexes could explain the markedly improved emissive properties of the composites.

# 3.3. Fluorescence spectroscopy

The emissive properties of the prepared composites are relying essentially on the photoluminescence of the embedded complexes. The characteristic narrow band emission of the  $[Eu(L)_3(H_2O)_3]$  and  $[Tb(L)_3(H_2O)_3]$  complexes is based on a classic metal centered photoluminescence mechanism where the efficient sensitization provided by the surrounding ligands triggers radiative transitions within 4f orbitals of the central cation.<sup>23</sup> In the case of the  $[Y(L)_3(H_2O)_3]$  complex the intense, wider band blue emission is governed by a different mechanism which involves the influence

of the heavy atom vicinity over the excited states of the ligands. The recorded luminescence lifetime decay curves sustain the previously mentioned mechanisms, with expected  $\mu$ s range lifetimes for the  $[Eu(L)_3(H_2O)_3]$  and  $[Tb(L)_3(H_2O)_3]$  complexes, while for the  $[Y(L)_3(H_2O)_3]$  the recorded value is placed in the ns range which is rather typical for organic fluorophores. From the practical perspective, a more important aspect is that the absolute PLQYs of all three complexes, irrespective of the involved luminescence mechanism, are comparable in terms of the recorded values (22 to 31%).

Through embedding in the PVA and PVP matrices, the luminescence properties of the complexes are favorably affected in terms of emission efficiency and spectral purity. As mentioned above, the new environment provided by the polymer matrices and the interactions occurring between functional groups could play the main roles in the observed enhancements of the photoluminescence properties. In Fig. 4a the excitation/emission spectra of the prepared PVA-[Eu(L)<sub>3</sub>(H<sub>2</sub>O)<sub>3</sub>] and PVP-[Eu(L)<sub>3</sub>(H<sub>2</sub>O)<sub>3</sub>] composites are presented while for comparison, the excitation/emission spectra of the free complex are also included. In all cases, the transitions responsible for the recorded emission peaks are as follows:  $^5D_0 \rightarrow ^7F_1$  for the 589–591 nm peaks;  $^5D_0 \rightarrow ^7F_2$  for the 613–616 nm peaks; the low intensity peaks located at 640 and

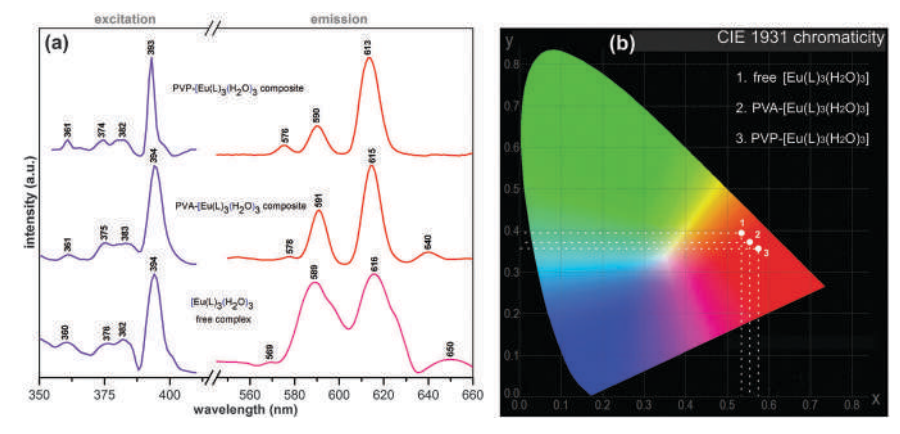


Fig. 4 (a) Excitation/emission spectra recorded for the [Eu(L)<sub>3</sub>(H<sub>2</sub>O)<sub>3</sub>], PVA-[Eu(L)<sub>3</sub>(H<sub>2</sub>O)<sub>3</sub>] PVP-[Eu(L)<sub>3</sub>(H<sub>2</sub>O)<sub>3</sub>], (b) CIE 1931 chromaticity parameters.

650 visible only in the PVA composite and free complex spectra are due to the  ${}^5D_0 \rightarrow {}^7F_3$  transition; the  ${}^5D_0 \rightarrow {}^7F_0$  transition is responsible for the barely observable 576-578 nm peaks. The  $^5\mathrm{D}_0 o {}^7\mathrm{F}_1$  parity-allowed magnetic dipole transition responsible for the peak centered around 590 nm is practically unaffected by the surrounding symmetry while the most intense 615 nm centered peaks due to the  ${}^5D_0 \rightarrow {}^7F_2$  electrical-dipole allowed hypersensitive transition are known to be highly affected by the surrounding symmetry degree.<sup>26</sup> The ratio between the emission intensities of these two peaks is an asymmetry parameter for the Eu<sup>3+</sup> surroundings, higher values indicating lower symmetry configurations.27

As could be noted, through embedding in the PVA matrix the intensity ratio between the 615 and 591 nm peaks is almost 2 while for the case of the free complex the intensities of these two peaks is practically equal. In the case of the PVP composite the ratio between the 613 and 590 nm peaks is  $\sim$  3.2 indicating an even more disordered configuration of the Eu<sup>3+</sup> surroundings. From the practical perspective, the most favorable situation is achieved in the case of the PVP-[Eu(L)<sub>3</sub>(H<sub>2</sub>O)<sub>3</sub>] composite where the dominant 613 nm peak provides photoluminescence emission with a higher level of chromatic purity, thus allowing "deeper" red (Fig. 4b) emission in the targeted applications. The excitation spectra (Fig. 4a) are very similar in all cases, with the highest intensity peak located in the UV-A region at 393-394 nm and a series of minor peaks located in the 360-383 nm range.

Fig. 5a presents the excitation/emission spectra of the prepared PVA-[Tb(L)<sub>3</sub>(H<sub>2</sub>O)<sub>3</sub>] and PVP-[Tb(L)<sub>3</sub>(H<sub>2</sub>O)<sub>3</sub>] composites and also of the free complex. As could be noted, in their case the emission spectra are similar in all cases; the recorded peaks occur as a result of the following radiative transitions:  ${}^5D_4 \rightarrow {}^7F_5$  is responsible for the most intense peak located at 542-544 nm,  ${}^5D_4 \rightarrow {}^7F_6$  for the medium intensity peak located at 487–488 nm while the  $^5D_4 \rightarrow ^7F_4$ and  ${}^5D_4 \rightarrow {}^7F_3$  transitions are responsible for the 582–583 nm and 619-620 nm lower intensity peaks.<sup>28</sup>

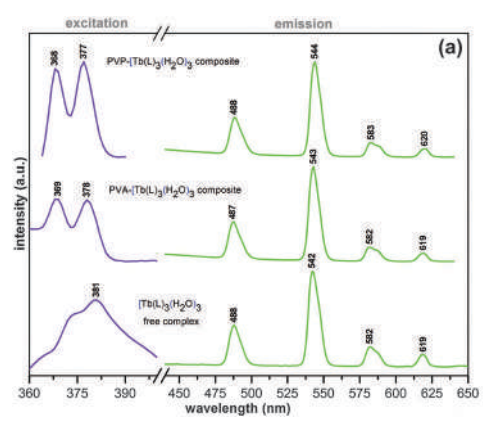
Unlike the Eu<sup>3+</sup> emissive center, the radiative transitions of the Tb<sup>3+</sup> cation responsible for the recorded peaks are practically unaffected by the surrounding symmetry, therefore no differences in the emission peak intensity ratio is expected, which is confirmed

also by the recorded chromaticity parameters (Fig. 5b). The excitation spectra of both composites present two distinct peaks with an almost equal intensity, both located in the UV-A region at 377-378 nm and 368-369 nm respectively.

In the case of the PVA- $[Y(L)_3(H_2O)_3]$  and PVP- $[Y(L)_3(H_2O)_3]$ composites (Fig. 6) several interesting modifications were observed in their recorded spectra (Fig. 6a) when compared with the free complex. The intense, wider band emission peaks arising from the intraligand radiative transitions are displaced to lower wavelengths (from 482 to 472-474 nm) allowing a "deeper" blue emission (Fig. 6b) which is also favorable for the targeted applications.

The most important modification appears in the excitation spectra where an important shift of the excitation peak was recorded. Thus, in the case of the free complex the peak is located in the violet-blue (418 nm) region of the visible spectra while in the case of the PVA and PVP composites the excitation peaks are located in the UV-A region (352, 377 nm). This important shift toward lower wavelengths of the excitation peaks could be attributed to the previously investigated interactions between the surrounding polymer matrix and the central cation or the functional groups of the ligand which influences the excited states responsible for radiative transitions. The shifting of the excitation peaks to lower wavelengths is very important from the application perspective since the excitation peaks of the RGB emissive composites are situated in a narrow 375-390 nm range, therefore are possible to be efficiently excited by just one type of source, for example, 375, 380 nm UV-LEDs. The overall excitation/emission characteristics are especially favorable in the case of the prepared PVP composites where the additional advantages of higher absolute PLQY and spectral purity making them better suited for the targeted applications.

The absolute PLQY values recorded at several excitation wavelengths are presented in Table 1. The highest values are achieved by the PVA-[Tb(L)<sub>3</sub>(H<sub>2</sub>O)<sub>3</sub>] and PVP-[Tb(L)<sub>3</sub>(H<sub>2</sub>O)<sub>3</sub>] and the overall results are better in the case of all PVP composites. Compared with the free complexes9 the recorded absolute PLQY values of the composites are more than two times higher, thus being closer to the requirements of a practical application. Such an enhancement of the PLQY values through embedding



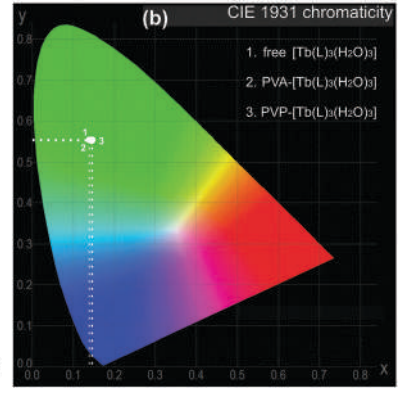


Fig. 5 (a) Excitation/emission spectra recorded for the [Tb(L)<sub>3</sub>(H<sub>2</sub>O)<sub>3</sub>], PVA-[Tb(L)<sub>3</sub>(H<sub>2</sub>O)<sub>3</sub>], PVP-[Tb(L)<sub>3</sub>(H<sub>2</sub>O)<sub>3</sub>], (b) CIE 1931 chromaticity parameters.

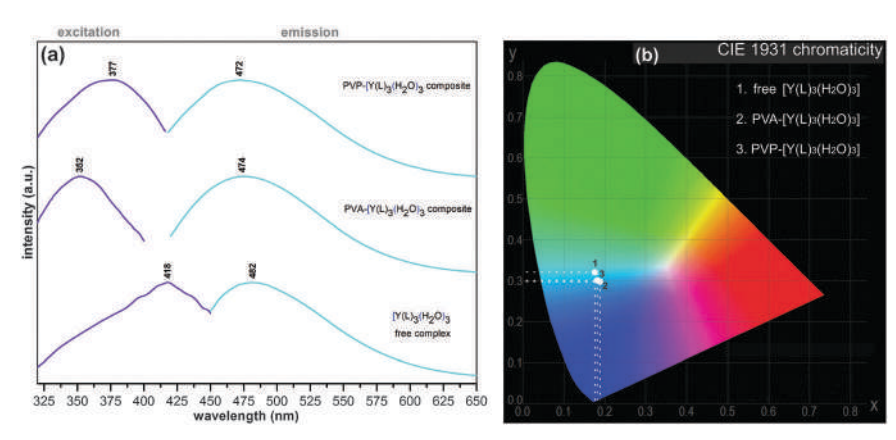


Fig. 6 (a) Excitation/emission spectra recorded for the [Y(L)<sub>3</sub>(H<sub>2</sub>O)<sub>3</sub>], PVA-[Y(L)<sub>3</sub>(H<sub>2</sub>O)<sub>3</sub>], PVP-[Y(L)<sub>3</sub>(H<sub>2</sub>O)<sub>3</sub>], (b) CIE 1931 chromaticity parameters.

Table 1 Absolute PLQY values recorded for the prepared composites

	Absolute PLQY (%)					
$\lambda$ excitation (nm)	PVA-[Tb(L) <sub>3</sub> (H <sub>2</sub> O) <sub>3</sub> ]	PVA- $[Eu(L)_3(H_2O)_3]$	PVA-[Y(L) <sub>3</sub> (H <sub>2</sub> O) <sub>3</sub> ]	PVP-[Tb(L) $_3$ (H $_2$ O) $_3$ ]	PVP-[Eu(L) <sub>3</sub> (H <sub>2</sub> O) <sub>3</sub> ]	PVP-[Y(L) <sub>3</sub> (H <sub>2</sub> O) <sub>3</sub> ]
350	54.81	36.90	47.16	_	_	_
360	61.96	41.04	43.50	53.55	44.61	38.79
370	67.54	51.22	38.53	61.11	49.10	47.03
380	_	53.17	33.28	69.21	53.81	52.41
390	_	58.49	_	_	59.09	_

of photoluminescent complexes in polymer matrices were also reported in other studies, <sup>12,29,30</sup> which is a result of the more favorable conditions in terms of excitation energy transfer to the emissive centers achieved in the new environment.

The lifetime investigation (luminescence decay curves presented in Fig. 7) is as expected, similar to those recorded in the case of the free complexes, due to the luminescence mechanism involved in each case. Thus, for the PVA, PVP composites (Fig. 7a) prepared with  $[Tb(L^1)_3(H_2O)_3]$  and  $[Eu(L^1)_3(H_2O)_3]$  complexes the emission lifetime is in the 343–970  $\mu$ s range; the values are specific to the classic metal centered luminescence arising from the 4f transitions of the trivalent lanthanide cations. The PVP composites present longer photoluminescence lifetimes. In the case of the composites prepared with  $[Y(L^1)_3(H_2O)_3]$  (Fig. 7b) the lifetimes, as expected, are situated in 40–50 ns range due to the specific of the

luminescence mechanism involved in this case, with a slightly higher lifetime in the case of the PVP- $[Y(L^1)_3(H_2O)_3]$ .

# 3.4. AFM investigation

The recorded AFM images highlighted the presence of submicronic structures relatively uniformly dispersed in the polymer matrices suggesting the presence of clustered complexes. In Fig. 8 the AFM images recorded for the prepared PVA-[Eu(L) $_3$ (H $_2$ O) $_3$ ] composite and PVP-[Tb(L) $_3$ (H $_2$ O) $_3$ ] respectively are presented. These AFM images are also typical for the rest of the prepared composites, no notable differences being visible in their cases.

In the case of the PVP composites the dimensions of the clustered complexes are slightly lower with an average diameter in the 100–200 nm range while in the case of the PVA composites the average diameter is in the 300–500 nm range. These particularities

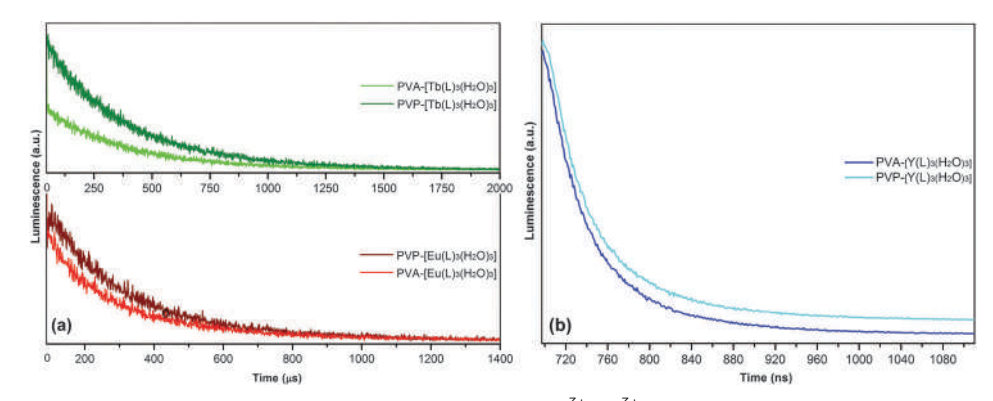


Fig. 7 Luminescence decay curves recorded for (a) PVA, PVP composites with Eu<sup>3+</sup>, Tb<sup>3+</sup> complexes, (b) PVA, PVP composites with the Y<sup>3+</sup> complex.

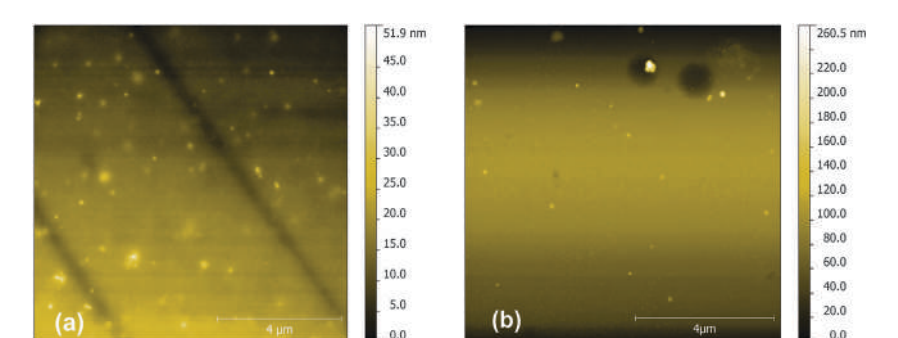


Fig. 8 AFM images recorded for the (a) PVA-[Eu(L)<sub>3</sub>(H<sub>2</sub>O)<sub>3</sub>], (b) PVP-[Tb(L)<sub>3</sub>(H<sub>2</sub>O)<sub>3</sub>] composites

are also visually detected by a more homogenous, transparent and glossier aspect of the PVP composites.

# 3.5. SEM investigation

NJC

SEM imaging was performed for the composites prepared in thick films; the recorded micrographs are presented in Fig. 9. It was found that the thick composite films are unstable under the equipment specific working conditions of high vacuum and accelerated electron beam scanning, and longer exposure time altering the aspect of the investigated samples. Nevertheless, the recoded images revealed the same clustering of the embedded complexes in the polymer matrices with a more homogenous aspect in the case of PVP composites.

# 4. Suggested application study

As previously suggested, the intense RGB emission of the prepared composites and their ability to be processed in thin or thicker films according to the application requirements may

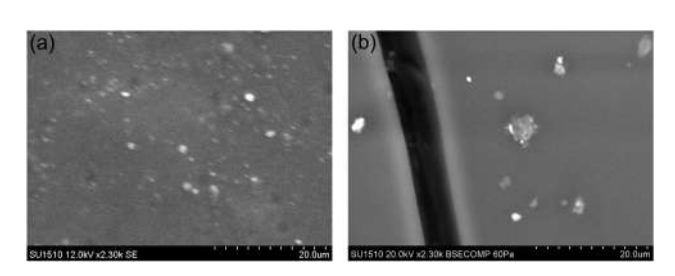


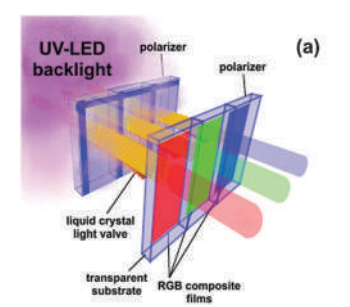
Fig. 9 SEM micrographs recorded for the (a) PVA-[Eu(L)<sub>3</sub>(H<sub>2</sub>O)<sub>3</sub>], (b) PVP-[Y(L)<sub>3</sub>(H<sub>2</sub>O)<sub>3</sub>] composites.

be usable in AMLCD displays. The composites could replace the usual RGB filters in a suggested configuration which uses UV-LEDs instead of white LEDs for backlighting. A possible approach is presented in Fig. 10a while in Fig. 10b an experimental study of alternating in line, spray coated RGB composites deposited on a transparent PMMA substrate is presented.

Besides the remarkable chromaticity attributes, their excitation range located in the same UV-A region makes it possible to use 375-385 nm SMD UV-LEDs in edge or matrix backlighting configurations. Several theoretical advantages may be achieved through this approach, the most notable are: a better color gamut due to the emission characteristics of the RGB composites; contrast enhancement and wider viewing angles through minimizing the "bleeding" effect of un-modulated visible light passing through the liquid crystal light valve.

# Conclusions

The paper reports red, green and blue emitting composites with remarkable photoluminescence properties obtained through embedding of Eu<sup>3+</sup>, Tb<sup>3+</sup> and Y<sup>3+</sup> complexes with 2-(1H-1,2,4triazol-3-yl)pyridine in poly(vinyl alcohol) and poly(n-vinyl pyrrolidone) matrices. Through embedding in the selected polymer matrices, the luminescence properties are markedly enhanced compared to the free complexes; the recorded PLQY values increasing from an average 25-30% to 52-69%, while the emission purity, especially in the case of Eu<sup>3+</sup> containing composites is greatly improved. The best results in terms of PLQY, color purity and convenience of the excitation range were achieved in the case of PVP composites. The environment provided



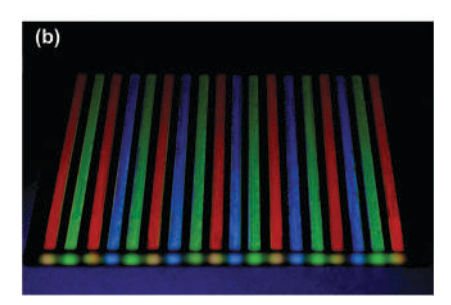


Fig. 10 (a) A possible approach for implementation in AMLCD; (b) experimental study of spray coated RGB composites under UV-A excitation.

by the polymer matrices and the interactions occurring between their functional groups and embedded complexes are most probably responsible for the recorded enhancements of the photoluminescence properties. The composites could be easily processed in thin or thicker films through spin/spray coating or jet printing according to the application requirements. Besides their preparation in thick films, the paper presents an experimental study of obtaining spray coated RGB composite films in an alternating, in line configuration which could be a possible replacement of color filters in AMLCD displays.

# Acknowledgements

This work was supported by a grant of the Romanian National Authority for Scientific Research, CNCS – UEFISCDI, project number PN-II-ID-PCE 2011-3-0708.

# References

- 1 A. N. Gusev, V. F. Shulgin, S. B. Meshkova, P. G. Doga, M. Hasegawa, G. G. Aleksandrov, I. L. Eremenko and W. Linert, *Inorg. Chim. Acta*, 2012, **387**, 321–326.
- 2 I. L. V. Rosa, P. C. de Sousa Filho, C. Roberto Neri, O. A. Serra, A. Teixeira de Figueiredo, J. Arana Varela and E. Longo, *J. Fluoresc.*, 2011, 21, 1575–1583.
- 3 J. P. Leonard and T. Gunnlaugsson, *J. Fluoresc.*, 2005, **15**, 585–595.
- 4 W. T. K. Chan, W. T. Wong, W. T. K. Chan and W. T. Wong, Polyhedron, 2014, 83, 150–158.
- 5 L. Armelao, S. Quici, F. Barigelletti, G. Accorsi, G. Bottaro, M. Cavazzini and E. Tondello, *Coord. Chem. Rev.*, 2010, 254, 487–505.
- 6 K. Binnemans, Chem. Rev., 2009, 109, 4283-4374.
- 7 A. B. Canaj, G. K. Tsikalas, A. Philippidis, A. Spyros and C. J. Milios, *Dalton Trans.*, 2014, 43, 12486–12494.
- 8 J. Andres, R. D. Hersch, J. E. Moser and A. S. Chauvin, *Adv. Funct. Mater.*, 2014, 24, 5029–5036.
- C. S. Stan, C. Peptu, M. Popa, D. Sutiman and P. Horlescu, *Inorg. Chim. Acta*, 2015, 429, 160–167.

- 10 B. Chen and J. Feng, J. Phys. Chem. C, 2015, 119, 7865-7872.
- 11 R. Puthiyottil, S. Varghese, U. Gopalakrishnapanicker and J. T. Guthrie, *Polym. Eng. Sci.*, 2012, 53, 119–124.
- 12 B. Yan and X. Chen, *J. Optoelectron. Adv. Mater.*, 2007, 9, 2091–2096.
- 13 G. Kaur and S. B. Rai, J. Phys. D: Appl. Phys., 2011, 44, 425306.
- 14 S. Di Pietro, D. Imbert and M. Mazzanti, *Chem. Commun.*, 2014, 50, 10323–10326.
- 15 M. Hasegawa, S. Kunisaki, H. Ohtsu and F. Werner, *Monatsh. Chem.*, 2009, **140**, 751–763.
- 16 H. Zhang, H. Song, H. Yu, S. Li, X. Bai, G. Pan, Q. Dai, T. Wang, W. Li, S. Lu, X. Ren, H. Zhao and X. Kong, *Appl. Phys. Lett.*, 2007, **90**, 103103.
- 17 D. J. R. Cristaldi, S. Pennisi and F. Pulvirenti, *Liquid Crystal Displays*, Springer, Science Business Media B.V., 2009.
- 18 W. A. Jabbar, N. F. Habubi and S. S. Chiad, *J. Arkansas Acad. Sci.*, 2010, **64**, 101–105.
- 19 E. Fonseca dos Reis, F. S. Campos, A. P. Lage, R. C. Leite, L. G. Heneine, W. L. Vasconcelos, Z. I. P. Lobato and H. S. Mansur, *Mater. Res.*, 2006, 9, 185–191.
- 20 F. Billes, H. Endredi and G. Keresztury, *J. Mol. Struct.: THEOCHEM*, 2000, **530**, 183–200.
- 21 D. J. C. Salamone, *Polymeric Materials Encyclopedia*, CRC Press, 1996, vol. 7.
- 22 P. Hemalatha, M. K. Veeraiah, S. P. Kumar, N. M. Madegowda and M. Manju, *Am. J. Polym. Sci.*, 2014, **4**, 16–23.
- 23 G. Liu and B. Jacquier, *Spectroscopic properties of rare earth in optical materials*, Springer, 2005.
- 24 A. Vogler and H. Kunkely, *Inorg. Chim. Acta*, 2006, **359**, 4130–4138.
- 25 M. Y. Berezin and S. Achilefu, Chem. Rev., 2010, 110, 2641-2684.
- 26 K. Binnemans, Coord. Chem. Rev., 2015, 295, 1-45.
- 27 J. C. G. Bünzli and S. V. Eliseeva, Chem. Sci., 2013, 4, 1939-1949.
- 28 P. Lenaerts, C. G. Walrand and K. Binnemans, *J. Lumin.*, 2006, **117**, 163–169.
- W. Li, P. Yan, G. Hou, H. Lia and G. Li, *Dalton Trans.*, 2013,
   42, 11537–11547.
- 30 T. Li, W. Shang, F. Zhang, L. Mao, C. Tang, M. Song, C. Du and Y. Wu, *Engineering*, 2011, 3, 301–311.

ELSEVIER

Contents lists available at ScienceDirect

# Inorganica Chimica Acta

journal homepage: www.elsevier.com/locate/ica



# Photoluminescent properties of novel Y(III), Sm(III), Eu(III), Gd(III) and Tb(III) complexes with 2-(1H-1,2,4-Triazol-3-yl)pyridine



Corneliu Sergiu Stan<sup>a,\*</sup>, Cristian Peptu<sup>b</sup>, Nathalie Marcotte<sup>c</sup>, Petronela Horlescu<sup>a</sup>, Daniel Sutiman<sup>a</sup>

- <sup>a</sup> TUIasi Gheorghe Asachi Technical University of Iasi, Faculty of Chemical Engineering and Environmental Protection, 73 Prof. Dr. docent Dimitrie Mangeron, 700050 Iasi, Romania
- <sup>b</sup> Petru Poni Institute of Macromolecular Chemistry, 41A Aleea Grigore Ghica Voda, Iasi, Romania
- c Institut Charles Gerhardt MACS, Ecole Nationale Supérieure de Chimie de Montpellier, 8 rue de l'Ecole Normale, 34296 Montpellier Cedex, France

### ARTICLE INFO

# Article history: Received 15 November 2014 Received in revised form 13 January 2015 Accepted 16 January 2015 Available online 18 February 2015

Keywords: Luminescence Lanthanide complexes Triazole–pyridine ligand

# ABSTRACT

2-(1H-1,2,4-Triazol-3-yl)pyridine was investigated as suitable ligand for the preparation of new Y(III), Sm(III), Eu(III), Gd(III) and Tb(III) complexes. Elemental analysis, mass spectrometry, thermal analysis, FT-IR and P-XRD methods were used to investigate their structural configuration. All the prepared complexes are highly luminescent, having an impressive visual emission under UV excitation. Fluorescence spectroscopy revealed in case of Sm(III), Eu(III) and Tb(III) complexes intense metal centered specific narrow band emissions from the f-f transitions within 4f orbitals, while in case of Gd(III) and Y(III) complexes intense wide band emissions were recorded most probable due the heavy atom effect over the excited intraligand states. The excitation peaks are conveniently located in UV-A region for all prepared complexes apart from Sm(III) complex where the excitation peak is located within the violet region of the spectrum. The remarkable luminescent properties might recommend these complexes for applications in optical devices, as photonic conversion media.

© 2015 Elsevier B.V. All rights reserved.

# 1. Introduction

The search for new suitable ligands capable of complexing lanthanides seems to attract much interest not only for expanding the knowledge about lanthanide chemistry but mainly due to the unique features of lanthanides which could be enhanced through complexation. Especially in the last two decades, more focus has been put on obtaining new lanthanide complexes due to their promising applications in state of the art optoelectronics, optical materials or as tracing agents in biological or medical analysis. In case of photoluminescent lanthanide complexes, ligands must fulfill a series of demands in agreement with particular properties of the lanthanide cations. Their characteristic narrow emission bands are due to the radiative transitions within 4f orbitals partially shielded by the 5s and 5p orbitals [1,2] which are barely affected by the molecular entities located in the vicinity. Owing to the small absorption coefficients of Ln3+ cations due to the shielded inner f orbitals, efficient radiative transitions can be triggered by an adequate energy transfer from the ligand to the emissive lanthanide center. The sensitization of the lanthanide cation may be achieved through the coordination of a chromophore containing ligand capable of energy absorption, which could be further efficiently

transferred to the emitting state of the lanthanide cation, which returns to its ground state by photon emission. Besides the efficient energy harvesting followed by transfer to the lanthanide center, a suitable ligand must avoid radiationless deactivation paths. The situation may be further complicated by various factors that influence the efficient energy transfer to the lanthanide cation. In many cases a chemical configuration of a particular ligand may prove to be effective for certain cations, while for others efficient sensitization is not achieved.

Among various classes of ligands, carboxylates, polyaminocarboxylates, phosphonates, phosphinates, β-diketonates or tripodal structures derived from pyrazole as tripyridylpyrazolylmethane were investigated for achieving an efficient sensitization of the lanthanide cations [2–4]. Various Gd³+ chelates derived from linear or macrocyclic polyamino polycarboxylates were prepared as suitable MRI agents for medical investigations [5]. Recently, 2,2′-bipyrimidine was found to be suitable for designing molecular complexes or polymeric lanthanide materials with photoluminescent and magnetic properties [6]. Lanthanide complexes based on thenoyltrifluoro-acetone, phenanthroline or dibenzoylmethane ligands are thoroughly investigated due to their electroluminescence in OLED devices [7,8].

Although yttrium is not part of the lanthanide group, its resemblances with lanthanides are very strong as regards to both physical properties and chemical behavior [9]. The close similarities

<sup>\*</sup> Corresponding author. Tel.: +40 232 278683; fax: +40 232 271311. *E-mail address:* stancs@tuiasi.ro (C.S. Stan).

with gadolinium or erbium can be noted and further sustained by the investigations related to the lanthanide complexes presented in this work, especially with the prepared gadolinium complex.

In this paper Y<sup>3+</sup>, Sm<sup>3+</sup>, Eu<sup>3+</sup>, Gd<sup>3+</sup> and Tb<sup>3+</sup>complexes with 2-(1H-1,2,4-Triazol-3-yl)pyridine as ligand, are prepared and studied. Triazole derivatives have been getting increased attention as suitable ligands for highly luminescent complexes of lanthanides or other transition metals. Mono and bistriazoles ligands were used to prepare strong red emission europium complexes [10]. Phenyl-1H-[1,2,3]triazoles were used as cyclometalating ligands in new iridium complexes showing remarkable photoluminescent properties [11]. Phosphonylated bis-pyrazolyl-pyridine ligands were tested for obtaining multifunctionalized lanthanide complexes with remarkable photoluminescent properties [12] while a close structurally resembling with the one reported in this work 2-(1H-1.2.3-Triazol-4-vl)-pyridine with a similar bidentate behavior was used to prepare homoleptic Ru<sup>2+</sup> complexes [13]. Beside their structural investigation, a particular attention has been given to their photoluminescent properties.

The fluorescence spectroscopy revealed interesting details on each of the complexes luminescence and the subsequent processes involved in their achievement. While for the Eu<sup>3+</sup>, Tb<sup>3+</sup>, Sm<sup>3+</sup> complexes their luminescence is achieved due to a "classic" ligand to metal energy transfer mechanism responsible for the specific narrow emission bands, in the cases of Gd<sup>3+</sup> and Y<sup>3+</sup> the intense wide band emission is achieved most probable through an unusual ligand to metal energy transfer whose excited states are back transferred to the ligand. From a practical perspective, the remarkable photoluminescent properties of the prepared complexes may be of potential interest especially for the applications in optical devices or through embedding in various compatible media as luminescent probes for biological and medical investigations.

# 2. Experimental

# 2.1. Materials

2-(1H-1,2,4-Triazol-3-yl)pyridine (97%) was purchased from Sigma–Aldrich while Yttrium chloride (YCl $_3 \times H_2O$ , 99.99%), Samarium chloride (SmCl $_3 \times H_2O$ , 99.99%), Europium chloride (EuCl $_3 \times H_2O$ , 99.9%), Gadolinium chloride (GdCl $_3 \times 6H_2O$ , 99.9%) and Terbium chloride (TbCl $_3 \times 6H_2O$ , 99.9%) were purchased from Alfa-Aesar. Ethanol absolute and high purity Milli-Q water were used for preparation and washing operations.

# 2.2. Preparation of 2-(1H-1,2,4-Triazol-3-yl)pyridine complexes

All the investigated complexes were prepared at 1:3 molar ratio (central atom to ligand). Firstly, aqueous solutions of Y, Tb, Sm, Eu, Gd chlorides are prepared by dissolving 1 mmol of each in 2 mL high purity Milli-Q water, in separate glass beakers provided with magnetic stirrers. Then, five similar solutions of 2-(1H-1,2,4-Triazol-3-yl)pyridine (denoted by HL) are prepared by dissolving

3 mmol of ligand in a mixture of 3 mL Milli-Q water and 1 mL ethanol. The dissolution process may be speeded up with the help of an ultrasonic bath. The complexes were obtained by mixing each prepared ligand solution with the corresponding Y, Tb, Sm, Eu, Gd chloride solutions. The complexation reactions were carried out under mild heating (40–45 °C) and stirring for about 180 min. After drying under ambient conditions, each prepared complex was washed with Milli-Q water. The reaction involved in the process and also the structures of ligand and prepared complexes are presented in Fig. 1.

The crystalline form of each prepared complex was obtained by removing slowly the remaining water through evaporation at room temperature followed by drying at 65–70 °C, under vacuum, till constant weight. The dried complexes are slightly hygroscopic so they should be placed in sealed glass containers for long term storage.

The generic structure of the prepared complexes, as presented in Fig. 1, is supported by the data recorded through investigation techniques employed in this work. The coordination number of trivalent yttrium and lanthanide cations used for preparing the investigated complexes is 9 through the bidentate behavior of the 2-(1H-1,2,4-Triazol-3-yl)pyridine (HL) ligand and also by the participation of 3 water molecules coordinated at the central cation. The small size of the lanthanides and yttrium trivalent cations involving high positive surface charge density leads to a hard Lewis acid behavior that justifies the presence of water in the first coordination sphere [14].

### 2.3. Characterization

Elemental chemical analysis was performed on Thermo Fisher Scientific Flash EA-1112CHNS/O equipment provided with Eager 300 software. The IR spectra were recorded in the 4000–400 cm<sup>-1</sup> range, using a Digilab FTS-2000 FT-IR spectrometer, according to KBr pellet method. The thermal stability was studied on a Mettler Toledo TGA-SDTA851e, under an airflow rate of 20 mL/min. The heating rate was adjusted to 10 °C/min in the 50–900 °C range. Prior to investigation, the samples were additionally dried under vacuum at 50 °C for about 6 h.

High-resolution MS and MS/MS spectra were acquired on an AGILENT 6520 QTOF mass spectrometer (Agilent Technologies) equipped with an ESI source. The ESI MS parameters optimized for the analyzed complexes were set as follows: Vcap = 4000 V, fragmentor voltage = 175 V, drying gas temperature = 325 °C, drying gas flow = 5 L/min and nebulizer pressure = 35 psig. The same direct infusion ESI MS analysis protocol was applied for all analyzed samples. The samples, 0.1 mM complex solutions in methanol, were injected using a syringe pump at a flow rate of 0.5 mL/min. Nitrogen was used as spraying gas. The MS/MS experiments were conducted in the collision cell using nitrogen as collision gas at a pressure of 18 psig inside the collision cell.

XRD patterns were recorded in the  $5-70^{\circ}$  2Theta range on a Panalytical X'Pert Pro diffractometer provided with a Cu K $\alpha$ 

Fig. 1. Reaction and structures of ligand and obtained complexes.

radiation source ( $\lambda$  = 0.154060 nm). Unit cell parameters of the investigated complexes were further refined with the help of Panalytical X'Pert High Score Plus software.

The steady state fluorescence, chromaticity and absolute quantum yields (PLQY) were recorded on a Horiba Fluoromax 4P provided with the Quanta- $\phi$  integration sphere. The life time measurements were performed with an Edinburgh Instruments FLS980 spectrometer equipped with the TCSPC module. For the prepared Y(III) and Gd(III) complexes with lifetimes in nanosecond range, the excitation was provided by a picosecond pulsed EPL-375 laser source whereas in case of Sm(III), Tb(III) and Eu(III) complexes the measurements were made using a 50 kHz pulsed, 60 W xenon lamp (model  $\mu F920$ ). Visual testing of photoluminescent properties was performed using a Philips UVA TL4WBLB lamp with the emission maximum located in the 370–390 nm range and a 405 nm laser diode.

### 3. Results and discussion

# 3.1. Chemical analysis

In Table 1 are presented the experimental results recorded for prepared complexes against the theoretical values. The experimental results are in very good agreement with the theoretical values and also with the data obtained from thermal analysis and mass spectroscopy. The slightly higher values recorded for oxygen and hydrogen contents are most probably due to the physical bonded water trapped in the structure.

 Table 1

 Chemical analysis experimental results compared with calculated values.

Complex Ex	Experimental values%				Calculated values%					
	C	Н	N	0	M	С	Н	N	0	
[YL <sub>3</sub> (H <sub>2</sub> O) <sub>3</sub> ]	43.48	4.20	30.45	9.07	15.37	43.61	3.66	29.06	8.3	
[SmL <sub>3</sub> (H <sub>2</sub> O) <sub>3</sub> ]	39.13	3.92	27.01	8.14	23.5	39.42	3.31	26.27	7.5	
$[EuL_3(H_2O)_3]$	39.09	3.51	25.74	8.21	23.69	39.32	3.3	26.2	7.48	
$[GdL_3(H_2O)_3]$	38.67	3.44	25.47	8.1	24.31	39.0	3.27	25.99	7.42	
[TbL3(H2O)3]	38.71	3.45	25.8	7.76	24.51	38.9	3.26	25.92	7.40	

**Table 2**Kinetic parameters in thermal decomposition of the free ligand and prepared complexes.

Decomposition stage	Parameter	Ligand	$[YL_3(H_2O)_3]$	$[SmL_3(H_2O)_3]$	$[EuL_3(H_2O)_3]$	$[GdL_3(H_2O)_3]$	$[TbL_3(H_2O)_3]$
Stage 1	A	$1.62 \times 10^{18}$	$7.6 \times 10^{15}$	$1.57 \times 10^{16}$	$2.5 \times 10^{14}$	$1.46 \times 10^{15}$	$2.8 \times 10^{15}$
•	Ea/kJ/mol	74.05	62.3	47.8	47.89	49.7	48.07
	n	0.33	0.68	0.45	1.61	0.57	1.03
	Ti	203-272	91-156	71-171	78-155	74-158	80-144
	% loss	88.1	11.7/*9.33	10.27/*8.44	10.93/*8.41	12.9/*8.34	11.2/*8.32
Stage 2	Α	$20.1\times10^{18}$	$1.77\times10^{17}$	$7.47\times10^{17}$	$6.26\times10^{14}$	$2.25\times10^{17}$	$5.59\times10^{18}$
	Ea/kJ/mol	45.3	72.8	65.67	68.10	61.34	59.13
	n	0.55	0.71	1.39	0.48	1.07	0.69
	Ti	365-516	220-336	350-458	249-449	292-465	229-481
	% loss	10.61	36.25	34.75	34.5	35.78	34.12
Stage 3	Α	_	$3.15\times10^{18}$	$2.6\times10^{15}$	$3.35\times10^{17}$	$3.73\times10^{20}$	$8.62 \times 10^{14}$
	Ea/kJ/mol	_	52.07	55.34	45.72	67.84	73.99
	n	_	0.81	0.36	0.28	1.42	0.69
	Ti	_	349-464	541-597	510-648	555-820	550-756
	% loss	_	11.19	9.69	25.52	22.5	25.02
Stage 4	Α	_	$2.57\times10^{16}$	$7.37\times10^{18}$	=	=	_
_	Ea/kJ/mol	_	63.8	153.98	_	_	_
	n	-	0.52	0.18	_	_	_
	Ti	-	500-851	659-730	_	_	_
	% loss	-	20.67	16.09	-	_	-
Residue%		1.31	20.2/**19.52	29.21/**27.04	29.07/**27.28	28.82/**27.88	29.65/**28.0

<sup>\*</sup> Calculated value for the presence of three water molecules coordinated at the central atom.

### 3.2. Thermal analysis

Based on the recorded derivatograms, the thermal behavior of free ligand and prepared complexes were evaluated. Table 2 presents the obtained results. For the free 2-(1H-1,2,4-Triazol-3-yl)pyridine ligand (HL) the decomposition takes place in 2 stages while in case of the prepared complexes 3 or 4 stages were recorded.

The decomposition of the complexes is summarized by the following processes:

$$(M(L)_3(H_2O)_3)_{(s)} \xrightarrow{t^*C} (M(L)_3)_{(s)} + 3(H_2O)_{(g)} \tag{1}$$

$$(M(L)_3)_{(s)} \xrightarrow{t^{\circ}C} B_{(g)} + M_2 O_{3(s)}$$
 (2)

where B represents volatiles.

In the first stages, the remnant small amounts of physical bonded water and also the coordinated water is lost (1). The existence of three water molecules coordinated at the central cation is supported by the mass loss values recorded for each prepared complex. In the case of yttrium the activation energy is higher compared with that of lanthanides due to its smaller ionic radius (0.93 Å compared to 1.04–1.00 Å). In the upper stages the decomposition processes evolves with further destructuration of the complexes accompanied by volatile exhaustions (2). Besides the volatile products, a series of intermediate products like yttrium and lanthanide oxocarbonates [15,16] may occur (3) which further decomposes to more stable  $M_2O_3$  products (4) [17,18].

<sup>\*\*</sup> Calculated value for the final Ln<sub>2</sub>O<sub>3</sub> decomposition product.

$$2[(C_xH_yO_zN)_3M] \overset{300-650\,^{\circ}c}{\longrightarrow} M_2O_2CO_3 + volatiles \tag{3}$$

$$M_2O_2CO_3 \xrightarrow{650-1000^{\circ}C} M_2O_3 + volatiles$$
 (4)

The recorded mass of the residue for each prepared complex suggests the  $M_2O_3$  as final decomposition product along with the presence of small amounts of residue resulting from decomposition of the ligand.

### 3.3. ESI MS and MS/MS characterization

Formation of the complexes was confirmed by ESI MS with direct injection of the sample using an external syringe into the electro spray source. The described peaks are gas phase proton charged complexes with a corresponding m/z value calculated as the mass of the complex added to the mass of the charge, which is one proton. For example, the  $[Gd(L)^{3+}H]^+$  has a corresponding m/z value of 594.08 (the given value is for the monoisotopical peak).

The obtained spectra, showed in Table 3, allowed to emphasize, due to their high resolution, the isotopical profiles of the peaks corresponding to each complex; when compared with the

theoretical ones the differences is not significant thus confirming the hypothesized elemental composition. Moreover, the peaks corresponding to each complex were subjected to collision induced dissociation experiments which allow structural conformation at molecular level.

In each case the lost neutral fragment had 146 Da (1) and the process was assigned as the cleavage of one 2-(1H-1,2,4-Triazol3-yl)pyridine ligand. The formation of daughter ions described as  $[M(L)_2]^+$  species (fragmentation spectrum of  $[Tb\ (L)^{3+}H]^+$  is given as example in Fig. 2.

Besides the main fragmentation pathway, a 104 Da loss was observed (2). This is assigned to the cleavage of the pyridine ring belonging to the ligand. The 104 Da loss appears also during the fragmentation of ligand alone thus confirming the structural assignment. The CID spectrum presented in Fig. 2 exemplifies the behavior of analyzed complexes. The collision energy determined for optimal fragmentation process is  $E_{\text{lab}} = 20 \text{ V}$ .

#### 3.4. IR analysis

Investigation of the recorded IR spectra revealed the interactions occurred between the 2-(1H-1,2,4-Triazol-3-yl)pyridine

**Table 3**Mass spectrometry description of the complexes

No.	Complex	Formula	Monoisotopic mass	Mass percent	Isotopical profiles experimental/simulated
1	[Y (L) <sub>3</sub> +H]*	C <sub>21</sub> H <sub>16</sub> N <sub>12</sub> Y	525.06	C 48.01%, H 3.07%, N 32.00%, Y 16.92%	100 525  100
2	[Sm (L) <sub>3</sub> +H] <sup>+</sup>	$C_{21}H_{16}N_{12}Sm$	588.08	C 42.98%, H 2.75%,N 28.65%, Sm 25.63%	105 28.5 327 325.5 328 5275 328 528 528 528 528 528 528 528 528 528 5
3	[Eu (L) <sub>3</sub> +H] <sup>+</sup>	C <sub>21</sub> H <sub>16</sub> N <sub>12</sub> Eu	589.08	C 42.86%, H 2.74%, N 28.57%, Eu 25.83%	569 569 569 569 569 569 569 569 569 569
4	[Gd (L) <sub>3</sub> +H] <sup>+</sup>	C <sub>21</sub> H <sub>16</sub> N <sub>12</sub> Gd	594.08	C 42.48%, H 2.72%, N 28.32%, Gd 26.49%	132 594 595 595 597 596 599 590 596 599 599 599 599 599 599 599 599 599
5	[Tb (L) <sub>3</sub> +H]*	C <sub>21</sub> H <sub>16</sub> N <sub>12</sub> Tb	595.08	C 42.36%, H 2.71%, N 28.24%, Tb 26.69%	Courter-ox Monato-Charge (entr)  Maps M/e  Maps M/e  Maps M/e  Maps M/e  Side Side Side Side Side Side Side Side

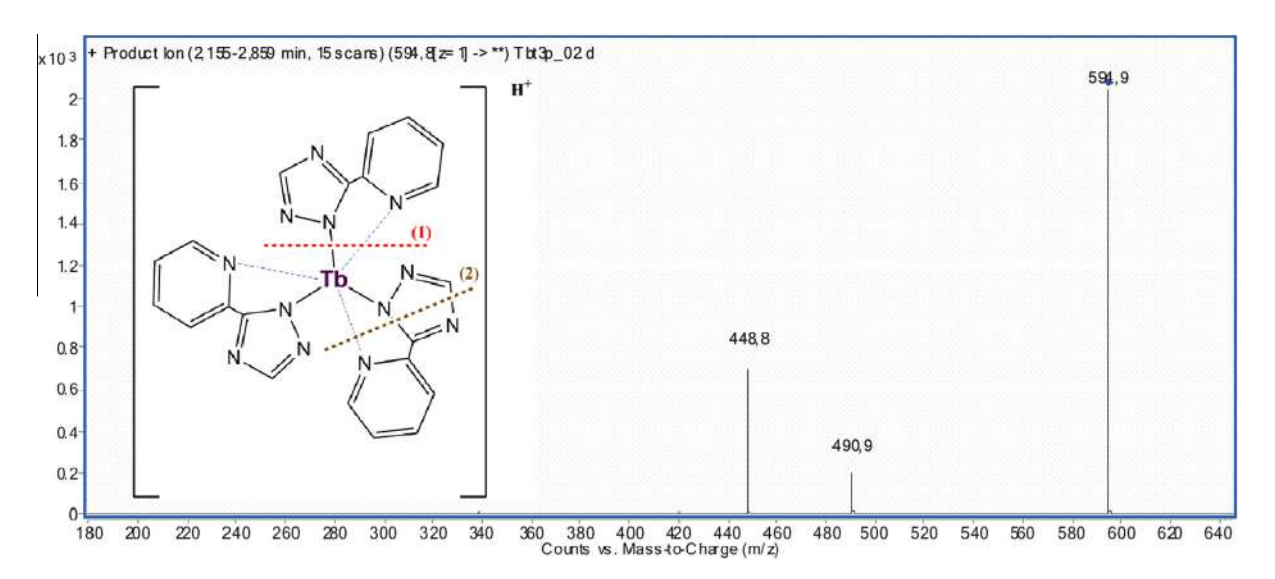


Fig. 2. Fragmentation spectrum of [Tb (L)3+H]+ species.

ligand (HL) and the selected trivalent cations. Fig. S1 (Supporting information) presents the recorded spectra for the free ligand and prepared complexes, for each case the significant absorption peaks was also included.

The initial investigation of the free ligand was required to pinpoint the modifications occurred during the complexation process.

The assignment of the recorded peaks of the functional groups specific to the free ligand are presented as follows [19–21]: 3445 cm<sup>-1</sup> is assigned to vN–H, 3144 cm<sup>-1</sup> – vN–H; 3086, 3066, 2932, 2862, 3144 cm<sup>-1</sup> – vC–H (pyridine and triazole ring); 1798 cm<sup>-1</sup> –  $\delta^{ip}$ HNC; 1601 cm<sup>-1</sup> – vC–N (pyridine ring); 1562 cm<sup>-1</sup> – vC–N (both rings); 1323, 1204 cm<sup>-1</sup> –  $\delta^{ip}$ C–H; 1400 cm<sup>-1</sup> – vC–N (both rings); 1323, 1204 cm<sup>-1</sup> –  $\delta^{C}$ H methylene, 1269, 1099 cm<sup>-1</sup> – vC–N (both rings); 1053 cm<sup>-1</sup> – vC–N (triazole ring); 1003 cm<sup>-1</sup> – planar deformation pyridine ring; 903, 752 cm<sup>-1</sup> –  $\delta^{cop}$ C–H; 802 cm<sup>-1</sup> –  $\delta^{cop}$ C–N; 714 cm<sup>-1</sup> –  $\gamma$ (triazole ring) and  $\gamma$ CN; 667 cm<sup>-1</sup> –  $\gamma$ (triazole ring) and  $\gamma$ NH; 625 cm<sup>-1</sup> –  $\gamma$ (triazole ring); 505 cm<sup>-1</sup> –  $\delta^{cop}$ N–H; 467 cm<sup>-1</sup> – non-planar pyridine ring deformation. (where v – stretching,  $\delta$  – deformation, ip – in plane, oop – out of plane,  $\gamma$  – out of plane bending).

Noticeable changes arising from the complexation process could be easily observed in the recorded spectrum of each prepared complex. For a better view, in Table 4 are presented the most significant changes occurred through complexation process.

Besides displacements of various peaks due to the rearrangements of various groups, through complexation a series of peaks as –NH specific stretching or deformation vibrations are no longer present in recorded spectra of all prepared complexes while new absorption peaks appear due to the establishment in covalent bonds between the central trivalent cation and nitrogen atom from

the former –NH group located in the triazole ring of the free ligand. These newly established covalent bonds were identified through the presence of moderate intensity peak located in the  $419-409~{\rm cm}^{-1}$  region [22,23], which is clearly visible in each spectrum of the prepared complexes, while in case of the free ligand is absent.

What is even more interesting is the correlation between the location of this peak and the placement of the cation in lanthanide series. Thus, with increasing of the atomic number, the wavenumber of the Ln–N bond increases. This fact is due to the decreasing of the ionic radii with increasing of the atomic number (lanthanide contraction), which leads to increasingly stronger bonding along the lanthanide series.

The  $v_{C=N}$  in the pyridine ring which occurs at 1601 cm<sup>-1</sup> in the free ligand, appears displaced in case of all prepared complexes due to the involvement in coordinative bonding with the central cation, which also triggers further planar or non-planar deformation of the pyridine ring. A significant number of changes are also observed in case of specific vibrations of various groups, which though are not directly involved, but only disturbed due to the rearrangements occurring in the complexation process. The alterations on the various absorption bands can be addressed as a consequence of complexation. The 1477 cm<sup>-1</sup> stretching vibration of C-N bond which appears as a strong peak in the free ligand is split and displaced to higher wavenumbers in case of complexes also as a result of various rearrangements occurred through interaction with the trivalent cations. The skeletal vibrations like stretching or bending of CH groups located both in pyridine and triazole rings are also influenced through complexation some of their specific peaks being broaden and slightly displaced compared with the free ligand. The diffuse broadening accompanied by the increase in

**Table 4**Significant changes occurred through complexation process.

Functional group/assignment	HL (cm <sup>-1</sup> )	$[YL_3(H_2O)_3]$	$[SmL_3(H_2O)_3]$	$[EuL_3(H_2O)_3]$	$[GdL_3(H_2O)_3]$	$[TbL_3(H_2O)_3]$
$\delta^{\mathrm{ip}}HNC$	1798	=	=	=	=	=
γΝΗ	667	_	_	_	_	_
$\delta^{\text{oop}}$ N-H	505	-	_	_	_	_
vM-N	_	409	412	413	416	419
vC=N (pyridine ring)	1601	1605	1593	1603	1597	1607
Non-planar pyridine ring def.	467	474	471	476	474	480
Planar pyridine ring def.	1003	988	988	991	988	995

absorption intensity in the upper region of the spectra (3600–3000 cm<sup>-1</sup>) is attributed of the presence of various types of water in the structure of the complexes. In this region beside the specific CH absorption bands, OH vibrations are overlaid due to the presence of coordination or crystallization water in the structure of prepared complexes. The results confirm the bidentate nature of the 2-(1H-1,2,4-Triazol-3-yl)pyridine ligand and the presence of coordinated water in the structure of the prepared complexes.

## 3.5. X-ray analysis

Calculated unit cell parameters of the prepared complexes are presented in Table 5, which also contains specific unit cell parameters of the 2-(1H-1,2,4-Triazol-3-yl)pyridine ligand (HL).

The crystallization system is triclinic for all prepared complexes while in case of free ligand a monoclinic configuration was found. The lower symmetry triclinic system found for all the complexes are in good agreement with the results further presented in sub Section 3.6, where a series of recorded radiative transitions are sensitive to the surroundings symmetry degree, especially in case of Sm<sup>3+</sup> and Eu<sup>3+</sup>.

#### 3.6. Fluorescence analysis

While the photoluminescence of all prepared complexes is quite remarkable, the mechanisms which govern their radiative transitions may be divided into two main categories. Sm3+, Eu3+ and Tb<sup>3+</sup> prepared complexes fall in one category as their emission occurs as a "classic" metal centered (MC) luminescence with characteristic narrow emission bands arising from inner transitions within 4f orbitals. Since the characteristic transitions within 4f orbitals of Ln3+ cations are parity or spin forbidden, with large radiative lifetimes ( $10^{-3}$  s range), which favor radiationless deactivation and also small absorption coefficients, an appropriate ligand is required to overcome these limitations and efficiently transfer energy to the excited states of the central cation. Lanthanide luminescence is possible only if the energy levels supplied by the excited states of the surrounding ligands to the emissive center are beyond the resonance levels specific for a certain trivalent lanthanide cation. Thus, in case of Sm<sup>3+</sup> the main resonance level is  $^4G_{5/2}$  (17800 cm<sup>-1</sup>), while in case of Eu<sup>3+</sup> and Tb<sup>3+</sup> the main resonance levels are  ${}^5D_0$  (17250 cm<sup>-1</sup>) and  ${}^5D_4$  (20430 cm<sup>-1</sup>) respectively [24]. Generally, aromatic or hetero-aromatic compounds with conjugated  $\pi$  configurations with high extinction coefficients and efficient intersystem crossing transitions are suitable for a good sensitization of the lanthanide cations. For the investigated complexes, the chemical structure of ligand and also the configuration achieved through complexation could explain the efficient sensitization for all three lanthanide cations. The process may rely on an indirect sensitization through the "antenna effect" [25] of the pyridine ring coupled to the triazole ring coordination site which subsequently transfers its excited states to the covalently bonded trivalent cation. The efficient sensitization process might be further aided by the presence of the coordinative bond between the nitrogen in the pyridine ring with the trivalent lanthanide cation. In Fig. 3a–c presents the excitation and emission spectra of the prepared Sm<sup>3+</sup>, Eu<sup>3+</sup> and Tb<sup>3+</sup> complexes.

The presence of water molecules in the first coordination sphere seems to have little effect over the efficiency of energy transfer to the central cation. Although it is well-known that the vicinity of OH oscillators favors vibrational coupling leading to non-radiative deactivation, these processes are especially efficient in aqueous solutions. Since the luminescence of the prepared complexes is achieved in their solid crystalline form, the influence of the OH oscillators is diminished to a degree which will not significantly alter the efficiency of the radiative processes.

The  $[SmL_3(H_2O)_3]$  complex presents the most intense emission peak at 595 nm (Fig. 3a) due to  ${}^4G_{5/2} \rightarrow {}^6H_{7/2}$  hypersensitive transition whose intensity increases as the surrounding symmetry of the luminescent center decreases [26]. The  ${}^4G_{5/2} \rightarrow {}^6H_{5/2}$  and  ${}^{4}G_{5/2} \rightarrow {}^{6}H_{9/2}$  transitions are responsible for the medium intensity peaks located at 559 and 641 nm, respectively, while the lowest intensity peak located at 702 nm is due to the  ${}^4G_{5/2} \rightarrow {}^6H_{11/2}$  transition [27]. The efficient sensitization induced by the ligand may be additionally sustained by the presence of the  ${}^4G_{5/2} \rightarrow {}^6H_{13/2}$  transition responsible for the 746 nm medium intensity peak at the upper edge of the NIR region. Several low intensity excitation peaks were recorded in the UV-A region between 360-390 nm but the maximum intensity peak is located in the visible region, at 404 nm and also a lower but significant peak located at 417 nm. For this reason the [SmL<sub>3</sub>(H<sub>2</sub>O)<sub>3</sub>] sample was efficiently excited with a 405 nm laser diode (embedded picture in Fig. 3a) while the rest of the prepared complexes were excited with a regular UV-A fluorescent lamp.

For the  $[EuL_3(H_2O)_3]$  complex (Fig. 3b) the most significant emission peaks are located at 589 and 616 nm due the  $^5D_0 \rightarrow ^7F_1$ and  ${}^5D_0 \rightarrow {}^7F_2$  transitions The intensity of the  ${}^5D_0 \rightarrow {}^7F_1$  parityallowed magnetic dipole transition is unaffected by the surroundings symmetry but the most intense  ${}^5D_0 \rightarrow {}^7F_2$  electrical-dipole allowed hypersensitive transition is known to be highly affected by surrounding symmetry degree. It is widely admitted that the ratio between the emission intensities of  ${}^5D_0 \rightarrow {}^7F_2$  and  ${}^5D_0 \rightarrow {}^7F_1$ is an asymmetry parameter for the Eu<sup>3+</sup> surrounding sites [28]. As in case of [SmL<sub>3</sub>(H<sub>2</sub>O)<sub>3</sub>] complex, lower symmetry surroundings favor higher intensities of the hypersensitive transitions. In both cases, the observations are consistent with the XRD investigations that revealed a triclinic crystallization system for the prepared complexes. The barely observable peak located at 650 nm is due to the  ${}^5D_0 \rightarrow {}^7F_3$  transition while the medium intensity peak centered at 695 nm is assigned to the  ${}^5D_0 \rightarrow {}^7F_4$  radiative transition. All the excitation peaks were recorded in the UV-A region, with the most intense peak located at 394 nm.

In case of  $[TbL_3(H_2O)_3]$  complex (Fig. 3c) the most intense emission peak is located at 542 nm due to  ${}^5D_4 \rightarrow {}^7F_5$  transition while a medium intensity peak was recorded at 488 nm due to the  ${}^5D_4 \rightarrow {}^7F_6$  transition. The intensities of both radiative transitions are practically unaffected by the symmetry of the crystalline field surroundings. The less intense 582 nm peak due to the  ${}^5D_4 \rightarrow {}^7F_4$  transition is moderately sensitive to the surroundings. The lowest intensity 619 nm peak is assigned to the  ${}^5D_4 \rightarrow {}^7F_3$  radiative

**Table 5**Calculated unit cell parameters of the ligand and prepared complexes.

Ligand/complex	a (Å)	b (Å)	c (Å)	α (°)	β (°)	γ (°)	Cell volume (ų)	Crystallization system
HL	10.53	3.96	8.90	90	110.7	90	347.15	monoclinic
$[YL_3(H_2O)_3]$	6.52	9.56	10.61	69.43	85.97	67.23	569.77	triclinic
$[SmL_3(H_2O)_3]$	7.25	8.75	13.56	80.24	120.4	79.94	695.81	triclinic
$[EuL_3(H_2O)_3]$	4.66	9.99	20.63	69.02	82.98	128.02	626.17	triclinic
[GdL3(H2O)3]	9.55	7.53	14.56	84.86	49.44	97.53	767.60	triclinic
$[TbL_3(H_2O)_3]$	7.75	12.01	13.02	63.76	96.53	55.73	782.97	triclinic

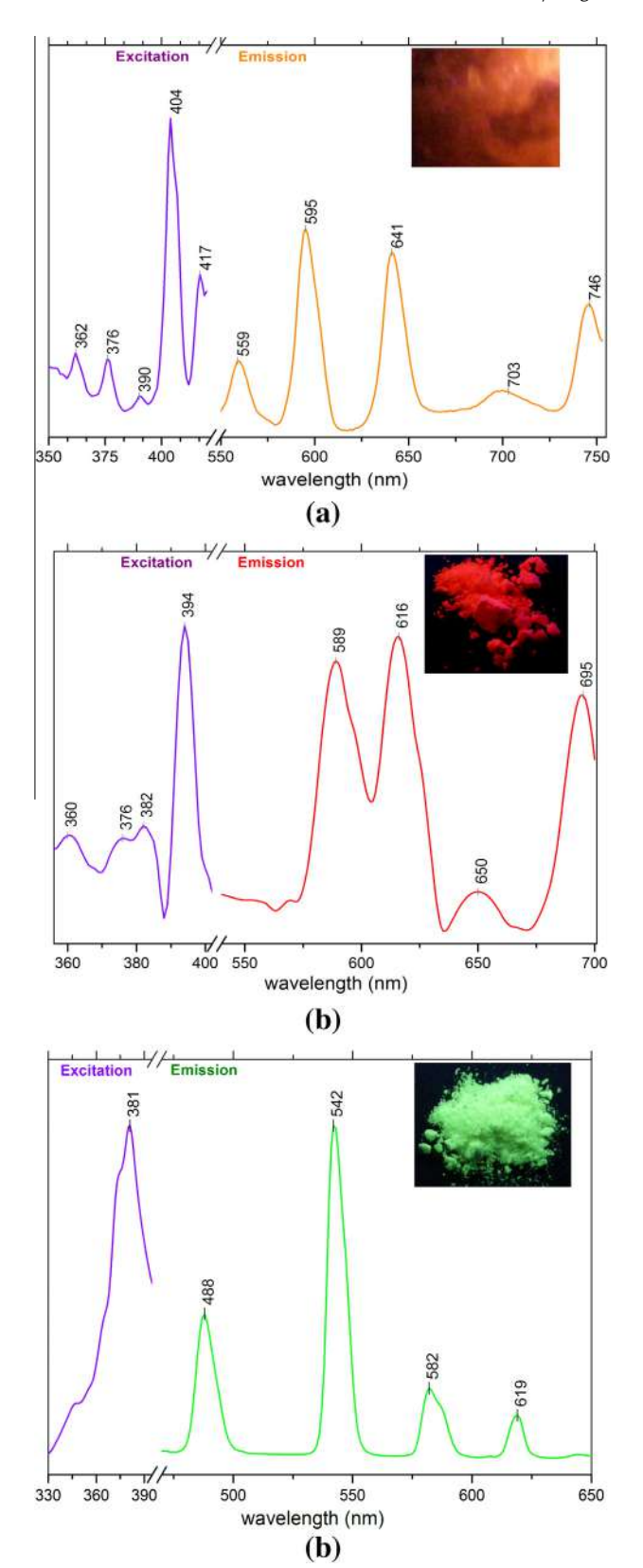


**Fig. 3.** Excitation/emission spectra of prepared (a)  $\rm Sm^{3+}$ , (b)  $\rm Eu^{3+}$ , (c)  $\rm Tb^{3+}$  complexes. Inset digital pictures show the corresponding complexes.

transition [29]. The recorded excitation spectra revealed an intense broader peak located also in the UV-A region at 381 nm.

In the second main category are included the  $[GdL_3(H_2O)_3]$  and  $[YL_3(H_2O)_3]$  complexes whose photoluminescent properties cannot

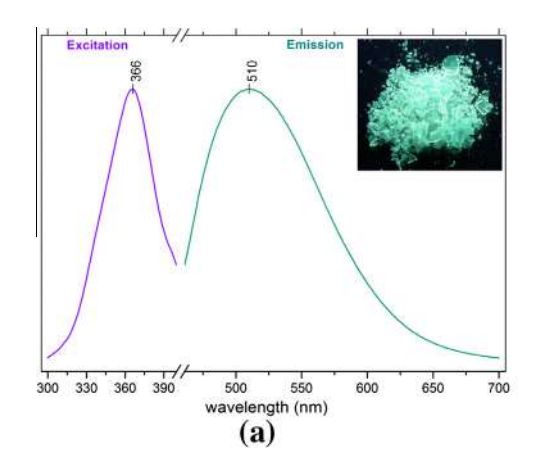
be attributed to transition within the central cation. While their recorded luminescence is strong, the characteristic emission spectra differ significantly when compared with those recorded for the complexes included in the first category. Interestingly, Bekiari et al. reported in their work an enhanced ligand centered fluorescence in a less usual approach, where Eu³+ and Tb³+ – 2,2′-bipymiridine complexes are prepared in low Mw poly(ethylene glycol) medium [30]. Fig. 4 presents excitation and emission spectra recorded for these two complexes. As could be noted, a broad emission spectrum was recorded in each case.

The photoluminescence of these two complexes is rather a result of the influence of heavy cation vicinity (Gd<sup>3+</sup> or Y<sup>3+</sup>) over the excited states of the ligand. The Gd<sup>3+</sup> cation is already known as an excellent candidate for triggering intraligand radiative processes, its paramagnetism with 7 unpaired electrons favoring intersystem crossing in ligands. In their work, Vogler and Kunkely [31] explored in detail the role of heavy atom, especially of lanthanides, in triggering radiative processes in a series of surrounding ligands. Also, their work emphasizes the role of the Gd<sup>3+</sup> in achieving enhanced photoluminescent properties due the intraligand radiative processes. What is even more interesting is that the observed photoluminescence of the [GdL<sub>3</sub>(H<sub>2</sub>O)<sub>3</sub>] prepared in this work is in total agreement with the studies over the Gd(tta)<sub>3</sub> or Gd(qu)<sub>3</sub> chelates [32] where the emission peaks were found at 510 nm. Exactly the same value was recorded for the new prepared complex (Fig. 4a).

The resemblance is further sustained by the fact that in all cases strong luminescence appears only if the complexes are in solid form or incorporated in a rigid matrix due to the avoidance of radiationless deactivation which is favored by a more flexible structure. For the prepared  $[GdL_3(H_2O)_3]$  complex the excitation peak is located in UV-A region, at 366 nm (Fig. 4a). In case of  $[YL_3(H_2O)_3]$  the processes involved in achieving the photoluminescent properties are similar. However, in its case the emission peak is located at 482 nm (Fig. 4b). The displacement at smaller wavelength compared with  $[GdL_3(H_2O)_3]$  may be explained by the smaller atomic mass and ionic radius of the  $Y^{3+}$  whose influence may affect slightly different the intraligand excited states of the surrounding ligands. The recorded excitation spectra is wider compared with the  $Gd^{3+}$  complex with a peak located in the upper region of the visible spectrum, centered around 418 nm (Fig. 4b).

Absolute photoluminescence quantum yields measurements (Table 6) place the Tb<sup>3+</sup> complex (32.09%) in most favorable situation (highest PLOY), whereas for the Sm<sup>3+</sup> complex the lowest value was recorded (12.63%). An interesting situation is encountered in case of  $Y^{3+}$  and  $Gd^{3+}$  complexes where the measured values are comparable, supporting the proposed photoluminescence mechanism based on heavy atom influence over the excited states of the surrounding ligands. The assumption is further sustained by the lifetime measurements which in case of these two complexes are located in 3-5 ns range, with very close recorded values  $(3.53 \text{ ns} \text{ for the } \text{Y}^{3+} \text{ and } 3.38 \text{ for the } \text{Gd}^{3+} \text{ complexes})$ . These nanosecond range lifetimes are typical for various organic fluorophores [33] in which category the 2-(1H-1,2,4-Triazol-3-yl)pyridine (HL) could be included. Therefore, the role of the central cation is to trigger the radiative transitions within the surrounding ligands.

The situation is markedly different in case of Sm<sup>3+</sup>, Tb<sup>3+</sup> and Eu<sup>3+</sup> complexes where long lifetimes (400–500 µs range) were recorded. The values are typical for "classic" metal centered luminescence, category in which these complexes are included, as already mentioned. Fig. S2a,b (Supporting information) present the typical luminescence decay curves recorded for prepared complex included in each main category previously described. Chromaticity parameters according to CIE 1931 color space



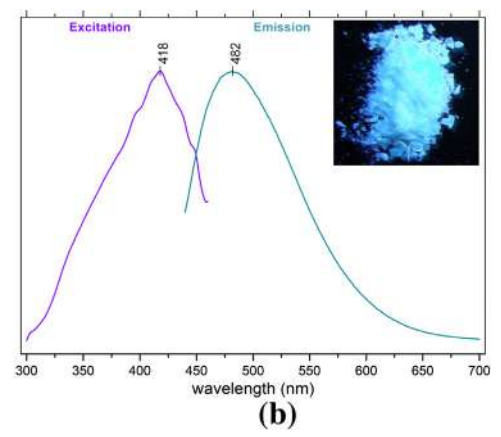


Fig. 4. Excitation/emission spectra of prepared (a) Gd3+ and (b) Y3+ complexes. Inset digital pictures show the corresponding complexes.

**Table 6**Absolute PLQY recorded for the investigated complexes.

Sample	Absolute PLQY (%)/excitation wavelength (nm)
[YL <sub>3</sub> (H <sub>2</sub> O) <sub>3</sub> ]	21.44/415
$[SmL_3(H_2O)_3]$	12.63/395
$[EuL_3(H_2O)_3]$	28.81/385
$[GdL_3(H_2O)_3]$	18.09/365
[TbL3(H2O)3]	32.09/375

recorded for each prepared complex are also included in Supporting information, Fig. S3.

#### 4. Conclusions

The paper reports five new complexes of yttrium and selected lanthanides with 2-(1H-1,2,4-Triazol-3-yl)pyridine as ligand, with remarkable photoluminescent properties. In all prepared complexes, the coordination number of the central cation was found to be 9 with three bidentate ligands and also three coordinated water molecules. The suggested structure was confirmed by elemental analysis, thermal analysis, mass spectroscopy and FT-IR analysis being in accordance with other studies concerning trivalent lanthanide complexes. Fluorescence spectroscopy investigations revealed not only their excellent photoluminescent properties but also brought interesting information regarding the radiative transitions involved in these properties. In case of Sm<sup>3+</sup>, Eu<sup>3+</sup>, Tb<sup>3+</sup> complexes a classic metal centered luminescence due to an efficient energy transfer from ligand was observed, while in case of  $Y^{3+}$  and  $G\bar{d}^{3+}$  complexes a less common intraligand luminescence due the vicinity of a heavy atom was recorded. The results recorded for the Gd<sup>3+</sup> complex are in agreement with other works where the investigations were focused on trivalent gadolinium influence over the excited intraligand states leading to photoluminescence under ambient conditions. Although the prepared complexes present their photoluminescent properties as prepared, further approaches for embedding them in polymer or silica matrices could lead to materials adapted for applications in light emitting or solar energy harvesting devices as photonic conversion mediums.

## Acknowledgments

This work was supported by a grant of the Romanian National Authority for Scientific Research, CNCS – UEFISCDI, project number PN-II-ID-PCE 2011-3-0708.

#### Appendix A. Supplementary material

Supplementary data associated with this article can be found, in the online version, at http://dx.doi.org/10.1016/j.ica.2015.01.041.

#### References

- S.A. Cotton, Lanthanide and Actinide Chemistry, Ed. Wiley & Sons, Ltd, Chichester, 2006.
- [2] L. Armelao, S. Quici, F. Barigelletti, G. Accorsi, G. Bottaro, M. Cavazzini, E. Tondello, Coord. Chem. Rev. 254 (2010) 487.
- [3] J.P. Leonard, T. Gunnlaugsson, J. Fluoresc. 15 (2005) 585.
- [4] F. Xue, Y. Ma, L. Fu, R. Hao, G. Shao, M. Tang, J. Zhang, Y. Wang, Phys. Chem. Chem. Phys. 12 (2010) 3195.
- [5] L. Lattuada, A. Barge, G. Cravotto, G.B. Giovenzana, L. Tei, Chem. Soc. Rev. 40 (2011) 3019.
- [6] G. Zucchi, Int. J. Inorg. Mater. 2011 (2011) 918435.
- [7] N.T. Kalyani, S.J. Dhoble, R.B. Pode, Adv. Mater. Lett. 2 (2011) 65.
- [8] K. Singh, S.K. Singh, H. Mishra, R. Prakash, S.B. Rai, J. Phys. Chem. B. 114 (2010) 13042.
- [9] S. Petricek, Acta Chim. Slov. 56 (2009) 426.
- [10] A.N. Gusev, V.F. Shulgin, S.B. Meshkova, P.G. Doga, M. Hasegawa, G.G. Aleksandrov, I.L. Eremenko, W. Linert, Inorg. Chim. Acta 387 (2012) 321.
- [11] B. Beyer, C. Ulbricht, D. Escudero, C. Friebe, A. Winter, L. Gonzalez, U.S. Schubert, Organometallics 28 (2009) 5478.
- [12] M. Starck, R. Ziessel, Dalton Trans. 41 (2012) 13298.
- [13] B. Happ, C. Friebe, A. Winter, M.D. Hager, R. Hoogenboom, U.S. Schubert, Chem. Asian J. 4 (2009) 154.
- [14] T. Kowall, F. Foglia, L. Helm, A.E. Merbach, J. Am. Chem. Soc. 117 (1995) 3790.
- [15] A. Kula, J. Therm. Anal. Calorim. 75 (2004) 79.
- [16] W. Brzyska, W. Ozga, Thermochim. Acta 195 (1992) 149.
- [17] C.R.S. Morais, A.G. Souza, P.A. Santa-Cruz, J. Alloys Compd. 344 (2002) 101.
- [18] J.J. Zhang, N. Ren, Y.X. Wang, S.L. Xu, R.F. Wang, S.P. Wang, J. Braz. Chem. Soc. 17 (2006) 1355.
- [19] F. Billes, H. Endredi, G. Keresztury, J. Mol. Struct. THEOCHEM 530 (2000) 183.
- [20] Y. Buyukmurat, S. Akyuz, J. Mol. Struct. 563-564 (2001) 545.
   [21] L. Tocon, M.S. Woolley, J.C. Otero, J.I. Marcos, J. Mol. Struct. 470 (1998) 241.
- [22] M. Singh, S. Anant, Int. J. Inorg. Mater. 2012 (2012) 767080.
- [22] M. Singn, S. Anant, Int. J. Inorg. Mater. 2012 (2012) 76708
- [23] K. Mohanan, M. Thankamony, B.S. Kumari, J. Rare Earths 26 (2008) 463.
- [24] K. Binnemans, Chem. Rev. 109 (2009) 4283.
- [25] A.M. Klonkowski, S. Lis, M. Pietraszkiewicz, Z. Hnatejko, I. Szałkowska, Glastech. Ber. Glass Sci. Technol. 75C2 (2002) 350.
- [26] S.M. Abo-Naf, M.A. Marzouk, R.L. Elwan, J. Mater. Sci. Mater. Electron. 23 (2012) 2293.
- [27] K. Lunstroot, P. Nockemann, K. Van Hecke, L. Van Meervelt, C. Gorller-Walrand, K. Binnemans, K. Driesen, Inorg. Chem. 48 (2009) 3018.
- [28] D.E. Henrie, R.L. Fellows, G.R. Choppin, Coord. Chem. Rev. 18 (1976) 199.
- [29] G. Liu, B. Jacquier, Spectroscopic Properties of Rare Earth in Optical Materials, Springer, New York, 2005.
- [30] V. Bekiari, K.A. Thiakou, C.P. Raptopoulou, S.P. Perlepes, P. Lianos, J. Lumin. 3 (2008) 481.
- [31] A. Vogler, H. Kunkely, Inorg. Chim. Acta 359 (2006) 4130.
- [32] A. Strasser, A. Vogler, Inorg. Chim. Acta 357 (2004) 2345.
- [33] Mikhail Y. Berezin, Samuel Achilefu, Chem. Rev. 110 (2010) 2641.

# Journal of Materials Chemistry C



**PAPER** 

View Article Online
View Journal | View Issue



Cite this: J. Mater. Chem. C, 2015, 3, 789

Received 21st October 2014 Accepted 19th November 2014

DOI: 10.1039/c4tc02382j

www.rsc.org/MaterialsC

## One step synthesis of fluorescent carbon dots through pyrolysis of N-hydroxysuccinimide†

C. S. Stan, \*a C. Albu, a A. Coroaba, M. Popa and D. Sutiman a

Fluorescent carbon dots were prepared *via* a simple and straightforward one-step pyrolytic process using *N*-hydroxysuccinimide. The prepared C-dots present remarkable photoluminescence with blue to green shifting emission and absolute quantum yields varying from 14 to 31% as a function of the excitation wavelength and selected dispersion media. Interestingly, up-conversion from NIR to the visible range was not only instrumentally recorded but even visually observable. Further, the composition and morphology of the prepared C-dots were studied using XPS, FT-IR, Raman, P-XRD, DLS and AFM as investigation methods. Since the majority of C-dot studies are biased towards fluorescent labeling in cellular imaging, their photoluminescence properties, physicochemical stability and ease of fabrication are expected to play a key role in applications ranging from sensors to efficient solar energy conversion or high performance optoelectronic devices.

## Introduction

Carbon dots are a new class of carbon based nanostructured materials which have received much research interest due to their remarkable properties such as tunable photoluminescence (PL) with high quantum yields (PLQY), lack of toxicity, chemical inertness, and resistance to photobleaching.<sup>1</sup> Although their photoluminescence is counted as one of the most interesting features considering the wide application potential, the exact PL mechanism is still a subject open for debate. In a number of studies<sup>2,3</sup> the quantum confinement effect is considered to be responsible for the C-dots' PL properties in a similar way to the "classic" semiconductor quantum dots while other opinions tend to emphasize the role of surface functional groups in achieving the excited states responsible for the excitation wavelength-dependent photoemission.<sup>4,5</sup> The search for an accurate description of the PL mechanism is further complicated by a significant number of studies which report up-conversion luminescence, 6,7 usually from NIR (800-850 nm) to the blue-green area of the visible spectrum. Whilst the observed up-conversion PL of the C-dots is still controversial,8 this feature, if confirmed, may be highly important for bioimaging applications9 or for attempts to further increase the efficiency of solar energy conversion systems. 10

As a consequence of the significant interest in C-dots, an increasing number of preparation paths were reported, generally divided into two main categories: chemical and physical methods. The chemical methods include electrochemical, 11 thermal, 12 combustion, 13 and acidic oxidation 14 with certain variations where the main process is microwave or ultrasound assisted. 15,16 Physical methods including arcdischarge, 17 laser ablation 18 or plasma treatment, 19 use various carbon sources like carbon nanotubes from graphite or graphite oxide, and the obtained C-dots usually require further surface treatment or passivation in order to increase the hydrophilicity and PL emission.

In most cases the chemical methods are significantly less demanding in terms of required equipment or starting materials used as carbon sources, having the additional advantage of producing already surface functionalized C-dots. Several reported preparation paths, which lead to highly fluorescent, tunable emission C-dots, use various commonly available materials or compounds as the carbon source. Among the most interesting or unusual approaches plant soot,<sup>20</sup> L-glutamic acid,<sup>21</sup> ethanolamine,<sup>22</sup> glucose,<sup>23</sup> and even orange or banana juice and soluble coffee<sup>24-26</sup> were thermally processed to obtain fluorescent C-dots.

In the present study, a facile one step pyrolysis process with N-hydroxysuccinimide (NHS) is described. Preliminary experimental parameters (temperature range, duration) of the pyrolytic decomposition of NHS were established through thermogravimetric analysis. The choice of NHS is based on our preliminary experiments which revealed its suitability for producing high quality C-dots in terms of PL properties, most probably due to some particular physicochemical properties such as a relatively low melting point ( $\sim$ 98 °C), favorable

<sup>&</sup>quot;TUIasi – Gheorghe Asachi Technical University of Iasi, Faculty of Chemical Engineering and Environmental Protection, 73 Prof. Dr Docent Dimitrie Mangeron, 700050, Iasi, Romania. E-mail: stancs@tuiasi.ro; Fax: +40 232 271311; Tel: +40 232 278683

<sup>&</sup>lt;sup>b</sup>Petru Poni Institute of Macromolecular Chemistry, 41A Aleea Grigore Ghica Voda, Iasi, Romania

<sup>†</sup> Electronic supplementary information (ESI) available. See DOI: 10.1039/c4tc02382j

The resulting C-dots are strongly photoluminescent in a relatively wide excitation range (350–420 nm) and easily dispersible in various solvents including water, ethylic alcohol, and acetone. Besides, the previously reported PL emission dependence on the excitation wavelength, the variation of the PL properties according to the dispersion medium and up-conversion from NIR to the visible spectrum were also noted and experimentally confirmed.

## Experimental

#### **Materials**

*N*-Hydroxysuccinimide (97%) was purchased from Sigma-Aldrich. Milli-Q water was used during preparation, purification and dimensional selection procedures. Reagent grade ethanol (EtOH) and acetone from Merck Chemicals were used as re-dispersion media.

## **Preparation**

In a typical synthesis procedure, 3 g of NHS is added in a 50 mL three neck Schlenk flask provided with a magnetic stirrer and a temperature controlled heating mantle. The temperature is raised to the melting point of NHS ( $\sim$ 98 °C) when the magnetic stirring is started. From this stage, the reaction proceeds under N<sub>2</sub> atmosphere with the temperature being gradually raised (about 10 °C min<sup>-1</sup>) to 180 °C and maintained at this value for 30 min. Then, the entire content of the flask is quickly transferred in 40 mL cold water and allowed to reach room temperature. The mixture is centrifuged at 5000 RPM for about 30 min. The resulting deep brown tinted supernatant is collected and additionally centrifuged at 15 000 RPM for 10 min. Again, the resulting brownish tinted aqueous supernatant containing dimensionally selected C-dots is collected and further freezedried. The prepared C-dots dried or re-dispersed in water, EtOH or acetone are kept as such for investigation purposes.

#### Methods

XPS analysis was performed on a KRATOS Axis Nova, using AlKα radiation with a 20 mA current and 15 kV voltage. The incident X-ray beam was focused on a 0.7 mm  $\times$  0.3 mm area of the surface. Wide XPS spectra were collected in the range of -10 to 1200 eV with a resolution of 1 eV and a pass energy of 160 eV. The high resolution spectra for all the elements identified from the survey spectra were collected using a pass energy of 20 eV and a step size of 0.1 eV. The FT-IR spectra were recorded in the  $400-4000~{\rm cm}^{-1}$  range using a Bruker Vector 22 spectrometer, according to the KBr pellet method. The Raman spectroscopy was performed in the  $100-3200~{\rm cm}^{-1}$  range with a Renishaw inVia Reflex confocal microscope equipped with a He–Ne laser at 633 nm (17 mW) and a CCD detector coupled to a Leica DM 2500M microscope. All measurements were made in

backscattering geometry using a 50× objective with a numerical aperture (NA) value of 0.75. The XRD patterns were recorded in the 5-85° 2-theta range, on a Panalytical X'Pert Pro diffractometer provided with a Cu-K $\alpha$  radiation source ( $\lambda$  = 0.154060 nm). Dimensional analysis (DLS) was performed on Shimadzu SALD-7001 equipment. Prior to investigation the aqueous C-dot dispersion was sonicated for about 10 min. The steady-state fluorescence, chromaticity and absolute quantum yields (PLQY) were recorded on a Horiba Fluoromax 4P provided with the Quanta- $\varphi$  integration sphere. The AFM measurements were performed using an Ntegra Spectra (NT-MDT, Russia) instrument operated in tapping mode under ambient conditions. Silicon cantilever tips (NSG 10) with a resonance frequency of 140-390 kHz, a force constant of 5.5-22.5 Nm<sup>-1</sup> and 10 nm tip curvature radius, were used. The sample was prepared by spin-coating the acetone dispersed C-dots on a glass slide at 1300 RPM using a Laurell WS-400-6NPP Spin Coater. TEM investigations were performed by means of Hitachi HT-7700 equipment, operated at 100 kV accelerating voltage, in high contrast mode. The C-dot samples were deposited from a highly diluted solution on 300 mesh carbon plated copper grids.

Visual testing of photoluminescent properties was performed using a Philips UVA TL4WBLB lamp with the emission maximum located in the 370–390 nm range and a 50 mW, 440 nm laser diode.

## Results and discussion

Fig. 1a summarizes the process taking place during the pyrolysis of NHS leading to C-dots. Related experiments performed at higher temperatures (200-240 °C) or longer thermal processing (45-90 min) times yielded significantly lower PL emitting C-dots due to advanced thermal destruction. In the optimized process (180 °C, 30 min), remnant quantities of NHS may act as a passivation agent which along with various functional groups located on the surface of the C-dots provides the conditions for reaching intense PL and high PLQY. This conclusion is supported by the thermal analysis of NHS (ESI, Fig. S1†) which revealed important mass losses (over 50%) in the 200-250 °C interval through volatile exhaustion, as a result of advanced destructuration, which drastically depletes the amount of functional groups located on the surface. Fig. 1b and c present the visually tested emission of the prepared C-dots dispersed in water under excitation with a UVA laboratory lamp (b) and a 440 nm laser (c). It can be noted that the excitation-dependent emission is clearly highlighted, as the PL emission is shifted

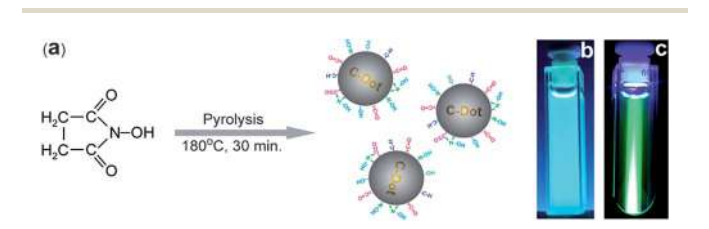
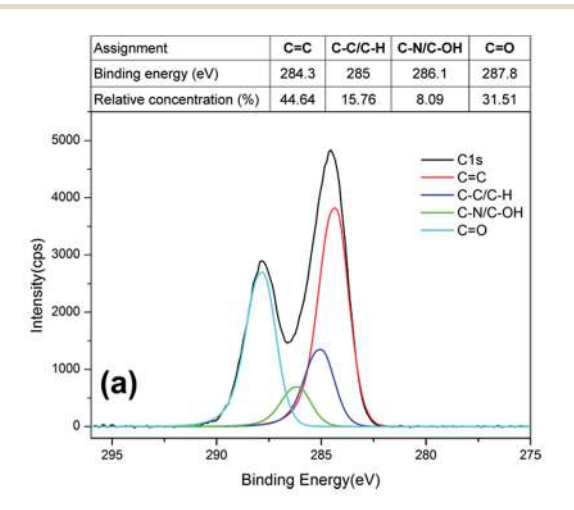
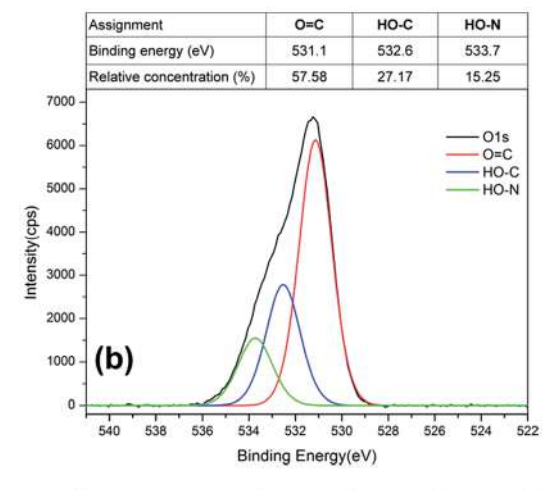


Fig. 1 (a) NHS pyrolysis scheme leading to C-dots, (b) water dispersed C-dots under UVA excitation and (c) under 440 nm laser excitation.

from blue to green. Chromaticity parameters according to the CIE 1931 color space recorded at the excitation wavelengths 360 and 420 nm are included in the ESI (Fig. S3†).

XPS investigation revealed the relative concentrations of various functional groups (Fig. 2a-c). The high resolution C 1s spectrum clearly highlighted the graphitic core with the sp<sup>2</sup>-bound carbons (Fig. 2a) along with the existence of carbonyl





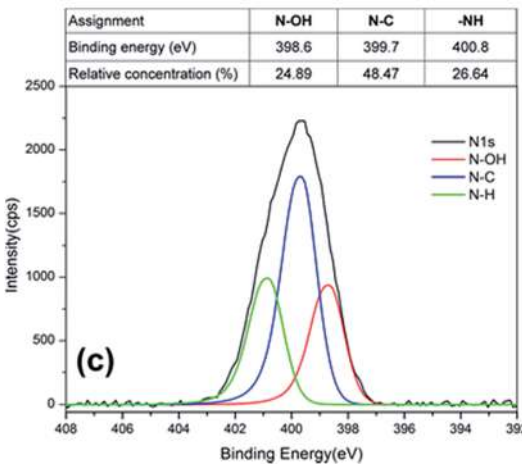


Fig. 2 High resolution XPS spectra of (a) C 1s, (b) O 1s, and (c) N 1s, and relative concentrations of various functional groups.

groups in high concentrations which, as presented later, could be responsible for the radiative transitions involved in the fluorescence emission of the C-dots.

The relatively high percentage (15%) of single-bound carbon is in agreement with the Raman investigation which also indicates structural defects of the graphitic core, most probably due to various edge- or surface-located functional groups. The high amount of functional groups on the surface is also highlighted in the high resolution O 1s and N 1s spectra, being in close agreement with the recorded FT-IR analysis. The overall O, N, C concentrations as a result of the XPS survey spectra are presented in Table 1.

Fig. 3 shows the recorded Raman spectrum of the prepared C-dots. The peaks centered at 1365 and 1565 cm<sup>-1</sup> are typical signatures for graphitic nanostructures, being in close agreement with those reported in other works. 15,21 The slight displacement of these peaks in various reported works is due to the laser parameters used for the Raman excitation in a specific measurement setup.28 The 1565 cm<sup>-1</sup> peak (G band) corresponds to the in-plane stretching vibration E20 mode of graphite, being related to the sp<sup>2</sup>-bound carbon atoms, while the 1365 cm<sup>-1</sup> peak (D band) originates from the swinging bond vibrations of carbon atoms located in the edge plane of disordered graphite, often referred to as the disorder or defect band. The intensity ratio between the D and G bands  $(I_D/I_G)$  is proportional to the disorder degree/presence of structural defects and also indicates the ratio of sp<sup>3</sup>/sp<sup>2</sup> carbons.<sup>1,29</sup> The prepared C-dots present an over-unity  $I_D/I_G$  ratio suggesting the intercalation of nitrogen atoms in the carbonaceous core and/or the presence of surface located edge functional groups leading to a somehow disordered structure. The assumed functional group-rich structure of the prepared C-dots is consistent with the results provided using FT-IR analysis (Fig. 4).

A multitude of peaks related to various functional groups is present in the recorded IR spectrum (see imprinted table in Fig. 4).

In fact, the recorded spectrum of the prepared C-dots is quite similar to the one recorded for NHS (ESI, Fig. S2†). Although most of the peaks are still present, in certain cases slightly displaced due to structural rearrangements, the significant difference lies in the ratio between the recorded peaks. While in unprocessed NHS the ratio between -CNC- asymmetric stretch (1220 cm<sup>-1</sup>) and -C=O asymmetric stretch (1707 cm<sup>-1</sup>) is almost 2/3, in the case of the prepared C-dots the value drops below 1/2 due to the losses which occurred during the thermal processing. The same effect is also noticeable in the case of other peaks corresponding to various functional groups. The presence of various functional groups, especially carbonyls and

Table 1 Overall C, N, O concentrations recorded for the prepared C-dots

Element	О	N	C
Atomic concentration (%)	26.44	14.12	59.44
Mass concentration (%)	31.70	14.82	53.48

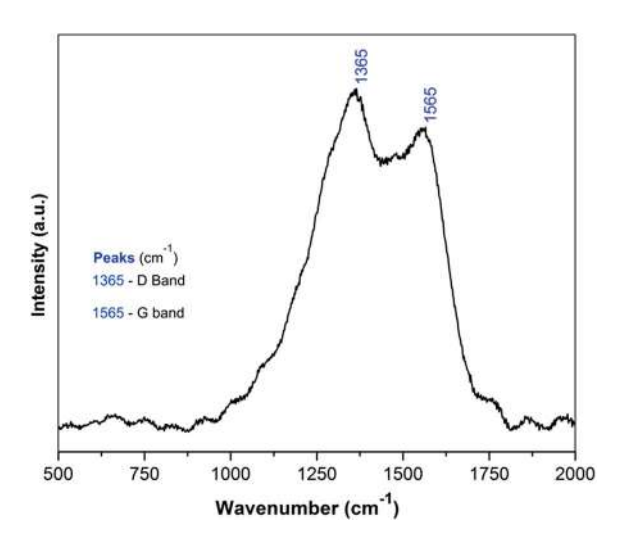


Fig. 3 Recorded Raman spectrum.

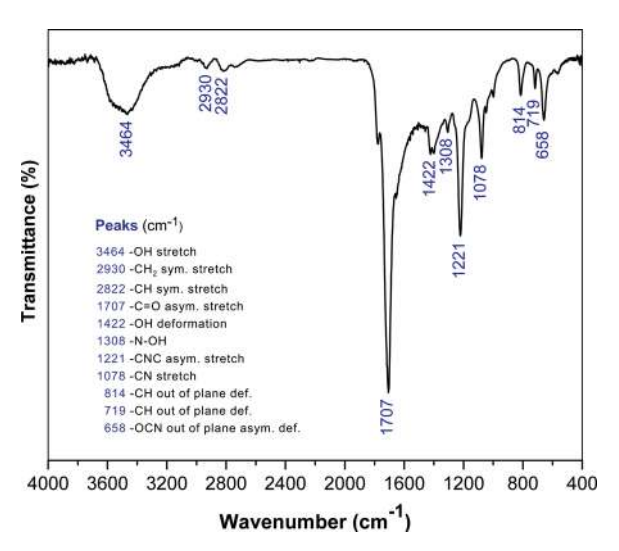


Fig. 4 Recorded FT-IR spectrum including functional group assignment.

nitrogen containing groups, located on the surface of the C-Dot is fundamentally important for their PL properties. 4,30

As recently described, the interaction of surface located functional groups with the dispersing solvent significantly alters the PL properties, especially the PLQY. As stated above, the pyrolysis parameters are particularly important for obtaining highly luminescent C-dots, and an advanced thermal destruction accompanied by nitrogen-rich volatile exhaustion is leading to a lower content of functional groups.

Fig. 5 shows the XRD pattern recorded for the investigated C-dots. The relatively broad peak located at  $27.48^{\circ}$   $2\theta$  is slightly shifted upward compared to the classic graphite peak located at  $26.4^{\circ}$   $2\theta$ , corresponding to a minor decrease in spacing between the carbon layers from 0.337 to 0.324 nm in the case of the C-dots. The slightly reduced spacing between the carbon layers could be explained by interactions occurring between the

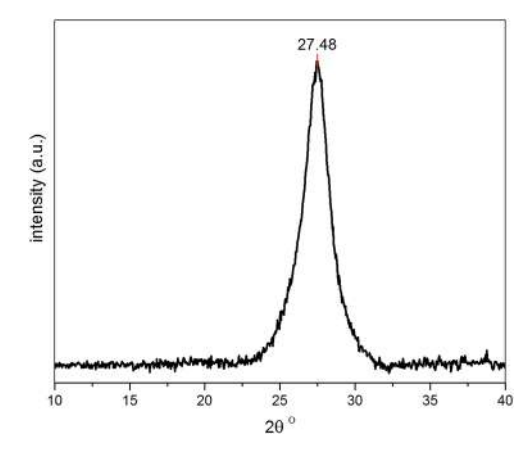


Fig. 5 XRD pattern of the prepared C-dots.

terminal functional groups, for example by hydrogen bonding between –OH groups.

The preparation of samples for the AFM investigation proved to be difficult due to an encountered agglomeration tendency even when a highly diluted acetone C-dot solution was drop spread on the glass surface. The agglomeration tendency was also previously reported in other works31 and solved by spin coating of the highly diluted solution on several glass slides subject to investigation. Even so, the AFM images revealed the existence of both small particles in the range of 20-50 nm as well as elongated aggregates (Fig. 6a and c), most probably due to the rapid drying and preferred orientation occurring during spin coating. The results are in good agreement with the DLS analysis which revealed a 20-30 nm average size of the prepared C-dots dispersed in water (Fig. 6b). TEM investigations were performed with the samples which were prepared via drop spreading of highly diluted C-dots in EtOH on carbon-coated 300 mesh copper grids.

Fig. 7a reveals aggregates in the 50–200 nm range due to the already mentioned particle-agglomeration tendency, which is also highlighted by the AFM investigation. A significant insight into the fine structuring of the aggregates is visible in the micrograph recorded at higher magnification (Fig. 7b). As may be also noted in Fig. 7b, both aggregates (arrows 1 and 2) have a granular appearance with finer visible details, which highlights the presence of differentiated entities suggesting the presence of very small C-dots in the 2–5 nm range in relation to the dimension of the aggregates ((1): approx. 120 nm; (2): approx. 20 nm).

## Fluorescence spectroscopy investigation

For the fluorescence related investigation, three samples were prepared by dispersing 1 mg freeze-dried C-dots in 3 mL  $_{2}$ O, EtOH or acetone. The steady-state fluorescence spectra (Fig. 8a–c) were recorded in the 350–420 nm excitation range (10 nm steps) whereas the up-converted emission (Fig. 8d) was studied in the 750–960 nm excitation range. As could be noted, the shifting of the down-conversion PL emission peaks according to the excitation wavelength occurs in all three cases.

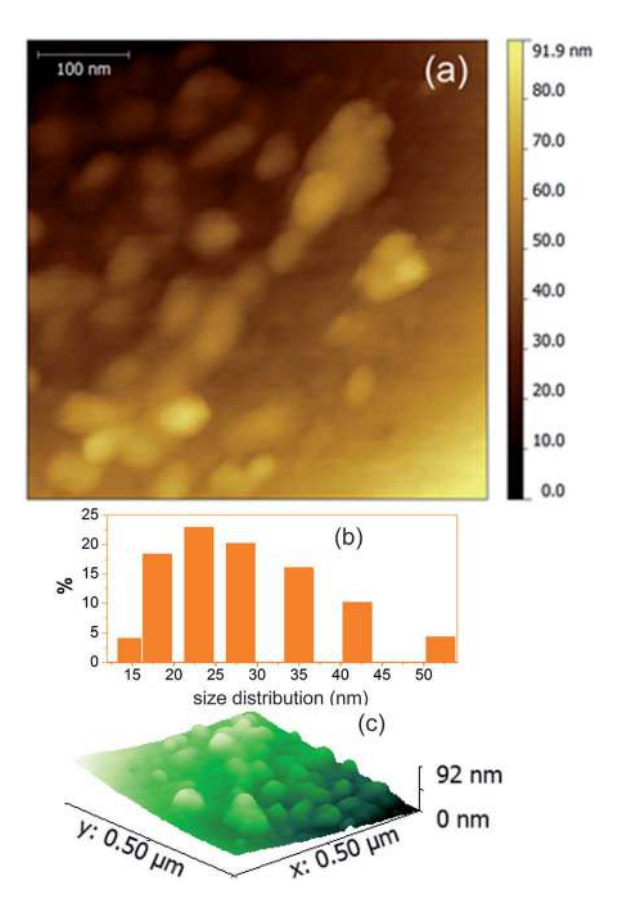


Fig. 6 (a) Recorded AFM image, (b) size distribution recorded using DLS, and (c) 3D AFM image of prepared C-dots.

The Stokes shifts and the recorded intensities are also significantly solvent-dependent. In the case of water, the emission peaks of the dispersed C-dots are located in the 437-516 nm range (Fig. 8a) with larger Stokes shifts, while, in the case of acetone, the range of the dispersed C-dots (Fig. 8c) is significantly narrower (447-493 nm), the Stokes shifts being accordingly lower. In the case of Et-OH, an in between situation was encountered for the dispersed C-dots (442-505 nm, Fig. 8b). The emission intensities were noticeably lower for the waterdispersed C-dots compared with those of the EtOH- and acetone-dispersed C-dots. The recorded results from the steadystate fluorescence measurement are in agreement with the absolute PLQY measurements, where the highest QY (31.74%) was recorded for the acetone-dispersed C-dots. Table 2 presents the absolute PLQY values recorded at different excitation wavelengths.

The results clearly indicate interactions between the solvent and surface located functional groups. Thus, as the polarity of the solvent increases (acetone  $\rightarrow$  EtOH  $\rightarrow$  H<sub>2</sub>O) the PL intensity and PLQY decrease. The peak emission range is also shifted to higher wavelengths as the polarity of the solvent increases and less energy photons are produced in the radiative processes. This indicates an excitation energy loss through various nonradiative deactivation processes. A possible explanation of the lower PL and PLQY recorded for the water-dispersed C-dots is a

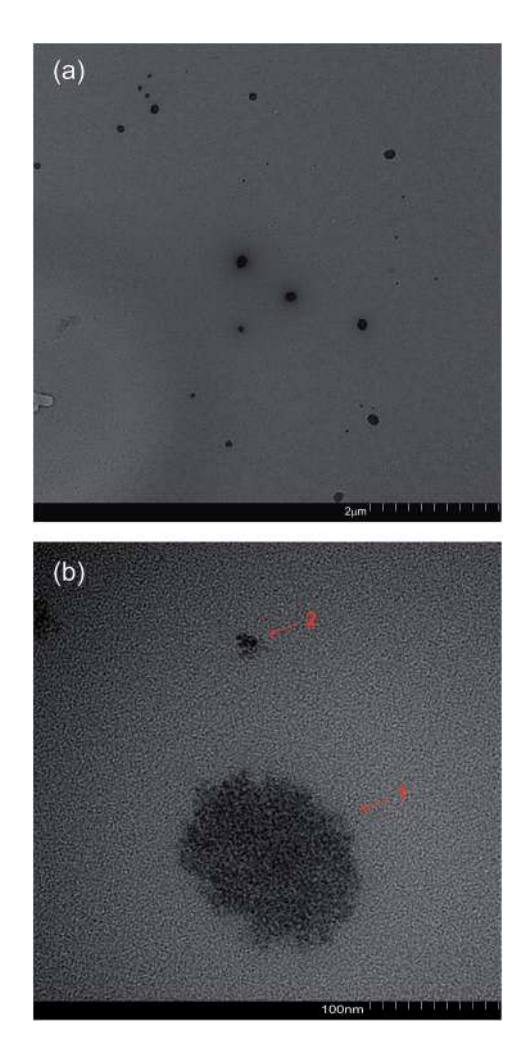


Fig. 7 TEM images recorded at (a) 35k and (b) 700k magnifications.

less efficient transfer of the excitation radiation to the states responsible for PL emission due to the vicinity to the -OH oscillators which are known to strongly quench the PL emission via vibronic coupling deactivation paths. In the most favorable case of the acetone-dispersed C-dots, the surface located functional groups responsible for PL emission are significantly less disturbed while the non-radiative deactivation paths are no longer present. The luminescence properties of the C-dots are rather a result of the radiative transitions occurring within or between the functional groups located on the C-dot surface and seem to be less dependent on their size. Recent studies emphasize the role of functional groups such as carbonyl, carboxyl and nitrogen containing groups in PL properties of C-dots and the possibility to alter the PL emission through modification of these surface localized groups. The surface located functional groups may be responsible for various trapping states, each with a different energy level, leading to an excitation-dependent emission. 4,32,33 The dimensional characteristics of C-dots may be important to a certain extent for achieving the PL properties, but we suspect an indirect relation between them. In various works related to C-dots, similar PL properties were reported in the case of <10 nm C-dots<sup>20,21</sup> but

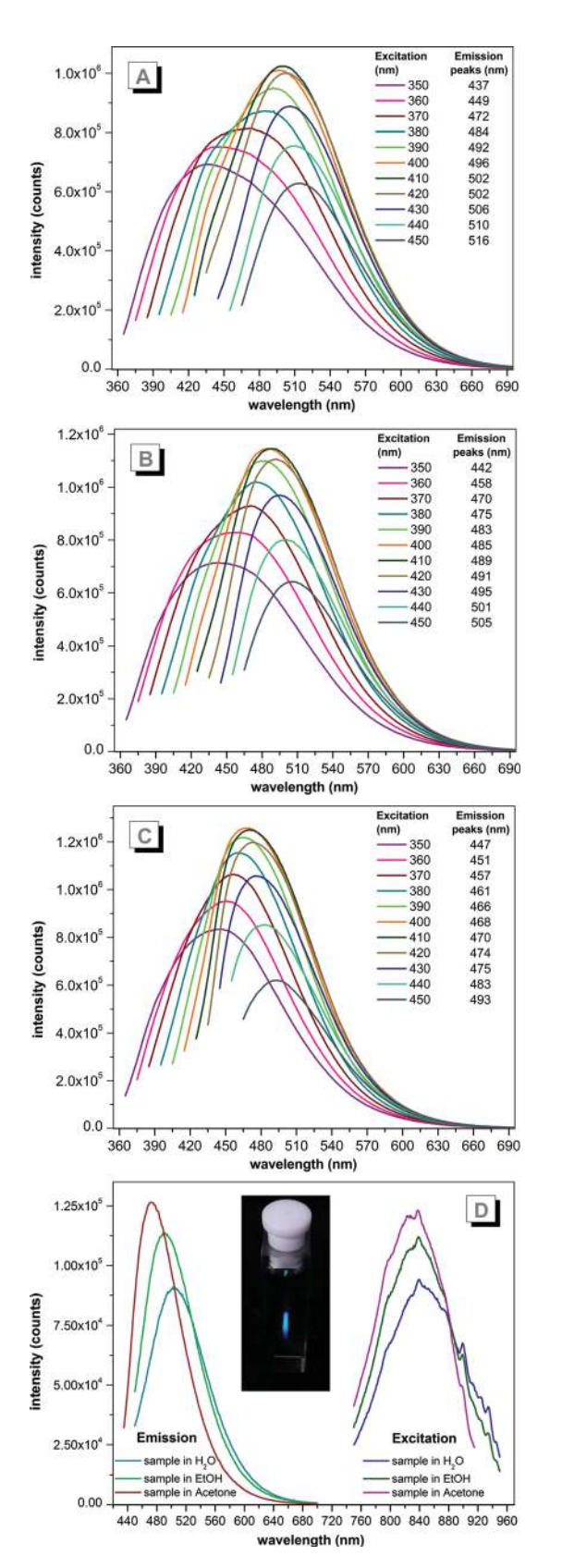


Fig. 8 PL emission spectra recorded for excitation wavelengths from 350 to 450 nm in 10 nm increments of the prepared C-dots dispersed in (a) water, (b) EtOH, and (c) acetone, and (d) up-conversion emission spectra recorded for the same samples. (Inserted image: visually observed up-converted PL emission.)

Table 2 Absolute PLQY values of the C-dots dispersed in  $H_2O$ , EtOH and acetone

	Absolute PLQY (%)							
	Excitation wavelength (nm)							
Sample/solvent	370	380	390	400	410	420		
C-dots/H <sub>2</sub> O	14.22	16.45	18.60	20.57	22.93	23.62		
C-dots/EtOH	14.23	16.86	19.08	21.53	24.38	24.96		
C-dots/acetone	17.59	21.07	23.77	25.37	30.59	31.74		

also for those in the 10–50 nm range. 24,31,34 One possible assumption is that a noticeable PL is achieved between certain dimensional limits. Beyond the upper limit, an oversized carbonaceous core may be less decorated with surface localized functional groups or these groups are less packed to achieve the type of interaction responsible for triggering the PL emission. The PL mechanism relying on functional groups attached to the surface of the C-dots may provide an additional insight into the observed excitation wavelength dependence of the emission peaks. While in certain studies 2,3 this dependence is explained by the concomitant presence of various dimensional species, each of them responsible for a particular emission peak, the functional group-based PL can be explained with the excited states achieved within or between various functional groups, each responsible for a particular emission peak.

The recorded up-conversion PL is not excitation wavelength dependent (Fig. 8d), but the PL emission peaks are different in each solvent (471 nm in acetone, 489 nm in EtOH and 502 nm in  $\rm H_2O$ ). In all cases the excitation peaks are recorded at 838–840 nm. Also, as in the case of down-conversion fluorescence, the PL intensity is influenced in the same way by the polarity of the solvent. A lower PL intensity and anti-Stokes shift ( $\sim$ 340 nm) were recorded for the water-dispersed C-dots while the most favorable results were again obtained for the acetone-dispersed C-dots ( $\sim$ 370 nm).

Although the up-conversion mechanism in C-dots is not entirely understood, a multi-photonic process is generally accepted<sup>1,6,7</sup> till further clarification. The up-converted PL emission is easily noticed with the naked eye as could be observed in the picture embedded in Fig. 8d.

## Conclusions

Highly fluorescent carbon dots were prepared *via* one-step pyrolytic processing of *N*-hydroxysuccinimide using a non-demanding experimental setup. The PL emission and absolute PLQY were studied in detail in several dispersion media. Besides, the previously reported shifting of the emission peaks according to the excitation wavelength, the intensities, Stokes shifts and absolute PLQY values were found to be markedly dependent on the polarity of the dispersing solvent. Based on the recorded results, we suggest that the fluorescence properties of C-dots are rather a result of the radiative processes occurring within or between the functional groups located on the C-dot

surface and less dependent on their size. Up-conversion from NIR (840 nm) to vis (479-502 nm) was instrumentally confirmed, the process being also visually noticeable. In depth investigations of the prepared C-dots using XPS, Raman, FT-IR, P-XRD revealed the graphitic nature of the prepared C-dots and also the abundance of various surface located functional groups. DLS and AFM were used to study the morphology of the prepared C-dots.

Although the majority of C-dot related studies are focused on bio-imaging, the C-dots' luminescence properties and ease of fabrication are expected to play a key role in applications ranging from sensors to efficient solar energy conversion or high performance optoelectronic devices.

## Acknowledgements

This work was supported by a grant of the Romanian National Authority for Scientific Research (CNCS - UEFISCDI, project number PN-II-ID-PCE 2011-3-0708-PN-II IDEI 335/2011).

## Notes and references

- 1 H. Li, Z. Kang, Y. Liu and S. T. Lee, J. Mater. Chem., 2012, 22, 24230-242353.
- 2 H. Li, X. He, Z. Kang, H. Huang, Y. Liu, J. Liu, S. Lian, C. H. A. Tsang, X. Yang and S. T. Lee, Angew. Chem., 2010, 49, 4430-4434.
- 3 Y. Xu, M. Wu, Y. Liu, X. Z. Feng, X. B. Yin, X. W. He and Y. K. Zhang, Chem.-Eur. J., 2013, 19, 2276-2283.
- 4 Y. Deng, X. Chen, F. Wang, X. Zhang, D. Zhao and D. Shen, Nanoscale, 2014, 17, 10388-10393.
- 5 D. Tan, S. Zhou, Y. Shimotsuma, K. Miura and J. Qiu, Opt. Mater. Express, 2014, 4, 213-219.
- 6 S. Gomez de Pedro, A. Salinas-Castillo, M. Ariza-Avidad, Lapresta-Fernández, Sánchez-González, C. S. Martínez-Cisneros, M. Puyol, L. F. Capitan-Vallvey and J. Alonso-Chamarro, Nanoscale, 2014, 6, 6018-6024.
- 7 A. Salinas-Castillo, M. Ariza-Avidad, C. Pritz, M. Camprubí-Robles, B. Fernández, M. J. Ruedas-Rama, A. Megia-Fernández, A. Lapresta-Fernández, F. Santoyo-Gonzalez and A. Schrott-Fischer, Chem. Commun., 2013, 49, 1103-
- 8 X. Wen, P. Yu, Y. R. Toh, X. Ma and J. Tang, Chem. Commun., 2014, 50, 4703-4706.
- 9 Y. Song, S. Zhua and B. Yang, RSC Adv., 2014, 4, 27184-27200.
- 10 C. Wang, X. Wu, X. Li, W. Wang, L. Wang, M. Gu and Q. Li, J. Mater. Chem., 2012, 22, 15522-15525.
- 11 H. Ming, Z. Ma, Y. Liu, K. Pan, H. Yu, F. Wang and Z. Kang, Dalton Trans., 2012, 41, 9526-9531.

- 12 X. W. Tan, A. N. B. Romainor, S. F. Chin and S. M. Ng, J. Anal. Appl. Pyrolysis, 2014, 105, 157-165.
- 13 K. M. Tripathi, A. K. Sonker, S. K. Sonkar and S. Sarkar, RSC Adv., 2014, 4, 30100-30107.
- 14 K. Wang, Z. Gao, G. Gao, Y. Wo, Y. Wang, G. Shen and D. Cui, Nanoscale Res. Lett., 2013, 8, 122-131.
- 15 X. Zhai, P. Zhang, C. Liu, T. Bai, W. Li, L. Dai and W. Liu, Chem. Commun., 2012, 48, 7955-7957.
- 16 L. Hui, Y. X. Xi, Z. J. Jia, L. Y. Fang and H. C. Zhi, Sci. Sin.: Chim., 2013, 43, 895-900.
- 17 X. Xu, R. Ray, Y. Gu, H. J. Ploehn, L. Gearheart, K. Raker and W. A. Scrivens, J. Am. Chem. Soc., 2004, 126, 12736-12737.
- 18 V. Thongpool, P. Asanithi and P. Limsuwan, Procedia Eng., 2012, 32, 1054-1060.
- 19 T. Gokus, R. R. Nair, A. Bonetti, M. Böhmler, A. Lombardo, K. S. Novoselov, A. K. Geim, A. C. Ferrari and A. Hartschuh, ACS Nano, 2009, 3, 3963-3968.
- 20 M. Tan, L. Zhang, R. Tang, X. Song, Y. Li, H. Wu, Y. Wang, G. Lv, W. Liu and X. Ma, Talanta, 2013, 115, 950-956.
- 21 X. Wu, F. Tian, W. Wang, J. Chen, M. Wub and J. X. Zhao, J. Mater. Chem., 2013, 1, 4676-4684.
- 22 X. Dong, Y. Su, H. Geng, Z. Li, C. Yang, X. Li and Y. Zhang, J. Mater. Chem. C, 2014, 2, 7477-7481, DOI: 10.1039/ c4tc01139b.
- 23 Z. Ma, H. Ming, H. Huang, Y. Liu and Z. Kang, New J. Chem., 2012, 36, 861-864.
- 24 S. Sahu, B. Behera, T. K. Maiti and S. Mohapatra, Chem. Commun., 2012, 48, 8835-8837.
- 25 B. De and N. Karak, RSC Adv., 2013, 3, 8286-8290.
- 26 C. Jiang, H. Wu, X. Song, X. Ma, J. Wang and M. Tan, Talanta, 2014, 127, 68-74.
- 27 P. C. Hsu and H. T. Chang, Chem. Commun., 2012, 48, 3984-3986.
- 28 K. Satoa, R. Saito, Y. Oyama, J. Jiang, L. G. Cançado, M. A. Pimenta, A. Jorio, G. G. Samsonidze, G. Dresselhaus and M. S. Dresselhaus, Chem. Phys. Lett., 2006, 427, 117-121.
- 29 A. Jorio, E. H. Martins Ferreira, M. V. O. Moutinho, F. Stavale, C. A. Achete and R. B. Capaz, Phys. Status Solidi B, 2010, 247, 2980-2982.
- 30 L. H. Mao, W. Q. Tang, Z. Y. Deng, S. S. Liu, C. F. Wang and S. Chen, Ind. Eng. Chem. Res., 2014, 53, 6417-6425.
- 31 S. C. Ray, A. Saha, N. R. Jana and R. Sarkar, J. Phys. Chem. C, 2009, 113, 18546-18551.
- 32 K. Hola, A. B. Bourlinos, O. Kozak, K. Berka, K. M. Siskova, M. Havrdova, J. Tucek, K. Safarova, M. Otyepka and E. P. Giannelis, Carbon, 2014, 70, 279-286.
- 33 R. Tian, S. Hu, L. Wu, Q. Chang, J. Yang and J. Liu, Appl. Surf. Sci., 2014, 301, 156-160.
- 34 J. Shen, Y. Zhu, C. Chen, X. Yang and C. Li, Chem. Commun., 2011, 47, 2580-2582.